17th INTERNATIONAL CONGRESS of the Geological Society of Greece

BULLETIN OF THE GEOLOGICAL SOCIETY OF GREECE, SP. PUBL.

EXTENDED ABSTRACT 061

Microfacies and species richness analyses of middle-late Eocene western Thrace Basin (Neotethys Ocean, Greece): Paleoenvironmental evolution and species-richness hotspot revealed

Dimou V.-G.[1], Koukousioura O.[1,2], Less G.[3], Triantaphyllou M.[4], Dimiza M.[4], Syrides G.[1], Langer M.R.[5]

(1) Aristotle University of Thessaloniki, Thessaloniki, Greece, dimouvaso@geo.auth.gr (2) University of Cologne, Cologne, Germany (3) University of Miskolc, Miskolc-Egyetemváros, Hungary (4) National and Kapodistrian University of Athens, Athens, Greece (5) Rheinische Friedrich-Wilhelms-Universität Bonn, Bonn, Germany

The Thrace region is a large Paleogene-Neogene molassic basin in the northern Aegean (Greece, NW Turkey, Bulgaria). Basin architecture is linked to middle-late Eocene NE-SW extension events, that led to the formation of a supra-detachment basin divided into three sub-basins (Alexandroupolis, Orestias and Petrota) that are characterized by a complex stratigraphy (Kopp, 1965; Papanikolaou and Triantaphyllou, 2010; Kilias *et al.*, 2013). The paleoenvironmental evolution and reconstruction of the Thrace basin (Neotethys Ocean, Greece), were carried out with the help of sedimentological, thin section and microfacies analyses (based on e.g., Flügel, 1982) and, above all, the analysis of larger benthic foraminifera (LBF) as proxies for the middle to upper Eocene carbonate deposits and their species richness.

The studied material derived from a total of 7 new sites (sub-basins of Alexandroupolis and Orestias), covering localities on the mainland [Maronia (MAR-1.2), Palagia (S1-3.2), Avantas (AVT1-15.1), Pylaea (PYL1-10) and Didymoticho (DDM1-5)] and the northeastern Aegean islands of Samothraki (SAM1-2.1) and Lemnos (LM1-2.1) (Fig. 1). In addition, results from the Kirki and Fanari sites were included in the present study (Dimou *et al.*, 2021, 2023).

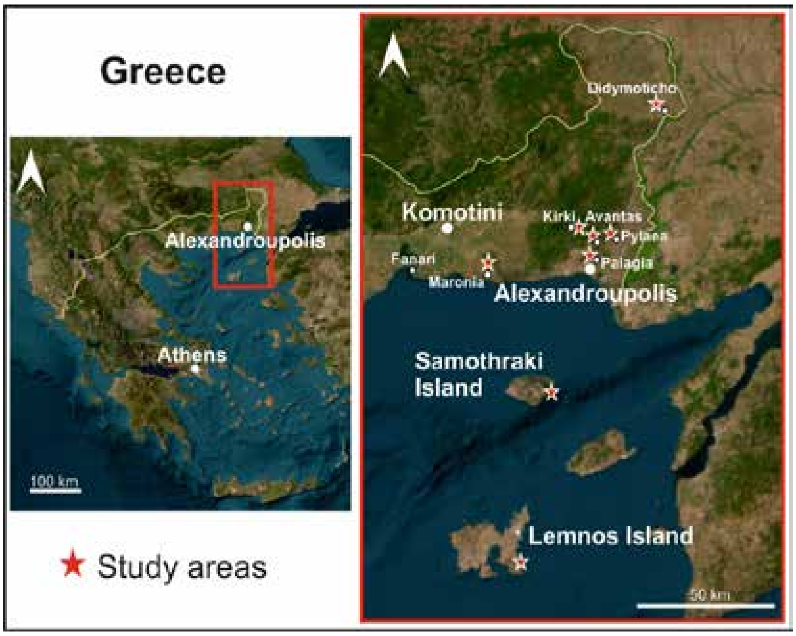

Figure 1. Overview map of Greece with the location of sampled sites marked by red stars (modified from Google Earth, Dimou *et al.*, 2024).

In total, nearly 100 species have been identified. The observed foraminiferal taxa are characterized mainly by benthic foraminifera, while a few planktonic ones were obtained. The assemblage is strongly dominated by calcareous-perforate forms throughout the sequence and less porcelaneous and agglutinated. The calcareous forms are represented by the perforate orders of Rotaliida (>45 species), Vaginulinida (7 species), Polymorphinida (4 species) and Nodosariida (11 species), while porcelaneous forms are represented by *Quinqueloculina* spp. and miliolid casts, that probably belong to more than three genera. Finally, the agglutinated (10 species) forms are represented by the orders of Astrorhizida (4 species), Spirillinida (1 species), Lituolida (2 species) and Textulariida (3 species).

Among them the LBF were very diverse (43 species), with the most abundant *Nummulites fabianii*, *N. incrassatus*, *Heterostegina reticulata*, *Spiroclypeus carpaticus*, *Pellatispira madaraszi*, orthophragmines and *Asterigerina* spp.

The combination of sedimentological features and biogenic components led to the distinction of 5 microfacies types (Table 1). These can be attributed to a sequence of inner to outer shelf environments and support a model of a rimmed carbonate shelf with isolated platforms. Water circulation patterns on and between the platforms were both open and restricted. In particular, the inner shelf is characterized as a restricted environment with vegetation cover and limited water circulation (back-reef settings, MF1 and MF2). The middle shelf refers to the reef-core and platform margins with high energy conditions (MF3a-d), that passes to a lower-energy regime at a fore-reef setting (MF4). Finally, the outer platform refers to its proximal part with maximum depth of 60 m (MF5).

The Thrace Basin region represents a shallow carbonate platform during the middle-late Eocene and comprises two stages of development. Based on the remains of a late Lutetian/early Bartonian assemblage (samples from Kirki; Dimou *et al*., 2021), the existence of an older platform has been suggested, which is either demolished due to the tectonics or underlies a new transgression. The second stage refers to the onset of a late Bartonian to Priabonian platform. The Bartonian is assigned to middle / outer shelf settings and is reported only from Lemnos Island. Unlikely, Priabonian is widespread into the mainland and comprises all three main environments.

During this time interval, the dynamic syn-rifting led to the development of topographic highs, that represent favoring regions on which productive and species-rich reef structures could flourish. Based on an extensive compilation of LBF species richness from the Western Tethys (e.g., Pignatti, 1995; Less *et al*., 2011; Ferràndez-Cañadel *et al.,* 2023), we document in the carbonate deposits of western Thrace basin, well preserved and hyperdiverse, late Eocene assemblages of larger symbiont-bearing foraminifera, characterizing the study area, with 60 species, as a hotspot of LBF diversity in the Neotethys ocean.

Table 1. Summary of distinguished facies and their interpretation.

Major Microfacies (MF) Type	**Texture**	**Main components**	**Minor components**	**Age**	**Paleoenvironmental interpretation**
MF1: encrusting and other rotaliids-miliolids grainstone (PYL10, S3.1.1-S3.1.3)	Sparitic matrix	Encrusting and other rotaliids, coralline red algae, textulariids, miliolids	*Nummulites*	Priabonian (SBZ20)?	Protected environment, lagoon
MF2: Heterosteginid-orthophragminid packstone (AVT5-13.1)	Micritic matrix	Heterosteginids, orthophragminids, coralline red algae	Other nummulitids, small rotaliids, miliolids, agglutinants, bryozoans, corals, molluscs, worm tubes	Priabonian (SBZ20)?	Back reef, close to the reef or as a reef flat
MF3a: coral, coralline red algae, gastropods, aragonite/ magnesian calcite cemented wackestone/ packstone (AVT3-4/14-15, SAM2)	Micritic matrix	Corals, coralline red algae, gastropods, radial fibrous cement	LBF, miliolids, small rotaliids, bryozoans, bivalves, echinoids, ostracods	Priabonian (SBZ20)	Reef core, platform margins
MF3b: Corraline algae, nummulitic, bivalve wackestone/ packstone (MAR1.1, DDM1-5)	Micritic matrix	Coral patches, coralline red algae, nummulitids	Other LBF, small rotaliids, miliolids, planktonic foraminifera, bryozoans, echinoids	Priabonian (SBZ20)	Platform margins, shoal reef areas, patch reef

MF3c: Nummulitic grainstone (MAR, S2F)/ *Assilina alpina*-coral packstone (SAM1)	Sparitic matrix	*Nummulites fabianii, Assilina alpina*	*Operculina* ex. *gr gomezi, Discocyclina* sp., small rotaliids, coralline red algae, molluscs / other nummulitids, *Discocyclina* sp., small rotaliids, *Silvestriella tetraedra*, corals, echinoids, bryozoans	Priabonian (SBZ19)?/ Priabonian (SBZ19B-20)	Platform margins
MF3d: Coralline-LBF wackestone (PYL5-8)	Micritic matrix	Coralline red algae, corals, *Silvestriella tetraedra*	Other LBF, small rotaliids, miliolids, planktonic foraminifera, molluscs	Priabonian (SBZ19-20)	Distal outer platform
MF4: FAN1-16	Micritic matrix	*Nummulites*, small rotaliids	Other LBF, miliolids, planktonic foraminifera, corals, coralline red algae, echinoids, bryozoans, molluscs	Priabonian (SBZ19-20)	Fore-reef
MF5: LBF packstone (PYL1-4,9, LM1-2, AVT1-2, FAN17-21)	Micritic matrix	Orphophragminids, nummulitids	Other LBF, small rotaliids, miliolids, planktonic foraminifera, coralline red algae, echinoids, bryozoans, molluscs, worm tubes	Priabonian (SBZ19-20)	Outer platform

Acknowledgements

The research by V.-G. Dimou was co-financed by Greece and the European Union (European Social Fund-ESF) through the Operational Programme “Human Resources Development, Education and Lifelong Learning” in the context of the Act “Enhancing Human Resources Research Potential by undertaking a Doctoral Research” Sub-action 2, implemented by the Scholarship Programme (IKY) for PhD candidates at Greek Universities.

References

Dimou, V.G., Koukousioura, O., Dimiza, D.M., Triantaphyllou, V.M., Less, G., Pomoni- Papaioannou, F., Syrides, G., 2021. A preliminary investigation of Eocene larger benthic foraminifera assemblages from Alpine and molasse-type deposits of the Hellenic peninsula (Greece). Rev. Micropaleontol., 70, 100468.

Dimou, V.G., Koukousioura, O., Less, G., Triantaphyllou, D.M., Dimiza, V.M., Syrides, G., 2023. Systematic paleontology and biostratigraphy of the upper Eocene Large Benthic Foraminifera of Fanari (Thrace Basin, Greece). Micropaleontology, 69 (4-5), 457-486.

Dimou, V.G., Koukousioura, O., Less, G., Triantaphyllou, D.M., Dimiza, V.M., Syrides, G., 2024. Microfacies and species richness analysis of upper Bartonian and Priabonian carbonate shelf deposits from the Thrace Basin (Tethyan Ocean, Greece): Paleoenvironmental evolution and species-richness hotspot revealed. Marine and Petroleum Geology, 170 (2024) 107126.

Ferràndez-Cañadell, C., Baumgartner-Mora, C., Baumgartner, P.O., Epard, J.-L., 2023. Priabonian (upper Eocene) larger foraminifera from the Helvetic Nappes of the Alps (Western Switzerland): new markers for shallow benthic zones 19-20. Micropaleontology, 69 (4-5), 407-455.

Flügel, E., 1982. Microfacies analysis of limestones. Springer, Berlin Heidelberg New York, 633 pp.

Kilias, A., Falalakis, G., Sfeikos, A., Papadimitriou, E., Vamvaka, A., Gkarlaouni, C., 2013. The Thrace basin in the Rhodope province of NE Greece - a tertiary supradetachment basin and its geodynamic implications. Tectonophysics, 595-596, 90-105.

Kopp, K.O., 1965. Geologie Thrakiens. III: Das Tertiär zwischen Rhodope und Evros. Ann. Géol. Pays Hellén., 16, 315-362.

Less, Gy., Özcan, E., Okay, I.-A., 2011. Stratigraphy and Larger Foraminifera of the Middle Eocene to lower Oligocene shallow-marine units in the northern and eastern parts of the Thrace Basin, NW Turkey. Turkish J. Earth Sci., 20, 793-845.

Papanikolaou, D., Triantaphyllou, M., 2010. Tectonostratigraphic observations in the western Thrace Basin in Greece and correlations with the eastern part in Turkey. Geol. Balcanica, 39 (1-2), 293-294.

Pignatti, J.S., 1995. Biostratigrafia die macroforaminiferi del Paleogene della Maiella nel quadro delle piattaforme periadriatiche. Studi Geol. Camerti sp (1994), 359-405.

17th INTERNATIONAL CONGRESS
of the Geological Society of Greece

BULLETIN OF THE GEOLOGICAL SOCIETY OF GREECE, SP. PUBL.

EXTENDED ABSTRACT 062

Using alternative methods to promote geoheritage: the Koziakas Mt., central Greece, case study.

Dittopoulos Panagiotis Sotirios[1], Chatzipetros Alexandros. [1]
Bsc Geologist
(1) School of Geology, Department of Structural, Historical and Applied Geology, Aristotle University of Thessaloniki, 54124, Greece, geo.dittopoulos@gmail.com

Research Highlights: This study demonstrates how GIS software, specifically QGIS, can effectively communicate geological research results to both the scientific community and the general public, enhancing data accessibility and interpretation while promoting geoheritage.

Introduction

Greece is renowned for its rich geological history, characterized by complex tectonic processes, diverse rock formations, and a plethora of geosites that possess scientific, educational, and cultural value. Among these, Koziakas Mt. in central Greece is an example of impressive geological formations, offering significant opportunities for both scientific research and the promotion of geoheritage. Its mountain range forms the edge of Pindos in the western part of Thessaly and rises imposingly from North to South. It covers a total area of about 400 km², making it an important landmark of the area. Geologically, the area is located at the eastern boundary of the Pindus zone and at the western boundary of the Sub-Pelagonian zone, including the important ophiolitic formations of Koziakas. The Koziakas unit, belonging to the Sub-Pelagonian, is the transitional stage from the Pindus to the Pelagonian zone.

The advent of GIS software suites has revolutionized the way geological data is collected, analyzed, and visualized. Open-source GIS programs, provide cost-effective, efficient and user-friendly platforms to create models and visualizations. These tools are instrumental in overcoming challenges associated with communicating geological information. Nonetheless, the effective communication of such data frequently encounters obstacles, such as the complexity of geological concepts, the limitations of impractical and intricate visual editing software, and the absence of user-friendly scientific data presentation platforms. The latter is of particular importance for the effective promotion of geoheritage. QGIS is the most renowned open-source GIS suite, supported by the largest community of users. This community has developed various methods, including the use of plugins, to address a range of challenges. However, the absence of geological modeling features in existing tools, hinders its adoption for geological 3D applications and visualisations. This paper explores how open-source tools, plugins and innovative visualisation techniques can address these challenges, using Koziakas Mt as a case study.

Methodology

The initial input to the area analysis is the geological maps and field data. For selected study areas, field data are collected, consisting of rock samples, images, linear, planar and point data such as rock formation dip planes, faults and locations of fossil finds. In addition, the input includes satellite orthophotos and Digital Elevation Models from the Hellenic Cadastre (Digital Elevation Model -DEM from the LSO25 project 25 m and LSO25 25 cm orthophotos, Hellenic Cadastre), the paths of the area from hellaspath.gr and OpenStreetMap for accessibility purposes (OpenStreetMap contributors, 2015).

The above, combined with the pre-existing geological knowledge for the area, results in the geological output data consisting of the West to East geological cross sections across the mountain, smaller scale flysch cross sections along the western valley, and fault raster and vector layers. Processing the data in QGIS results in the creation of background layers such as hillshade, slope aspect, contours and multispectral satellite layers, as well as vector layers such as the hydrology network.

For the visual results, the input data consists mainly of the above geological and geomorphological outputs. This is followed by processing through QGIS to create well presentable information layers, and later through the qgis2threejs plugin to structure the data using the three.js JavaScript framework and WebGL technology into a locally running 3D web view model. The layers containing the model's data were selected via the plugin's menu, utilising also the data from the National Cadastre. Furthermore, a custom plane was incorporated to facilitate altitude experiments, concurrently serving as a water level surface to simulate local flooding scenarios. To enhance comprehension of the broader area's orientation, geological planes, and azimuth measurements, the north arrow option was enabled. The map's boundaries were defined using a polygon layer, and the model's background was set to resemble the sky. To enable the user to have multiple layers open simultaneously, one focused on the specific study area and another providing a broader context, the background raster images were separated into two layers: surroundings and background.

The visual outputs are divided into two categories: static and dynamic. The static output comprises 2.5D perspective images, which interpret the geological setting and geomorphology. These images can be used to accompany a digital or printed file. The dynamic output consists of a 3D interactive web model, which showcases all the study's data in multiple layers. This model can be accessed either locally or on the web (as outlined below). The 3D web model can be uploaded for online access, facilitating optimal practicality, via export to an HTML file. Uploading to OneDrive or a similar online drive service platform is then required. The model can be published via Drive2web's free serverless hosting website and viewed through a link on any web browser. The use of a link shortening website can achieve a better optical result. The workflow involved in the publication process can be seen in Figure 1.

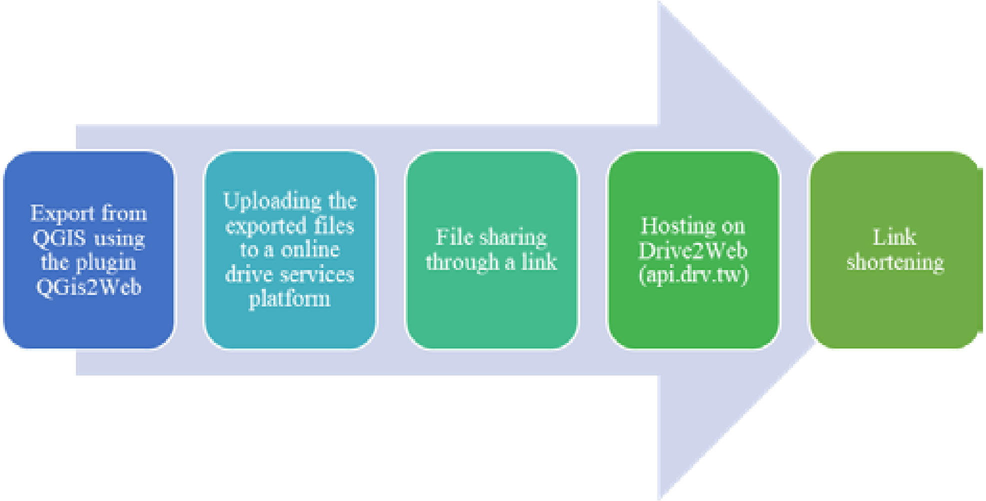

Figure 1. Illustration of the process that was followed from exporting using Qgis2threejs, to the hosting of the model.

Results and conclusions

The geological outcomes of the implemented methodology, which are directly associated with the geological aspect of the study, consist of the 2.5D static images, incorporating the geological cross-sections, as seen in Figure 2. As demonstrated in Figure 3, the integration of the two 2.5D static images in a single illustration serves to emphasize their position in relation to the Koziakas mountain range. The visual results include the most significant element of this study, the 3D web model (Figure 4). The link for the model is the following: https://koziakas-3d-model-qgis2threejs.on.drv.tw/Koziakas%20Website/KoziakasComplete7.html.

Accessible via any web browser, the interactive 3D model provides a detailed visual representation of scientific data while highlighting the geological features of the Koziakas study area. The final model integrates various layers, including geological maps, cross sections, hydrology data, field observations (e.g. fault strike and dip, fossils, faults, and folds), contours, slope aspect maps, hillshade maps, satellite imagery, and nearby hiking trails. The user can create numerous combinations by utilizing all the layers and background data to extract the required information. Background layers, by lacking 3D morphology, place more emphasis on the study region. Hillshade and slope-aspect maps, products from DEM processing from the National Cadastre (Digital Elevation Model -DEM from the LSO25 project (25 m), Hellenic Cadastre), geological maps of IGME (Savoyat and Lalechos, 1972; Karfakis, 1993) and contour topographical map are some of the additional raster layers. Figure 4 displays the model with all information layers activated and Figure 5 demonstrates a different layer combination, showcasing the diverse range of potential applications.

Although not of great significance, the limitations of the plugin have led to the adoption of an alternative visualisation strategy for certain information layers. To address the constraints of the selected plugin and ensure that crucial data remains visible, line elements such as hydrology, faults, and paths have been slightly elevated. Additionally, some product types, like the hillshade-fault map, have been separated into raster and vector layers. This approach mitigates the lower resolution projection caused by the plugin, resulting in improved visualisation. Moreover, the satellite image is observed to exhibit a markedly higher level of clarity when viewed in 3D view within QGIS, in comparison to the final output produced by the Qgis2threejs plugin. Furthermore, it has been demonstrated that the model is efficacious in capturing screenshots, which were subsequently utilized to generate the 2.5D static images.

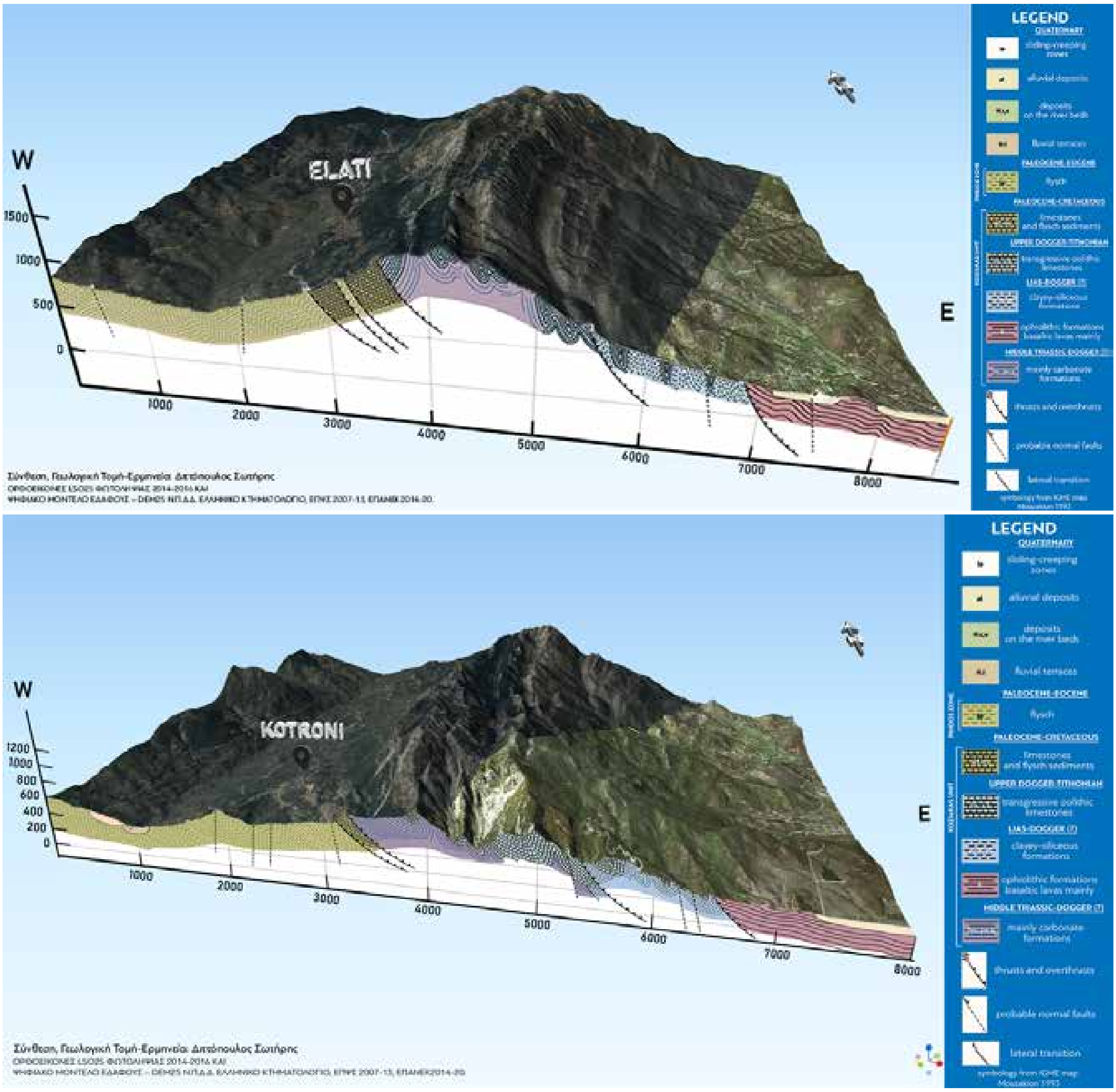

Figure 2. Illustration of the two 2.5D models featuring the geological cross-sections and their respective geological legends. Top: the northernmost geological cross section, located near the settlement of Elati. Bottom: the southernmost geological cross section, located near the settlement of Kotroni. The Qgis2threejs plugin model was utilized to capture the screenshots (Digital Elevation Model -DEM from the LSO25 project (25 m) and LSO25 (25 cm) orthophotos, Hellenic Cadastre).

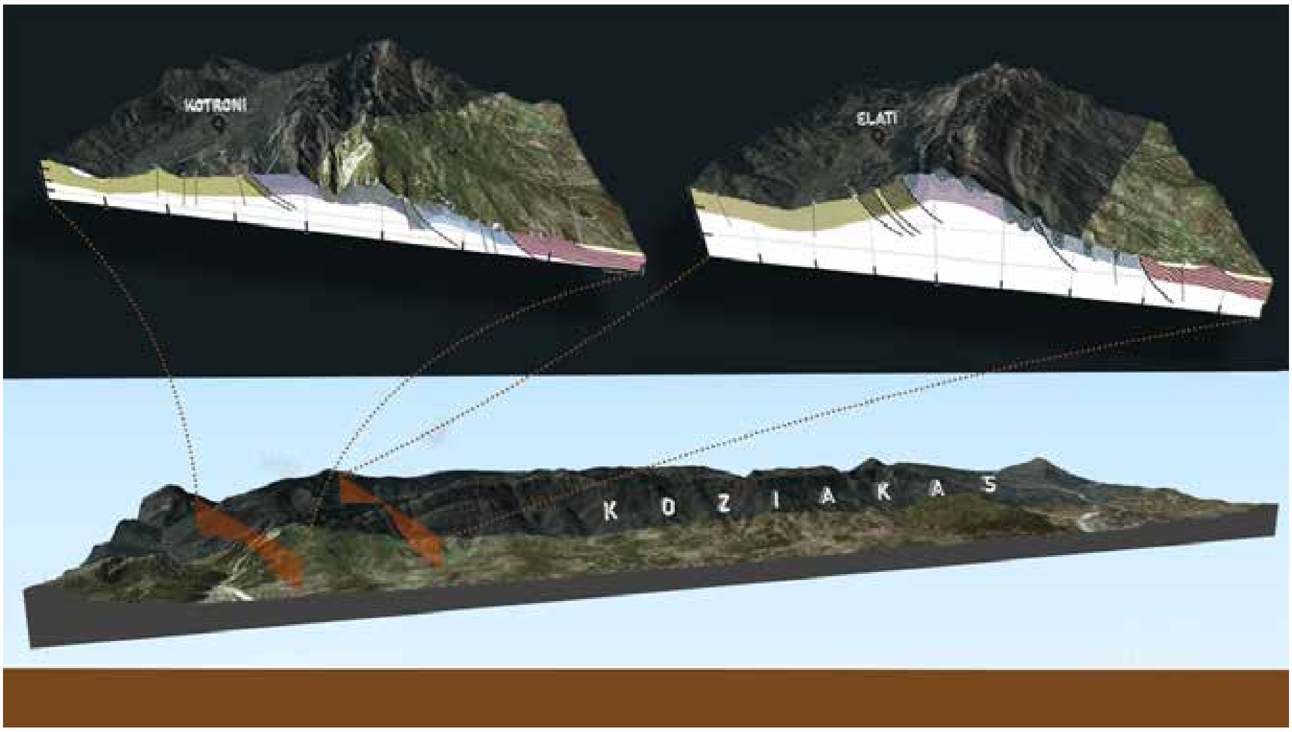

Figure 3. Illustration of the two 2.5D models featuring the geological cross-sections and their position in relation with the Koziakas mountain range. The Qgis2threejs plugin model was utilized to capture the screenshots (Digital Elevation Model -DEM from the LSO25 project (25 m) and LSO25 (25 cm) orthophotos, Hellenic Cadastre).

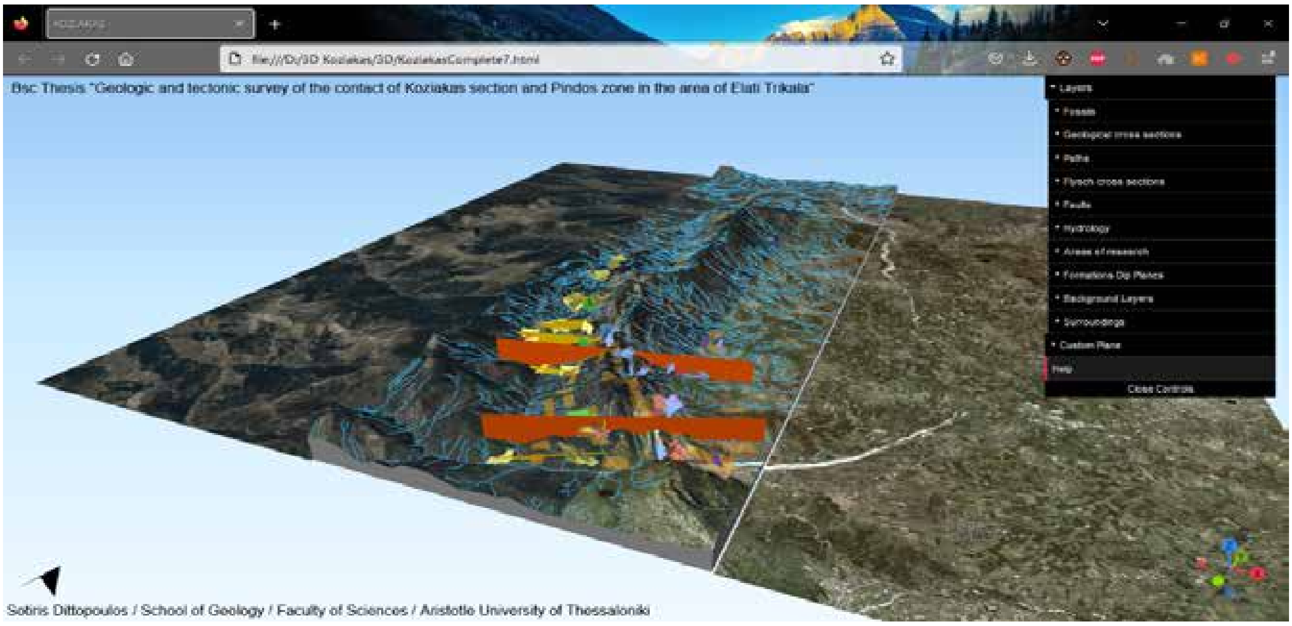

file:///D:/3D Koziakas/3D/KoziakasComplete7.html

Bsc Thesis "Geologic and tectonic survey of the contact of Koziakas section and Pindos zone in the area of Elati Trikala"

Sotiris Dittopoulos / School of Geology / Faculty of Sciences / Aristotle University of Thessaloniki

Figure 4. Screenshot of the model, illustrating the information of three layers: locations of geological cross sections (orange), locations of flysch cross sections (yellow), background layers: high resolution satellite image from the Hellenic Cadastre (Digital Elevation Model -DEM from the LSO25 project (25 m) and LSO25 (25 cm) orthophotos, Hellenic Cadastre).

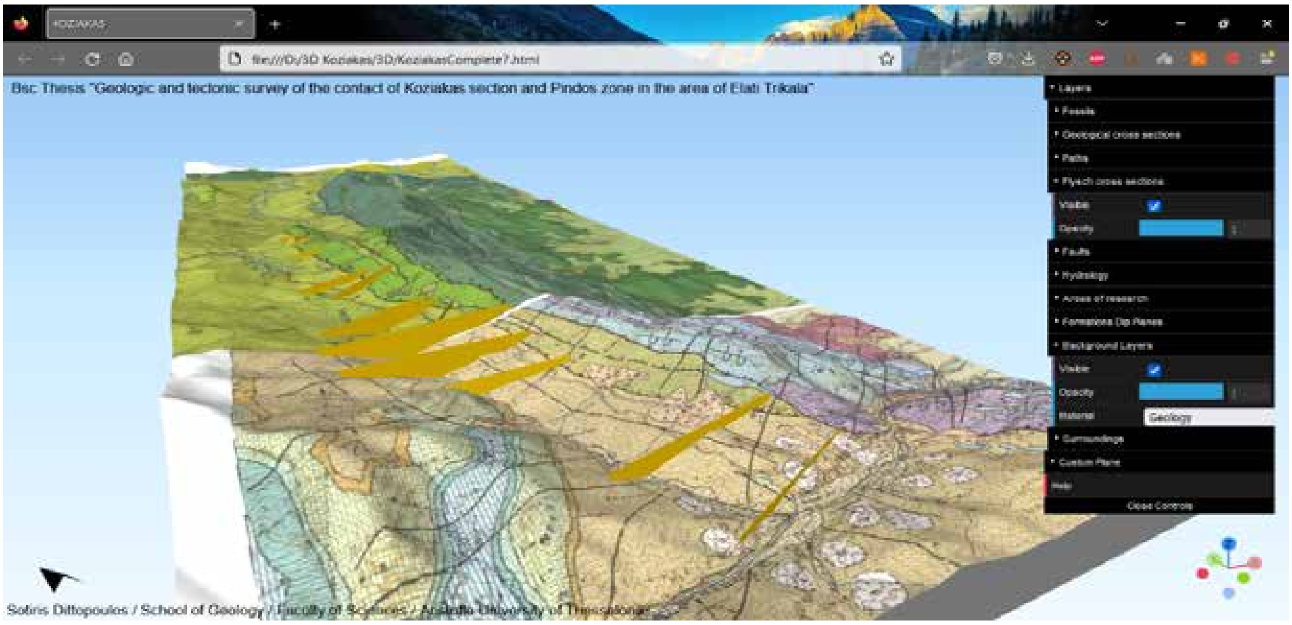

Bsc Thesis "Geologic and tectonic survey of the contact of Koziakas section and Pindos zone in the area of Elati Trikala"

Sotiris Dittopoulos / School of Geology / Faculty of Sciences / Aristotle University of Thessaloniki

Figure 5. Screenshot of the model, illustrating the information of two layers: locations of flysch cross sections and background layer: geological map of IGME (Mouzakion and Kalambaka sheets, Savoyat and Lalechos, 1972; Karfakis, 1993).

Discussion

The process of transforming complex spatial data into clear, visually engaging outputs is often challenging, particularly when using specialized tools such as the Qgis2threejs plugin. Despite its versatility, the plugin requires experimentation to achieve the intended visualizations, as its performance can be heavily influenced by the underlying hardware. Exporting data, especially in high-resolution formats, can take several hours on systems with outdated or insufficient processing power. To enhance the workflow and optimize efficiency, it is essential to ensure that the hardware capabilities are in alignment with the demands of QGIS and its extensions.

Regarding the enhancements that could be made to improve the end result, one of the primary concerns is the potential to incorporate a geological cross-section illustration within the interactive model. Furthermore, the hydrographic network could be segmented into branches (for example, according to Strahler's classification), integrated into the river basins and accompanied by river name labels. Another significant enhancement would be the capability to include images of the features, visible upon selection. To optimise the presentation for educational purposes, a camera flight plan could be devised to guide the viewer upon entering the model. Faults could be accompanied by arrows, indicating the movement direction, and paths could be equipped with additional information such as distance and estimated walking time. The incorporation of videos and descriptions could further augment the model, resulting in a comprehensive interactive webpage that offers a detailed exposition of the study area.

The Qgis2threejs plugin offers a significant advantage in its ability to export 3D models in the glTF format. This format is a widely recognized standard for 3D computer graphics (3DCG) and 3D printing. This capability opens opportunities for users to move beyond traditional GIS applications, enabling the creation of interactive 3D visualizations or detailed physical models. The potential of these models is significant for the effective promotion and preservation of geoheritage through digital innovation. The visualizations created with this tool facilitate a deeper engagement with geological and cultural heritage sites, providing users with virtual access to areas that may be difficult to visit physically due to geographic or environmental constraints. Moreover, this creates a dynamic way to educate the public about their geological history. Studies have shown that dynamic visualization has a greater positive impact on educational outcomes compared to static visualization. This effect is particularly evident in the learning results and intrinsic motivation of science students, especially in subjects like Biology, Chemistry, and Geology. As highlighted by e.g. Berney & Bétrancourt (2016) and Teplá et al. (2022), dynamic visualization can enhance attention and more effectively demonstrate abstract procedures (Ayres et al. 2009; Schwan & Riempp 2004; Teplá et al. 2022) and processes that change over space and time (Ainsworth & VanLabeke 2004; Rieber 1990; Schnotz & Lowe 2003; Teplá et al. 2022). Furthermore, the 3D printing allows the physical replicas of geoheritage, and features such as rock formations, fossil sites, faults and folds, to be produced and displayed in educational institutions, museums, or cultural centres. The potential for these models to foster appreciation and awareness is significant, and their capacity to aid in conservation efforts is equally noteworthy.

Acknowledgements

We would like to express our gratitude to the local community of Elati, for their collaboration and the valuable information provided regarding the accessibility of the area. Additionally, we would like to thank the Legal Entity of Public Law Hellenic Cadastre for providing the Digital Elevation Model and Orthophotos used in our analysis.

References

Berney, S., & Bétrancourt, M. (2016). Does animation enhance learning? A meta-analysis. Computers & Education, 101, 150-167.

Karfakis I. (1993). Geological map of Greece, 1:50,000 scale – Mouzakion sheet. Institute of Geological and Mineral Exploration, Athens, Greece.

Savoyat E. and Lalechos N. (1972). Geological map of Greece, 1:50,000 scale – Kalambaka sheet. Institute of Geological and Mineral Exploration, Athens, Greece.

Teplá, M., Teplý, P. & Šmejkal, P. Influence of 3D models and animations on students in natural subjects. IJ STEM Ed 9, 65 (2022). https://doi.org/10.1186/s40594-022-00382-8

Tools

Drive2Web: https://api.drv.tw/

[Github user] Minorua. (2024). Qgis2threejs plugin for QGIS 3.4.0. Originally written by Minoru Akagi. Version 2.7.3. Retrieved from https://github.com/minorua/Qgis2threejs [Accessed: March 30, 2024]

Digital data

Digital Elevation Model -DEM from the LSO25 project (25m), Hellenic Cadastre. Available online: https://www.ktimanet.gr/geoportal/catalog/search/resource/details.page?uuid=%7B2945C504-A861-4CB9-B086-B6244E0D08EF%7D [Accessed: March 30, 2024]

LSO25 (25cm) orthophotos, Hellenic Cadastre. Available online: https://www.ktimanet.gr/geoportal/catalog/search/resource/details.page?uuid=%7B6803818C-284B-442F-8185-707FDB654A22%7D [Accessed: March 30, 2024]

HellasPath: http://www.hellaspath.gr/

One Drive Microsoft: https://onedrive.live.com

OpenStreetMap contributors. (n.d.). OpenStreetMap. Retrieved [Accessed: March 30, 2024], from https://www.openstreetmap.org

Assessment of fault hazard in the broader area of Sitia, Eastern Crete

Dretaki A.[1], Chatzipetros A.[1]
(1) School of Geology, Aristotle University of Thessaloniki, , Greece, antoniadret@hotmail.com

Research Highlights: Potential earthquake magnitudes for fault zones in Eastern Crete were determined using empirical relationships, highlighting significant seismic hazards. The Ierapetra, Mesa Mouliana, Sitia, and Xerocampos-Goudouras Fault Zones are identified as the most active and hazardous in the area, indicating the need for further research.

The area of Crete is one of the most tectonically active in Greece and its study has been at the centre of interest of many researchers. Eastern Crete is considered to be the area where 80% of the future normal fault earthquakes will occur (Nicol *et al.,* 2020), so seismic hazard assessment is a necessity. The Ierapetra fault zone is considered the most dangerous and important, as two major earthquakes have occurred in the past, destroying completely the city of Ierapetra. Therefore, the mapping and analysis of the area's major fault zones can provide substantial insight into the seismic hazard of the region.

The study area is located in the eastern part of Lasithi and includes the municipality of Sitia and part of the municipality of Ierapetra. It is characterised by a relatively mountainous landscape with numerous gorges formed in the limestone bedrock. The geological structure of the area, from the lowest to the highest units, consists of the following units: Plattenkalk unit, Tripali unit, Phyllite-Quartzite unit *s. str.,* the pre-alpine basement, the Tyros Unit, the Tripoli Unit, the Pindos Unit and then, above all, the younger post-alpine sedimentary series (Fassoulas, 1995, ten Veen and Postma, 1999, Seidel, 1968; Krahl *et al.*, 1983; Zulauf *et al.,* 2008, Klein *et al.,* 2008, Mountrakis, 2010, Krahl *et al.,* 1986; Zulauf *et al.,* 2013, Robertson, 2006; Robertson, 2008; Robertson, 2022).

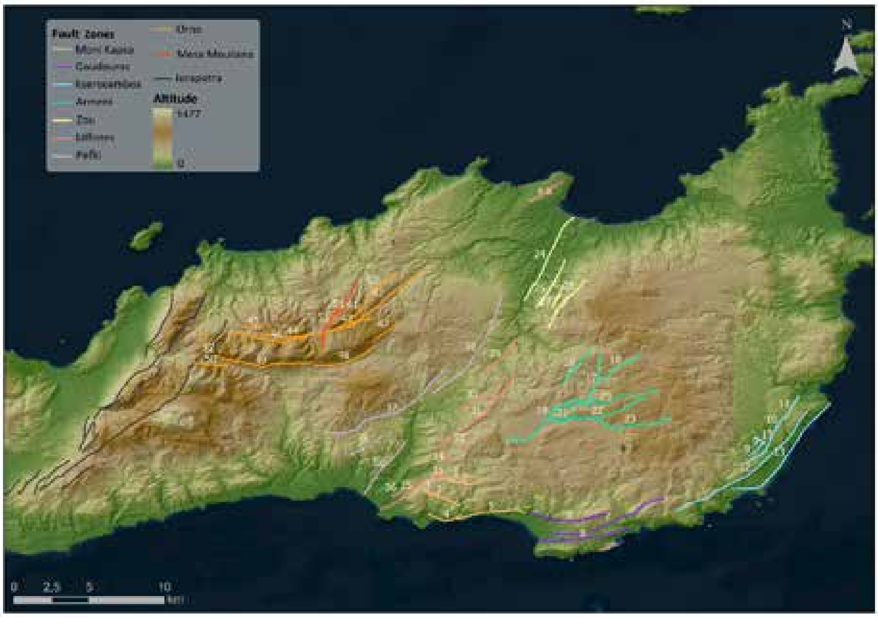

Figure 1. Neotectonic map of fault zones and numbered segments referred on Tables 1 to 3 (Dretaki, 2024). For source of the DEM see text for details.

Active faults in the area are normal or normal-oblique ones. They are numerous and can be grouped into two main trends: the NNE-SSW trending fault group and the E-W to ESE-WNW trending fault group. The Ierapetra Fault Zone, as mentioned above, has been mapped and analysed in detail. Other fault zones mentioned in previous research include the Sitia Fault Zone and other minor offshore and onshore structures, such as the Goudouras Fault, the Mouliana Fault and the Orno Fault (ten Veen and Postma, 1999, Caputo *et al.,* 2010, Caputo and Pavlides, 2013, Mason *et al.,* 2016, Pavlides *et al.,* 2018, Veliz *et al.,* 2018, Mechernich et *al.,* 2023). On 12 October 2021, an M 6.3 earthquake occurred on an offshore NNE-SSW fault, its focal mechanism (data from the National Observatory of Greece, Dretaki *et al.,* 2022), showed that the active stress field is compatible with several onshore fault zones and indicating the need for further research into the tectonic activity of the area.

To estimate the seismic hazard, empirical relationships are used that relate the surface rupture (L) to the energy released by the earthquake (magnitude Ms) (Pavlides, 2016). Many researchers have already calculated the possible magnitudes of some faults in the area and the results are shown in Table 1.

During the field mapping, measurements of faults and structures were taken where possible. Then, using ArcGIS Pro software, they were analysed and correlated with the satellite imagery and DEM in order to better map them in the field. From the above analysis, the structures were divided into five fault zones, Xerocampos - Goudouras, Sitia, Orno, Mesa Mouliana and Ierapetra (Figure 1). Each was divided into individual fault subzones based on their segmentation and correlated with the satellite data, Digital Elevation Model (Data Source: Legal Entity of Public Law Hellenic Cadastre, Operational Programme Competitiveness, Entrepreneurship and Innovation 2014-2020 (EPAnEK)) and digitized geological map (IGME 1959). The hydrographic network was also used, since the way it develops can be strongly influenced by the tectonic regime of a region.

All of the above, combined with the analysis of morphotectonic indices and data published in the literature, led to the assessment of the activity of each zone. Then, the seismic hazard was calculated, using empirical relationships, for each segment of sufficient length, combinations of segments, the entire fault zone, combinations of fault zones and the entire deformation zone. For the calculation of the Ms magnitude of the faults the empirical relationships of Wells & Coppersmith (1994), Papazachos *et al.* (2004) and Pavlides & Caputo (2004) were used

First, the surface length L or SRL (Surface Rupture Length) of each section was calculated separately in km using the ArcGIS Pro application for the mapped sections. Then the values of the potential magnitudes and the Maximum Vertical Displacement (MVD) were calculated. The values were calculated for each individual segment, combinations of segments and the whole zone and the results are shown in Tables 1, 2 and 3.

Previous work in the area (Dretaki, 2024) confirmed that both groups are active, with the NNE-SSW faults being more active than the E-W ones. The above analysis, in addition with previous studies, shows that the Ierapetra, Mesa Mouliana, Sitia and Xerocampos - Goudoura Fault Zones are the most active in the region. In the Ierapetra Fault Zone there are historical records of its activation. Segment 52 (Figure 1), which was recently mapped during fieldwork (Dretaki, 2024), shows evidence of activity as it deforms recent deposits and has the potential for a magnitude Ms 5.7 event (Pavlides and Caputo, 2004). Further investigation of this fault segment is considered important. The Mesa Mouliana Fault Zone is considered to be as active as the Ierapetra one, with potential similar to that of Lastros fault (Mechernich et al. 2023), with calculated Ms 5.7 (Pavlides and Caputo, 2004). It intersects the Orno Fault Zone, which is also considered to be active, creating strong relief and slope debris have been deposited in the hanging wall. Orno fault has a potential magnitude of Ms 6.8 (Pavlides and Caputo, 2004). Sitia Fault Zone is an active zone with signs of activity migration towards the centre of the basin. The younger parts of it intersect the Neogene deposits, but more importantly they intersect the beachrocks of Sitia beach, indicating that it was active during the Holocene. The activation of the entire fault zone could cause an earthquake of Ms 7.1 (Pavlides and Caputo, 2004), similar to Ierapetra and Xerocambos-Goudouras Fault Zones. Xerocampos Fault Zone, as well as the large expected earthquake magnitude derived from empirical relationships, appears to be part of the same system as the 12 October 2021 earthquake.

Based on the above, as well as the results from Tables 1 to 3, we can conclude that further research on each area is mandatory. This research could include the monitoring of micro-movements by installing instruments in the most active sections, geophysical surveys and paleoseismological trenching. Although the study area is the least developed in terms of tourism compared to the rest of Crete, it receives many visitors each year. Combined with the permanent population, especially in the settlements close to the fault zones, the seismic risk of the area is greatly increased due to the age of most of the settlements, the short distance from the seismic sources and the permanent human presence.

Table 1. Xerocambos – Goudouras Fault Zone

Fault zone	Segment	Length	Wells & Coppersmith (1994)	Papazachos et al. (2004)		Pavlides & Caputo (2004)			
		km	Ms	M	MD (m)	+	Ms	-	MVD (m)
Moni Kapsa	1+2+3	7.0	6.0	5.4		6.4	6.2	5.6	0.20
	4+5	5.8	5.9	5.2		6.4	6.2	5.4	0.16
	1+2+3+4+5	12.8	6.3	5.9		6.7	6.5	5.9	0.37
Goudouras	6	4.4	5.7	5.0		6.2	6.1	5.3	0.12
	7	6.9	6.0	5.4		6.4	6.2	5.5	0.19
	8	5.0	5.8	5.1		6.3	6.1	5.4	0.14
	6+7	11.3	6.3	5.8		6.7	6.4	5.9	0.32
	6+8	9.4	6.1	5.7		6.6	6.4	5.7	0.27
	7+8	11.8	6.3	5.9		6.7	6.4	5.9	0.34
	6+7+8	16.3	6.5	6.1	0.40	6.8	6.6	6.1	0.47

Fault zone	Segment	Length	Wells & Coppersmith (1994)	Papazachos et al. (2004)		Pavlides & Caputo (2004)			
Xerocampos	9	1.5	5.1	4.1		5.8	5.6	4.6	0.04
	12	10.1	6.2	5.7		6.6	6.4	5.8	0.29
	13	8.3	6.1	5.6		6.5	6.3	5.7	0.24
	14+15	0.9	4.8	3.6		5.6	5.4	4.3	
	10+11	5.6	5.8	5.2		6.3	6.2	5.4	0.16
	9+10+11	7.1	6.0	5.4		6.5	6.2	5.6	0.20
	12+13	18.4	6.5	6.2	0.48	6.9	6.6	6.2	0.53
	9+10+11+12+13	25.5	6.7	6.5	0.77	7.0	6.7	6.4	0.74
	9+10+11+12+13+14+15	26.4	6.7	6.6	0.80	7.0	6.8	6.4	0.77
Moni Kapsa + Goudoura	5+6	8.2	6.1	5.5		6.5	6.3	5.7	0.23
	4+5+6	10.2	6.2	5.7		6.6	6.4	5.8	0.29
	All segments	29.1	6.8	6.6	0.93	7.1	6.8	6.4	0.85
Goudouras + Xerocambos	8+12	15.1	6.4	6.1	0.36	6.8	6.5	6.0	0.43
	7+12	17.0	6.5	6.2	0.43	6.8	6.6	6.1	0.49
	7+13	15.1	6.4	6.1	0.36	6.8	6.5	6.0	0.43
	8+13	13.3	6.3	6.0	0.30	6.7	6.5	6.0	0.38
	7+8+12+13	30.2	6.8	6.7	0.98	7.1	6.8	6.5	0.88
	All segments	42.7	7.0	7.0	1.61	7.2	6.9	6.7	1.26
Moni Kapsa + Goudouras + Xerocambos	All segments	55.5	7.2	7.2	2.35	7.3	7.1	6.8	1.65

Table 2. Sitia Fault Zone

Fault zone	Segment	Length	Wells & Coppersmith (1994)	Papazachos et al. (2004)		Pavlides & Caputo (2004)			
		km	Ms	M	MD (m)	+	Ms	-	MVD (m)
Armeni	20	6.1	5.9	5.3		6.4	6.2	5.5	0.17
	22	5.7	5.9	5.2		6.4	6.2	5.4	0.16
	23	4.6	5.7	5.0		6.3	6.1	5.3	0.13
	16+19	8.8	6.1	5.6		6.5	6.3	5.7	0.25
	17+18	6.0	5.9	5.3		6.4	6.2	5.5	0.17
	16+17+18+19	14.8	6.4	6.1		6.8	6.5	6.0	0.43
	19+20	12.3	6.3	5.9		6.7	6.5	5.9	0.35
	21+22+23	11.9	6.3	5.9		6.7	6.4	5.9	0.34
	16 to 23	32.9	6.9	6.8	1.10	7.1	6.8	6.5	0.96
Zou	24	6.2	5.9	5.3		6.4	6.2	5.5	0.17
	25	3.6	5.6	4.8		6.2	6.0	5.2	0.10
	28	3.8	5.6	4.9		6.2	6.0	5.2	0.10
	26+27+28	6.2	5.9	5.3		6.4	6.2	5.5	0.17
	24+25	9.8	6.2	5.7		6.6	6.4	5.8	0.28
	24+25+26+27	12.2	6.3	5.9		6.7	6.5	5.9	0.35
	24 to 28	16	6.4	6.1	0.39	6.8	6.6	6.1	0.46

Fault zone	Segment	Length	Wells & Coppersmith (1994)	Papazachos et al. (2004)		Pavlides & Caputo (2004)			
Lithines	29	3.4	5.6	4.8		6.1	6.0	5.1	0.09
	30	1.9	5.2	4.3		5.9	5.7	4.8	0.05
	31	6.7	6.0	5.4		6.4	6.2	5.5	0.19
	35	4.9	5.8	5.1		6.3	6.1	5.3	0.14
	29+30	5.3	5.8	5.2		6.3	6.1	5.4	0.15
	35+36	6.1	5.9	5.3		6.4	6.2	5.5	0.17
	29+30+31	12	6.3	5.9		6.7	6.5	5.9	0.34
	32+33+34+35	6.9	6.0	5.4		6.4	6.2	5.5	0.19
	32+33+34+35+36	8.7	6.1	5.6		6.5	6.3	5.7	0.25
	30+31+32+33+34	10.63	6.2	5.8		6.6	6.4	5.8	0.30
	30+31+32+33+34+35+36	16.73	6.5	6.2	0.42	6.8	6.6	6.1	0.48
	29 to 36	20.1	6.6	6.3	0.54	6.9	6.7	6.2	0.58
Pefki	37	7.9	6.0	5.5		6.5	6.3	5.6	0.22
	38	8.5	6.1	5.6		6.5	6.3	5.7	0.24
	39	2.2	5.3	4.4		5.9	5.8	4.9	0.06
	40	4.2	5.7	5.0		6.2	6.0	5.2	0.12
	37+38	16.4	6.5	6.1	0.41	6.8	6.6	6.1	0.47
	38+39	10.7	6.2	5.8	0.01	6.6	6.4	5.8	0.30
	38+39+40	14.9	6.4	6.1	0.35	6.8	6.5	6.0	0.43
	37+38+39+40	22.8	6.7	6.4	0.65	7.0	6.7	6.3	0.66
Zou + Lithines	All segments	36.1	6.9	6.8	1.26	7.2	6.9	6.6	1.06
Zou + Pefki	All segments	38.8	7.0	6.9	1.40	7.2	6.9	6.6	1.14
Pefki + Lithines	All segments	42.9	7.0	7.0	1.62	7.2	6.9	6.7	1.26
Armeni + Lithines	All segments	53.0	7.1	7.2	2.19	7.3	7.0	6.8	1.57
Zou + Lithines + Pefki	All segments	58.9	7.2	7.3	2.55	7.4	7.1	6.9	1.75
Zou + Lithines + Pefki + Armeni	All segments	91.7	7.5	7.6	4.84	7.6	7.2	7.1	2.76

Table 3. Orno, Mesa Mouliana and Ierapetra Fault Zone

Fault zone	Segment	Length	Wells & Coppersmith (1994)	Papazachos et al. (2004)		Pavlides & Caputo (2004)			
		km	Ms	M	MD (m)	+	Ms	-	MVD (m)

Fault zone	Segment	Length	Wells & Coppersmith (1994)	Papazachos et al. (2004)		Pavlides & Caputo (2004)			
Orno	43	6.7	5.9	5.4		6.4	6.2	5.5	0.19
	44	2.8	5.5	4.6		6.0	5.9	5.0	0.08
	45	2.7	5.4	4.6		6.0	5.9	5.0	0.07
	46	1.4	5.0	4.0		5.7	5.6	4.6	0.04
	47	5.4	5.8	5.2		6.3	6.1	5.4	0.15
	48	1.9	5.2	4.3		5.9	5.7	4.7	0.05
	49	3.8	5.6	4.9		6.2	6.0	5.2	0.10
	50	5.7	5.9	5.2		6.4	6.2	5.4	0.16
	51	1.8	5.2	4.2		5.9	5.7	4.7	0.05
	41+42	4.0	5.7	4.9		6.2	6.0	5.2	0.11
	43+44	9.5	6.1	5.7		6.6	6.4	5.7	0.27
	41+42+43+44	9.5	6.1	5.7		6.6	6.4	5.7	0.27
	43+44+45	12.2	6.3	5.9		6.7	6.5	5.9	0.35
	45+46	4.1	5.7	4.9		6.2	6.0	5.2	0.11
	43+44+45+47	17.6	6.5	6.2	0.45	6.8	6.6	6.1	0.51
	43 to 47	18.9	6.5	6.3	0.50	6.9	6.6	6.2	0.55
	41+42+43+44+45+46+48	20.8	6.6	6.4	0.57	6.9	6.7	6.2	0.60
	48+49	5.6	5.9	5.2		6.4	6.2	5.4	0.16
	48+49+50	11.3	6.3	5.8		6.7	6.4	5.9	0.32
	49+50	9.4	6.1	5.7		6.6	6.4	5.7	0.27
	50+51	7.5	6.0	5.5		6.5	6.3	5.6	0.21
	49+50+51	11.3	6.2	5.8		6.7	6.4	5.9	0.32
	48+49+50+51	13.1	6.3	6.0	0.29	6.7	6.5	5.9	0.38
	41 to 51	32.0	6.8	6.7	1.06	7.1	6.8	6.5	0.94
Mesa Mouliana	51	5.2	5.8	5.2		6.3	6.1	5.4	0.15
Ierapetra	52	1.6	5.1	4.1		5.8	5.7	4.6	0.04

Acknowledgements

The authors would like to acknowledge the invaluable support and contributions that made this research possible. The first author is grateful to Sotiris Dittopoulos, BSc geologist, for his collaboration and assistance. The authors would also like to thank the *Geositia project* for Sitia UNESCO Global Geopark, during which many field data were collected and presented as part of the project deliverables. The administration of the Geopark, as well as the Municipality of Sitia through MADES S.A. provided financial support for part of the research, and their contribution is greatly appreciated. The Digital Elevation Model used in the analysis was kindly provided by the Legal Entity of Public Law Hellenic Cadastre. This paper summarizes part of the first author's MSc Thesis at the University of the Aegean, completed under the Inter-Institutional «Natural Hazards and Disaster Mitigation» Master Course programme. The contributions of Professor Emeritus Spyros Pavlides (Aristotle University of Thessaloniki) and Dr Charalambos Fassoulas (Natural History Museum of Crete of the University of Crete) were crucial, pivotal and greatly improved the Thesis text; the authors would like to express their sincere gratitude towards them.

References

Caputo, R., Pavlides, S., 2013. The Greek Database of Seismogenic Sources (GreDaSS), version 2.0.0: A compilation of potential seismogenic sources (Mw > 5.5) in the Aegean Region. doi:10.15160/unife/gredass/0200

Caputo, R., Catalano, S., Monaco, C., Romagnoli, G., Tortorici, G., Tortorici, L., 2010. Active faulting on the island of Crete (Greece). Geophysical Journal International, 183(3), 111-126. doi:10.1111/j.1365-246x.2010.04749.x

Dretaki, A., Chatzipetros, A., Psomadakis, S., 2022. Site effects and surface deformation associated with the M 6.3 Sitia (eastern Crete). 16th International Congress of the Geological Society of Greece, Bulletin of the Geological Society of Greece, Sp. Publ. 10, p. 418-419. Patra.

Dretaki, A., 2024. Neotectonic study of Sitia area, eastern Crete, and assessment of the faults' seismic potential. Master Thesis, School of Geography, University of the Aegean, Inter-Institutional Postgraduate Studies Program "Natural Hazards and Disaster Mitigation", 236 pp.

Fassoulas, Ch., 1995. Kinematics and deformation of the nappe pile of Central Crete: Aristotle University of Thessaloniki, Phd thesis (in greek).

IGME., 1959. Geological map of Greece, scale 1:50.000 - sheet ZIROS. Athens: IGME.

IGME., 1959. Geological map of Greece, scale 1:50,000 - sheet IERAPETRA. Athens: IGME.

IGME., 1959. Geological map of Greece, scale 1:50,000 - sheet SITEIA. Athens: IGME.

Klein, T., Reichhardt, H., Klinger, L., Grigull, S., Wostal, G., Kowalczyk, G., Zulauf, G., 2008. Reverse slip along the contact Phyllite-Quartzite Unit/Tripolitsa Unit in eastern Crete: implications for the geodynamic evolution of the External Hellenides. Zeitschrift der deutschen Gesellschaft für Geowissenschaften, 159(3), 375-398. doi:https://doi.org/10.1127/1860-1804/2008/0159-0375

Mason, J., Schneiderwind, S., Pallikarakis, A., Wiatr, T., Mechernich, S., Papanikolaou, I., Reicherter, K., 2016. Fault structure and deformation rates at the Lastros-Sfaka Graben, Crete. Tectonophysics, 638, 216-232. doi:https://doi.org/10.1016/j.tecto.2016.06.036

Mechernich, S., Reicherter, K., Deligiannakis, G., Papanikolaou, I., 2023. Tectonic geomorphology of active faults in Eastern Crete (Greece) with slip rates and earthquake history from cosmogenic 36Cl dating of the Lastros and Orno faults. Quaternary International, 651, 77-91. doi:https://doi.org/10.1016/j.quaint.2022.04.007

Mountrakis, D., 2010. Geology And Geotectonic Evolution Of Greece (1st ed.). Thessaloniki: University Studio Press.

Nicol, A., Mouslopoulou, V., Begg, J., Oncken, O., 2020. Displacement accumulation and sampling of paleoearthquakes on active normal faults of Crete in the eastern Mediterranean. Geochemistry, Geophysics, Geosystems. doi:10.1029/2020gc009265

Papazachos, B., Skordilis, E., Panagiotopoulos, D., Papazachos, C., Karakaisis, G., 2004. Global relations between seismic fault parameters and moment magnitude of earthquakes. Bulletin of the Geological Society of Greece, 36(3), 1482-1489.

Pavlides, S., Caputo, R., 2004. Magnitude versus faults' surface parameters: quantitative relationships from the Aegean Region. Tectonophysics, 380(3-4), 159-188. doi:10.1016/j.tecto.2003.09.019

Pavlides, S., 2016. Geology of earthquakes (2nd ed.). Thessaloniki: University Studio Press.

Pavlides, S., Chatzipetros, A., Sboras, S., 2018. Active faults as seismogenic sources in the Aegean region. 9th International INQUA Meeting on Paleoseismology, Active Tectonics and Archeoseismology. Possidi

Robertson, A., 2006. Sedimentary evidence from the south Mediterranean region (Sicily, Crete, Peloponnese, Evia) used to test alternative models for the regional tectonic setting of Tethys during Late Palaeozoic-Early Mesozoic time. Geological Society, London, Special Publications, 260(1), 91-154.

Robertson, A., 2022. Palaeozoic-Early Mesozoic transition from Palaeotethys to Neotethys: Synthesis of data and interpretations from the northern periphery of Gondwana (central and western Anatolia, Aegean, Balkans and Sicily). Earth-Science Reviews, 230.

Ten Veen, J., Postma., 1999. Neogene tectonics and basin fill patterns in the Hellenic outer-arc (Crete, Greece). . Basin Research, 11(3), 223–241. doi:10.1046/j.1365-2117.1999.00097.x

Veliz, V., Mouslopoulou, V., Nicol, A., Fassoulas, C., Begg, J., Oncken, O., 2018. Millennial to million year normal-fault interactions in the forearc of a subduction margin, Crete, Greece. Journal of Structural Geology, 113, 225-241. doi:10.1016/j.jsg.2018.05.019

Wells, D., Coppersmith, K., 1994. New empirical relationships among magnitude, rupture length, rupture width, rupture area, and surface displacement. Bulletin of the seismological Society of America, 84(4), 974-1002.

Zulauf, G., Blau, J., Dorr, W., Klein, T., Krahl, J., Kustatscher, E., Petschick, R., Van De Schootbrugge, B., 2013. New U-Pb zircon and biostratigraphic data of the Tyros Unit, eastern Crete: Constraints on Triassic palaeogeography and depositional environment of the eastern Mediterranean. Zeitschrift Der Deutschen Gesellschaft Fur Geowissenschaften, 164(2). doi:https://doi.org/10.1127/1860-1804/2013/0009

Zulauf, G., Kowalczyk, G., Krahl, J., Romano, S., 2008. The Mirsini syncline of eastern Crete, Greece: a key area for understanding. At P. Xypolias, G. Zulauf, New results and Concepts on the Regional. Z. dt. Ges. Geowiss.

17th INTERNATIONAL CONGRESS
of the Geological Society of Greece

BULLETIN OF THE GEOLOGICAL
SOCIETY OF GREECE, SP. PUBL.

EXTENDED ABSTRACT 064

Formation of Sitia’s Geopark (Crete Island, Greece) caves in correlation with the structural setting of the area

Dretaki Antonia.[1], Dittopoulos Panagiotis Sotirios[1], Chatzipetros Alexandros[1], Papavasiliou Vasilios[2], Papavasiliou Vasilios[3], Paspaliaris Nikolaos[2], Tsirakakis Georgios[2], Perakis Evangelos[4]

(1) Department of Structural, Historical and Applied Geology, School of Geology Aristotle University of Thessaloniki, 54124, Greece, antoniadret@hotmail.com (2) FORSS, Sitia, Greece (3) Mountaineering Club of Hania, Chania, Greece (4) Sitia UNESCO Global Geopark

Research Highlights: The Sitia Geopark caves, including Pelekita, Kato Peristeras, Ano Peristeras, Chonos, and Vreiko, demonstrate significant tectonic influences on their formation. The tectonic setting, marked by E-W and NNE-SSW faults, shapes the orientation and development of these caves.

Introduction and background

The region of Sitia, distinguished by its topography marked by rugged mountains, intense tectonic activity, and a rich karst landscape, hosts several caves that are of significant historical importance in Greece. Consequently, the area has become a focal point for speleological studies, with numerous teams dedicating their efforts to mapping and exploring the region’s cave systems. The caves of the Sitia Geopark include five caves in the Lassithi region, which were studied during a project targeted towards documenting the Geopark’s geotopes (Geositia project): Pelekita, Kato Peristeras, Ano Peristeras, Chonos and Vreiko. The formation of these subterranean karst formations is attributed to the combined effects of erosion and chemical dissolution, resulting from the movement of groundwater through fissures in the rock formations. The structural characteristics and three-dimensional patterns of these caves are influenced by the rock type in which they were formed. The hydrochemical factors that influence them depend on petrological, tectonic, climatic, and other conditions. Whether cave forms are composed of active, under-formation or residual features, there is a possibility that they will diversify in the future under completely different conditions (Ford and Williams 2007).

The caves of eastern Crete were primarily formed within limestones and dolomites belonging to the Tripoli and Pindos Units, and along their contact with the Phyllite-Quartzite Unit s.l. (IGME, 1959). This process occurred under the influence of intense tectonic uplift conditions prevailing on the island, caused by the northward subduction of the African plate beneath the Eurasian one (Fassoulas, 2017).

The tectonic history of Crete is marked by significant extensional and compressional episodes. Since the Neogene, the island has experienced three major faulting events that have dissected the island in several blocks. The earliest fault group, formed during the Early Messinian (7-6 Myr), is characterised by E-W trending faults resulting from the southward roll-back of the subduction zone. This was followed by the Late Messinian to Early Pliocene (5 Myr) stage, characterised by N-S trending faults due to the extrusion of the Anatolian plate and regional stress field perturbations. The most recent fault group, dating from the Middle Pliocene to the present (4 Myr), comprises NE-SW and NW-SE trending faults driven by ongoing geodynamic processes (Fassoulas, 2017). More specifically, the active normal faults in the area are numerous and can be grouped into two main trends: the NNE-SSW trending fault group and the E-W to ESE-WNW trending fault group. They can be divided into the following Fault Zones: Ierapetra, Sitia, Orno, Mesa Mouliana and Xerocambos-Goudouras (Dretaki, 2024).

The above tectonic setting can influence the development of the topography of the area, and more precisely, the orientation of the drainage network, which includes the underground network of rivers and caves. The cave structures tend to develop inside fragmented limestone, along pre-existing fractures and faults. The present study is focused on investigating the influence that these intense tectonic settings had on the formation of the caves within Sitia Geopark. Furthermore, the study explores how caves contribute to the unravelling of tectonic structures that remain hidden beneath the surface, leading to a better mapping and understanding of the tectonic setting.

Methodology

Cave mapping is a fundamental aspect of speleology, providing a detailed and accurate representation of the underground environment. These maps are essential tools for understanding the spatial layout, geological features and environmental conditions of caves. The mapping process combines traditional surveying techniques with modern technology to capture the intricate details of cave systems. Cave mapping is carried out by dividing the cave into small imaginary rectilinear sections. In each section, the length, direction relative to magnetic north and inclination relative to the horizontal plane are measured. At the end of each section, the distances from the cave walls are measured to record the dimensions of the

cave. These measurements are processed by a computer program, producing a map in Cartesian coordinates.
The hardware used for mapping included the BRIC5 and DistoX1, an analogue compass, an analogue inclinometer, a tape measure and a laser rangefinder. In terms of software, the BRIC5 measurements were accompanied by the Topodroid app for Android and the processing was done using Visual Topo for Windows.
During the fieldwork of the GeoSitia project and the thesis of Dretaki (2024), fault measurements were obtained using a geological compass and the Android program FieldMove. Further processing and analysis of the data was carried out using QGIS and ArcGIS Pro. The rose diagrams were created using the QGIS plugin "Line direction histogram". Furthermore, for the creation of the drainage network as well as the hillshade of the study area, the Digital Elevation Model of the Legal Entity of Public Law Hellenic Cadastre was used [Operational Programme Competitiveness, Entrepreneurship and Innovation 2014-2020 (EPAnEK)]. To achieve a more comprehensive interpretation of the landscape, the Digital Elevation Model (DEM) was used in combination with Google Earth Software.

Field data

The cave of Ano Peristeras is located west of the settlement of Karydi and is among the most significant and largest caves in Greece (Figure 1). It is situated within the limestones of Tripoli Unit (IGME, 1959). The cave's entrance, shaped as a semi-circular doline with a radius measuring approximately 24 m, is situated at an altitude of 600 m. The broader area of the doline exhibits the contact between the Tripoli Unit and the Phyllites-Quartzites Unit. The first chamber is notable for its substantial dimensions, measuring 30 m in width and 90 m in height. This is followed by a second chamber that is comparatively smaller in size, with dimensions of 35 m in width and 13 m in height. Its total length is 8,250 m, making it the third longest cave in Greece. Through hydrologic data and pressure gauges, it is assumed that the Ano Peristeras Cave discharges to the Flega spring (Chailloux, 2015). The entrance of the cave is developed in a SSW-NNE direction, and another branch follows the same direction upstream, to the west of the entrance. The main branch develops in a W-E direction until the central part, where it turns NW-SE. These directions are due to the tectonics of the area and the NNE-SSW fault zone trending (as shown in yellow, Figure 1), as well as the older E-W faults (as shown in orange, Figure 1), which is confirmed by the correlation of the fault trend and cave branches rose diagrams (Figure 5). The dashed yellow lines indicate possible faults along which several branches of the cave were developed, parallel to the younger active Sitia Fault Zone (as shown in yellow, Figure 1). The tectonic stress of the limestone accelerates its disintegration and thus the formation of the cave along the fault zone. In addition, a large part of the cave is situated at the tectonic contact (thrust) of the limestones of the Tripoli Unit, which overlie the phyllites of the Phyllite-Quartzite Unit. A smooth limestone surface appears on the roof of the cave, in the part of the cave that develops within the red phyllites.

Figure 1. Map showing Ano Peristeras (lower, longer red line) and Chonos (upper, shorter red line) cave systems and their correlation with faults in the area. DEM Source: Legal Entity of Public Law Hellenic Cadastre, Operational Programme Competitiveness, Entrepreneurship and Innovation 2014-2020 (EPAnEK).

The cave of Chonos is located south of the homonymous settlement, a term employed in the Cretan dialect to denote a sinkhole (Figure 1). It has been determined that the cave develops at the point of contact between the upper layers of the Toplou beds of the Tyros Unit and the limestones of the Tripoli Unit (IGME, 1959, Klein *et al.*, 2008, Zulauf *et al.,* 2018). The cave's entrance, measuring 120 by 130 m and 25 m in depth, is a doline that appears to have been influenced by probable NE-SW trending faults. The cave development extends for approximately 700 m and reaches a depth of 90 m The first section of the cave is vertical, and then it transitions parallel to the contact between the Tyros Unit and the limestones of the Tripoli Unit. It is plausible that the cave discharges in the same underground drainage system as Ano Peristeras, and the presence of water is seasonal. The presence of speleothems, formed through the accumulation of mineral deposits, indicates that the cave is periodically filled with water, which then escapes through fissures at the cave's end. Mapping of the cave reveals the presence of two branches, which later connect. The main branch of the cave exhibits a WNW-ESE direction (as shown in orange, Figure 1), aligning parallel to the fault zone that brings the Tyros Unit into contact with the limestones of the Tripoli Unit (Klein *et al.,* 2008). The disintegration of limestone is accelerated by tectonic stress, leading to the formation of caves along the fault zone. The second branch, located a short distance west of the entrance and originating at the contact of the two Units, exhibits an NNE-SSW orientation and appears to develop within the same zone as certain branches of the Ano Peristeras (as shown in dashed yellow, Figure 1). The main branch exhibits a bend with a NNE-SSW orientation in its western segment, indicative of its influence by NNE-SSW trending faults (as shown in yellow, Figure 1). The above is confirmed with the correlation between the fault trend and the cave branches' rose diagrams (Figure 5 and 6).

Figure 2. Map showing Kato Peristeras and its correlation with possible faults in the area. Legend as in Figure 1. Basemap: Google Satellite.

The cave of Kato Peristeras is located 1.5 km from the settlement of Karidi, on the road to the settlement of Adravasti (Figure 2). It is located north of the road and can be reached by following a path for 350 m. The cave is developed in limestones of the Pindos Unit (IGME, 1959, Klein *et al.,* 2008). It is a horizontal cave with its entrance at an altitude of 615 m, in the area of Kato Platyvolo. Its entrance is a doline measuring 45 by 25 m and 20-25 m deep, which collapsed to reveal the cave. According to the primary mapping of the E.S.E. (Hellenic Speleological Society) it has a length of 100 m, a maximum ceiling height of 12 m, a depth of 63 m and a total area of 2800 m² (Petrochilou, 1970). The main chamber of the cave measures 75 by 35 m and is 3-10 m high. It is quite steep, with several limestone blocks sloping down towards the interior. At the end of this chamber, water escapes through fractures and discontinuities in the rock. To the left of the main chamber, there is a much smaller one, 19 by 11 m and 1.5-6 m high, with stalagmite speleothems, which joins the main chamber at two points. The cave develops primarily towards the W, in the direction of the NW-SE shear zone (as shown in dashed yellow, Figure 2). Inside the cave, especially in the left part of the chamber, several fault surfaces of a second NW-SE fault zone can be found during the descent. As shown in the rose diagrams (Figures 5 and 6), some smaller branches of the cave follow the NNE-SSW and the E-W trending faults. The tectonic stress on the limestone creates the conditions for faster dissolution and formation of the cave along this zone.

The geotope of the cave of Pelekita is located 3 km away from the settlement of Kato Zakros, following the E4 path to Karoumes beach (Figure 3). The cave is developed in limestones and dolomites of Tripoli Unit (IGME, 1959). The cave of Pelekita, named after the nearby ancient quarry, is located at an altitude of 100 m in the foothills of Traostalos. According to the primary mapping conducted by the Hellenic Speleological Society (E.S.E.) in 1970, the cave's length is 310 m (Ioannou, 1970). However, more recent mapping by FORS Sitia has revealed a length of 370 m and a depth of 95 m The cave's entrance, measuring 15 m in diameter and 8 m in height, is oriented towards the east (Bruins *et al.,* 2019). The first chamber measures 20 m in length, 20 m in width, and 7.5 m in height. It is a horizontal cave that is developed sub-parallelly to the coastline, oriented NW-SE. The total number of chambers in this cave is four, including the entrance. The second chamber is considered the largest cave chamber in Crete and one of the largest in Greece, with a volume of about 300 m². It is characterized by a rich variety of speleothems, with an abundance of stalactites and stalagmites. At the base of the third and fourth rooms, there are small brackish water ponds, which are at the same altitude as the sea level. Between the last two chambers, there is a pile of limestone fragments, coming from the roof, due to the angle of the limestone bedding, which favours their collapse. In the eastern part of the cave, a relatively smooth surface is found, exhibiting characteristics of a fault surface, which extends to the south and is likely associated with an older possible NW-SE trending fault (as shown in dashed yellow, Figure 3). Based on the rose diagram (Figures 5 and 7), the mean trending direction is similar to Vreiko's cave, while smaller branches follow the NNE-SSW to N-S direction.

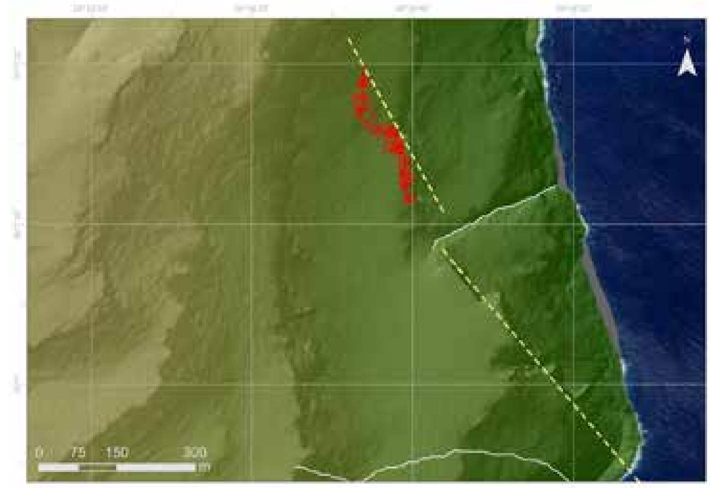

Figure 3. Map showing Pelekita and its correlation with possible faults in the area. Legend as in Figure 1. DEM Source: Legal Entity of Public Law Hellenic Cadastre, Operational Programme Competitiveness, Entrepreneurship and Innovation 2014-2020 (EPAnEK).

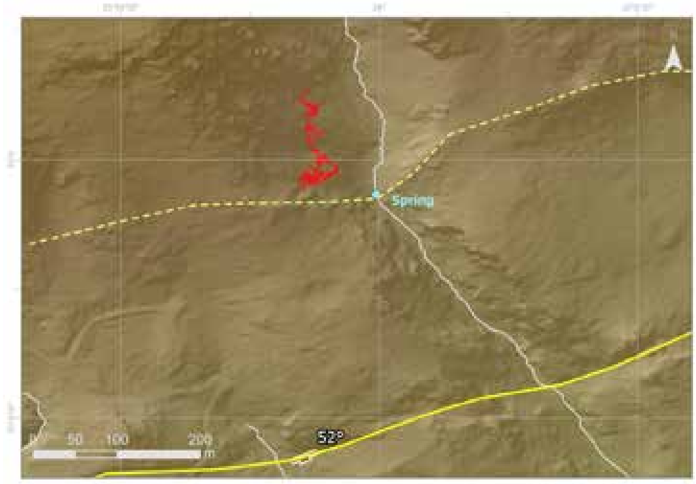

Figure 4. Map showing Vreiko and its correlation with faults in the area. Legend as in Figure 1. DEM Source: Legal Entity of Public Law Hellenic Cadastre, Operational Programme Competitiveness, Entrepreneurship and Innovation 2014-2020 (EPAnEK).

Vreiko Cave is located about 2 km north-east of the village of Pefki, following the road first to Makri Gyalos and then further north to the church of Estavromenos near the peak of Sarakinika (Figure 4). A 300 m path leads to the entrance of the cave. The cave develops within the limestones of the Tripoli Unit (IGME, 1959). The cave entrance is located at an altitude of 565 m and is a 7 m deep depression (Georgiakakis *et al.,* 2006) created by the collapse of the cave ceiling. It has a total length of 277 m and a maximum decline of 47 m. There is one entrance to the NW and two entrances to the south. In the northern part of the cave there are two chambers, the first measuring 60 by 5-22 m with a maximum height of 11.5 m (Georgiakakis *et al.,* 2006). The two chambers are separated by a pile of talus and surface sediments, above which there is an opening at a height of 9.5 m (Georgiakakis *et al.,* 2006), which is the second entrance to the cave. Continuing north, there is a second room leading to an outer porch and the third entrance to the cave . In the southern part of the cave there is a wide opening that leads to the deepest part of the cave, which is 34 m lower. The chamber measures 50 by 22.5-27.5 m and is 3-5.5 m high, with a shallow lake 3-5 m in diameter at its deepest point (Georgiakakis *et al.,* 2006). It has more impressive cave landforms than the northern room, with large stalactite columns and speleothems on the walls. To the left is another room measuring 31 by 7.5 m and 7.5 m high, at the end of which, in a small chamber, Byzantine pottery has been found consolidated with calcite material (Georgiakakis *et al.,* 2006). Just below the entrance to the cave, a spring flows near the vegetated area, which is in line with the southernmost point of the cave. There is a possible ENE-WSW trending fault that contributes to the surface discharge of water, inside the limestone bedrock (as shown in dashed yellow and blue dot as the spring, Figure 4). The fault is indicated by the topography, but also by the parallel development of a synthetic fault structure further south (Dretaki, 2024). The end and lowest part of the cave follows the direction of the above possible fault (Figure 4), which is also evident from the rose diagram (Figure 5 and 7).

Results and conclusions

In most cases, the development of the caves has been directly influenced by the local tectonic setting, including both older and newer faults and lithology. This phenomenon was clear through the correlation of fault zones and cave branch trends, the change in direction of the local drainage network, and in some cases, the existence of springs indicative of fault activity. The major E-W trending development of the caves corresponds with the same trending faults in the area as well as the NNE-SSW trending faults, but to a lesser extent. This finding suggests that the former were active for a longer period than the latter, indicating that the latter are more recent. The data gathered through field measurements offers further evidence to support this interpretation. However, additional field research is necessary to ensure more accurate conclusions. Such research could involve creating a more extensive network of measurements, which would allow for the confirmation or rejection of potential faults and thus correlations. To achieve this, a more in-depth caving mission would be required, with a skilled team that possesses a multidisciplinary understanding of speleology and geology. Regarding the deeper data interpretation, an analysis of 3D models through the software of Visual Topo could also lead to more detailed examination of underground tectonic formations, while experimenting with area proportional and no weighted-on length options in Line Direction Histogram could lead to a safer multivariate rose diagram data analysis.

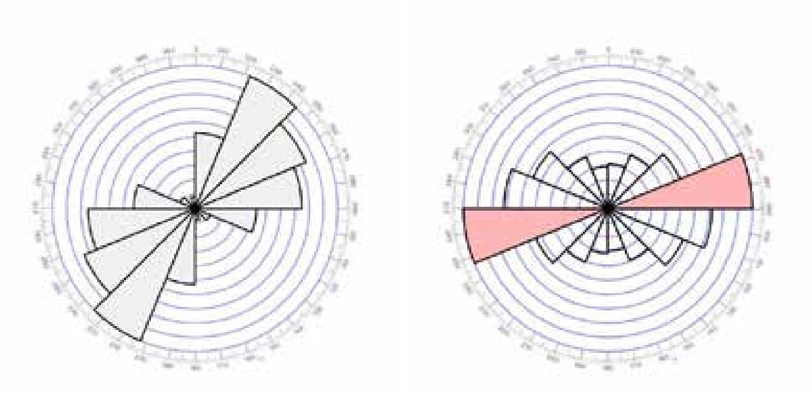

Figure 5. Left: Rose diagram showing the trend of faults in the study area (no weight on length). Right: Rose diagram showing the trend of the cave development of Ano Peristeras (weight on length, red= direction trend).

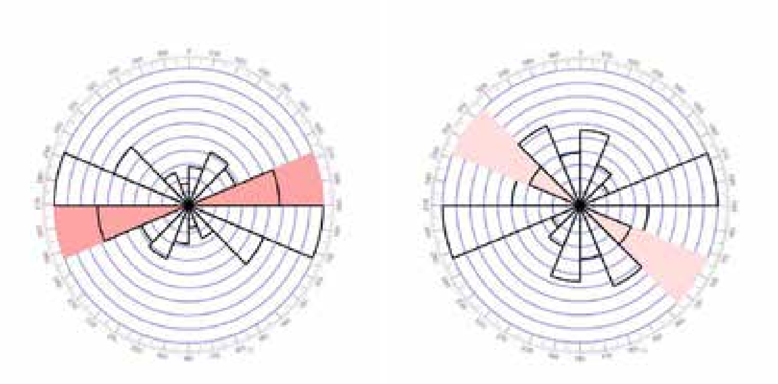

Figure 6. Rose diagram showing the trend of the cave development branches (weight on length, red= direction trend). Left: Chonos, Right: Kato Peristeras.

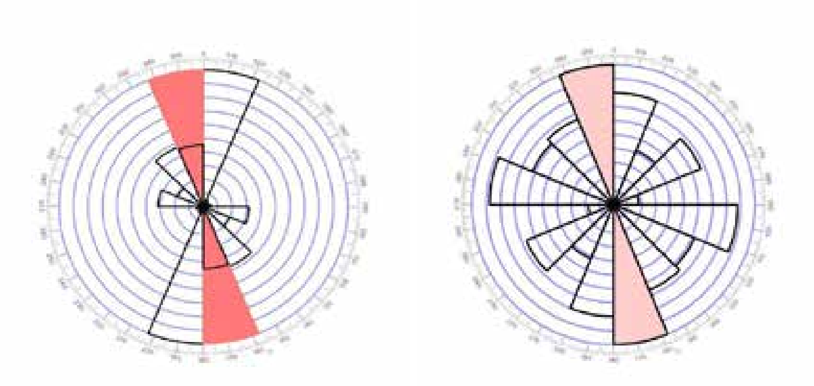

Figure 7. Rose diagram showing the trend of the cave development branches (weight on length, red= direction trend). Left: Pelekita, Right: Vreiko

Acknowledgements

This study is part of the GeoSitia project, which concerns the scientific documentation of Sitia Geopark geotopes. As part of this project, there were many contributors who made it possible, and we are thankful for their invaluable collaboration and guidance. We would like to thank the following speleologists, individuals or teams, for sharing their data: Lille Université Club Spéléo, Bruno Lemee, Christophe Emiel, Caroline Menet, Jean Luc Carron, Aurelien Depret, Frank Maciejak, Stanislas Francfort, Olivier Gaspe, Christophe Depin, Julien Tournois, Olivier Dufourneau, Frederic Bonacossa, Grigoris Anastasopoulos, Panagiotis Vavilis and Rigas Manos. Special thanks to Aristotle University of Thessaloniki and Municipality of Sitia, for supporting the project. We would like to thank the Legal Entity of Public Law Hellenic Cadastre for providing the Digital Elevation Model used in our analysis.

References

Bruins, H. J., Keller, J., Klügel, A., Kisch, H. J., Katra, I., & van der Plicht, J. (2019). Tephra in caves: Distal deposits of the Minoan Santorini eruption and the Campanian super-eruption. Quaternary international, 499, 135-147.

Chailloux, D. (2015). La Perte de la Colombe (Ano Peristeras) Karydi – Crête: Positionnement de la topographie de la Perte de la Colombe par radiolocalisation VLF.

Dretaki, A., 2024. Neotectonic study of Sitia area, eastern Crete, and assessment of the faults' seismic potential. Master Thesis, School of Geography, University of the Aegean, Inter-Institutional Postgraduate Studies Program "Natural Hazards and Disaster Mitigation", 236 pp.

Fassoulas, C., 2017. The geological setting of Crete: An overview. Minoan Earthquakes—Breaking the Myth Through Interdisciplinarity; Jusseret, S., Sintubin, M., Eds, pp.135-164.

Ford, D., & Williams, P. D. (2007). Karst hydrogeology and geomorphology. John Wiley & Sons.

Georgiakakis, P., Paragamian, K., Foteinakis, K., Papadaki, M. & Barlas, P. (2006). The caves Latsida Vreikou and Apoloustres in Pefki of Makry Gialos (Lassithi) [in Greek]. Proceedings of the 2nd Cretan Speleological Symposium in Memoriam of Eleutherios Platakis, May 29 2005, Herakleion, Crete, Greece, Hellenic Speleological Society, Department of Crete, Herakleion, pp. 47-51.

IGME., 1959. Geological map of Greece, scale 1:50.000 - sheet ZIROS. Athens: IGME.

IGME., 1959. Geological map of Greece, scale 1:50,000 - sheet IERAPETRA. Athens: IGME.

IGME., 1959. Geological map of Greece, scale 1:50,000 - sheet SITEIA. Athens: IGME.

Ioannou, I., (1970). The Cave of Pelekita in Kato Zakros, Sitia, Crete. Bulletin of the Hellenic Speleological Society, 10.6, pp. 40-46.
[in Greek].

Klein, T., Reichhardt, H., Klinger, L., Grigull, S., Wostal, G., Kowalczyk, G., Zulauf, G., 2008. Reverse slip along the contact Phyllite-Quartzite Unit/Tripolitsa Unit in eastern Crete: implications for the geodynamic evolution of the External Hellenides. Zeitschrift der deutschen Gesellschaft für Geowissenschaften, 159(3), 375-398. doi:https://doi.org/10.1127/1860-1804/2008/0159-0375

Petrochilou, A. (1970). The Cave of Peristeri, Karydi, Sitia, Crete. Bulletin of the Hellenic Speleological Society, 10.6, pp. 50-54. [in Greek].

Zulauf, G., Dörr, W., Marko, L., & Krahl, J. (2018). The late Eo-Cimmerian evolution of the external Hellenides: constraints from microfabrics and U–Pb detrital zircon ages of Upper Triassic (meta) sediments (Crete, Greece). International Journal of Earth Sciences, 107(8), 2859-2894.

Digital data

Digital Elevation Model-DEM from Legal Entity of Public Law Hellenic Cadastre, Operational Programme Competitiveness, Entrepreneurship and Innovation 2014-2020 (EPAnEK).

17th INTERNATIONAL CONGRESS of the Geological Society of Greece

BULLETIN OF THE GEOLOGICAL SOCIETY OF GREECE, SP. PUBL.

EXTENDED ABSTRACT 065

Enhancing Geoheritage through GEOAM: A Case Study of Tinos Island, central Aegean Sea, Greece

H. Drinia[1] G. Zafeiropoulos[1],

(1) Faculty of Geology & Geoenvironment, National and Kapodistrian University of Athens, Panepistimioupolis 15784, Zographou, Greece, cntrinia@geol.uoa.gr

Introduction

Geoheritage encompasses the recognition, conservation, and promotion of geologically significant sites and their cultural, educational, and ecological value. In this context, Tinos Island in the Cyclades stands out as a remarkable locale due to its complex geological history and the coexistence of geological formations with architectural features tied to human activity. This study employs the GEOAM (Geoeducational Assessment Method), an innovative framework proposed by Zafeiropoulos and Drinia (2023) and Zafeiropoulos (2024), to evaluate the geoheritage potential of Tinos Island and explore the interplay between its natural and built environments.

Tinos Island belongs to the Atticocycladic geological mass and is characterized by its complex metamorphic history and structural geology, deeply influenced by tectonic activities in the Aegean region (Figure 1). This geological mass comprises several distinct metamorphic units, including the Upper Unit, the Cycladic Blueschist Unit, and the Basal Unit. The Upper Unit, which has undergone greenschist-facies metamorphism, consists of serpentinites, meta-gabbros, and phyllitic rocks. The Cycladic Blueschist Unit, notable for its high-pressure metamorphism, includes marbles, calcschists, and various metasediments, reflecting the intense subduction processes that have shaped the region. At the lowest stratigraphic level, the Basal Unit contains a diverse array of metamorphic carbonate rocks. These units collectively highlight a dynamic tectonic environment with multiple detachments, showcasing the geological complexity and ongoing metamorphic processes defining Tinos within the Cyclades complex. Further illustrating this complexity, the island's stratigraphy includes additional divisions such as the Akrotiri Unit, predominantly in the southern region, comprising amphibolites, paragneisses, and minor silicate marbles. This unit is separated from the Upper Unit by the low-angle Vari detachment, emphasizing distinct tectonic settings (Bröcker and Franz, 1998). Beneath the Akrotiri Unit, the Upper Unit presents a metamorphic history shaped by diverse rock types and intricate tectonic interactions. Below these lies the Cycladic Blueschist Unit, marked by high-pressure metamorphism at approximately 450–500°C and pressures around 4–7 kbar. At the lowest level, the Basal Unit, mainly found in the northeastern part of the island, reveals a history of geological transformations influenced by regional metamorphism and magmatic intrusions. The presence of multiple detachments, discussed by Brichau et al. (2007) and Jolivet et al. (2010), underscores the dynamic tectonic regime of Tinos, with the North Cycladic Detachment System reactivating older geological structures such as the Vardar oceanic suture zone. Mapping and analyzing these geological units, based on fieldwork and historical data, provide a comprehensive understanding of Tinos Island's geological framework, offering valuable insights into the Cycladic region's tectonic and metamorphic history while aiding in the prediction of future geological developments in this seismically active area.

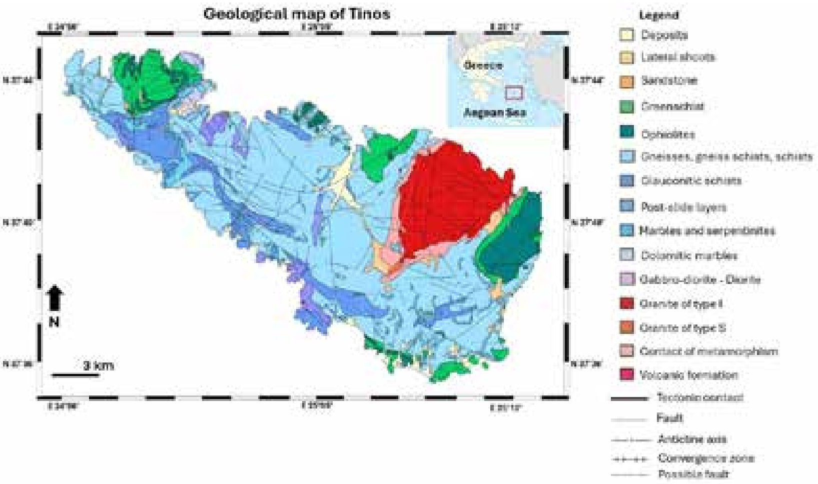

Figure 1. Geological Map of Tinos island after Lamont et al., (2000) and Leonidopoulou (2004), modified

Methodology

To assess and enhance the geoheritage of Tinos, the Geoeducational Assessment Method (GEOAM) was employed. The GEOAM assessment method is a comprehensive framework designed to evaluate the educational value, conservation status, and overall potential of geosites. By applying eight key criteria—Site Management and Visitor Experience (SMVE), Natural Resource Management (NRM), Environmental Education and Interpretation (EEI), Cultural and Historical Significance (CHS), Geoethics (GE), Economic Viability (EV), Community Involvement and Engagement (CIE), and Sustainable Development (SD)—along with their respective subcriteria, GEOAM provides a detailed scoring system that assesses various aspects of a geosite, such as accessibility, biodiversity conservation, interpretive resources, cultural importance, and sustainable practices. Scores are assigned on a scale of 1 to 5 for each subcriterion, weighted according to their importance, and combined to calculate an overall score using a specific formula. The final score categorizes geosites into five levels, from Low Implementation (LI) to Extremely High Implementation (EHI), offering a measurable and adaptable tool for enhancing the geoeducational value and sustainable development of geosites.

The application of GEOAM involved selecting six representative geosites on Tinos, including marble quarries, tafone, alveoles, tors, core stones and the iconic granite outcrop of Exombourgo (Figure 2). Each site was evaluated using a weighted scoring system, highlighting their strengths and areas for improvement. The methodology's focus on education and community involvement ensures that conservation efforts are both inclusive and impactful. This approach is particularly valuable in addressing the dual goals of heritage preservation and tourism promotion according to sustainable principles.

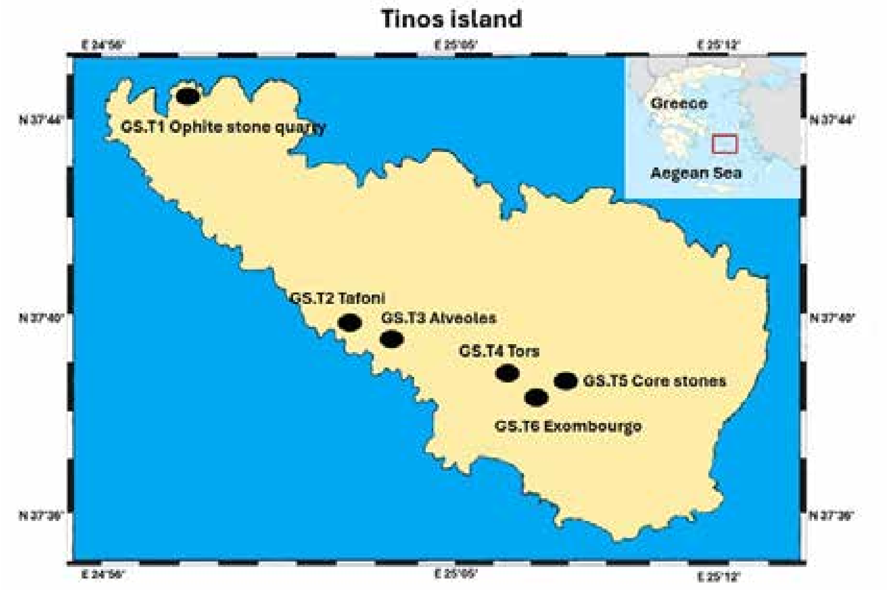

Figure 2. The selected geomorphosites in the island of Tinos

Results

The evaluation of the criteria using the GEOAM intricately revealed the following results (Table 1):

Table 1. Final scores for the geosites of Tinos

Criteria	Weight	GS.T1	GS.T2	GS.T3	GS.T4	GS.T5	GS.T6
SMVE	10%	2.66	2.83	2.5	3.16	2.5	2.66
NRM	10%	2.4	3.2	3	3.4	3	3.4
EEI	30%	2	2.4	2.2	2.4	2	2
CHS	10%	3.25	3	2.5	3.75	2.25	3.5
GE	20%	3.4	3.8	2.6	4	2.4	4
EV	5%	3.6	3.8	2.4	4	2.2	3.8
CIE	5%	3.5	4	2.25	4.5	2.25	4
SD	10%	3	3.33	2.33	3.33	2.66	3
Final Score		2.76	3.10	2.44	3.30	2.34	3.04
Characterization of score		MI	HI	MI	HI	MI	HI

Discussion

According to Table 1, it is evident that all geosites demonstrate significant importance, as none received a low score. Notably, three out of six geosites are classified under High Implementation (HI) in the final score characterization. Specifically, GS.T4 achieves the highest score of 3.30 (Table 10), indicating its strong potential for further development and the initiation of more community-driven strategies for its rational management.

Additionally, GS.T2 and GS.T6 showcase their geoheritage value, offering opportunities to drive collective management efforts. This approach could enable the local community to reap the benefits of their geosites within a sustainable development framework. On the other hand, GS.T1, GS.T3, and GS.T5 record the lowest scores of 2.76, 2.44, and 2.34, respectively. These lower scores highlight a lack of geoenvironmental activities and initiatives to enhance the visibility and value of these geosites. This is further reflected in the fact that the Environmental Education and Interpretation (EEI) criterion consistently receives the lowest scores across all geosites.

To address this issue, collaboration among the local community, stakeholders, and policymakers is essential. Such cooperative efforts would enable a holistic approach to enhancing the geoheritage value of these areas. At the same time, this would safeguard the cultural dynamics of the region, which, according to a European study, face certain threats. Geo-education, through organized geoeducational activities or recreational initiatives, could play a constructive role in benefiting society, delivering economic, social, and environmental advantages.

Furthermore, promoting structured geoeducational activities can foster a geoethical mindset and instill sustainable values in participants. By aligning with the principles of sustainable development, such initiatives would create a society that exists harmoniously with the natural environment..

Conclusions

Tinos Island showcases a remarkable intersection of geology, culture, and geotourism potential. The island's unique geomorphology, shaped by its dynamic tectonic history, offers diverse features such as granitic tors, core stones, and tafoni formations, which contribute to its high geoheritage value. Additionally, Tinos' cultural identity is enriched by its marble craftsmanship, recognized by UNESCO, and its rich tradition of artistic expression.

Evaluating its geosites using the GEOAM method highlighted both strengths and areas for improvement. Geosites like GS.T4 exhibit high implementation potential for geoeducational activities, while others lack necessary infrastructure and environmental education elements. Integrating local communities, stakeholders, and policymakers is critical for sustainable development of the island.

By fostering geoethical awareness and promoting alternative tourism, Tinos can balance cultural preservation with economic and environmental benefits, ensuring its legacy as a dynamic and sustainable destination.

Acknowledgements

The authors extend their heartfelt thanks to the organizing committee of the 17th International Congress of the Geological Society of Greece and the anonymous reviewers for their thorough consideration of this extended abstract.

References

Brichau, S.; Ring, U.; Carter, A.; Monié, P.; Bolhar, R.; Stockli, D.; Brunel, M., 2007. Extensional Faulting on Tinos Island, Aegean Sea, Greece: How Many Detachments? Tectonics , 26, TC4009. https://doi.org/10.1029/2006TC001969.

Bröcker, M.; Franz, L. 1998. Rb–Sr Isotope Studies on Tinos Island (Cyclades, Greece): Additional Time Constraints for Metamorphism, Extent of Infiltration-Controlled Overprinting and Deformational Activity. Geological Magazine, 135, 369–382. https://doi.org/10.1017/S0016756898008681

Jolivet, L.; Lecomte, E.; Huet, B.; Denèle, Y.; Lacombe, O.; Labrousse, L.; Pourhiet, L.; Mehl, C., 2010 The North Cycladic Detachment System. Earth Planet. Sci. Lett., 289, 87–104. https://doi.org/10.1016/j.epsl.2009.10.032 .

Lamont, T.N.; Roberts, N.M.; Searle, M.P.; Gopon, P.; Waters, D.J.; Millar, I., 2020. The Age, Origin, and Emplacement of the Tsiknias Ophiolite, Tinos, Greece. Tectonics, 39, e2019TC005677. https://doi.org/10.1029/2019TC005677

Leonidopoulou, D., 2004. Geological and Geomorphological Factors in the Formation of Intrinsic Vulnerability of Fractured Rocks: Application on the Island of Tinos. Ph.D. Thesis, Department of Physical Geography-Climatology, Department of Geology, National and Kapodistrian University of Athens, Athens, Greece. Available online: http://dx.doi.org/10.12681/eadd/17314 (accessed on 29 June 2024).

Melidonis, N.G.; Triantaphyllis, M., 2003. IGME Geological Map of Greece, Tinos–Yaros Sheet, 1:50000; Institute of Geology and Mineral Exploration: Athens, Greece.

Zafeiropoulos, G. 2024. The Importance of Geoenvironmental Education in Understanding Geological Heritage and Promoting Geoethical Awareness: Development and Implementation of an Innovative Assessment Method, with a Case Study of the Southeast Aegean Islands. Ph.D. Thesis, National and Kapodistrian University of Athens, Faculty of Science, Department of Geology and Geoenvironment, Athens, Greece, 227 p.

Zafeiropoulos, G., Drinia, H., 2023. GEOAM: A Holistic Assessment Tool for Unveiling the Geoeducational Potential of Geosites. Geosciences 2023, 13, 210. https://doi.org/10.3390/geosciences13070210

BULLETIN OF THE GEOLOGICAL SOCIETY OF GREECE, SP. PUBL.
EXTENDED ABSTRACT 066

Tinos Island, Aegean Sea, Greece, Geopark: A Pioneering Initiative in Climate Change Resilience and Geoconservation

H. Drinia[1], G. Zafeiropoulos[1]
(1) Faculty of Geology & Geoenvironment, National and Kapodistrian University of Athens, Panepistimioupolis 15784, Zographou, Greece, cntrinia@geol.uoa.gr

Introduction

Tinos Island, part of the Cyclades in Greece, boasts a remarkable granitic landscape with geomorphs of significant geological, cultural, and educational value. These geomorphological features, shaped over millennia, are increasingly vulnerable to the impacts of climate change, which can accelerate erosion, alter landforms, and threaten the preservation of the island's natural heritage. This study explores the feasibility of establishing a Geopark on Tinos Island, with a central mission to protect, promote, and utilize the island's natural and cultural heritage. Special emphasis is placed on addressing climate change and advancing geoconservation practices to mitigate the effects of environmental changes on these unique geomorphs. Unlike existing Geoparks, this project stands out by integrating the unique geological features of Tinos with the island's cultural narratives, offering an innovative approach to linking geoconservation with sustainable development and community engagement.

Geological Setting and Cultural Significance

Tinos Island, part of the Cyclades plateau in the Aegean Sea, boasts a complex geological setting shaped by tectonic processes associated with the Alpine orogeny. It lies within the Attic-Cycladic Metamorphic Complex, a region that showcases the dynamic interplay of subduction, high-pressure metamorphism, and subsequent extensional tectonics during the Tertiary period (Figure 1). These processes have given rise to a diverse range of geological features, making Tinos a natural laboratory for understanding Earth's dynamic systems.

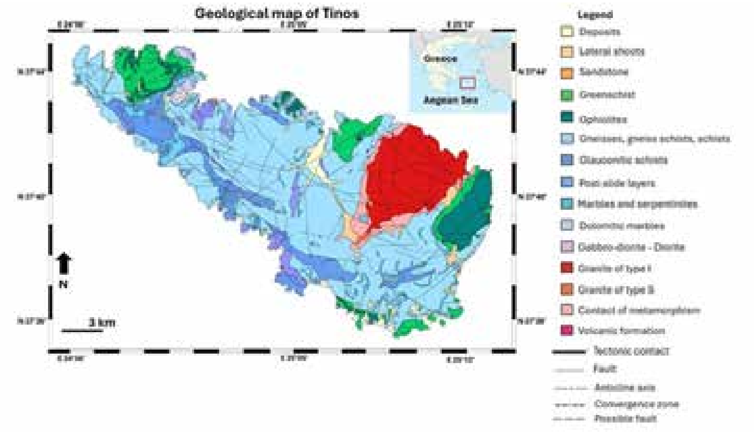

Figure 1. Geological Map of Tinos island after Lamont et al., (2000) and Leonidopoulou (2004), modified

The island's lithology is dominated by metamorphic rocks, including schists, marbles, gneisses, and amphibolites. These rocks were formed under high-pressure, low-temperature conditions during subduction. Tinos is particularly renowned for its high-quality marbles, which have been used extensively in art and architecture since antiquity. Schists and gneisses, characterized by their foliated textures, also contribute to the island's distinct geological character. Adding to this diversity are granitic and granodioritic intrusions from the Miocene period, dated to approximately 18–13 million years ago. These granitoids, formed during post-orogenic extension, are a hallmark of the Cyclades and play a crucial role in shaping Tinos' geomorphology (Stournaras 2006). This granitic landscape, covering 22.6 km², forms a triangular pattern with vertices at Exomvourgo, Livadia Bay, and Kakia Skala. Notable geomorphs, including tors and tafoni, have developed due to spheroidal weathering, creating a visually striking terrain. The area around the village of Falatados, located in the semi-mountainous Pano Meri region between Tinos' highest mountains, Exomvourgo and Tsiknias, contains significant clusters of these geomorphs (Figure 2). These geological features, intertwined with local folklore, architecture, and agricultural traditions, add layers of cultural and social value to the landscape.

Figure 2. Granitic geomorphs around the village of Falatados

Tinos' geology holds significant cultural, scientific, and economic value. Its marbles, known for their exceptional quality, have been used in iconic structures like the Parthenon. The island's geological features attract researchers and geotourists, offering insights into tectonic and metamorphic processes while showcasing the interplay between geological heritage and human history. The unique geomorphic features and the island's potential as a Geopark underscore the importance of integrating geoconservation with sustainable development

Climate Change and Geoconservation Focus

Climate change poses challenges to the preservation of Tinos' granitic landscape. Rising temperatures, shifting precipitation patterns, and increased weathering rates threaten the stability and appearance of the granite geomorphs. The proposed Geopark aims to serve as a hub for studying these impacts while implementing adaptive geoconservation measures. This project is original in its commitment to directly addressing the intersection of climate change, geological heritage, and community well-being, setting a benchmark for future initiatives in similar environments. Key initiatives include a) the establishment of research programs to monitor weathering rates and the effects of climate variability on the granitic formations, b) the development of techniques to stabilize vulnerable geomorphs and preserve traditional stone buildings against climatic impacts, c) the assessment of how climate change influences the surrounding ecosystems and integrating findings into conservation strategies.

To achieve its objectives, the following interventions are proposed:

- Creation of new paths and improvement of existing ones to enhance accessibility while minimizing environmental impact.
- Development of information and visitor service infrastructure, including a central information center.
- Promotion and protection of granite massifs and geomorphs, emphasizing their vulnerability to climate change.
- Restoration, promotion, conservation, and protection of traditional stone buildings as part of the island's cultural heritage.
- Establishment of rest areas and educational zones for visitors.
- Installation of interpretative signs to provide information about the geological, ecological, and cultural significance of the sites.
- Organization of educational and cultural events to raise awareness of climate change and geoconservation

Discussion - Conclusions

The proposed Tinos Island Geopark will serve as a catalyst for addressing climate change and promoting geoconservation while celebrating the island's unique geological and cultural heritage. By combining research, education, and sustainable tourism, the Geopark will enhance the resilience of the local landscape and community, ensuring its preservation for future generations. Its originality lies in its innovative integration of climate change research, community-driven geoconservation, and the sustainable promotion of one of Greece's most distinctive geological landscapes.

Acknowledgements

The authors extend their heartfelt thanks to the organizing committee of the 17th International Congress of the Geological Society of Greece and the anonymous reviewers for their thorough consideration of this extended abstract.

References

Lamont, T.N.; Roberts, N.M.; Searle, M.P.; Gopon, P.; Waters, D.J.; Millar, I., 2020. The Age, Origin, and Emplacement of the Tsiknias Ophiolite, Tinos, Greece. Tectonics, 39, e2019TC005677. https://doi.org/10.1029/2019TC005677

Leonidopoulou, D., 2004. Geological and Geomorphological Factors in the Formation of Intrinsic Vulnerability of Fractured Rocks: Application on the Island of Tinos. Ph.D. Thesis, Department of Physical Geography-Climatology, Department of Geology, National and Kapodistrian University of Athens, Athens, Greece. Available online: http://dx.doi.org/10.12681/eadd/17314 (accessed on 29 June 2024).

Stournaras, G., 2006, “The granite field of Volax (Tinos island, Hellas), Proceedings of the 4th European geoparks meeting, 2-5 October 2003 Anogia Crete, p. 85-91.

17th INTERNATIONAL CONGRESS
of the Geological Society of Greece

BULLETIN OF THE GEOLOGICAL
SOCIETY OF GREECE, SP. PUBL.

EXTENDED ABSTRACT 067

Hydrogeochemical Characteristics of Alfeios River and the wider hydrographic Network in the Lignite Basin Area of Megalopolis.

Christos Drougas [1] , Efstratios Kelepertzis [1] , Zacharenia Kypritidou [1] , Evangelia Sigala [2], Christos Roumpos [3] , Georgios Louloudis [3] , Eleni Mertiri [3], Evangelos Oikonomopoulos[2]

(1) Department of Geology and Geoenvironment, National and Kapodistrian University of Athens, Panepistimiopolis, Zographou, 15784, Athens, Greece

(2) Laboratory of Environmental Chemistry and Special Materials, Public Power Corporation (PPC) Innovation Hub, Leontariou 9, Leontario 15351, Athens, Greece

(3) Department of Mining Engineering and Closure Planning, Public Power Corporation of Greece,10432 Athens, Greece

Research highlights

- Strong lithological control on dissolved constituents in surface waters, influenced by regional geology.
- Nitrogen species mainly originate from sewage inputs from Megalopolis, with minimal lignite mining impact on Alfeios River water quality.

Abstract

This study aims at the hydrogeochemical evaluation of surface waters and the possible anthropogenic impact affecting the surface water quality in the complex environment of the Megalopolis basin, including over 50 years of lignite mining. The results can guide sustainable restoration strategies and environmental policies in the transition era of mine closure. In March 2024, 24 surface water samples were collected from upstream to downstream locations along the Alfeios River and its tributaries, which flow near the lignite operations. The chemical parameters of NH_4^+ (maximum 3 mg/L), SO_4^{2-} (range from 3 to 1010 mg/L), Mn (range from 1 to 338 μg/L), and Mo (range from 0.2 to 1027 μg/L) were identified as the most of environmental concern, exhibiting significant variability among samples. The presence of SO_4^{2-}, Mn, and Mo in the water samples indicates a geogenic origin, strongly influenced by the regional lithology, including lignite deposits, postAlpine sediments, and geological formations within the Pindos zone. The samples were categorized into three clusters (C1, C2, and C3) according to Hierarchical Cluster Analysis (HCA). Samples in Cluster 3, located near the old mining area, showed the highest concentrations of major and trace elements, exceeding the EU limits for Mn (50 μg/L) and SO_4^{2-} (250 mg/L) and were classified as Ca_2^+-SO_4^{2-} type waters. In contrast, C1 and C2 samples had a Ca^{2+}-HCO_3^- hydrochemical type. The scatter plot of NO_3^-/Cl^- ratios vs Cl^- indicated that the dominant source of NO_3^- was sewage from the town of Megalopolis. The Alfeios River appeared to be minimally affected by lignite activities, with no significant changes in water chemistry observed before and after the mining area, except for slightly elevated Mn and Mo levels, most of which remained below WHO and EU limits.

Keywords: Hydrogeochemistry, Surface Water, Lignite Mining, Post Mining

Introduction / Background

Lignite mining has been a major source of energy, significantly contributing to local and national economies, including that of Greece. Many studies have extensively examined the contamination and geochemistry of surface and groundwater resources near coal mines across various locations and different geological environments (GonzálezMartínez et al., 2019; Yang et al., 2023). However, environmental concerns related to coal mining activities and water resources will remain significant, even after the closure of mines (Liu et al., 2020). The geology of a region is a primary factor influencing the chemical composition of waters and the release of different types of contaminants, including metals and major ions, due to the geochemical conditions and anthropogenic activities (Kelepertzis et al., 2023; Yang et al., 2023). Coal mining can potentially contaminate surface and ground waters with pollutants such as sulfates and metals, resulting from coal processing and the exposure of sulfide minerals in atmospheric conditions (An et al., 2024). Also, various types of wastes affect water quality, including acid mine drainage, waste disposal (e.g. dumping sites), waste rocks, tailing storages, and liquid industrial wastes from power plants (Welch et al., 2021). The post-mining reclamation process has also been shown to affect geochemical conditions in abandoned or closed areas. Studies have shown that exposure of mineral residues and waste from lignite could potentially affect heavy metal and ion concentrations in surface water for many years after mine closure, making monitoring necessary (Liu et al. al., 2020; An et al., 2024). Lastly, differences in the chemical composition of the river are associated with various land uses and activities such as agricultural (fertilizer leaching etc.), domestic sewage, and industrial wastes

(Kypritidou et al., 2024).

Surface water quality of the Alfeios River in Megalopolis has shown elevated concentrations of some ions, e.g. Ca^{2+}, Mg^{2+} and SO_4^{2-} in the river water (Dimitrakopoulos et al., 2007). Louloudis (2017) applied Principal Component Analysis (PCA) to determine the correlation between different types of water in the region, such as surface waters, groundwaters, aquitards, and pit lakes. It was found that karstic waters, surface waters, and aquitard waters are not affected by mine waters in the region. Despite the above studies, there is no comprehensive systematic environmental monitoring of surface water quality in the region. The aim of this study is to cover this gap by sampling all rivers and tributaries flowing through the lignite mining area to define the pollution sources that influence the water hydrochemistry. The findings of this research aim to provide useful information regarding the hydrogeochemical status of surface waters, the geological influence in water geochemistry and imprint the environmental pressures from the human activities in the region. The geochemical stability of the region is one of the main key criteria to consider for the environmental rehabilitation of the Megalopolis Lignite Center (Sokratidou et al., 2018).

This study can establish geochemical baseline conditions before post-mining activities and help for a better understanding of the hydrogeochemical status of the area and support environmental rehabilitation and monitoring plans. The specific objectives are: a) To determine the hydrogeochemistry of all surface waters in the area and their effect on the Alfeios River and, b) to investigate the influence of the regional geological structure and any anthropogenic contamination on major ion and trace element concentration.

Description of the study area

Megalopolis region is located in the center of the Peloponnese peninsula Greece. The basin exhibits an elliptical form, with its major axis oriented in an NNW–SSE direction, stretching over a length of 18 km. The study area could be characterized as small hydrological basin due to the complicated hydromorphology of the region where many small tributaries flow near the Megalopolis town, the lignite mining works and the sites of the external waste dumps. The main river of the area is Alfeios River flowing from the south to Northwest direction, spanning 127 km before discharging into the Gulf of Kyparissia. This study focuses on the Southern part of the basin, where the river traverses the lignite basin of Megalopolis. The biggest tributaries are Elissonas and Xerilas, which flow from East to West and South to North direction and finally flow into Alfeios River.

The geology of the region is shown in Fig. 1. The Pindos unit is the main geological unit in surrounding mountains with limestones, cherts, dolomites, and flysch. In the eastern part of the basin, the Gavrovo-Tripolis Unit appears mainly with limestones, dolomites, Flysch and the Volcano-sedimentary unit (Tyros Beds). Only in small exchanges northeast of the basin does the quartzite-phyllite series show up with marble, schist, and phyllites (IGME, 1997). Lastly, Mesozoic ultramafic rocks also occur in small extensive throughout the basin's marginal rocks. The central part of the basin is covered by different ages of post-alpine sediments from the upper Pliocene with Makryssion formation up to the Holocene Alfeios river terraces with clays, marls, red loam, coarse clastic sediments and lignites.

Figure 1: Geological map of the study area with the sampling locations.

Land use and Mine activity

The main economic sectors are primary (7% of the population) with cultivated land, secondary (36%) by limited industrial and artisanal activity, and tertiary (40%) tourist and economic centres (Energy and Climate Action Plan, 2021). The dominant economic activity was lignite mining by the Public Power Corporation (PPC), starting with the Thoknia mine in 1970. The other lignite fields include: Marathousa (started at 1989) ceased the exploitation in-2015, Kyparissia lignite field (started 1987) finished in 2012 and Choremi lignite field, which was the only active mine site since 1970 until the end of 2024. In the area two (2) Power Plans (PP) exist, with a total of four lignite power units: I and II (19702011), III (1975-2022) (PP A), and IV (1991- end of 2024) (PP B), with a total installed capacity of 850MW. There is also a natural gas Unit V with 811 MW total capacity. In March 2024, only two factories remained operational: a lignitefired power plan (Unit IV), which works when the energy demand is high, and the fully operational natural gas factory (Unit V). By the end of 2024, all lignite power plants were ceased, leaving only the gas unit. New activities like agriculture, renewable energy, and environmental projects will replace lignite operations (Louloudis et al., 2024) considering the master plan for the post mining areas.

Methods

The sampling campaign took place during March 2024 (wet period), collecting 24 surface water samples; ten samples from the Alfeios River (A0-A9) and 12 water samples from tributaries (ZR1, X1, KF1, ZG1, E1, E2, K1, LG1, ZT1, P1, ZM1, T1, SIK1) that discharge directly or indirectly into Alfeios River (Fig. 1). The physicochemical parameters (pH, EC, TDS, Eh, and Dissolved Oxygen) were determined in situ with a pre-calibrated portable multiparameter. The samples were collected in triple-rinsed high-density polyethylene bottles for further analyses. All water samples for analysis of trace elements and major cations were filtered on-site through 0.45 μm membrane filters and acidified down to pH<2 with conc. HNO3 (65%). All water samples were stored at 4 0C or frozen condition until further analysis.

Laboratory analysis and treatment of data

All water samples were analyzed for major cations (Ca^{2+}, K^+, Mg^{2+}, Na^+) with the ICP-OES (Agilent 5800), trace elements (B, Li, Be, Al, V, Cr, Mn, Fe, Co, Ni, Cu, Zn, As, Se, Sr, Mo, Cd, Sn, Sb, Hg, Ti and Pb) with ICP-MS/MS (Triple Quad 8900), major anions (Cl^-, NO_2^-, NO_3^-, PO_4^{3-}, SO_4^{2-}) with ion chromatography (DIONEX ICS-2000). Ammonium ion (NH4+) was analyzed only in the sampling sites of Alfeios (A0-A9) and Zarzakis (ZR1) with the HACK LANGE DR 3900. All water analyses were carried out in the PPC Innovation hub in the Laboratory of Environmental Chemistry and Special Materials (PPC) and standardized according to ELOT EN ISO/IEC 17025. Bicarbonate (HCO_3^-) was measured at the Laboratory of Economic Geology and Geochemistry at the Department of Geology and Geoenvironment (NKUA) by the acid titration method using H2SO4 (1.6 N) until a pH of 4.5. The ionic charge balance error (CBE%) was below 5% for all samples, except for P1 (8.6%) and ZT1 (7.2%). Statistical and graphical analysis of the acquired data was done with the Minitab 7 ® v 17.1 statistical software analysis. Elemental concentrations close to or below the method detection limits were excluded from further data processing. Statistical analysis was restricted to parameters that showed great variability (EC, Ca^{2+}, Mg^{2+}, K^+, Na^+, Cl, HCO_3^-, SO_4^{2-}, NO_3^-, Mn, Mo and Sr). The statistical methods that were used are: Hierarchical cluster analysis (HCA) with the Ward method and Boxplot of the parameters.

Results and Discussions

All water samples, except SIK1 (pH 6.5, slightly acidic), were near-neutral to mildly alkaline. Oxidationreduction potential (Eh) in most samples was indicative of oxidizing conditions, except for samples E2 and P1, where Eh values were slightly reduced (-47 and -26 mV, respectively). Electrical conductivity (E.C.) varied widely between 415 μS/cm and 2150 μS/cm, with an average of 788 μS/cm, indicating strong differences in chemical composition. Dissolved oxygen (DO) ranged from 6.6 to 10.3 mg/L. Calcium (Ca^{2+}) levels ranged from 63 mg/L to 421 mg/L, with a median of 115 mg/L; specific samples like P1, T1, SIK1, and ZT1 had elevated levels (>195 mg/L). Bicarbonate (HCO_3^-) was stable at 200–300 mg/L, except for SIK1, which exhibited a low value of 98 mg/L. Sodium (Na^+), K^+, and Mg^{2+} were generally low, except for T1, where Na^+, K^+, and Mg^{2+} were detected at higher levels 42 mg/L, 22 mg/L, and 44 mg/L, respectively. Sulfate (SO_4^{2-}) ranged from 3 mg/L to 1010 mg/L, with the highest values in SIK1 (553 mg/L) and T1 (1010 mg/L), P1 (274 mg/L) and ZT1 (318 mg/L), exceeded the acceptable drinking water for sulfate ions 250 mg/L(WHO 2022). Chloride (Cl^-) was generally below 20 mg/L, except for T1 (61 mg/L) and ZT1 (26 mg/L), both well below the acceptable limit for drinking water of 250 mg/L (WHO 2022).

Nutrient levels were low, with NO_3^- ranging from 8 to 16 mg/L in the Alfeios River, and most tributaries below 1 mg/L, except for ZR1 (13 mg/L) and T1 (11 mg/L), all within the WHO-acceptable drinking limit of 50 mg/L. Ammonium (NH_4^+) varied from <0.02 mg/L to 3.04 mg/L, with ZR1 showing the highest value above the drinking water limits of 0.5 mg/L (EU, 2020; WHO, 2022). In the Alfeios River, NH_4^+ values were below 1.45 mg/L and decreased downstream (A8) to 0.34 mg/L. Phosphate (PO_4^{3-}) was generally undetectable, except for ZR1, T1, and ZT1, which had elevated concentrations (0.3 mg/L, 1.8 mg/L, and 0.5 mg/L, respectively). Trace elements such as Pb, Tl, Ag, Sb, Cd, and others were mostly below detection limits, but higher concentrations of Se, Ni, Fe, Mn, and Mo were observed in specific samples. Manganese (Mn) ranged from 1 μg/L to 338 μg/L, with several samples (P1, ZR1, T1) exceeding the WHO, (2022) limit of 80 μg/L. Molybdenum (Mo) had a median value of 3 μg/L, with three samples (E2, T1, ZT1) exceeding the WHO, (2022) limit of 70 μg/L.

Boxplot analysis (Fig. 2) revealed that Cluster 1 shows the lowest concentrations of all chemical parameters, with only a few outliers for Mn (PAN1) and Mo (E2). Cluster 2 exhibits higher concentrations than Cluster 1 across all parameters, especially for NO_3^- (>8 mg/L). Cluster 3 exhibited the highest variability and concentrations for most chemical parameters, except for NO_3^- (<8 mg/L). According to Piper classification diagram (Fig. 3) the water samples of Cluster 1 and Cluster 2 are of Ca^{2+} - HCO_3^- type. The samples from Cluster 3 are of Ca^{2+}-SO_4^{2-} type.

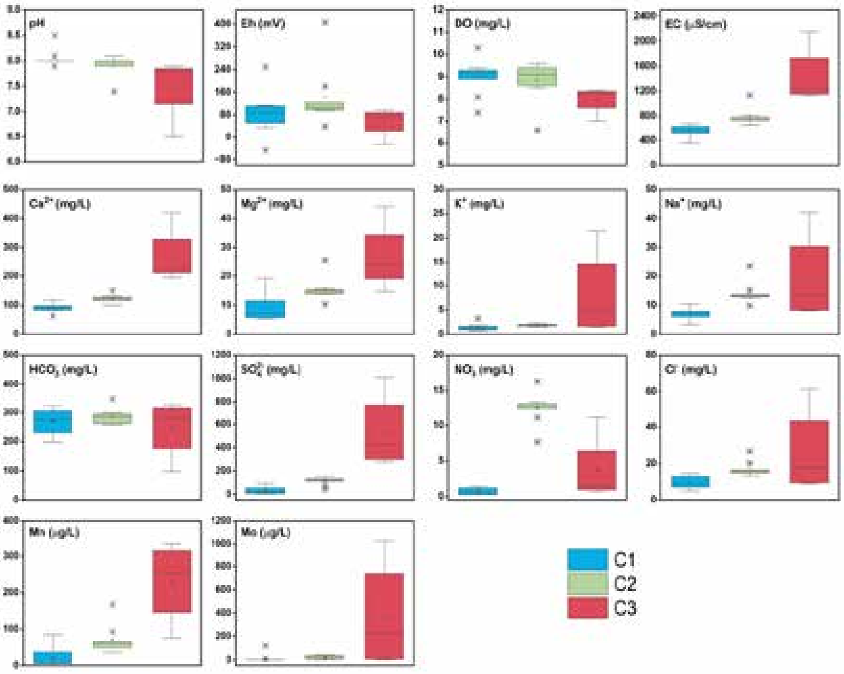

Figure 2: Boxplot of major chemical parameters based on the classification of surface water samples according to HCA.

The presence of Na^+, K^+, and Mg^{2+} in surface waters is associated with the dissolution of the clay minerals existing in the area. Kelepertzis and Kontis (1997) found that these elements have a strong association with clay minerals and plagioclase feldspar. Moreover, the sources of SO_4^{2-} are the geogenic factors of the region, as the composition of lignite is strongly associated with the geological environment of Megalopolis region. The low NO_3^-/Cl^- ratios and high Cl^- concentrations along the Alfeios river indicate sewage contamination from Megalopolis town as the main NO_3^- source (Fig. 4). High Mn content is primarily due to the presence of the Pindos zone in the Peloponnese, which contains high amounts of Mn, with Mn content ranging from 100 ppm to as much as 10,900 ppm, as well as localized small Mn deposits (Pe-Piper & Piper, 1989; Photiades & Perseil, 2002). Secondly Mn originated from the sediments of the area and lastly from the mafic and ultramafic rocks in the area. Mo is generally absent from local waters, except for two notable sources. The first is located downstream in Elissonas river (E2) and the second source of Mo enrichment is associated with the Gavros tributary (T1 sample). As suggested by Dimitrakopoulos et al. (2016), Mo shows high leaching potential because it is mobile and soluble in alkaline environment, and in Megalopolis, the geochemical composition of the lignite ore is particularly enriched in Mo.

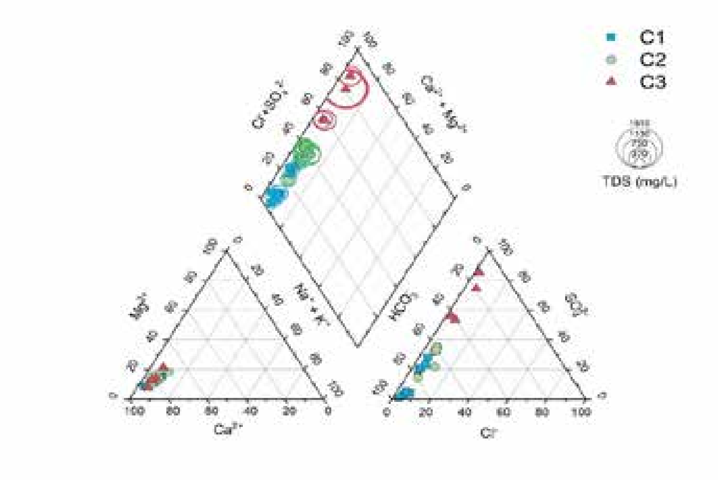

Figure 3: Piper diagram for the surface samples of the study area based on the classification of surface samples according to the results of HCA

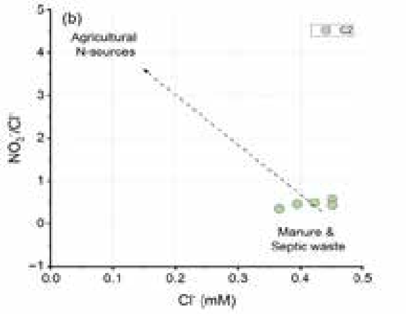

Figure 4: Scatter plot of NO3−/Cl− ratios and Cl−. The limits for agricultural activities and manure/sewage have been taken by Su et al., (2024).

Conclusions

- The Alfeios River appeared to be minimally affected by lignite activities, with no significant changes in water chemistry observed before and after the mining area.
- High Ca^{2+}, Mg^{2+}, Na^+, K^+, and SO_4^{2-} concentrations are observed in tributaries flowing near the external waste dumps and near Thoknia mine.
- High NH_4^+, Cl^- concentrations and low NO_3^-/Cl^- ratios in the Zarzakis stream, point to septic waste from Megalopolis town as the main source of NO_3^- contamination that affects the entire length of the Alfeios river.
- Trace elements such as Mn and Mo exhibit distinct sources of enrichment. Manganese appears to originate both from the Chert series (Pindos zone) and post-Alpine sediments in the western basin. In contrast, Mo enrichment is observed in samples after the Elissonas River confluences with the Alfeios River. This enrichment could be attributed to the dissolution of material from the external waste disposal site. The influence of fly ash deposits potentially could be considered as an additional Mo source; however, the external trenches network in the mine perimeter, diverts the surface runoff into external and internal reservoirs, where the concentrated water is pumped and used for the rewetting of desulfurization and fly ash solid waste deposits inside the Thoknia mine area. Therefore, the surface water, that is in contact with the with fly ash deposits, is recycled inside the mine, and leaks in the outside are prevented.

Acknowledgements

This study was partially funded by the Special Account for Research Grants, NKUA project no. 21070 (Educational, research and operational requirements of the Department of Geology & Geoenvironment).

References

An, L., Li, Q., Wu, P., Lu, W., Li, X., Zhang, C., & Zhang, R. (2024). Potential impacts of coal mining activities on nitrate sources and transport in a karst river basin in southwest China. Environmental Science and Pollution Research, 31(10), 15412–15423. https://doi.org/10.1007/s11356-024-32167-7 **[Journal Article]**

Dimitrakopoulos D., Vasileiou E., Stathopoulos N., Dimitrakopoulou S. (2016). Estimation of the qualitative characteristics of post mining lakes in different lignite fields in Greece. **[Journal Article]**

Dimitrakopoulos, D., Vassiliou, E., & Founda, M. (2007). Impacts of mining activities on water resources to Megalopolis lignite district area. In Geophysical Research Abstracts (Vol. 9). **[Journal Article]**

Energy and Climate Action Plan, (2021). The "Sustainable Energy and Climate Action Plan (SECAP) of the Municipality of Megalopolis. (Greek) **[Report]**

EU, 2020. Directive (EU) 2020/2184 of the European Parliament and of the council of 16 December 2020 on the quality of water intended for human consumption. Off. J. Eur. Union 435 (L435), 1–62. **[Report]**

González-Martínez, M. D., Huguet, C., Pearse, J., McIntyre, N., & Camacho, L. A. (2019). Assessment of potential contamination of Paramo soil and downstream water supplies in a coal-mining region of Colombia. Applied Geochemistry, 108. https://doi.org/10.1016/j.apgeochem.2019.104382 **[Journal Article]**

IGME., (1997). Geological Map of Greece, 1:50,000, Megalopolis Sheet. Institute of Geology and Mineral Exploration, Athens, Greece. **[Journal Article]**

Kelepertzis, E., Matiatos, I., Botsou, F., Antonopoulou, C., Lappas, I., Dotsika, E., Chrastný, V., Boeckx, P., Karavoltsos, S., & Komárek, M. (2023). Assessment of natural and anthropogenic contamination sources in a Mediterranean aquifer by combining hydrochemical and stable isotope techniques. Science of the Total Environment, 858. https://doi.org/10.1016/j.scitotenv.2022.159763. **[Journal Article]**

Kelepertsis, A.E., Kontis, E (1997). Geochemical and mineralogical characteristics of Pleistocene lignites and associated sediments of Marathousa coal field, Central Peloponnese, Greece. Chin. J. Geochem. 16, 8–19 (1997). **[Journal Article]**

Kypritidou, Z., Kelepertzis, E., Kritikos, I., Kapaj, E., Skoulika, I., Kostakis, M., Vassilakis, E., Karavoltsos, S., Boeckx, P., & Matiatos, I. (2024). Geochemistry and origin of inorganic contaminants in soil, river sediment and surface water in a heavily urbanized river basin. Science of the Total Environment, 927. https://doi.org/10.1016/j.scitotenv.2024.172250 **[Journal Article]**

Liu, W., Liu, S., Tang, C., Qin, W., Pan, H. & Zhang J. (2020). Evaluation of surface water quality after mine closure in the coalmining region of Guizhou, China. Environ Earth Science 79, 427. **[Journal Article]**

Louloudis G., Kasfikis G., Mertiri E. (2024). Hydrogeological Study for the environmental monitoring and management of the Water potential of Megalopolis mines during the year 2023. Department of Hydrogeological Studies of the Directorate of Mine Exploitation and Completion Studies (DMEPO) of the General Directorate of Production Planning & Development PPC S.A.

(Greek language). **[Report]**

Louloudis G. (2017). The worth of hydrogeochemical data factor analysis (PCA) in interpretation of underground water origin. Megalopolis lignite bearing fields mine water and regional waters relations case study, Proceedings of 15th International Conference on Environmental Science and Technology Rhodes, Greece, 31. **[Journal Article]**

Pe-Piper, G., & Piper, D. J. W. (1989). The geological significance of manganese distribution in Jurassic-Cretaceous rocks of the Pindos Basin, Peloponnese, Greece. In Sedimentary Geology (Vol. 65). https://doi.org/10.1016/0037-0738(89)90010-9 **[Journal Article]**

Photiades, A., Perseil, E.A., 2002. The cu-Ni-Bearing Todorokite from Western Pindos Series (Peloponnese, Greece): Analogous to

Todorokite in Deep-Sea Manganese Nodules, in: Proceedings of XVII. Congress of Carpathian-Balkan Geological Association, Bratislava. [Journal Article]

Sokratidou, A., Roumpos, C., Kaimaki, S., Gkouvatsou, E., Perdiou, A., & Tsagkarakis, G. (2018). Innovative Approaches to Coal Surface Mine Sites Rehabilitation: A Case Study of Megalopolis Lignite Fields. **[Journal Article]**

Su, D., Zhou, Z., Gong, X., Yan, L., Ding, S., Dong, H., Zhang, Y., Wang, X., 2024. Identification of nitrate sources and transformation in karst cave water using hydrochemistry and NO3− isotopes (δ15N/δ18O) combined with a Bayesian mixing model. All Earth 36, 1–17. https://doi.org/10.1080/27669645.2024.2356138 **[Journal Article]**

Welch, C., Barbour, S. L., & Hendry, M. J. (2021). The geochemistry and hydrology of coal waste rock dumps: A systematic global review. In Science of the Total Environment (Vol. 795). Elsevier B.V. https://doi.org/10.1016/j.scitotenv.2021.148798 **[Journal**

Article]

World Health Organization WHO. (2022). Guidelines for drinking-water quality: fourth edition incorporating the first and second addenda. Geneva: World Health Organization; 2022. **[Journal Article]**

Yang, Y., Mei, A., Gao, S., & Zhao, D. (2023). Both natural and anthropogenic factors control surface water and groundwater chemistry and quality in the Ningtiaota coalfield of Ordos Basin, Northwestern China. Environmental Science and Pollution Research, 30(25), 67227–67249. https://doi.org/10.1007/s11356-023-27147-2 **[Journal Article]**

17th INTERNATIONAL CONGRESS of the Geological Society of Greece

BULLETIN OF THE GEOLOGICAL SOCIETY OF GREECE, SP. PUBL.

EXTENDED ABSTRACT 068

Integrating cutting-edge methodological and technological solutions, enabling the development of a next-generation network of Near Fault Observatories across Europe (project TRANSFORM²)

Panagiotis Elias[1], Gaetano Festa[2,3], Lauro Chiaraluce[3], Pascal Bernard[4], George Kaviris[5], Christos Evangelidis[6], Efthimios Sokos[1], John Clinton[7], Alexandru Marmureanu[8], Simona Colombelli[2], Mariano Supino[3], Dimitris Paronis[6], Vassilis Karastathis[6], Men-Andrin Meier[7], Semih Ergintav[9], Alessandro Vuan[10], Tomas Fischer[11], Stanka Sebela[12], Dimitris Paliatsas[1], Anna Serpetsidaki[1] and Andreas Karakonstantis[1]

(1) University of Patras, Patra, Greece
(2) Università di Napoli Federico II, Naples, Italy
(3) Istituto Nazionale di Geofisica e Vulcanologia, Rome, Italy
(4) Institut de Physique du Globe de Paris, Paris, France
(5) Section of Geophysics-Geothermics, Department of Geology and Geoenvironment, National and Kapodistrian University of Athens, 15784 Athens, Greece
(6) National Observatory of Athens, Athens, Greece
(7) ETH Zurich, Switzerland
(8) National Institute for Earth Physics, Bucurest, Romania
(9) Boğaziçi University, Kandilli Observatory and Earthquake Research Institute, Department of Geodesy, Istanbul, (Turkey
(10) National Institute of Oceanography and Applied Geophysics – OGS, Trieste, Italy
(11) Faculty of Natural Sciences, Charles University, Prague, Czechia
(12) Research Centre of the Slovenian Academy of Sciences and Arts – ZRC SAZU, Postojna, Slovenia

Introduction

A Near Fault Observatory (NFO) is a natural laboratory undergoing active, and complex geophysical processes at or in proximity to densely populated urban areas. NFOs bound relatively small areas and provide researchers from various disciplines (e.g. geophysics, geodesy, and geochemistry) the opportunity to access and (re-)use a vast wealth of data and derive scientific products. This allows a better understanding of the multi-scale, physical/chemical processes, responsible for earthquake generation. This can only be achieved by the acquisition of continuous, long-term, high-resolution multidisciplinary data and the application of consistent, reliable state-of-the-art data processing. Six NFOs in Europe have been identified by the European Plate Observing System (EPOS), Figure 1, as long-term Research Infrastructures; three additional NFOs are in observer status. NFOs target the enhanced understanding of the mechanics of earthquakes to unravel the anatomy of complex seismogenic faults.

Figure 1: Map of the Near Fault Observatories (in red) and those being in observer status (in orange) across Europe.

Vision of TRANSFORM²

The TRANSFORM² project has the ambitious goal to improve and transform the existing NFOs, by integrating cutting-edge methodological and technological solutions, paving the way for the next generation of NFOs across Europe. This will be achieved by:

- Conducting tests, horizon scanning and feasibility studies, performing gap-analysis and assessing user needs in order to gain knowledge of the available state-of-the-art sensor equipment, evaluating its appropriateness and applicability for their deployment in the NFOs.
- Accelerating sensor development and testing where possible.
- Creating, developing, and applying workflows that will revolutionize the capacity of NFOs to detect and characterize seismicity and ongoing seismic sequences in real-time, leveraging machine learning as well as the existing and next-generation instrumentation.
- Establishing new paradigms in Earthquake Early Warning (EEW) that are optimized for the dense NFO networks. Assessing the developed workflow's suitability on EEW applications targeting the decision-makers and, consequently, society.
- Transforming the interaction with stakeholders and decision-makers, underpinned by a deeper understanding of their needs and demands and ultimately the benefits that they can gain from the RIs.
- Assessing the capacity and opening of new pathways for the existing NFOs to function as powerful test-beds for the development, calibration, and testing of new measuring equipment and systems.
- Identifying possible funding mechanisms and sources and providing recommendations to national administration authorities and the European Commission on potential calls for the long-term sustainability of the RIs.

Main Pillars

TRANSFORM² is based on the four pillars and on a coherent strategy for communication and liaison activities with researchers, scientists, and stakeholders, securing their active engagement, as well as the assessment and control of the project's outcomes, long-term scientific and socio-economic impact. These are:

Pillar I – New generation of sensors and analytical solutions in basic and applied research related to earthquake processes. These new technologies will contribute to the design of innovative studies and the opening of new perspectives to forecast natural disasters and mitigate associated risks and impact. The scientific and technological advancements of the last decade allowed the scientific community to use a new generation of sensors and analytical solutions in basic and applied research. Near Fault Observatories (NFOs) are the most suitable infrastructures to develop and test advancements in technology because they maintain the facilities and cover a large scientific knowledge to challenge the design, realization, testing, and use of innovative instrumentations. We aim to develop innovative instruments that will go beyond the state-of-the-art, improving NFOs capabilities for interdisciplinary (seismology, acoustics, geodesy, geochemistry) observational and monitoring purposes. We will exploit recent technological advancements (fiber optic-based systems, fully autonomous low-cost seismic devices, ferroelectric acoustic sensors, high-rate multi-constellation GNSS, automated geochemical sensors) to generate a new generation of multidisciplinary data that will allow for the first time to investigate earthquake nucleation processes in more details and from different perspectives.

Pillar II – Novel automatic workflow concept for enhancing detectability and characterization of earthquakes. Development of workflows for improving earthquake detection and source characterization across magnitude ranges. The emergence of Machine Learning (ML) algorithms and Digital Acoustic Sensing (DAS) of fiber optic cables are having a disruptive and transformative effect on seismology today, enabling new and fundamental insights into earthquake processes. The impact of NFOs can be expected to be particularly significant. We aim to exploit these technologies by exploring novel methodologies that will be transformed into operational-quality software, enabling application across the NFOs, with a focus on real-time applications. The first effort focuses on applying machine learning in order to deepen and enrich earthquake catalogues founded on traditional seismic instrumentation. A final effort will be focused on earthquake source characterisation - the elevated event-detectability provides new opportunities for this topic. The characterization of earthquakes might be supplemented by the HR-GNSS instrumentation solutions. Although accelerometers measure the waveform with orders of magnitude higher resolution and at higher frequencies than GNSS, they do not guarantee the representation of the overall event in a unique reference frame and may suffer from the so-called baseline shift (acceleration bias) and data clipping during large events.

Pillar III – New platforms for supporting decision-makers: Earthquake Early Warning concept, combining regional and on-site systems, new communication systems beyond telemetry, and tailored applications to citizens and stakeholders. In the seconds following earthquake initiation, Earthquake Early Warning Systems (EEWS) can provide prompt notification of the incoming strong ground motion and estimate the potential damage, using real-time, modern information systems, leveraging fast telemetry and data processing from dense instrument arrays deployed in the source region of the event of concern. Despite this scientific and experimental effort, EEWS at the European scale are far from being considered a consolidated and standard technology. The real-time information released by EEWS often suffers from large uncertainties and inaccuracy of the predicted ground shaking amplitude. Additionally, the existing prototype EEWS at European scale are conceived to trigger a generic alert release and are often disconnected from the specific community and environment to be protected. Both factors complicate the effective implementation of EEW methodologies and prevent the use of real-time alerts for automatic decision-making processes during emergencies. Taking advantage of the recent progress in sensors and communication technologies, alongside new theories and observations on the earthquake nucleation process, here we want to set the grounds for the development of the new concept of EEWS, having the next-generation NFOs as backbone infrastructures.

Pillar IV – Next generation of accessibility: Test-bed concept, for testing and development of new cutting-edge measuring sensors. The raised research infrastructure will be exploited as a testbed for the equipment to be developed, workflows, early warning, and decision-making platforms, for demonstration and proof of concept purposes. The main goal is to use and test new measuring sensors and methodologies for studying natural systems at several sites (test-beds). These test-beds might be natural underground cavities, underground basements or even perpendicular escape branches of tunnels. A big challenging task is the in-situ demonstration of new instruments based on innovative optical recordings and processing. These new instruments and technologies, such as the commercial DAS or Brillouin Optical Time-Domain Reflectometer (BOTDR) systems, require long optical cables. For the EEW-ready NFOs, a difficult task will be represented by the improvement of EEW capabilities by extending the EEWS software and exporting the Decision Module, a platform that will be able to issue alerts from multiple locations that act independently. Several prototype applications will be developed to test the end-to-end chain going from data acquisition, and real-time processing of multiple algorithms to output combination and alert release. In several test sites we will involve stakeholders to evaluate the performance of the developed Decision Module.

Communication acivities

TRANSFORM² will focus on the active engagement of the stakeholders through targeted actions.

In the framework of TRANSFORM², industrial partners are given the opportunity to participate by interacting with the scientific and research community through the various planned initiatives. Towards this direction, we propose the development of the SolidEarth Innovation Hub (SEIH), the organization of two dialogue forums and two info-days dedicated to industry.

SolidEarth Innovation Hub is a web-based platform for exposing TRANSFORM²'s activities to stakeholders in a stakeholder-friendly manner and for evolving ideas to innovation and to realized outputs and services

Dialogue forums: Two dialogue forums will be organized by the Region of Western Greece with the participation of invited representatives from local authorities of the countries participating in the NFOs, industrial partners, researchers, scientists, and other target groups. Our aim is to trigger interest and promote the potential opportunities offered to the stakeholders through their active engagement.

Info-days for industry: TRANSFORM² will organize two info-days to engage stakeholders from the commercial world and communicate the projects and NFOs' potential involvement in their domains.

Last but not least, at the project's completion, a comprehensive **'White Book'** will be compiled which will document how associated data, products and services from the next-generation RI can be exploited for the benefit of different target groups among the research community, the stakeholders, and the society and propose ways for a sustainable funding of the RI in the future.

Acknowledgements

TRANSFORM² is funded by the European Union under project number 101188365 within the HORIZON-INFRA-2024-DEV-01-01 call. We would like to acknowledge all the TRANSFORM² colleagues involved in the proposal.

17th INTERNATIONAL CONGRESS
of the Geological Society of Greece

BULLETIN OF THE GEOLOGICAL SOCIETY OF GREECE, SP. PUBL.

EXTENDED ABSTRACT 069

The Syros GeoPark Project

Engi M.[1], Gialoglou A.[2], Koutsabasis P.[3], Laurent V.[4], Mavrogonatos C. G.[5]

(1) University of Bern, Switzerland, martin.engi@unibe.ch (2) Syros, Greece agialoglou@mou.gr (3) University of the Aegean, Syros, Greece kgp@aegean.gr (4) Imperial College, London, UK v.laurent@imperial.ac.uk (5) University of Pisa, Italy konstantinos.mavrogonatos@unipi.it

Highlights

Apart from educational and cultural objectives, this project emphasizes the sustainable development of geo-tourism in Syros, with extended seasons, respect for sensitive areas, and supporting ecological preservation efforts.

Background and Motivation

Syros is renowned worldwide among geologists, mainly because its subduction / exhumation history is so well displayed. This realization has attracted countless Earth scientists to Syros since the 1960s, and people on the island have certainly noted these “odd tourists”, equipped with hammers and maps. But hardly any of the locals know what keeps attracting so many field geologists to their island. To this day, a general awareness of the outstanding significance of Syros – and the neighboring Cycladic islands – is lacking. Plenty of scientific research papers on Syros have appeared, but only scientists read these. Sadly, the plate tectonic spectacle evident in Syros remains obscure to most people!

The Syros GeoPark Project aims to change this : The public shall get the opportunity to recognize some of the many geological features visible in Syros and find out how these formed. Interested visitors of the Syros GeoPark shall learn what dramatic history is hidden in the Cyclades. For Syros locals, becoming aware of how their island evolved is part of their cultural identification, their local root system and pride. As a result, ecological sensitivity will spread as well.

Beyond such educational goals, the Syros GeoPark Project aims to form a basis for sustainable economic development by promoting geo-tourism. Opportunities for soft tourism shall be offered in a balanced program combining geological, archaeological, historical and ecological topics. Tourism groups are increasingly keen on discovery programs with an environmental and popular science touch, or on combining physical fitness with family fun. Most hikers prefer moderate weather conditions, they favour spring and fall months over the hot summer. Geo-tourism promises calmer, substantially extended seasons, beyond the brief tourist hype.

Ambitions and Challenges

Over the past 50 years, intense research worldwide has been focusing on subduction-related processes. Studies conducted in the Cyclades have substantially contributed to our current understanding in this field. On Syros in particular, numerous structural, petrological and geochemical investigations have elucidated the evolution in great detail. Hence a vast body of knowledge now exists on the tectonic history of the Aegean-Cycladic archipelago. It is difficult, even for specialists, to integrate so many relevant research results, and bridging the gap to the general public amounts to an enormous challenge.

In view of these considerations, the Syros GeoPark Project has developed two complementary elements : a **GeoCenter** with museum-style displays and activities, and a series of **GeoPaths** offering (self-)guided excursions for hiking-tourists. The goal of both elements is to motivate visitors to enter an enjoyable learning process. The challenge is to stimulate their curiosity, irrespective of prior knowledge and initial interest, so as to guide them to appreciate aspects of Syros beyond sun and fun at the beach…

The ambition of the **GeoPaths** is to provide incentive and information that will motivate locals and tourists to explore *Apano Meria*, the splendid northern part of Syros. An existing network of hiking trails exists, and along these visitors are guided to observe the magnificent landscape, to stop at points of interest (POIs), where they are introduced to specific phenomena, outcrops or (geo)morphological features. A GIS-based app has been specially developed (*Syros GeoPaths App,* Koutsabasis *et al*., 2023) to make necessary information available to visitors, to assist them in planning their hikes and to offer real-time guidance and explanations along each of the GeoPaths. This app will freely be available to download on smartphones or tablets.

The **GeoCenter** will establish the main focus of the Syros GeoPark in a historic building in Ermoupolis. The aim is to immerse visitors in a wide spectrum of geology-related topics relevant to Syros. Fundamental aspects, such as the vast time-scales in Earth science, are introduced, with links from history to archaeology, and from geology to cosmology. The origin of our solar system, its planets and our moon are explained, as are meteorites. From the fundamental structure of planets, displays move on to Earth dynamics, global plate tectonics, and subduction-related processes in particular. The complex history of the Mediterranean is reviewed. Emphasis is placed on showing visitors how researchers combine various disciplines, how progress in Earth science results from working together at many scales. The splendid minerals and rocks found in Syros are displayed not only for their beauty, but to convey how such samples, metamorphosed at high pressure, provide insight into processes deep inside the Earth, at tectonic plate boundaries. Interactive models, both digital and analog, are used to make many of the concepts understandable, and visitors will also enjoy playing the field assistant to a geologist in a VR game.

Above all, the GeoCenter aims to motivate visitors to explore more of what they learnt by hiking along the GeoPaths. Conversely, observing phenomena in Apano Meria while hiking may well bring up questions that may steer people to visit the GeoCenter.

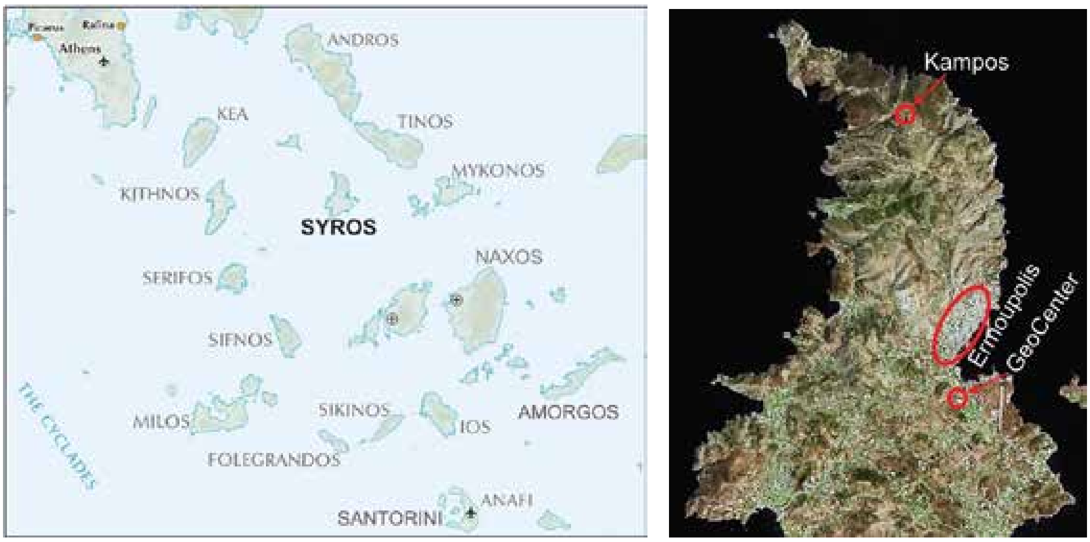

Figure 1. Overview map of the Cyclades (left), with locations relevant for the Syros GeoPark (right).

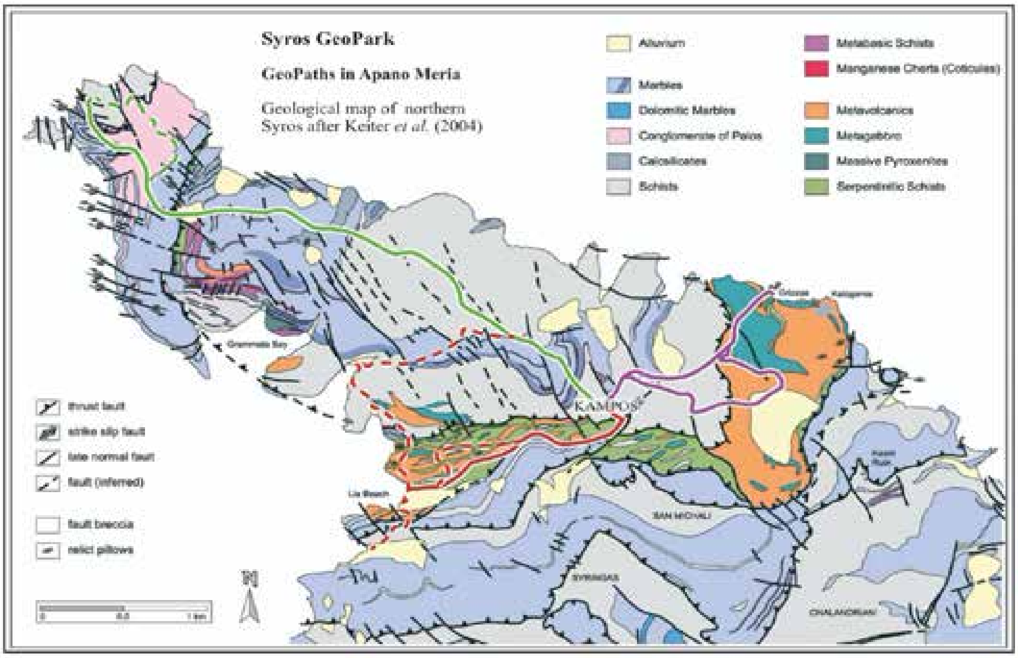

Figure 2. Geological base map of northern Syros (Keiter et al. 2004). GeoPaths from Kampos indicated by colored traces.

The Syros GeoPaths

The network of the GeoPaths is centered at Kampos, a tiny hamlet some 8 km north of Ermoupolis, where the road ends. All hikes start and finish all start at Kampos, they take between 3 and 6 hours round-trip (plus time for swimming etc.). Each GeoPath focuses on one or more geological themes (Table 1), so there is plenty to discover and enjoy.

Table 1. Characteristics of the GeoPaths in the Syros GeoPArk.

Path	Main topics of interest	Distances[1]	POIs, specials
Kampos – Lia	High-pressure shear-zone, tectonic contacts, brittle and ductile deformation, hydration phenomena, metasomatism, eclogite and glaucophane schists, marbles and metavolcanic rocks	H: 3.3 km V: 180 m	10 POIs Pretty beach “Aerolithos”
Kampos – Marmàri – Lia	Marble quarry, lawsonite pseudomorphs, cross section through shear zone, metasomatism, valley formation, mass flow	H: 4.5 km V: 310 m	11 POIs Nice beaches (3!)
Kampos – Diapori – Ryakas	Primary and tectonic contacts, fluid activity, erosional processes and features, soil formation, geomorphology, metaconglomerate, sedimentary *versus* tectonic origin	H: 8.4 km V: 410 m	13 POIs Fabulous views on clear days
Kampos – Grizzas	Intact (primary?) sequence of sedimentary and volcanic origin, metamorphic mineral growth, historic remnants, deformation in metagabbro, magmatic relics, chaotic breccia deposits, erosional morphology	H: 6.2 km V: 420 m	11 POIs Pebble beach “Cyclopic hand”
Kampos - Trochós	Metasediments and metavolcanics, karst formation in marble, eclogite lens, great views to Bronze-age Kastri fortress, historic Trochòs settlement and remnants, magmatic “factory”, veining	H: 2.8 km V: 110 m	5 POI Best view of Kastri

1: Approximate hiking distances. Horizontal (H) in kilometers for round trip. Vertical (V) in meters, necessarily up and down!

Popular destinations include the valley from Kampos to Lia beach, arguably the best researched transect in Syros. It displays an exceptionally well preserved high-pressure shear zone, that is interpreted as an exhumed part of a subduction channel. It presents a tectonic mélange containing massive eclogite fragments, elongate trails of metavolcanics and marble, all immersed in a highly tectonized serpentinite matrix, now composed mainly of talc-chlorite schist. The eclogite lenses display thin metasomatic rims and spectacular glaucophane veins, attesting to hydration of eclogite during exhumation. Most of the giant eclogite lenses are fragmented, but one boulder, known as “Aerolithos”, still stands over to 20 meters high. Its characteristic outline gave the Syros GeoPark its emblem (Fig. 3).

Figure 3. The “Aerolithos”, a giant eclogite fragment overlooking the bay of Lia

The Syros GeoCenter

The GeoCenter utilizes part of a 19th century industrial building, formerly one of the important tanneries in Syros. The impressive architecture of the Kornilaki building (Fig. 4) and its location slightly outside the busiest parts of central Ermoupolis offer a very suitable space for a museum-type installation.

Two floors of very distinct character lend themselves for displays. In preparation, some basic constructions were required to adapt the internal structure, notably to separate the display halls on the top floor from the building’s central court. In total, the plans (Fig. 5) now encompass an entry and two display spaces at ground level, plus five exhibition halls upstairs.

Figure 4. The Kornilaki building in Ermoupolis, housing the GeoCenter and the library of the University of the Aegean

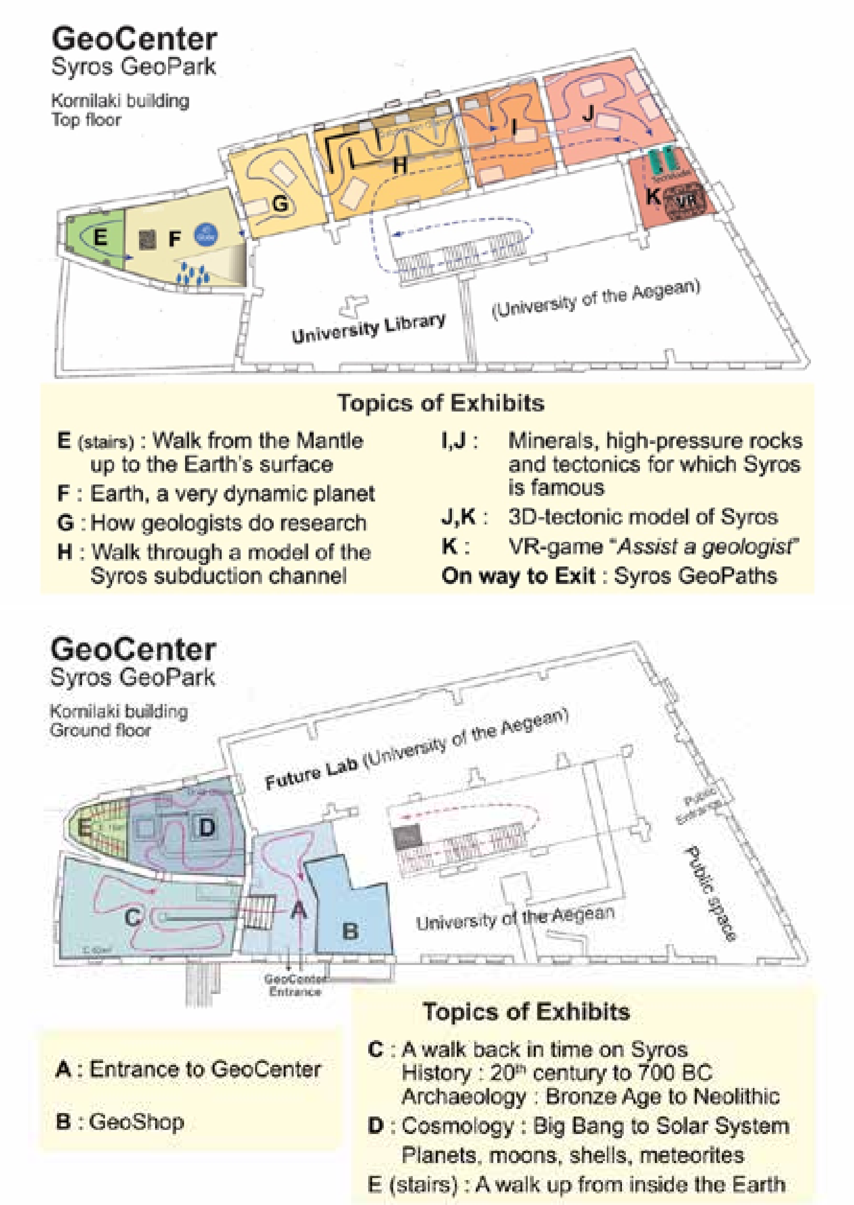

Figure 5. Floor plans at the GeoCenter, space distribution and topics of planned exhibits

Figure 6. Peeking into one of the exhibition halls of the GeoCenter

Project Organisation, Timeline, and Outlook

The Syros GeoPark was conceived as a project in 2017 by M. Engi and A. Gialoglou. In 2018 it received major funding through the SPECIAL PURPOSE DEVELOPMENT PROGRAMME for the SOUTH AEGEAN. In 2023 an extension with additional funds was granted. The project runs under the auspices of the Municipality of Syros, which has provided substantial support as well. A strong partnership with the University of the Aegean was established with P. Koutsabasis in 2018, and several international universities have been actively collaborating.

Regrettably, the initial time plan has been repeatedly disrupted due to the pandemic, an inefficient public administration, and a couple of individuals seeking to harm the project. Serious difficulties still remain due to urgently needed roof repairs on the Kornilaki building, as well as complicated negotiations with some of the land owners. Nevertheless, an optimistic time-plan presently counts on rapid progress over the next months, such that the Syros GeoPark should officially open in October 2025.

All along eight long years of preparation, the prospect of the GeoPark has generated growing enthusiasm in Syros, not only in the tourism sector, but equally among people with ecological, historical and archaeological interests. Strong connections have been established between the GeoCenter and sections of the University of the Aegean, some of which share the Kornilaki building. Beyond Greece, the many partners involved in the project have been spreading news about the project in international geological circles.

The idea of integrating the Syros GeoPark into a larger framework by associating it the with interested neighboring islands, so as to establish a topically broad Cycladic GeoPark has been discussed. No concrete plans exist so far, but at that scale an integration into the global network of UNESCO geoparks would appear both attractive and realistic.

Acknowledgements

Substantial funding for the Syros GeoPark Project by the Greek Public Investment Program is gratefully acknowledged. We thank the Municipality of Syros for all the support provided. Countless friends have collaborated with us – too many to name you all, but we do sincerely thank you, as this project could not be realized without you!

References

Keiter, M., Piepjohn, K., Ballhaus, C., Lagos, M., Bode, M., 2004. Structural development of high-pressure metamorphic rocks on Syros island (Cyclades, Greece). Journal of Structural Geology 26, 1433-1445.

Koutsabasis, P., Nikolarakis, A., Panopoulou, E., Georgiadi, S., Mavrogonatos, C., Engi, M., 2023. Mobile User Experience to Learn About Geology While Hiking: The Syros GeoPaths app. Proceedings of the 2nd International Conference of the ACM Greek SIGCHI, Athens. 1-8.

17th INTERNATIONAL CONGRESS
of the Geological Society of Greece

BULLETIN OF THE GEOLOGICAL SOCIETY OF GREECE, SP. PUBL.

EXTENDED ABSTRACT 070

The 2024–2025 Seismic Sequence in the Santorini-Amorgos Region: High-Resolution Seismological Insights into a Volcano-Tectonic Crisis

Evangelidis C.P.[1] and Fountoulakis I. [1]
(1) National Observatory of Athens, Institute of Geodynamics, cevan@noa.gr

Introduction

The Santorini-Amorgos (SA) region lies within one of the most active segments of the South Aegean Volcanic Arc (SAVA), where complex interactions between tectonic structures and volcanic systems are driven by the ongoing subduction of the African plate beneath Eurasia (Fig. 1a). This region is characterized by extensional deformation along NE–SW-trending faults and includes prominent volcanic centers such as Santorini and Kolumbo. In mid-2024, low-level seismicity began beneath Santorini, gradually intensifying and migrating northeastward by early 2025. This development raised significant concern due to its location along known fault systems and in proximity to active volcanic centers. Historically, the area has shown evidence of tectono-magmatic activity, and the emerging sequence prompted the need for detailed monitoring and analysis. The primary objective of this study is to investigate the evolution and underlying processes of the 2024–2025 seismic sequence using high-resolution seismic monitoring. Specifically, we aim to enhance the existing seismic catalog through machine-learning-driven workflows, resolve spatial and temporal patterns of earthquake occurrence, and assess the physical nature of the events—particularly whether they result from tectonic faulting, magmatic intrusion, or a combination of both. A secondary goal is to develop and implement a near-real-time operational framework to support crisis response and long-term scientific research.

Methods

Seismic data were acquired from 23 broadband, short-period, and strong-motion stations, with coverage significantly improved by the installation of station HT.ANYD on Anydros Island in early February 2025. The analysis focused on the period between June 2024 and March 2025. Using continuous waveform data, seismic phases were automatically picked with EQTransformer (Mousavi et al., 2020), a deep-learning tool optimized for volcanic environments, and associated with the PyOcto phase associator (Münchmeyer, 2024). Initial event locations were determined with NonLinLoc and refined using a source-specific station term (SSST) relocation (Lomax et al., 2014; Lomax and Savvaidis, 2022), and the GrowClust algorithm (Trugman and Shearer, 2017) based on waveform cross-correlation. This workflow produced a final catalog of nearly 14,000 high-precision events. For larger earthquakes (ML ≥ 3.5), full moment tensor (MT) solutions were computed using Gisola (Triantafyllis et al., 2021), a high-performance implementation of the ISOLA method. The seismic signals were further analyzed using the Frequency Index (FI) metric, which estimates relative spectral content and provides insight into source complexity and potential magmatic influence.

Results

The relocated seismicity revealed a clear evolution of the sequence, beginning with shallow clusters beneath the Santorini caldera and shifting northeastward to greater depths beneath Kolumbo volcano (~20 km) (Fig.1b, 1a-b). The seismicity then migrated toward Anydros, forming a broad, diffuse seismogenic zone between 10–15 km depth, extending ~20 km in length and aligning with NE–SW-trending tectonic structures. Cross-sections indicate both steeply dipping and antithetic faults, consistent with transtensional deformation (Fig.1a-b, g-h, i-j). Moment tensor solutions display a dominant normal-faulting regime with significant non-double-couple components, especially positive isotropic and CLVD terms, suggesting crack-opening processes linked to magmatic fluid movement. The FI metric further supports this interpretation, revealing spatial variation in frequency content, with higher-FI events concentrated northeast of Anydros, where the activity appears more tectonic in nature, and lower-FI events toward the southwest, potentially indicating stronger magmatic involvement. Seismic migration patterns also exhibit rapid back-and-forth behavior with velocities up to 2.8 km/h.

Conclusions

The 2024–2025 SA sequence presents a compelling case of tectono-magmatic interaction, with seismicity progressing from deep initiation beneath Kolumbo to shallower zones aligned with known tectonic features. The combination of moment tensor inversion and frequency content analysis suggests that the sequence was not purely tectonic but involved magmatic processes such as dike injection or fluid migration. The study demonstrates the effectiveness of machine-learning-based workflows for real-time seismic monitoring during volcanic crises. The resulting high-resolution catalog provides valuable insights into the geodynamic behavior of the region and is now openly available for future studies. This work establishes an operational framework that may serve as a model for future seismic and volcanic crises in similar geodynamic environments.

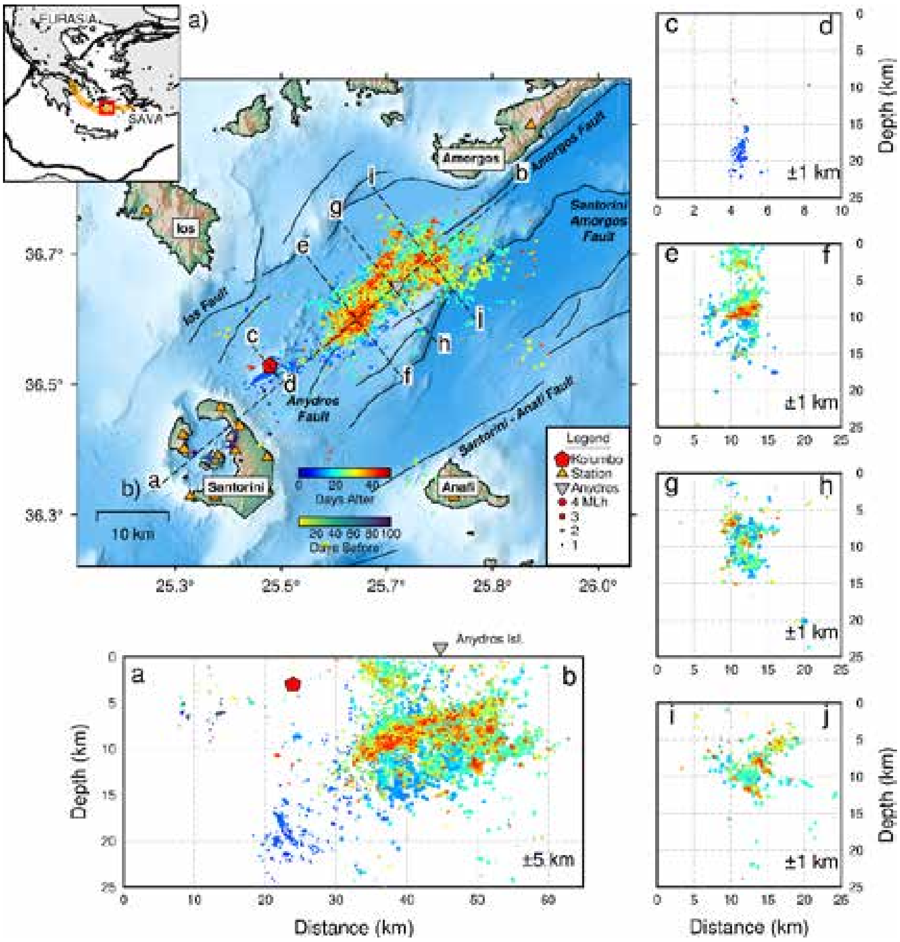

Figure 1. (a) General illustration of the broader Hellenic arc region, showing the main plate boundaries. The SAVA is highlighted in orange, with the study area shown in b) marked by a red rectangle. (b) Relocated seismic events, color-coded based on their occurrence date relative to 20/01/2025 (DD:MM:YYYY) and scaled according to their local magnitude (ML). Black lines represent the main fault traces in the area (Nomikou et al., 2018), while the red polygon defines the Kolumbo volcano chamber (2-4 km depth based on Chrapkiewicz et al. (2022)). The inverted triangle marks the location of Anydros Island, and triangles indicate the seismic stations used in this study. Vertical cross-sections (a-b to i-j) are also shown.

Acknowledgements

Figures and maps were created using the Pythonic interface of the Generic Mapping Tools (PyGMT) software (Tian et al., 2025) and the Matplotlib library (Hunter, 2007). Additionally, parts of the analysis were conducted using ObsPy (Beyreuther et al., 2010). We are thankful to all those scientists and personnel who maintain and operate their networks at the National Observatory of Athens-Institute of Geodynamics, Aristotle University of Thessaloniki-Seismological Station and National Kapodistrian University of Athens-Seismological Laboratory.

References

Beyreuther, M., Barsch, R., Krischer, L., Megies, T., Behr, Y., Wassermann, J., 2010. ObsPy: A Python Toolbox for Seismology. *Seismological Research Letters* 81, 530–533. doi: 10.1785/gssrl.81.3.530.

Chrapkiewicz, K., Paulatto, M., Heath, B.A., Hooft, E.E.E., Nomikou, P., Papazachos, C.B., Schmid, F., Toomey, D.R., Warner, M.R., Morgan, J.V., 2022. Magma Chamber Detected Beneath an Arc Volcano With Full-Waveform Inversion of Active-Source Seismic Data. *Geochemistry, Geophysics, Geosystems* 23(11), e2022GC010475. doi: https://doi.org/10.1029/2022GC010475.

Hunter, J.D., 2007. Matplotlib: A 2D Graphics Environment. *Computing in Science & Engineering* 9(3), 90–95. doi: 10.1109/

MCSE.2007.55.

Lomax, A., Michelini, A., Curtis, A., 2014. Earthquake Location, Direct, Global-Search Methods. In: Lee, W.H.K. (Ed.), *Encyclopedia of Complexity and Systems Science*. Springer New York, pp. 1–33. doi: 10.1007/978-3-642-27737-5150 − 2.

Lomax, A., Savvaidis, A., 2022. High-precision earthquake location using source-specific station terms and inter-event waveform similarity. *Journal of Geophysical Research: Solid Earth* 127(1), e2021JB023190.

Mousavi, S.M., Ellsworth, W.L., Zhu, W., Chuang, L.Y., Beroza, G.C., 2020. Earthquake Transformer—An Attentive Deep-Learning Model for Simultaneous Earthquake Detection and Phase Picking. *Nature Communications* 11, 3952. doi: 10.1038/s41467-020-17591-w.

Münchmeyer, J., 2024. PyOcto: A high-throughput seismic phase associator. *Seismica* 3(1). doi: 10.26443/seismica.v3i1.1130.

Nomikou, P., Hübscher, C., Papanikolaou, D., Farangitakis, G., Ruhnau, M., Lampridou, D., 2018. Expanding extension, subsidence and lateral segmentation within the Santorini - Amorgos basins during Quaternary: Implications for the 1956 Amorgos events, central - south Aegean Sea, Greece. *Tectonophysics* 722, 138–153. doi: https://doi.org/10.1016/j.tecto.2017.10.016.

Tian, D., Uieda, L., Leong, W.J., Fröhlich, Y., Schlitzer, W., Grund, M., Jones, M., Toney, L., Yao, J., Tong, J.-H., et al., 2025. PyGMT: A Python interface for the Generic Mapping Tools. https://doi.org/10.5281/zenodo.14868324.

Triantafyllis, N., Venetis, I.E., Fountoulakis, I., Pikoulis, E., Sokos, E., Evangelidis, C.P., 2021. Gisola: A High-Performance Computing Application for Real-Time Moment Tensor Inversion. *Seismological Research Letters* 93(2A), 957–966. doi: 10.1785/0220210153.

Trugman, D.T., Shearer, P.M., 2017. GrowClust: A Hierarchical Clustering Algorithm for Relative Earthquake Relocation, with Application to the Spanish Springs and Sheldon, Nevada, Earthquake Sequences. *Seismological Research Letters* 88(2A), 379–391. doi: 10.1785/0220160188.

17th INTERNATIONAL CONGRESS
of the Geological Society of Greece

BULLETIN OF THE GEOLOGICAL SOCIETY OF GREECE, SP. PUBL.

EXTENDED ABSTRACT 071

Tooth enamel meso- and microstructure of fossilized Hipparionine horses of Pikermi (Attica, Greece)

Fasoli D.[1], Stathopoulou E.[1]
(1) National and Kapodistrian University of Athens, Department of Geology and Geoenvironment, Panepistimiopolis, 15784 Zografou, Greece, dionfasoli@gmail.com , estathop@geol.uoa.gr

Research Highlights

There are no major differences in the microstructure of enamel between the two main subgenera of Pikermi. However, slight distinctions are present, in enamel thickness and Type III enamel presence.

Introduction / Background

Equidae teeth have a highly complex structure, consisting of heavily plicated enamel. Hypsodonty, along with enamel microstructure alterations, helped them adapt to changes in dietary conditions (Pfretzschner, 1993). Due to its unique diversity, enamel often allows for the identification and classification of mammals, shedding light also on their phylogenetic relations. Tooth enamel microstructure is known to be an indicator of dietary adaptations and biomechanical stress due to its unalterable nature (Koenigswald and Pfretzschner, 1991).

The objective of this study was to describe and compare the traits of Hipparionine dental enamel from the famous fossiliferous site of Pikermi (Attica, Greece). Any unique characteristics could offer crucial phylogenetic information and could even be used for the identification of the different species that have been recorded at the site, but till now they were only identified based on macroscopic features. This information was also correlated to the mesoscopic characteristics of tooth enamel, which in the case of these specific animals is extremely complicated, as well as fascinating. Intense plications and variations of the enamel thickness within a single tooth are extraordinary. This is the first attempt to discriminate different hipparionine species at the site based on enamel microstructure.

Materials and Methods

Twenty-four dental samples (upper cheek teeth) from the fossiliferous locality of Pikermi (Attica, Greece) were acquired, to test for distinctions between two subgenera belonging to the Pikermi fauna, in meso- and micro-scale. The physical characteristics and size of Pikermi hipparions allow us to discriminate between at least two species, *Hippotherium brachypus and Cremohipparion mediterraneum* (Böhme *et al.,* 2018) (*H. brachypus* and *H. mediterraneum* in Koufos, 1987, Koufos *et al.,* 2022). These subgenera descended from different lineages and show different cranial and limb bone characters (Koufos, 1987).

The rich terrestrial vertebrate fauna has been extracted from the Pikermi Formation, an up to 30-meter-thick series of mostly reddish silts with subordinate clastic channels of conglomerates and sandstones (Roussiakis *et al.,* 2019), with its deposition starting in the Early Tortonian (Vallesian) (Böhme *et al.,* 2017). The material at the site has been dated back to the Tortonian – Messinian boundary (middle Turolian) (circa. 7,25 Ma B.P.) (Koufos, 2013; Böhme *et al.,* 2017).

The material was grouped based on macroscopic and mesoscopic characters and measurements (height from the root, occlusal length, occlusal width, protocone length, number of enamel plications pointing at the protocone – plis caballins, number of rest of plications, shape of protocone) (Figures. 1,2), according to Eisenmann *et al.,* 1988.

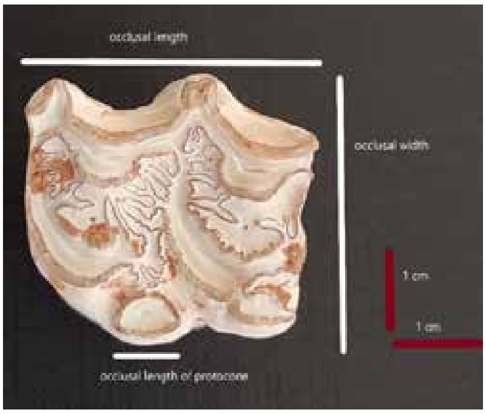

Figure 1. Macroscopic and mesoscopic measurements on the dental occlusal surface of sample Π89/39, according to Eisenmann *et al.,* 1988.

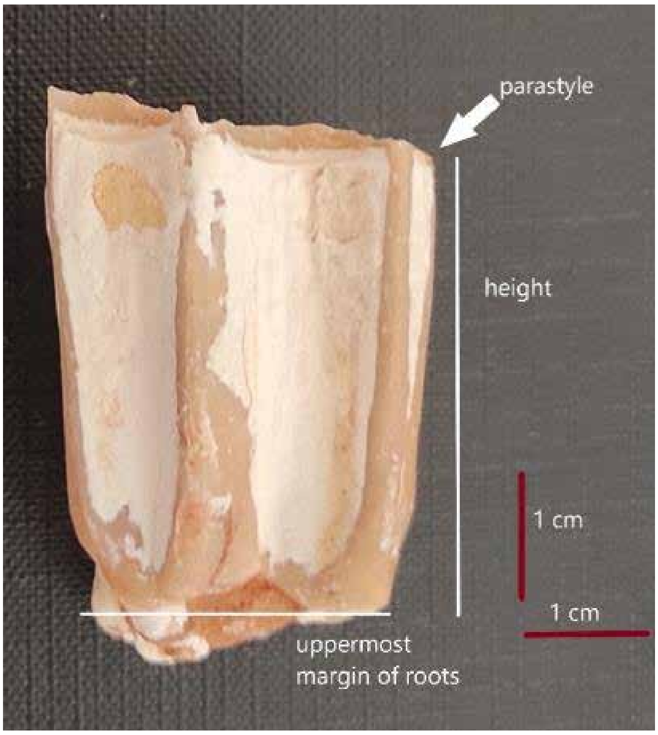

Figure 2. Macroscopic measurements on dental sample Π89/39 (vestibular view), according to Eisenmann et al., 1988.

Samples of each group were examined via stereoscope and Scanning Electron Microscope (SEM), regarding changes in the number of enamel plications while moving closer to the root (cut at 3, 2, and 1 cm from the root), enamel thickness, and enamel types and distribution. To study the enamel microstructure of the selected teeth, they were embedded in resin and cut at 1, 2 and 3 cm above the root of the samples. The embedded samples were prepared according to a specific procedure which includes etching with HCl, to enhance the enamel's characteristic features (Koeningswald and Rose, 2005), and after being coated with Au-Pd they were observed with a Jeol JSM 6390 Scanning Electron Microscope. SEM is considered essential for the observation of specimen histology.

Results – Discussion

No increase/decrease pattern was detected in the number of plications while moving closer to the root, although all samples, at 1 cm from the root, showed a simpler structure. There was the exception of one sample whose plis caballins (8) exceeded the range given by Koufos, 1987 (1-5).

Enamel maximum thickness ranged between 1000 – 1400 μm in peripheral enamel, 800 – 1400 μm in protocones, and 1000 – 1300 in the fossettes. The group with 1 pli caballin showed average maximum thickness of 1,3 mm in peripheral enamel, 1,17 mm in protocone, and 1,21 mm in the fossettes, while the group with >3 plis caballins showed average maximum thickness of 1,16 mm in peripheral enamel, 1,02 mm in protocone, and 1,16 mm in the fossettes.

Three main enamel types are seen in Equidae with hypsodonty. Modified enamel (or Type I enamel) closer to the EDJ (enamel – dentine junction) consisting of radial rows of prisms separated by relatively thick rows of IPM (inter – prismatic matrix), radial enamel (or Type II) closer to the ECJ (enamel – cementum junction) which consists of prisms of various sizes and shapes (horseshoe, keyhole, oval) with noticeably thinner – to – non-existent IPM, and a honeycomb – like structure (or Type III enamel) making small appearances in either the EDJ or the ECJ or both, composed of round- shaped prisms separated by thick IPM (Kilic *et al.,* 1997; Pfretzschner, 1992; Demeshkant *et al.,* 2023).

All samples showed all the aforementioned enamel types (Figures 3 – 5). The samples with 1 pli caballin had more Type III enamel than the ones with >3 plis caballins, in various areas, and even far from the junctions. Most plications showed irregularities regarding the enamel prisms and IPM orientations at the invaginations, with no distinct pattern (irregular enamel type) (Figure 6), while elsewhere the enamel prisms and IPM followed a relatively radial path between the boundaries, and in others HSBs (Hunter – Schreger bands) appeared. The plications of all the samples had triangular - like or rounded shapes and were either deep or shallow.

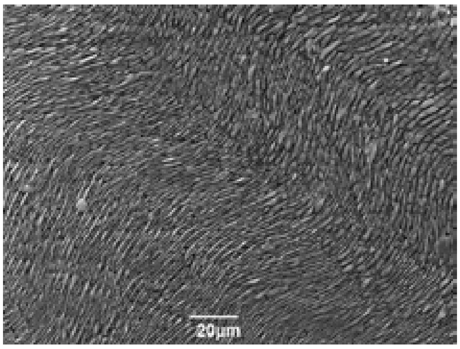

Figure 3. Type I enamel (modified) in sample Π89/9 (2cm distance from the root).

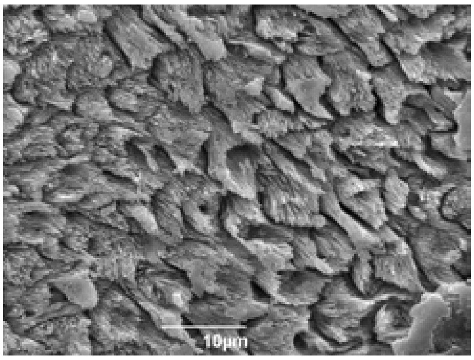

Figure 4. Prisms of Type II enamel (radial) in sample Π89/12 (2cm distance from the root).

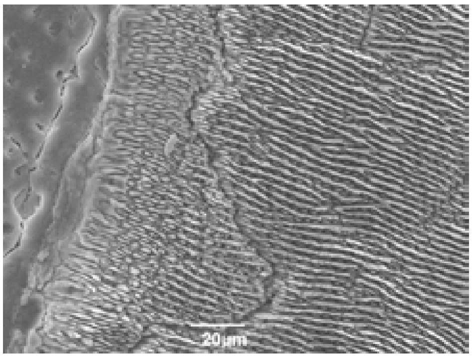

Figure 5. Type III enamel (honeycomb – like) (left) and Type I enamel (modified) (right) in sample Π89/9 (2cm distance from the root).

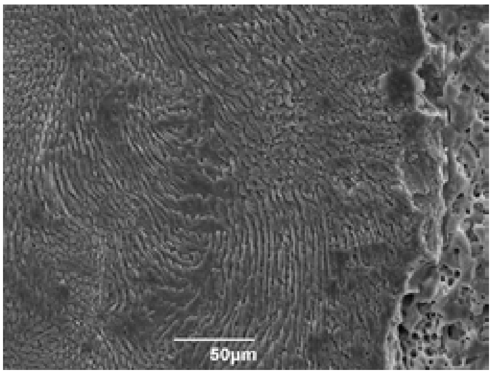

Figure 6. Irregularities appearing in one of the plis caballins of sample Π89/12_2

The presence of modified enamel (Type I) shows the evolutionary track of hipparionine horses, as the diet of Equidae altered from browsing to grazing (Pfretzschner, 1993). As the enamel microstructure in this genus (and in Equidae in general) is very complicated, a clear distinction between the two subgenera was not possible, as all samples exhibited the same features under SEM, similar distribution of enamel types, fragmented protocones, and similar plication forms, with the differences being the number of plications, the enamel thickness, and the more distinct presence of Type III enamel in samples with 1 pli caballin. Ongoing research will allow for further investigation of this hypothesis.

References

Böhme, M., Spassov, N., Ebner, M., Geraads, D., Hristova, L., Kirscher, U., Kötter, S., Linnemann, U., Prieto, J., Roussiakis, S. and Theodorou, G., 2017. Messinian age and savannah environment of the possible hominin Graecopithecus from Europe. PloS one 12(5), e0177347.

Böhme, M., Van Baak, C.G., Prieto, J., Winklhofer, M. and Spassov, N., 2018. Late Miocene stratigraphy, palaeoclimate and evolution of the Sandanski Basin (Bulgaria) and the chronology of the Pikermian faunal changes. Global and planetary change 170, 1-19.

Demeshkant, V., Biegalski, M. and Rekovets, L., 2023. Teeth Enamel Ultrastructural Analysis of Selected Equidae Taxa. Diversity 15(11), 1141.

Eisenmann, V., Alberdi, M.T., De Giuli, C. and Staesche, U., 1988. Studying fossil horses. EJ Brill, Leiden, The Netherlands.

Kilic, S., Dixon, P.M. and Kempson, S.A., 1997. A light microscopic and ultrastructural examination of calcified dental tissues of horses: 2. Ultrastructural enamel findings. Equine Veterinary Journal 29(3), 198-205.

Koenigswald, W. and Pfretzschner, H.U., 1991. Biomechanics in the enamel of mammalian teeth, in: Constructional morphology and evolution. Berlin, Heidelberg: Springer Berlin Heidelberg, 113-125.

Koenigswald, W.V. and Rose, K.D., 2005. The enamel microstructure of the early Eocene pantodont Coryphodon and the nature of the zigzag enamel. Journal of Mammalian Evolution 12, 419-432.

Koufos, G.D., 1987. Study of the Pikermi hipparions. Part I: Generalities and taxonomy. Bulletin du Muséum national d'Histoire naturelle 9, 197-252.

Koufos, G.D., 2013. Chapter 28. Neogene mammal biostratigraphy and chronology of Greece. In Fossil mammals of Asia: Neogene biostratigraphy and chronology. Columbia University Press. pp.595-626

Koufos, G.D., Vlachou, T.D. and Gkeme, A.G., 2022. The fossil record of equids (Mammalia: Perissodactyla: Equidae) in Greece. Fossil vertebrates of Greece Vol. 2: Laurasiatherians, artiodactyles, perissodactyles, carnivorans, and island endemics, 351-401.

Pfretzschner, H.U., 1992. Enamel microstructure and hypsodonty in large mammals. Structure, function and evolution of teeth, 147-162.

Pfretzschner, H.U., 1993. Enamel microstructure in the phylogeny of the Equidae. Journal of vertebrate paleontology 13(3), 342-349.

Roussiakis, S., Filis, P., Sklavounou, S., Giaourtsakis, I., Kargopoulos, N. and Theodorou, G., 2019. Pikermi: a classical European fossil mammal geotope in the spotlight. European Geologist 48, pp.28-32.

17th INTERNATIONAL CONGRESS
of the Geological Society of Greece

BULLETIN OF THE GEOLOGICAL
SOCIETY OF GREECE, SP. PUBL.

EXTENDED ABSTRACT 072

Local driven protection of a tectonic geosite, in Crete, Greece: The Paligremnos Protected Landscape

Fassoulas C.[1], Staridas S.[2], Nikolakakis E.[3]
(1) Natural History Museum of Crete- University of Crete, Heraklion, Greece, fasoulas@nhmc.uoc.gr (2) Staridas Geography, Heraklion, Greece, (3) University of Crete, Heraklion, Greece

Introduction

Protection of geodiversity is an urgent need of modern societies as it represents the crucial link between abiotic and biotic nature. Although in nowadays protection of biodiversity is one of the highest priorities of our societies, the same does not apply for geodiversity, which is under additional pressures related with row materials and development of big infrastructures that are so necessary for our technology. The oldest efforts for conservation of geoheritage are dated back to the 18th century in several European countries, followed by the establishment of the first National Parks in USA (Grand Canyon, Yellowstone etc.) with core geological features (Gray 2004).

In Greece, the first efforts to protect elements of our geoheritage can be found in the establishment of the two National Parks of Olympus (1938) and Samaria (1962), however without any concern or the direct protection of their geological values (Zouros & Fassoulas 2006). Yet, national legislation is very weak in respect to geoconservation and has changed several times overturing former positive initiatives. The first law with a clear provision for the protection of abiotic nature was the 1650/1986 which was foreseen that some aspects of geodiversity, like caves, gorges, plateau and fossil sites could be preserved as Natural Monuments. Application of this legislation was though incredibly difficult as it was requesting the elaboration of Special Environmental Studies of high cost and time consumption that were approved by the Ministry of Environment. As a consequence, no geological monument was protected under this law. In 1985 Lesvos Petrified Forest was declared by the Ministry of Culture as a Protected Monument of Nature, and in 1988 Meteora were nominated as a World Heritage Site mainly for its cultural value. A big step forward was achieved with the Law 3937/2011 which for the first time defined what a geosite is and foresaw the establishment of geoparks in the form of National or Regional Nature Parks, with much simpler studies checked by Regional Authorities. Implementation of this legislation was relative flexible permitting the protection of two geological monuments as Protected Landscapes, the Almyri Panagia in Lesvos and Limnos Petrified Forest. In 2020 legislation changed again with the Law 4685/2020 which abrogated the Nature Parks and thus geoparks and transferred the decision-making process back to the Ministry of Environment, Energy and Climate Change.

A milestone for the geoconservation in Greece was the establishment in 2015 of the UNESCO Global Geoparks by UNESCO, that recognized five territories in Greece under this program, namely the Lesvos Petrified Forest, Psiloritis, Chelmos-Vouraikos, Vikos-Aoos and Sitia. Still the nine existing UGGps in Greece lack of authorization and recognition by law. Concluding, the geological elements that are under protection in Greece are quit few, despite the extraordinary value of Greek Geological Heritage.

In 2022 an important geosite of Crete, the Paligremnos fault scarp (Fig. 1) was placed under serious threat by the initiation of excavations at the top of its scarp by a private company for the construction of touristic apartments. Being a local landmark, a postcard of Crete since the 1970's, an aesthetic landscape, an international climbing field, a well-studied fault (Angelier 1979) and a mapped geosite for Crete with at least regional value (Fassoulas et al. 2007), Paligremnos received an immense and unexpected support by locals, foreign residents, visitors and the climbing community of Greece. Just a week after the excavations, more than 1500 people gathered at Paligremnos protesting against its destruction and the construction of the apartments, requesting by the regional and local authorities its protection under the moto “We become a rock for the protection of our rock”. In July 2022 the Municipality of Agios Vassilios in Rethimno assigned Natural History Museum of Crete the elaboration of a special study for the nomination and protection of Paligremnos as a Protected Landscape, whereas together with the protesting society, undertook legal actions to cancel the building license of the construction. Both actions were successful and finally the Paligremnos was declared in 2023 as a Protected Landscape and Protected Natural Formation due to its geological importance, with the Ministry Decision GGG 535/23-62023. This article presents the main geological features, their assessment and the documentation of the broader area of Paligremnos as a Protected Landscape due to the national value of its geological heritage.

Figure 1. The Paligremnos fault scarp in Plakias bay

Methodology

The Natural History Museum of Crete established a study group including various specialists such as a geologist, geographer, a biologist and an IT specialist with the aim to (1) Identify the area of interest, (2) identify, map, study and document the main geological and biological values of the area (3) Qualitatively and quantitatively assess the geological values of the area (4) identify the potential human and natural risks (5) document the reasons for monument's protection and preparation of a Ministry Decision under the 4685/2020 Law.

In Automn 2022 both geological and biological missions and inventories were contacted at the area, a detailed geological and tectonic mapping at a scale 1:5000 was applied, satellite images were analyzed, an UAV-based photogrammetric survey was conducted and a digital relief model was created for detailed measurements of the scarp, while existing literature was analyzed. Finally, we applied the quantitative geotope assessment method of Fassoulas et al. (2012) to demonstrate the touristic and educational potential of the monument and its vulnerability.

All collected data resulted in the compilation of the Special Geological Study foreseen by the L.3937/2011, which was quite similar to the well-known Special Environmental Studies of the L1650/1986, that was submitted to the regional and national authorities for the characterization of the broader Paligremnos area as Protected Landscape.

Results

The broader area of Paligremnos is characterized by the presence of Jurassic and Eocene limestones of the Tripolitsa nappe and small outcrops of the Eocene flysch, that cover a small peninsula named Psarela, opposite to the well-known tourist destination of Plakias in Rethimnon (Fig. 2). An east-west trending basin exists between the cape Psarela and the Asiderotas mts at the north, covered by late Miocene sediments in which an important amphibian and terrestrial fauna was discovered (Georgalis et al. 2016), while small sand dunes are formed at the southern part of the beach. The monument is located over the north facing steep cliff of the peninsula on which three parallel fault scarps were mapped along the east-west direction (Fig. 2). The first scarp (F1) is the Paligremnos, an almost vertical fault surface with two generations of striations present, as well as large corrugations and kinematic indicators pointing to a normal sense of shear. The second scarp (F2) located uphill is quite long dipping into the sea westwards. This scarp has a moderated dip towards north, and although more weathered it presents also several corrugations, while two coastal caves exist at its surface. A small tunnel was opened during the WWII reaching the caves, to transfer coal excavated inland at the far-most cave where ships could deliver it. The tunnel was supported by fortification establishments too. The higher scarp (F3) has smaller extent, moderate dip with polished surfaces at places, where one set (the oldest) of slickensides can be seen. The analyses of the photogrametric data and the digital relief model (Fig. 3) revealed that the Paligremnos scarp is 132 m long and 42 m high, with a total surface of 5274,1 m^2. Field and other historical data proved that the scarp was naturally exposed. Finally, another older normal fault (F4) oriented northwest-southeast has been mapped on top of the hill forming together the F3 a high escarpment at the Tripolitsa limestone.

Along the coastal cliffs and in several cases on the F2 fault scarp, a sea notch at 1.4m above m.s.l. indicates the tectonic uplift of the whole territory related with the 365 A.D earthquake. Geomorphotectonic mapping and study revealed five distinct marine terraces on the peninsula (Fig.4), the lowest at about 15m height, and the highest at about 120m. showing the gradual rock uplift recorded at the southern coastal zone of Crete during the upper Pleistocene (Ott et al. 2019).

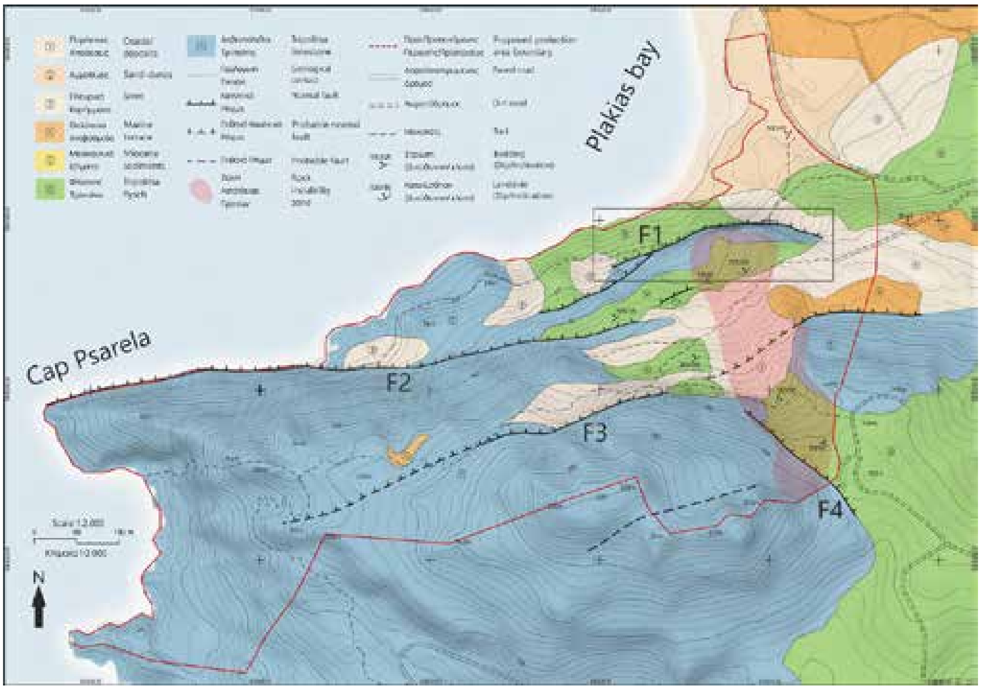

Figure 2. Geological map of study area. F1,..,4 refer to faults in text, square shows Paligremnos scarp

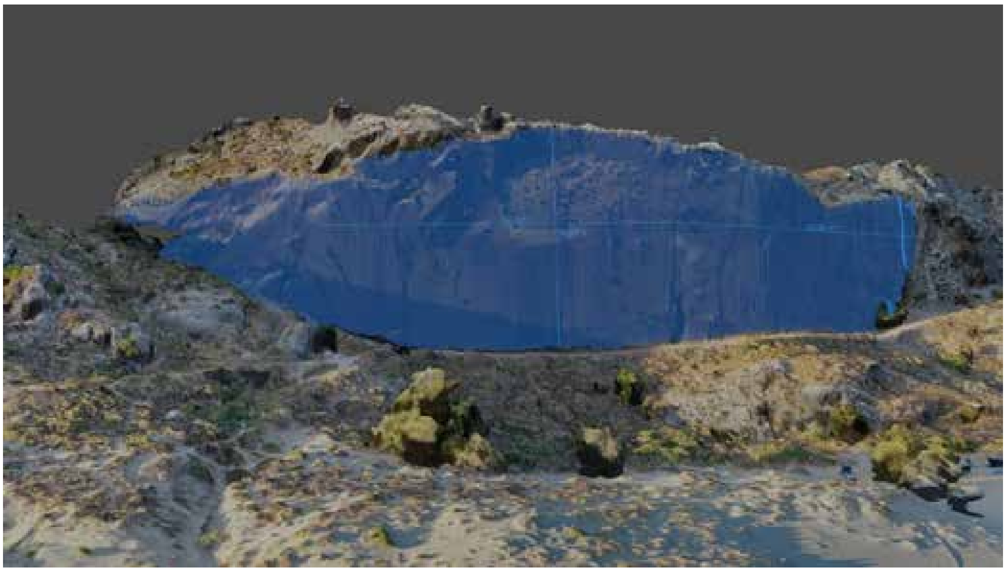

Figure 3. The 3-d relief model of Paligremnos scarp developed for the accurate measurements of its surface

Fault kinematic analyses, using Stereonet software, revealed for the older set of striations a stress field with the maximum extensional axis gently dipping towards the NNW direction and an almost vertical maximum compressional axis, pointing out, together with the kinematic indicators, to a normal sense of shear (Fig 5a). The younger set of lineations indicated a normal sense of shear with considerable lateral component, and the maximum extensional axis almost horizontal dipping towards NNE direction (Fig 5b). This latest stress field is the same with the stress field recognized by Mouslopoulou et al. (2014) for the nearby active Spili fault. In addition, the Paligremnos faults appear to act as antithetic to the main fault zone of Sellia- Assomatos, located north of Plakias basin. Sellia-Assomatos fault zone appears to be the eastwards continuation of the Sfakia fault zone, which is considered as the most important active zone of the southwestern cost of Crete (Nicol et. all, 2020; Ott et al. 2019). The vertical inclination of the Paligremnos scarp was thus interpreted as a rotated surface due to the main activation of the Sellia-Assomatos fault, indicating that the fault zone should be considered as active too.

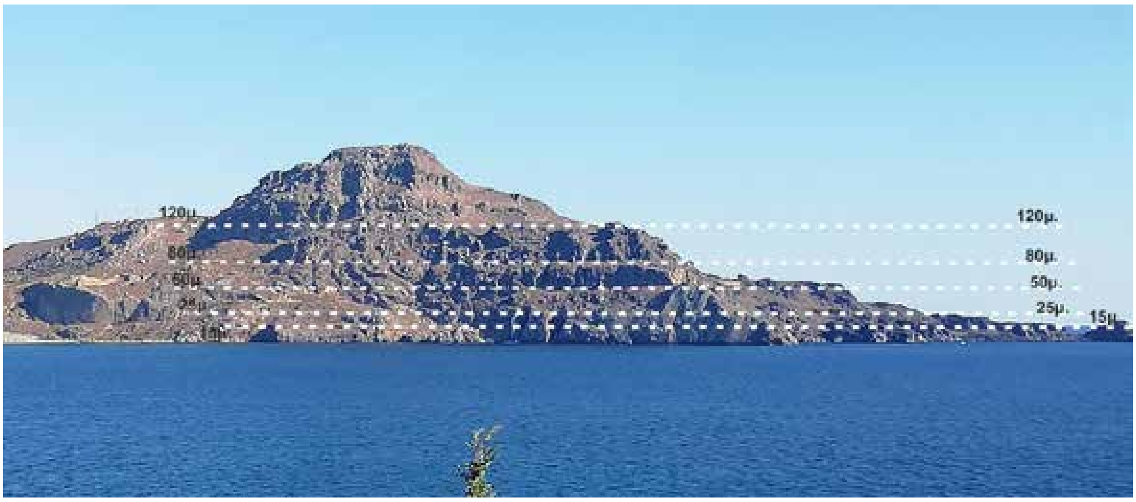

Figure 4. The five marine terraces recognized on the Psarela cape

In respect to other geomorphological features, geological mapping identified a rock instability zone just over the Paligremnos fault scarp initiated at the crosscutting of the F3 and F4 faults on top of the hill. Scattered boulders and large rock blocks seem that have been fallen from the escarpment and then slid on the clay flysch of Tripolitsa reaching finally the edge of the Paligremnos fault scarp. This instability zone covers the area of the touristic constructions imposing a high risk on it.

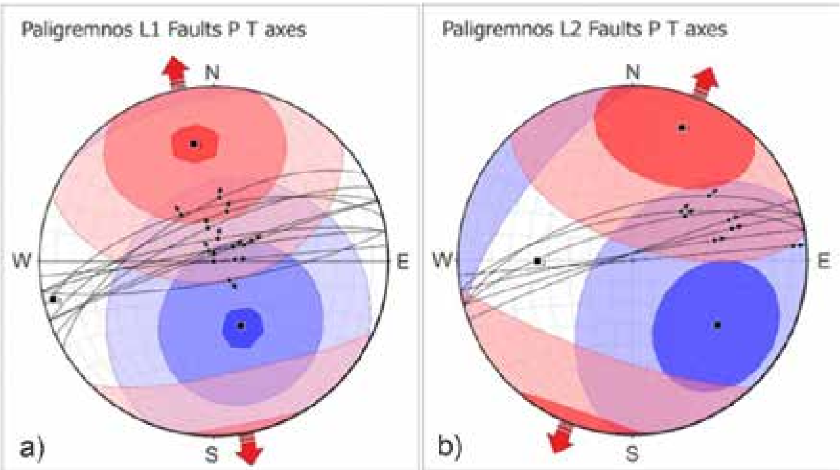

Figure 5. Paleostress analyses of the two striae generations the older a) and newer b)

In what regards the biological value of the area, apart from the sand dunes at the beach that host some very important local flora and are very sensitive ecosystems, the study identified another important area at the western part of the peninsula where, over one of the intermediate marine terraces, a seasonal pond is developed that is crucial for bird fauna. Based on all the above data the suggested area for the protection of the monument was drawn, including all the important geological (fault scarps, notches, marine terraces), biological (part of the dunes and the seasonal pond) and the cultural elements (the tunnel and the remains of the WWII railway and the fortifications) of the monument (Fig. 2).

The qualitative and quantitative assessment that followed documented the value of the area and the reasons to be nominated as a Protected Landscape. The fault scarp is the largest naturally exposed fault scarp in Greece, with the second larger in dimensions but artificially exposed, being the Arkitsa fault (Kokkalas et al. 2007). The Paligremnos fault zone is an active fault zone forming together with the Sellia-Assomatos fault the Plakias graben since the Miocene times. Together with the five marine terraces and the 365 AD notch demonstrate impressively and didactically the Pleistocene rock uplift of the southern coasts of Crete. The Paligremnos fault scarp tucked into the embrace of Plakias bay constitutes a unique and outstanding landscape that forms one of the most attractive landmarks of Crete, listed in geological text books and Atlases (Papanikolaou & Sideris 2013; Mountrakis et al. 2002). Quantitative analyses of the geosite indicated in addition, that the area has of the highest scientific and aesthetic values among the geosites studied with that method in

Greece, and of the highest potential for touristic and educational development. In addition, the vulnerability of the geosite is higher than the normal mean values, mainly due to the thread that touristic constructions may impose.

Conclusions

Based on the processing of bibliographic data, the geological mapping, the analyses of the data collected during the fieldwork and the data provided by residents and visitors of the area, it is demonstrated that the “Paligremnos - Akrotiri Psarela” area of Plakias, Municipality of Agios Vasilios, Rethimno has special and remarkable characteristics of the geological and geomorphological environment, hosts endemic forms of flora and fauna of Crete and gathers some rare and unique for Crete cultural elements related to mining and quarrying activities of the past. It is obvious that the dominant and special characteristics, worthy of protection, are the geomorphological and geological formations that crop out in almost the entire area under consideration, but specifically at the Paligremnos fault scarp that appears to be the largest, naturally exposed fault scarp in Greece. Due to all these values the area finally was declared as a Protected Landscape and Protected Natural Formation under the Greek legislation in 2023, crowning the efforts of local communities to protect their nature.

As an outcome of this study and in order to further promote the values of this area we have developed a virtual tour based on UAV shots and 360° panoramas that virtually guides visitors, step by step, along the main features of the Paligremnos and cape Psarela area. In addition, the tour offers panoramic view of the whole Plakias bay and graben. The tour can be visited thought the following link https://tours.panotours.gr/plakias/.

Acknowledgements

This study is based on the Special Study for the Nomination of the area as Protected Landscape and Protected Natural Formation, assigned to the Natural History Museum of University of Crete by the Municiaplity of Agios Vassilios in Rethimnon. We would like to thank Agios Vassilios Municipality for all the support that has provided during and after the implementation of the Study. We owe special thanks though, to the inhabitants, locals and foreigners, the Climbing and Speleological community of Crete and other specialists who have provided valuable information and data for the development of the Study and the strong motivation and support they offered for the nomination and protection of the area. The final result is dedicated to all of them.

References

Angelier, J., 1979. Neotectonique de l’arc egeen, vol. 3. Society Geologic du Nord Special Publication, pp. 1-418.

Fassoulas C., Paragamian K. & Iliopoulos G. (2007). Identification and assessment of Cretan Geotopes. Bull. Geol. Soc. Greece, vol. XXXVII, 1780 – 1795.

Fassoulas C., Mouriki D., Dimitriou-Nikolakis P. & Iliopoulos G. (2012). Quantitative assessment of geotopes as an effective tool for geoheritage management. GEOHERITAGE, v4, 3, 177-193, DOI 10.1007/s12371-011-0046-9.

Georgalis, G. L., Villa, A., Vlachos, E., & Delfino, M. (2016). Fossil amphibians and reptiles from Plakias, Crete: a glimpse into the earliest late Miocene herpetofaunas of southeastern Europe. Geobios, 49(6), 433-444. https://doi.org/10.1016/j.geobios.2016.09.004

Gray M. (2004). Geodiversity: Valuing and Conserving Abiotic Nature. Wiley-Blackwell eds, 512 p.

Kokkalas S., Jones R. R., McCaffrey K. J. W., and Clegg P. (2007). Quantitative fault Analysis at Arkitsa, central Greece, using terrestrial laser-scanning. Bulletin of the Geological Society of Greece vol. XXXVII, 2007 Proceedings of the 11th International Congress, Athens, May, 2007

Mouslopoulou V., Moraetis D, Benedetti L., Guillou V., Bellier O, & Hristopulos D. 2014. Normal faulting in the forearc of the Hellenic subduction margin: Paleoearthquake history and kinematics of the Spili Fault, Crete, Greece. Journal of Structural Geology 66 (2014) 298-308

Mountrakis, D., Zouros, N. & Soulakelis, N. (2002). Atlas of geological monuments of Aegean, Greece. Ministry of Aegean, Lesvos, pp.352.

Nicol A., Mouslopoulou V., Begg J., Oncken O., (2020). Displacement accumulation and sampling of paleoearthquakes on active normal faults of Crete in the eastern Mediterranean. Geochemistry, Geophysics, Geosystems, https://doi.org/10.1029/2020GC009265

Ott R.F, Gallen S.F., Wegmann K.W., Biswas R.H., Herman F., Willett S.D. (2019). Pleistocene terrace formation, Quaternary rock uplift rates and geodynamics of the Hellenic Subduction Zone revealed from dating of paleoshorelines on Crete, Greece. Earth and Planetary Science Letters, 525(2019, 115757

Papanikolaou D. & Sideris Ch. (2013). Geology the discipline of the earth (in greek). Pattakis eds. Athens, 296 p.

Zouros, N. & Fassoulas, C. (2006). Geodiversity in Greek National Parks. In: 2nd UNESCO Inter. Conf. on Geoparks, Belfast 2006, Abst. Vol., 62.

Tsimi, C., Ganas, A., Ferrier, G., Drakatos, G., Pope, R.J. and C. Fassoulas, (2007). Morphotectonics of the Sfakia normal fault, south-western Crete, Greece. 8th Pan-Hellenic Geographical Conference, volume 1 (186-194), 4 - 7 October 2007, Athens (Greece).

17th INTERNATIONAL CONGRESS of the Geological Society of Greece

BULLETIN OF THE GEOLOGICAL SOCIETY OF GREECE, SP. PUBL.

EXTENDED ABSTRACT 073

Assessing the management of Arkalochori EQ crisis in Crete, Greece under the implementation of RESILIAGE project in order to strengthen community resilience

Fassoulas C.[1], Tamborrino R.[2], Bolca, P.[2], Marra G.[2], Mezzalama G.[2], Tackacs V.[3], Leonhardmair N.[4], Demir M. E.[5]

(1) Natural History Museum, Univ. of Crete, Crete, Greece, fassoulas@nhmc.uoc.gr (2) Politecnico di Torino, Torino, Italy (3) DeepBlue, Rome, Italy (4) Vienna Centre for Social Security, Vienna, Austria (5) Demir Energy, Istanbul, Turkey

Introduction

It is well documented that only preparedness and prevention can support modern communities in respect to the earthquake risk. Being one of the most seismic prone areas in the world, Greece has invested a lot in the prevention of the impacts of future earthquakes and in the increase of preparedness of the structured and non-structured elements of our societies. Prevention is achieved through interventions and actions aiming at the identification of hazard zones, minimizing the exposures on the build environment and developing plans and regulations to manage crises. In most cases preparedness is achieved by strengthening and improving the behavior of material elements and infrastructures, the increase of knowledge regarding the hazard and its impact, as well as the improvement of the self-protection of citizens. In the past years, repeated Earthquake crises revealed that further improvements both on prevention and preparedness are necessary which can be made only if assessment of past crises' management is performed.

The earthquake of Arkalochori in central Crete is of one the most recent and most peculiar crises in Greece. The foreshock sequence started on the beginning of June 2021, just at the end of the COVID 19 crisis, and lasted almost three months having one strong earthquake of 4,8 R on July 24. The long foreshock period enabled the establishment of many seismic instruments in the broader area to monitor the phenomenon. The main shock took place early in the morning on September 21st, 2021 with a magnitude of 6 R scale and focal point 10 kms below the town of Arkalochori (Ganas et al. 2021). The earthquake took place along a well-known active fault in the area, the Kasteli fault (Fassoulas 2001) that has produced a swam of small eq in 1995 too (Delibasis et al. 1999). The town, that is one of the largest of rural Crete with a population of about 4000 inhabitants and many nearby villages were seriously affected with collapses and damages of old and more recent constructions, while even the city of Heraklion experienced moderate intensities with minor impacts. This was the first strong earthquake onshore Crete for more than a century (Papadopoulos 2011), and fortunately, there was only one human victim that was killed by a strong aftershock that happened few hours after the main event.

The most peculiar feature of this crisis was though the very long aftershock period that lasted almost a year with several events between 4 and 5 R scale. It was estimated that more than 4750 earthquakes took place on the broader area over a period of one year (Vallianatos et al. 2022) challenging the structural behavior of the buildings and the mental health of local population. The response of the Civil Protection mechanism was immediate with first responders and civil protection volunteers taking action soon after the main shock installing temporary camps at the Arkalochori and several other villages, and a more organized shelter at the Exhibition Center of Arkalochori few days after. The response of the local population was remarkable with hundreds of them arriving at Arkalochori from the first day to support the victims. This huge offer of volunteers created problems till a mechanism to manage them was set, but their contribution in compensating the burden of the local people and supporting their daily needs was invaluable even months after the earthquake.

The total toll of impacts counts more than 7000 houses heavily damaged by the main shock and its aftershocks with about 3900 of them to be demolished. Within these structures occur many local schools and churches. Apart from the first financial support that state provided soon after the earthquake to those affected by, the recovery process according to the locals failed totally to cover the needs of local societies (p.c. K. Gantatsios, president of "Elpis" the association of the victims of the earthquake 2024). Three years after the earthquake many families still live at preconstructed houses at the temporary shelter, from the 7000 applications for financial aid to repair houses that have been submitted only few tens have been elaborated by the relative services and the broader area presents images of abandonment and depopulation that was obvious at the recent census.

It is important to mention that the psychological burden of the local communities was not only increased by the long-lasting aftershocks but also from rumors and fake news that were circulated at social media but even the national broadcasting channels. Rumors for stronger earthquakes were appearing after interviews or posts of “earthquake specialists” in national and international media. Fake news about the reasons of the long seismicity were repeatedly circulated connecting the earthquakes with the construction nearby of a new airport, the existence of a dam few kms away from the epicenters, but even the overfilling of a chapel under the runway of the new airport, that further increased the communication chaos.

The Arkalochori earthquake is a case study under RESILIAGE project funded by the Horizon Europe and coordinated by the Polytechnic of Torino, in which the University of Crete is among the 18 partners that aim to build sustainable resilient communities with local heritage drivers (https://resiliage.eu/). In general, recent crises and disasters have affected the European citizens’ lives, livelihoods, and environment in unforeseen and unprecedented ways. These disasters are exacerbated by social inequality, lack of adequate information and technology, as well as economic and political crises, that reduce the effective preparedness and response. The main objectives of the project are thus focused on understanding citizen reaction in case of crisis, on cocreating new knowledge encompassing the local heritage drivers that make communities stronger and new tools that provide more accurate information and make it accessible through easy-to-use tools and finally, lightweighting solutions to support first responders and empower citizens in crisis and disaster situations. The project has defined five Systemic Resilience Innovation (SyRI) frameworks focusing on Adaptive Governance, Health and Wellbeing, Active Memory, Social Interaction and Inclusiveness and Socio-economic Resilience that are examined in five European territories facing variable risks. The Region of Crete is one of them addressed to the Active Memory in respect to the earthquake risk.

Hereby we present the results of two workshops that have been developed in Crete under RESILIAGE in order to assess the management of Arkalochori EQ crisis, to identify the cultural factors that may influence local resilience, to build local networks through synergies and collaborative actions, and to identify the gaps in the management crisis operation in order to develop proposals for future improvement.

Figure 1. Implementation of focus groups discussions during the first workshop of RESILIAGE at Cretan CORE Lab on May 2024.

Methodology

The RESILIAGE project has foreseen the organization of five Community Resilience Laboratories (CORE Labs) in five European territories that have suffered in the past from various disasters. These include the City of Trondheim in Norway that faces the risk of landslides (slow clay) and focusses on Health and wellbeing, the Famenne-Ardenne UNESCO Global Geopark in Belgium which has been affected by serious floods several years ago and focuses on Socio-economic resilience, the Region of Crete focusing on the earthquakes and the Active Memory, the Naturtejo UNESCO Global Geopark in Portugal which repeatedly experiences wild fires and focusses on Social Interaction and Inclusiveness and the town of Karsiyaka in Turkey that is facing risks form heatwaves and focusses on the Adaptive Governance.

The relative partners in these counties were obliged to set the CORE Labs by inviting local stakeholders. In Crete the Natural History Museum of Crete invited various stakeholders that are engaged in crisis management, or represent certain local target groups, education and communication organizations and citizens. The CORE Lab was thus formed by representatives of First Responders (National Center of Immediate Aid, Fire Brigade, and Volunteer groups), Local Municipalities and the Region of Crete, Local Development Companies, The Church of Crete, Local Museums, Educational Centers, Local Cultural Clubs and Associations, Sport Clubs and Citizens.

Two onsite workshops were organized in Crete using the focus group methodology (Wilkinson 1998) associated by structured interviews and web questionnaires. In each workshop we used boards, concept, interaction and territorial maps, discussion recordings and the assistance of facilitators to gather and analyse local data in a qualitative manner. The first WS took place on the 21st and 22nd of May 2024 at the premises of Natural History Museum with 30 participants (Figure 1). The aims of the WS were to understand how the local community define its territory in terms of main environmental, historical, and cultural characterizations, understand how local community interacts with the environment from a cultural and historical perspective, gather local narratives of disaster risk reduction, extract cascade effects related to the historical, cultural and environmental factors that intervene in crisis response, and identify lessons learned related to the historical, cultural and environmental factors that intervene in crisis response, having as case study the Arkalochori EQ crisis. During the WS field visit to Arkalochori and nearby areas was organized to discuss with the local stakeholders and inhabitants there (Figure 2).

Figure 2. Pupils performing local dances during the visit of RESILIAGE partners at the preconstructed classrooms hosting the primary school of Arkalochori on May 2024.

The second workshop took place on the 7th of February 2025 again at the Natural History Museum of Crete with the participation of 19 people (Figure 3). This WS was aiming on mapping certain heritage elements recorded at the collective memory that can be used to strengthen local resilience and improve preparedness planning. Activities were thus focused on the co-mapping of local cultural elements supportive to strengthen citizen's resilience, on the co-creation of synergies and collaborations to safeguard those heritage elements through the establishment of a local agreement to safeguard them, and on proposing actions for the inclusion of local communities and vulnerable groups in the crisis management plans through the improvement of communications, the raise of awareness and sensitization of citizens and improving adaptive governance. In this second workshop more advanced methodologies and means were used like serious game, stickers, card boards, thematic maps etc. (Figure 4).

The data collected through these onsite CORE Lab activities were further elaborated by the research partners to step on and develop soft solutions and digital tools that will be evaluated by CORE Lab in a second phase of the project implementation.

Results

The main priority of Civil Protection is always the proper management of a crisis putting more efforts and means though on the response phase. Preparedness and prevention are less developed, whereas the recovery phase is the one that is less considered. RESILIAGE invests in the improvement of preparedness of local communities using their cultural assets and local heritage as potential drivers for establishing strong community resilience that can contribute in a more effective recovery phase. The inventory of these drivers and the assessment of crisis management is the main tool to identify the local needs, capacities and strengths, on which new tools and actions are being developed. The main results under the scopes of RESILIAGE project from the CORE Lab activities in Crete may be summarized as follows.

Figure 3. Co-mapping of cultural and natural heritage elements during the second workshop of RESILIAGE in February 2025.

Cultural bonds remain very strong in the island of Crete based on traditions and ethics dated back in time. Dances, songs, “mantinades” (local rhymes) and common celebrations under various occasions tightened relationships between communities and helped a lot the citizens to cope with the Arkalochori EQ consequences and long-standing impacts (Figure 2). The oral traditions and transfer of myths and stories between generations appears to be a key channel for the preservation of values and collective memory, connecting generations through shared narratives. The workshops also highlighted issues related to social ethics and values as well as the strong blood bond that highlights the importance of family ties that can influence social interactions and contribute to shaping the resilience of the community. At the same time, the workshops underscore that in each settlement there are dozens of reference points and monuments that connect residents to the place and history and offer relief and a source of encouragement in times of crisis, that must be preserved. The existence of social interaction spaces where people can meet and promote social interactions is an important foundation in the event of crises that must be maintained during the operation of temporary shelters.

In places where social interaction was intense, like in Arkalochori where a local sport club and the community were organizing various annual events, this played a crucial role in managing the crisis and offering immediate support to the victims. Their role was remarkable in providing food, immediate aim, managing and organizing the many volunteers and retaining community alive for long period. The engagement of young people in such social and community activities enforces the local cohesion and reduces the vulnerability of the communities. The local Church is also a very important actor in the post crisis phase because it has the organization and means to support immediately the victims especially at the rural areas, with material and immaterial aid. The existence of local volunteer groups is also a very important factor to manage a crisis as they can offer assistance to CP mechanism, support the victims and palliate the psychological burden.

The need for reliable information and proper communication, before but especially during the crisis, emerged as the top problem in the case of the Arkalochori earthquakes. The absence of reliable and timely information, as well as of corresponding official state communication channels, contributed to the increase in the spreading of fake news and rumors that increased further the stress of those affected. The battle with fake news and incorrect information was lost very early on as there was no way to deal with this on social networks. Throughout the long post-earthquake sequence, residents felt the lack of communication and information from the official authorities, a problem that was much more intense in elder people. In these cases, the Church could play an important role, if proper cooperation has been developed between the Church, the relevant scientific bodies and the State. To enhance disaster preparedness and response, it is crucial to adopt a more proactive and comprehensive approach to communication. This should include regular awareness campaigns before a disaster, accessible guidance for individual groups after a disaster and ensure that all relevant information sources are easily identifiable and accessible.

Figure 4. The concept board for the assessing of Crisis Management plan after the implementation of the second workshop of RESILIAGE in February 2025.

Regarding the crisis management it was obvious that the CP mechanism responded immediately after the main shock establishing shelters and providing support to the affected societies, following a well operational management plan. However, it is apparent that despite the comprehensive national policies and documentation, shortcomings exist in resources evaluation and cooperation mechanisms at the local level, which hinder effective disaster response. The strong building codes and regulations didn't prevent the numerous damages and destructions, mainly because of the weakness of the relative authorities to monitor and ensure their implementation. The case of Arkalochori EQs underpin the fact that in rural areas older infrastructure remains vulnerable, highlighting a need for reinforcement and modernization. In addition, and under the threat of Climate Change it was highlighted that disaster risk management plans are not integrated with climate adaptation strategies, causing missed opportunities to leverage ecosystems in disaster management.

Under this scope it was also stressed that detailed risk assessments are outdated and require revisions. The risk and vulnerability assessments identify key vulnerabilities within the adaptation plan, such as: socio-demographic factors (population distribution and vulnerable groups), impacts on buildings and infrastructure, and cultural heritage considerations. The assessment should thus consider agriculture, forestry, biodiversity, and fisheries, as well as references to vulnerable groups such as the elderly and disabled at the national or regional level.

The crisis management was further exacerbated by the fact that the financial legislation lacks detailed information regarding funding mechanisms available for disaster management. Alternative financing mechanisms for risk reduction are scarce, while state financial resources for risk reduction are insufficient, limiting the implementation of disaster resilience measures. The total failure of the CP mechanism in the recovery phase is indicated by the fact that three years after the crisis from the thousands of applications seeking state support to reconstruct the damaged properties, only few tens have been elaborated so far. This situation is not only socially inappropriate, but ethically and morally too as a large number of the Arkalochori victims were elder.

Acknowledgements

This study is funded under the EU's Horizon Europe, key funding programme for research and innovation, with title: "RESILIAGE – Advancing holistic understanding of community RESILIence and heritAGE drivers through community-based methodologies (GA no. 101121231)".

References

Delibasis, N.D.; Ziazia, M.; Voulgaris, N.; Papadopoulos, T.; Stavrakakis, G.N.; Papanastassiou, D.; Drakatos, G. Microseismic activity and seismotectonics of Heraklion Area (central Crete Island, Greece). Tectonophysics 1999, 308, 237–248.

Fassoulas, C., 2001. The tectonic development of a Neogene basin at the leading edge of the active European margin: the Heraklion basin, Crete, Greece. J. Geodyn. 31, 49–70. https://doi.org/10.1016/S0264-3707(00)00017-X.

Ganas, A., Hamiel, Y., Serpetsidaki, A., Briole, P., Valkaniotis, S., Fassoulas, C., Piatibratova, O., Kranis, H., Tsironi, V., Karamitros, I., Elias, P., Vassilakis, E., 2022. The Arkalochori Mw =5.9 earthquake of 27 September 2021 inside the Heraklion basin: a shallow, blind rupture event highlighting the orthogonal extension of central Crete. Geosciences 12, 220. https://doi.org/10.3390/geosciences12060220.

Papadopoulos, G.A. A Seismic History of Crete: Earthquakes and Tsunamis, 2000 B.C.–A.D. 2010, 1st ed.; Ocelotos Publ.: Athens, Greece, 2011; p. 415. ISBN 978-960-9499-68-2.

Vallianatos, F., Karakonstantis, A., Michas, G., Pavlou, K., Kouli, M., Sakkas, V., 2022. On the Patterns and Scaling Properties of the 2021–2022 Arkalochori Earthquake Sequence (Central Crete, Greece) Based on Seismological, Geophysical and Satellite Observations. Appl. Sci. 2022, 12, 7716. https://doi.org/10.3390/app12157716

Wilkinson, S., 1998. Focus group methodology: a review. International Journal of Social Research Methodology, 1(3), 181–203. https://doi.org/10.1080/13645579.1998.10846874

17th INTERNATIONAL CONGRESS
of the Geological Society of Greece

BULLETIN OF THE GEOLOGICAL SOCIETY OF GREECE, SP. PUBL.

EXTENDED ABSTRACT 074

Quaternary eustatic cycles and their impact on the Paleoceanography of the Gulf of Corinth (NE Mediterranean Sea)

Fatourou E.[1], Kafetzidou A.[1], Marret F. [2], Panagiotopoulos K.[1,3], Kouli K.[1]

[1]*National and Kapodistrian University of Athens, School of Science, Geology and Geoenvironment, GREECE (efatourou@geol.uoa.gr)*

[2]*School of Environmental Sciences, University of Liverpool, UK*

[3]*Forschungszentrum Jülich, Jülich, GERMANY*

Introduction / Background

The Gulf of Corinth (GoC), which is a semi-isolated marine basin derived from a geologically young active rift (McNeill *et al.,* 2019b), offers a unique opportunity to study changes in environmental conditions during the Quaternary period in a region where long sequences are few. The GoC is linked to the global ocean via the Gulf of Patras in the Ionian Sea. This connection is facilitated by the Rion Strait to the west and the Corinth Isthmus to the east. The Rion Strait forms a narrow and deep marine embayment, resembling a fjord, with fully marine conditions (Poulos *et al.,* 1996). The recent IODP expedition (IODP381) has retrieved three long sequences (M0078A, M0079 and M0080) recovering most of the Quaternary period and providing the first comprehensive insight on the evolution of a young active rift (McNeill *et al.,* 2019b). The sedimentary sequence drilled 610.43 mbsf that were divided into two main Lithostratigraphic Units (LU). Deposition during the upper one, LU1 (0–385.14 mbsf), is primarily controlled by eustatic sea level and dominated by detrital clay- and silt-grade carbonate, this interval has been divided into 16 subunits (LU1.1-1.16) with respect to the alternation of marine and isolated/semi-isolated intervals, while below 385.14 mbsf, LU2 is composed almost entirely of weakly laminated to homogeneous highly bioturbated mud (McNeill *et al.,* 2019a).

Preliminary observations of conventional biological proxies used for determining past palaeoceanographic conditions during the onshore party of IODP 381 expedition (*McNeill et al., 2019b*) have highlighted an unexpected richness in dinoflagellate cyst taxa, notably species that were only known from the Marmara-Black Sea corridor (e.g., Marret *et al.,* 2004; Mudie *et al.,* 2004; 2017). Due to periods of isolation during Quaternary lowstands, the water conditions were not favorable for the occurrence of conventional palaeoceanographical proxies such as planktonic foraminifera. Fatourou *et al.* (2023) presented an initial study of organic-walled dinoflagellate cyst assemblages from site M0078A, covering the upper 384m (~Marine Isotopic Stage 18), highlighting distinct shifts related to fluctuations in sea-surface temperature and salinity in response to global sea-level changes.

Table 1: List of identified dinoflagellate cyst taxa, with micropalaeontological (cyst) name and associated biological name, trophic level (P: Phototrophic; H: Heterotrophic), and environmental conditions (B: brackish; M: marine) of the Gulf of Corinth.

Cyst name	Biological name	Code	Trophic level	Environmental conditions
Achomosphaera sp.	*Gonyaulax* sp.	Achs	P	M
A. choane	*Gonyaulax* sp.	Acho	P	M
B. tepikiense	*Gonyaulax* sp.	Btep	P	M
Brigantedinium sp. (*B. caracoense* and *B. simplex*)	*Protoperidinium* sp. (*Protoperidinium avellanum* and *Protoperidinium conicoides*)	Brisp	H	B to M
C. rugosum	Unknown	Crug	P	B
E. zonneveldii	Unknown	Ezon	H	M
I. caspienense	*Gonyaulax baltica*	Icas	P	B
I. aculeatum	*Gonyaulax sp.*	Iacu	P	M
I. paradoxum	*Gonyaulax sp.*	Ipar	P	M
I. patulum	*Gonyaulax sp.*	Ipat	P	M
I. plicatum	*Gonyaulax sp.*	Ipli	P	M
I. sphaericum	*Gonyaulax sp.*	Isph	P	M
I. strialatum	*Gonyaulax sp.*	Istr	P	M
L. oliva	Unknown	Loli	H	M
L.machaerophorum s.l.	*Lingulodinium polyedrum*	Lmacsl	P	M
L.machaerophorum s.p.	*Lingulodinium polyedrum*	Lmacsp	P	B
N. labyrinthus	*Gonyalax spinifera*	Nlab	P	M

O. centrocarpum sensu Wall and Dale, 1967	*Protoceratium reticulatum*	Ocen	P	M
P. zoharyi	*Pyrodinium bahamense*	Pzoh	P	M
cysts of *P. dalei*	*P. dalei*	Pdal	P	M
P. psilata	Unknown	Ppsi	P	B
Q. concreta	*Protoperidinium leone*	Qcon	H	M
S. nephroides	*Protoperidinium subinerme*	Snep	H	M
S. quanta	*Protoperidinium conicum*	Squa	H	M
S. belerius	*Gonyalax scrippsae*	Sbel	P	M
S. bentorii	*Gonyalax digitale*	Sben	P	B to M
S. bulloideus	*Gonyalax scrippsae*	Sbul	P	M
S. cruciformis	*Gonyalax* sp.	Scru	P	B
S. delicatus	*Gonyalax* sp.	Sdel	P	M
S. hyperacanthus	*Gonyalax* sp.	Shyp	P	M
S. lazus	*Gonyalax* sp.	Slaz	P	M
S. membranaceus	*Gonyalax* sp.	Smem	P	M
S. mirabilis	*Gonyalax spinifera*	Smir	P	M
S. ramosus	*Gonyalax* sp.	Sram	P	M
T. pellitum	*Gonyalax spinifera*	Tpel	P	M
T. vancampoae	*Pyrophacus steinii*	Tvan	P	M
X. xanthum	*Protoperidinium divaricatum*	Xxan	H	M

We present here a continuous record of dinoflagellate cyst assemblages of the last 1.1 Ma aiming to examine the shifts between marine and isolated/semi-isolated depositional environments in response to eustatic sea level changes in the GoC. The dinocyst assemblages encountered within the intervals described below consist of the low salinity indicators *S. cruciformis*, *P. psilata*, *Caspidinium rugosum, Impagidinium caspienense* and *Lingulodinium machaerophorum* s.p.. *Spiniferites cruciformis* and *P. psilata* are the most dominant species during those intervals, however, a distinct variability in those assemblages is recorded. The dinocyst assemblages recovered within the marine intervals of M0078A record are characterised by a high diversity (30 different species) and with mean concentrations of 24,632 cysts/g. In addition, results from other proxies (aquatic palynomorphs, foraminifera and diatoms) offer an integrated perspective on the evolution of the basin and its surroundings. The freshwater and brackish diatoms, as well as the euryhaline foraminifera identified during the onshore phase of the IODP 381 expedition (McNeill *et al.,* 2019) seem to correlate well with the isolated LUs and the brackish dinocyst assemblages. During the Holocene, the presence of several dinoflagellate cysts, alongside with the decreased TOC and TOC/N at the upper part of LU1.1 (Holocene) confirm the occurrence of well-oxygenated bottom waters in the basin.

Figure 1: Shade plot: visual representation of the species encountered in the different LUs (LU1.1 to LU1.16) and Marine Isotope Stages (MIS). Samples were arranged based on core depth. White colour indicates absence, black the highest abundance in the dataset, while all the different colours suggest low (blue colour), medium (green colour) and high presence (orange and red) (Fatourou, 2024).

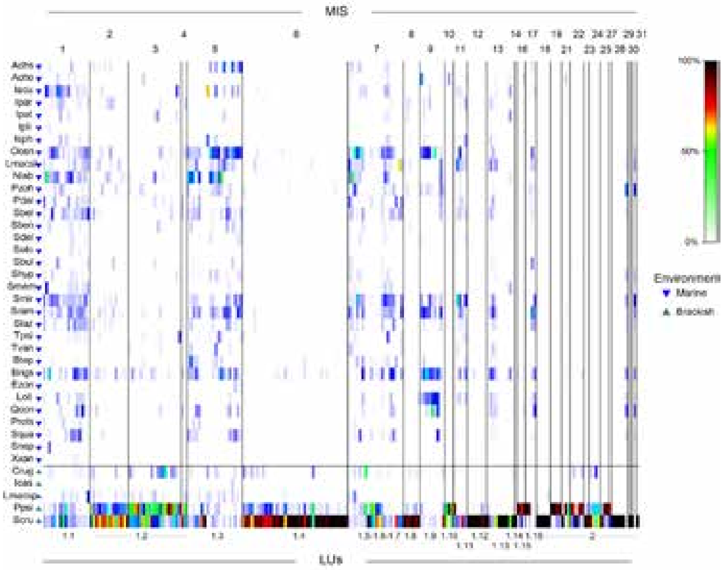

This record aims to fill a gap in palaeoceanographic studies in Eastern Mediterranean region and to provide a better understanding of how shallow-sill connected basins respond to global climate changes. Dinocysts and other palynomorphs (NPPs) suggest that the GoC was repeatedly isolated and reconnected to the Mediterranean Sea during global sea-level lowstands associated with glacials. These proxies combined suggest that marine water flowed into the GoC during the eustatic highstands associated with interglacials. The dinocyst assemblages show a close affinity to modern assemblages from the Black, Caspian, and Marmara Seas (e.g., Marret *et al.,* 2004; Mudie *et al.,* 2004; 2017).

Acknowledgements

The study material was retrieved during the IODP Exp. 381. The research work was supported by the Hellenic Foundation of Research and Innovation (H.F.R.I) under the “First Call for H.F.R.I. Research Projects to support Faculty members and Researchers and the procurement of high-cost research equipment grant” (Project Number: 1026, Quaternary Environmental Changes in the Corinth Rift Area: the IODP 381 palynological record: QECCoRA).

References

Fatourou E., 2024. Depositional environment development and ecosystem response in the Gulf of Corinth during the Quaternary climatic cycles. Ph.D. Thesis, Department of Geology and Geoenvironment, National and Kapodistrian University of Athens, pp. 290.

Fatourou, E., Kafetzidou, A., Marret, F., Panagiotopoulos, K., Kouli, K., 2023. Late Quaternary Ponto-Caspian dinoflagellate cyst assemblages from the Gulf of Corinth, Central Greece (eastern Mediterranean Sea). Mar. Micropaleontol 179. https://doi.org/10.1016/j.marmicro.2023.102211

Marret, F., Leroy, S., Chalié, F., Françoise, F., 2004. New organic-walled dinoflagellate cysts from recent sediments of Central Asian seas. Rev. Palaeobot. Palyno. 129, 1–20. https://doi.org/10.1016/j.revpalbo.2003.10.002

McNeill, L.C., Shillington, D.J., Carter, G., Everest, J.D., Gawthorpe, R.L., Miller, C., Phillips, M.P., Collier, R.E.Ll., Cvetkoska, A., De Gelder, G., Diz, P., Doan M.-L., Ford, M., Geraga, M., Gillespie, J., Hemelsdaël, R., Herrero-Bervera, E., Ismaiel, M., Janikian, L., Kouli, K., Le Ber, E., Li, S., Maffione, M., Mahoney, C., Machlus, M.L., Michas, G., Nixon, C.W., Oflaz, S.A., Omale, A.P., Panagiotopoulos, K., Pechlivanidou, S., Sauer, S., Senguin, J., Sergiou, S., Zakharova, N.V., Green, S., 2019a. High-resolution record reveals climate-driven environmental and sedimentary changes in an active rift. Scientific Reports 9, 1–11.

McNeill, L.C., Shillington, D.J., Carter, G.D.O., Everest, J.D., Le Ber, E., Collier, R.E., Cvetkoska, A., De Gelder, G., Diz P., Doan, M. L., Ford M., Gawthorpe, R. L., Geraga, M., Gillespie, J., Hemelsdaël, R., Herrero-Bervera, E., Ismaiel, M., Janikian, L., Kouli, K., Li, S., Machlus, M.L., Maffione, M., Mahoney, C., Michas, G., Miller, C., Nixon, C. W., Oflaz, S. A., Omale, A.P., Panagiotopoulos, K., Pechlivanidou, S., Phillips, M.P., Sauer S., Seguin, J., Sergiou, S., Zakharova, N.V., 2019b. Corinth active rift development. Proceedings of the International Ocean Discovery Prog, 381. https://doi.org/10.14379/iodp.proc.381.104.2019

Mudie, P.J., Marret, F., Mertens, K.N., Shumilovskikh, L., Leroy, S.A., 2017. Atlas of modern dinoflagellate cyst distributions in the Black Sea Corridor: from Aegean to Aral Seas, including Marmara, Black, Azov and Caspian Seas. Mar. Micropaleontol. 134, 1–152. https://doi.org/10.1016/j.marmicro.2017.05.004

Mudie, P.J., Rochon, A., Aksu, A.E., Gillespie, H., 2004. Late glacial, Holocene, and modern dinoflagellate cyst assemblages in the Aegean–Marmara–Black Sea corridor: statistical analysis and re-interpretation of the early Holocene Noah’s Flood hypothesis. Rev. Palaeobot. Palyno. 128, 143–167. 9

Poulos, S.E., Collins, M.B., Pattiaratchi, C., Cramp, A., Gull, W., Tsimplis, M., Papatheodorou, G., 1996. Oceanography and sedimentation in the semi-enclosed, deep-water Gulf of Corinth (Greece). Mar. Geol. 134, 213–235. https://doi.org/10.1016/0025-3227(96)00028-X

17th INTERNATIONAL CONGRESS of the Geological Society of Greece

BULLETIN OF THE GEOLOGICAL SOCIETY OF GREECE, SP. PUBL.

EXTENDED ABSTRACT 075

Underground rivers in Greece

Fellachidou K.[1], Lazaridis G.[1]

(1) Aristotle University of Thessaloniki, School of Geology, Department of Structural, Historical and Applied Geology, Laboratory of Geology and Paleontology, Thessaloniki, Greece, fellachid@gmail.com

Research highlights

This study presents the first national-scale mapping of underground rivers in Greece, documenting a total of 60 systems. It also offers the first systematic classification of the underground rivers, emphasizing their spatial distribution and characteristics in relation to tectonostratigraphic units. Spatial analysis reveals the dominance of the External Hellenides in speleogenesis, as they host 67% of the documented underground rivers. Limestone hosts 21 underground rivers, highlighting its critical role in speleogenesis. High-relief regions (>900m) host the majority of these systems, influenced probably by climatic and hydrological conditions. Conversely, the Internal Hellenides display fewer and more isolated underground rivers due to their complex geological history and diverse lithologies. Overall, the findings enhance the theoretical understanding of underground river systems while providing practical applications for water resource management, environmental protection, and geological risk assessment.

Introduction

Underground rivers represent a unique and significant geological feature, particularly in regions such as Greece, where complex geological formations and hydrological conditions prevail. Their formation is attributed to processes of epigene speleogenesis. These processes occur when meteoric water infiltrates from the surface, utilizing its dissolving capacity derived from surface environmental conditions. Specifically, the water acquires its ability to dissolve carbonate rocks by absorbing carbon dioxide from the atmosphere, particularly within the soil. As the water percolates through limestone or other soluble lithologies, its flow transitions from diffuse pathways to more convergent routes, eventually emerging at discrete springs in adjacent valleys (Audra & Palmer, 2011).

These caves form under specific geological and environmental conditions, influenced by factors such as lithology, tectonics, the type of recharge and base-level changes. In most cases, the passages of epigene caves develop along discontinuities, such as bedding planes, fractures and faults (Gunn, 2004), forming cave patterns that include isolated passages or branchworks, with angular configurations (Audra & Palmer, 2011).

According to Ford (2007), as the frequency of permeable discontinuities increases significantly, resistance to water flow is drastically reduced. This allows water to follow the pathway closest to the water table, which is also the shortest route to spring. This process results in the formation of “ideal” water table caves. As the fluvial base level drops, new phreatic passages form at successively lower levels, while pauses in base-level lowering result in the creation of cave levels that correlate with river terraces (Audra & Palmer, 2011). Vadose shafts and canyons extend downward to the new water table, while older conduits become abandoned, often filled with sediments and intersected by newer passages. This dynamic process leads to the integration of multiple cave levels, preserving a record of successive stages of base-level lowering. A notable example is the Stefanina Cave in northern Greece, where tectonic discontinuities, including joints and bedding planes, have played a key role in guiding water flow and shaping the underground river’s morphology (Lazaridis et al., 2021). Additionally, scallops, small-scale dissolution features typically formed in shallow phreatic environments, found within the cave have enabled the estimation of past flow velocities and discharge rates.

The geotectonic setting of Greece consists of the Hellenides showing an arcuate orogenic belt, subdivided into two distinct tectonostratigraphic domains, the External and Internal Hellenides zones. The Internal Hellenides comprise Paleozoic basement overlain by Mesozoic carbonate platform sediments, obducted by Neo-Tethyan ophiolites during the Mid-Late Jurassic, exhibiting a multiphase tectonic history and significant metamorphism during the Alpine orogeny. During the Eocene-Oligocene, the Internal Hellenides overthrusted the External Hellenides which are primarily composed of Mesozoic and Cenozoic sediments from deep-sea and shallow-water environments, characterized by continuous sedimentation that took place during the Paleocene to Miocene period, forming a complex thrust and fold belt with no significant metamorphism (Kilias, 2024).

Methodological approach

This study employs a systematic approach that combines bibliographic review, data collection, processing and analysis. The methodology follows a structured framework that integrates both primary and secondary data sources, tools and comparative evaluations. The first step involved an extensive bibliographic review to gather relevant scientific information. Searching was conducted in databases such as Scopus, ScienceDirect, ResearchGate, Google Scholar, Academia and Theophrastos digital library of Aristotle University of Thessaloniki. Additional information was gathered from online resources, archives of speleological associations in Greece and the Bulletin of the Hellenic Speleological Society to address gaps in the existing literature. Each source was critically analyzed for quality and reliability and the literature was categorized based on themes and regions.

Next, the study proceeded with the collection and recording of data, which included both primary and secondary sources. Primary data were derived from spatial analyses, while secondary data were extracted from bibliographic sources and existing studies. Data were systematically stored and classified based on criteria such as geographical region, tectonostratigraphic unit and morphological characteristics of the underground rivers, forming the basis for a detailed catalog of Greece's underground rivers (Fellachidou, 2024 and references therein).

The data processing phase involved both statistical and spatial analyses. Quantitative data were analyzed using tools such as Excel, allowing for the identification of trends and patterns across variables. Spatial analysis was performed using the QGIS tool enabling detailed mapping of underground river distribution and their relationship with geological and tectonic features. Data visualization, including the creation of charts, graphs and maps, further supported the interpretation and presentation of results.

Results and discussion

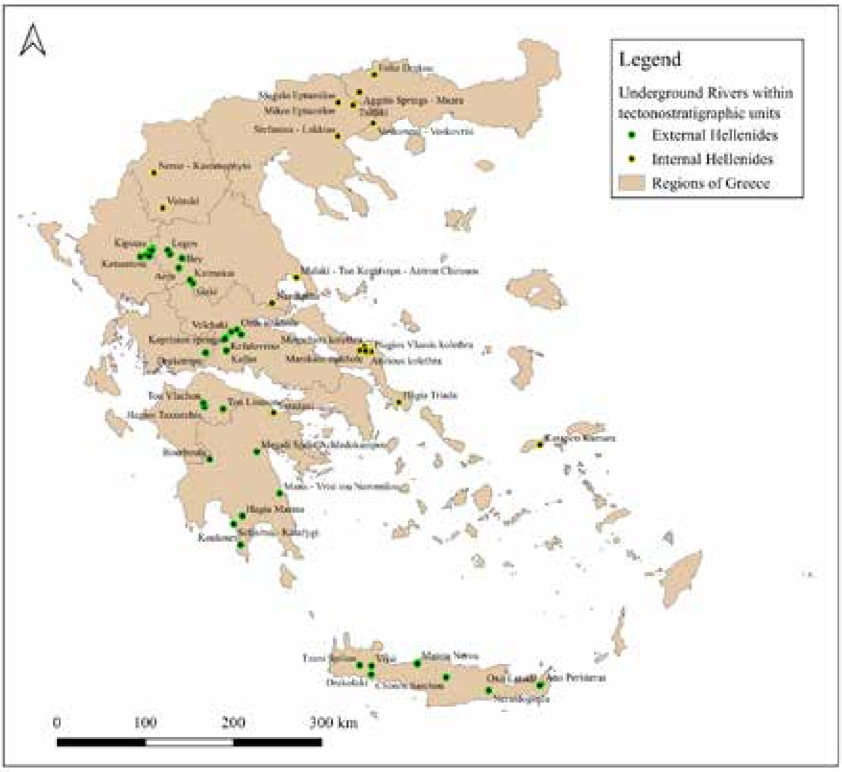

Figure 1. Geographical distribution of underground rivers across 13 Greece's regions, categorized by tectonostratigraphic units. Locations marked green represent underground rivers within the External Hellenides (40 in number), while those in yellow correspond to the Internal Hellenides (20 in number). (Regions of Greece retrieved from https://geodata.gov.gr/en/)

The analysis revealed significant insights into the distribution, geological characteristics and morphology of Greece's underground rivers. The compiled catalog of underground rivers served as the basis for constructing a map depicting their spatial distribution. The map (Fig. 1) presents a detailed spatial representation of underground river systems in Greece, categorized into two primary tectonostratigraphic units: the Internal Hellenides and External Hellenides. It reveals a total of 60 documented underground rivers, with 40 concentrated within the External Hellenides mainly along the Pindos mountain chain. Conversely, only 20 underground rivers are documented within the Internal Hellenides, where they are more sporadically distributed, with notable examples including Karapeti Kamara in the South Aegean and Neron-Kastanophyto in Western Macedonia. Furthermore, Aggitis River, the longest underground cave of Greece is also located in the Internal Hellenides.

Notable clusters are observed in Epirus region (e.g., Anemotripa, Klifkis, Kipon, Katsantoni, Kipinas, Stafyla, Gouva Mare, Galazio Nero), in Sterea Ellada region (e.g., Koprision springs, Kefalovriso, Velchaki, Oitis sinkhole, Sklithraki) and the Euboea Island (e.g., Metochiou kolethra, Genitsari, Manikion sinkhole, Atsitous kolethra, Hagios Vlassis kolethra). Crete Island also emerges as a significant region, hosting nine underground rivers such as Tzani Spilios, Drakolaki and Chonos Sarochou, Manna Nerou, Ano Peristeras etc.) reflecting its dynamic karstic systems. The geographical distribution highlights regional variability, with certain areas, such as the South Aegean, Ionian Islands and Attica, lacking any recorded underground rivers.

Overall, the External Hellenides account for 67% of the recorded underground rivers in Greece (Fig. 2A), emphasizing their dominant role in karst system development. In contrast, the Internal Hellenides, shaped by a complex geological history involving metamorphic processes, host fewer and more isolated underground rivers.

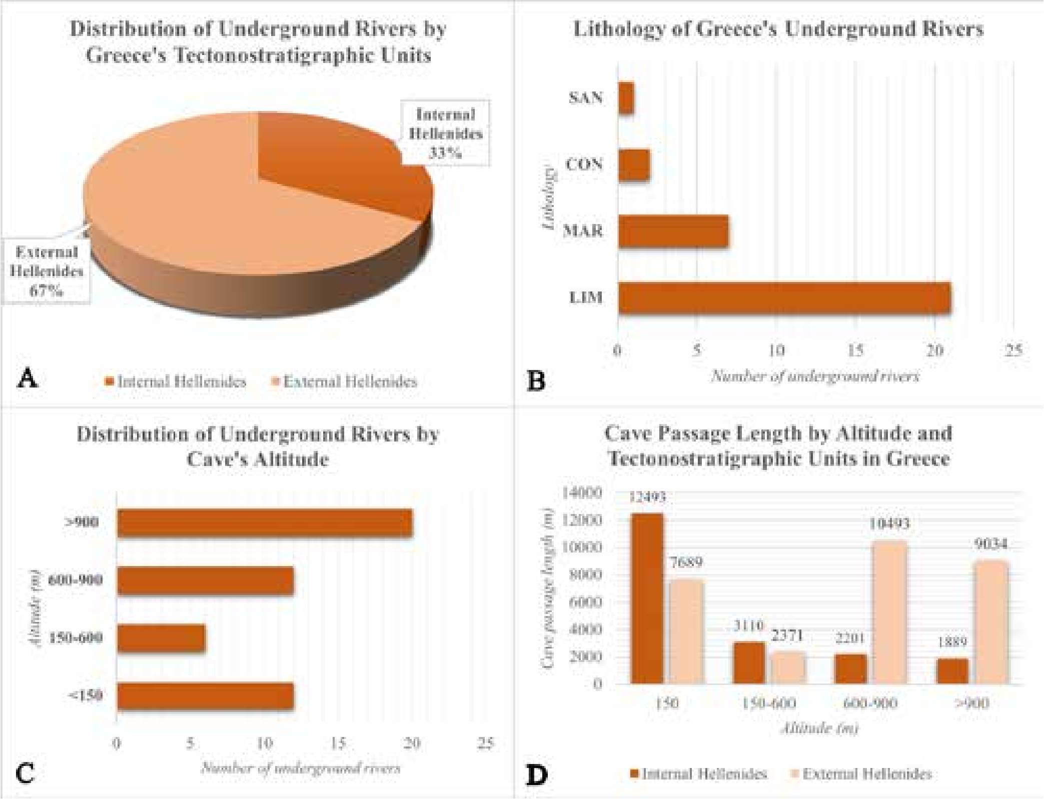

Figure 2. A: Proportion of underground rivers distributed between the two tectonostratigraphic units in Greece, the Internal Hellenides and the External Hellenides. B: Number of underground rivers associated with different lithologies in Greece. SAN: Sandstones, CON: Conglomerates, MAR: Marbles, LIM: Limestones. C: Number of underground rivers found at different elevation ranges in Greece according to Dikau (1989) classification system (>900: mountainous areas, 600-900: semi-mountainous areas, 150-600: hilly areas, <150: lowland areas). D: Total length of underground river cave passages (speleogenesis in meters) within the Internal and External Hellenides across different altitude ranges in Greece.

Figure 2B delves into the influence of lithology on speleogenesis, highlighting the critical role of carbonate rocks. Limestone, due to its high solubility, hosts the majority of underground rivers (21), underscoring its dominance in karst development. Marble, while also capable of supporting karst systems, accommodates fewer rivers (7). Conglomerates and sandstones, which account for just 2 and 1 rivers respectively, further emphasize that lithology is a key determinant in the formation and distribution of underground river systems.

Elevation plays a critical role in the distribution of underground rivers (Fig. 2C). Mountainous areas (>900m) host the highest number of underground rivers (20), followed by semi-mountainous (600-900m) and lowland areas (<150m), each with 12 rivers, while hilly areas (150-600m) contain only 6. This high concentration of underground rivers in high-relief regions can be attributed to the unique climatic and hydrological conditions of these areas. In mountainous regions, colder infiltrating water retains higher levels of carbon dioxide, enhancing its aggressivity and promoting extended speleogenetic processes. Additionally, seasonal climatic variations, including snow accumulation in winter, rapid snowmelt in spring and intense summer thunderstorms, lead to periods of extreme discharge and flooding, which significantly influence cave development and morphology through the interplay of climatic factors and speleogenesis (White & Culver, 2012).

Finally, the relationship between altitude and tectonostratigraphic units is further elaborated (Fig. 2D). At lower altitudes (<150m), the Internal Hellenides exhibit longer cave passages, reflecting prolonged water flow and underground karst development. In contrast, at higher altitudes (600-900m and >900m), the External Hellenides dominate in terms of cave passage length, highlighting their structural and geological suitability for high-altitude underground river development. These observations reinforce the role of both altitude and tectonostratigraphic context in shaping speleogenetic processes.

Concluding Remarks

In summary, the distribution, lithological dependence, geomorphological and tectonostratigraphic influences collectively reveal the complexity of underground river formation in Greece. Detailed examination of the general geographical distribution to specific geological factors, provides a clear narrative of how various processes interact to shape these unique systems. This multi-layered analysis highlights the intricate interplay between geology, hydrogeology, tectonics and topography in determining the characteristics of underground rivers in Greece.

- This study provides a comprehensive insight into the underground rivers of Greece, representing the first national-scale mapping effort.
- The distribution, lithological dependence, geomorphological and tectonostratigraphic influences collectively reveal the complexity of underground river formation in Greece.
- Significant insights are provided into the spatial and geological dynamics that shape these systems, demonstrating the dominant role of the External Hellenides and carbonate lithologies in underground karst system development.
- Areas within the Internal Hellenides, where geological complexity and mixed lithologies prevail, display fewer and more sporadically distributed underground rivers.
- Low altitude concentration of underground rivers occurs in Internal Hellenides, in contrast to the External Hellenides, where these caves are developed mainly in higher altitudes.
- The results contribute to theoretical knowledge and may have practical implications for water resource management, environmental protection and geological risk assessment.
- Future studies can build upon this foundation to explore more localized patterns and predict potential changes in underground hydrological systems.

References

Audra, P., & Palmer, A.N., 2011. The pattern of caves: controls of epigenic speleogenesis. Structure des réseaux karstiques : Les contrôles de la spéléogenèse épigène. Geomorphologie: Relief, Processus, Environnement, 4, 359–378.

Fellachidou, K.K., 2024. Underground rivers in Greece: Documentation, geology, speleogenesis. Undergraduate Thesis, Department of Geology, Aristotle University of Thessaloniki.

Ford, D., & Williams, P., 2007. Karst Hydrogeology and Geomorphology. John Wiley & Sons.

Gunn, J., 2004. Encyclopedia of caves and karst science. Fitzroy Dearborn, Taylor & Francis Group.

Kilias, A., 2023. The Alpine Geological History of the Hellenides from the Triassic to the Present—Compression vs. Extension, a Dynamic Pair for Orogen Structural Configuration: A Synthesis. Geosciences, 14(1), 10.

Lazaridis, G.T., Fellachidou, K.K., & Georgaki, M.N., 2021. Paleohydrology of the Stefanina Cave (Greece). Bulletin of the Geological Society of Greece, 57(1), p. 52-67.

Dikau, R., 1989. The application of digital relief model to landform analysis in geomorphology. Three Dimensional Application in Geographic Information Systems, 51–77.

White, W.B., & Culver, D.C., 2012. Encyclopedia of caves, 2nd ed. Academic Press.

BULLETIN OF THE GEOLOGICAL
SOCIETY OF GREECE, SP. PUBL.

EXTENDED ABSTRACT 076

Preliminary estimation of the recession coefficient of the "Kefalari Agios Ioannis" spring, Dimitsana, Peloponnesus, Greece

Filis, C.[1], Skourtsos, E.[1], Korovesai, A.[1], Andreadakis, E.[1], Kapourani, E.[1], Karalemas, N.[1], Alexopoulos, A.[1]

(1) National and Kapodistrian University of Athens, Department of Geology and Geoenvironment, Athens, Greece
chfilis@geol.uoa.gr

Introduction

A hydrograph is the discharge (Q) diagram of a spring or a watercourse as a function of time (t). From the study of hydrographs of karst spring areas, it is possible to (Lundberg & Worsfold, 1993; Ford & Williams, 2007; Zhou & Li, 2010; Ma & Zhang, 2016):

- Find a "transformation coefficient", that is, a relationship that connects the input of the karst system to the output, i.e., the spring.
- Make predictions of the spring discharge and calculate the reserves.
- Provide information about the organization and operation of the karst system.
- Characterize the hydrogeological system that feeds a spring based on the slope of the depletion line between two given discharges (Q_1) and (Q_2). The change in slope from one year to the next indicates either water withdrawals from the aquifer (increase in slope), or recharge of the aquifer during the dry period from irrigation returns (decrease in slope), or changes in the structure of the aquifer, such as due to seismic activity.
- Calculate the water reserves in the system, which are located higher than the outflow point (discharge point) and equal to ($Q_t t_d$) at any given time.

Large values of the depletion coefficient (a) (in the range of 10^{-1} to 10^{-2}) mean that the karst system has conduits and generally large diameter voids with adequate continuity. In contrast, small values of (a) (in the range of 10^{-3}) mean that the water flows through fractures and intra-stratigraphic voids. In the first case, we typically have massive limestones, while in the second case, stratified ones (Soulios, 1985).

The spring "Kefalari Agios Ioannis" is located at an elevation of approximately 871 m, about 1,650 m south-southeast of the picturesque village of Dimitsana (Peloponnesus, Greece) discharging a karst aquifer. Its water is used for drinking water supply and irrigation. The clarification of the hydraulic characteristics of the karst aquifer, through the "Kefalari Agios Ioannis" spring, is of immense importance for the sustainable management of water resources in the broader area of Dimitsana, which is continuously developing in terms of tourism.

Geological Setting

The area of Dimitsana is composed of geological formations belonging to the lower Tripolitza Unit (Blumenthal, 1933; Dercourt, 1964; Lekkas, 1978; Tsaila – Monopolis, 1977; Fleury, 1980; Thiebault, 1982) and the higher Pindos Unit (Aubouin, 1959; Dercourt, 1964; De Wever, 1975; Fleury, 1980). Post-alpine sediments have locally unconformably covered the alpine formations.

The post-alpine formations comprise the following (Exindavelonis, 1988):

- Alluvial deposits (H.al) consisting of pebbles, gravels and clayey-sandy materials.
- Scree and talus cones (H.sc,cs) mainly consisting of carbonate fragments of local origin.

The Pindos Unit includes the following formations (Exindavelonis, 1988):

- Platy limestones (Ks-Pc.k) dated Upper Cretaceous to Paleocene of green-gray and locally reddish colour with nodules and thin chert intercalations. The upper parts of the formation correspond to the transitional beds towards the flysch and comprise alternations of thin-platy limestones, sandstones and breccia limestones.
- Red cherts, siltstones and "First Flysch" (Js-Ki.fl) dated Upper Jurassic to Lower Cretaceous consisting of alternations of cherts, siltstones, shales, sandstones and clastic limestones often containing chert angular pebbles.

The Tripolitza Unit comprises the following formations (Exindavelonis, 1988):

- Flysch (Ft) consisting of alternations of grey marls, sandstones with intercalations or lenses of breccia limestones and conglomerates.
- Limestones, dolomites and dolomitic limestones (Ks-Es.k,d) dated Upper Cretaceous to Upper Eocene consisting of grey to black, thick-bedded limestones and dolomitic limestones.

The formations of both the Pindos and Tripolitza Units are juxtaposed through thrust faults and high-angle normal faults. This deformation can be ascribed to a compressional tectonic episode that transpired during the Middle Eocene to the Lower Miocene followed by an extensional one since Middle Miocene.

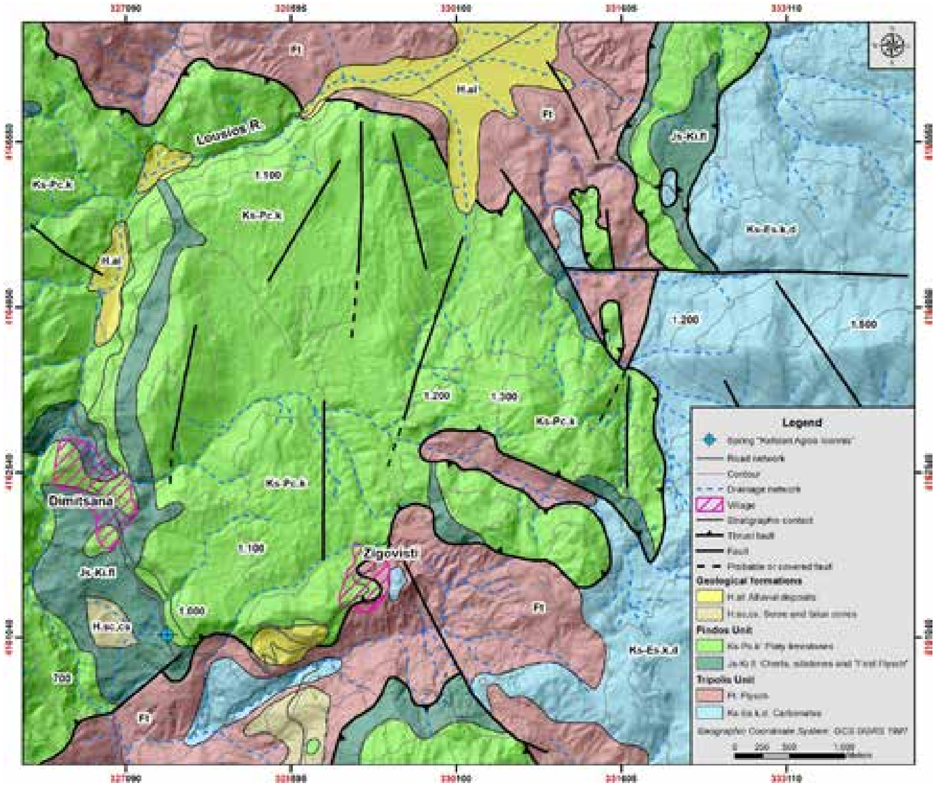

Figure 1. Geological map of the study area (modified from Exindavelonis, 1988).

Hydrogeological Conditions

The geological formations of the study area fall into the following categories, according to the standards of the International Association of Hydrogeologists (Struckmeier & Margat, 1995; Nikas et al., 2010):

- Alluvial deposits (H.al): They develop local and thin aquifers with high yield or extensive aquifers with moderate yield (Subclass 1b).
- Scree and talus cones (H.sc,cs): They develop local and thin aquifers with high yield or extensive aquifers with moderate yield (Subclass 1b).
- Platy limestones (Ks-Pc.k): This formation generates local and thin aquifers with high yield or extensive aquifers with moderate yield (Subclass 2b).
- Red cherts, siltstones and "First Flysch" (Js-Ki.fl): They develop aquifers of minor practical significance or non-aquifer formations (Subclass 3b).
- Flysch (Ft): This formation develops aquifers of minor practical significance or non-aquifer formations (Subclass 3b).
- Carbonates (Ks-Es.k,d): This formation generates extensive aquifers with high yield (Subclass 2a).

The carbonate formations of the Pindos Unit (Ks-Pc.k), characterized by their multifold and fractured structure, give rise to a karst aquifer of moderate capacity situated to the east of Dimitsana. The underlying impermeable substratum is comprised primarily of the flysch (Ft) of the Tripolitza Unit, predominantly located to the north, east, and south, as well as the red cherts and siltstones and "First Flysch" (Js-Ki.fl) of the Pindos Unit, mainly to the west.

Conversely, the carbonate formations of the Tripolitza Unit (Ks-Es.k,d) exhibit considerable fragmentation and fissuring, revealing two or more primary joint systems, accompanied by additional secondary systems that display distinctive karstification. These formations give rise to a deep karst aquifer of substantial capacity.

It is noteworthy that in certain regions, the carbonate formations of the Pindos Unit directly overly those of the Tripolitza Unit, facilitating the transfer of groundwater to greater depths through lateral hydraulic connectivity.

Recession coefficient of the "Kefalari Agios Ioannis" spring

The contact spring "Kefalari Agios Ioannis" (Figure 2) discharges the karst aquifer that develops in the platy limestones (Ks-Pc.k) of the Pindos Unit at their contact with the underlying and impermeable red cherts, siltstones and "First Flysch" (Js-Ki.fl) of the Pindos Unit, as shown in Figure 1.

Figure 2. View of the “Kefalari Agios Ioannis” spring on 26-11-2023. The turbidity of the water is due to the heavy rainfall of the previous days.

For the evaluation of the quantitative status of the “Kefalari Agios Ioannis” spring, flow measurements were conducted using an appropriate flow gauge within the rectangular cross-section of the concrete channel to which the water flows, leading to the Open-Air Water Power Museum of the Piraeus Cultural Foundation (Table 1, Figure 3 & Figure 4).

Table 1. The dates of the flow measurements, along with the quantitative data (discharge) and qualitative data (water temperature, pH, and electrical conductivity) of the “Kefalari Agios Ioannis” spring.

Seq. No.	Date	Discharge (m^3/h)	T °C Water	pH	Electric Conductivity (μS/cm)
1.	18-04-2024	711.1	12.9	7.7	320.0
2.	04-05-2024	468.9	12.7	7.6	320.0
3.	16-05-2024	312.3	12.6	7.7	300.0
4.	30-05-2024	245.2	12.9	7.6	300.0
5.	14-07-2024	101.7	14.4	7.4	310.0
6.	07-08-2024	98.2	13.5	7.4	280.0
7.	07-09-2024	84.7	13.7	7.6	290.0
8.	29-09-2024	70.3	13.7	7.6	260.0
9.	27-10-2024	69.4	13.8	7.6	270.0

Figure 3. Flow measurements taken with an appropriate flow gauge at the “Kefalari Agios Ioannis” spring on 04-05-2024.

Figure 4. Flow measurements taken with an appropriate flow gauge at the “Kefalari Agios Ioannis” spring on 30-05-2024 (up) and on 14-07-2024 (down).

Quantitative analysis of the “Kefalari Agios Ioannis” spring hydrograph is based on the equation proposed by Maillet (1905), who suggested that the discharge of a spring is a function of the volume of water held in storage and is described by an exponential equation.

The “Kefalari Agios Ioannis” spring hydrograph based on the flow measurements, which were conducted from 18-04-2024 to 27-10-2024 (Table 1) is presented in Figure 5. For the calculation of the recession coefficient of the “Kefalari Agios Ioannis” spring, flow measurements which were conducted from 14-07-2024 to 27-10-2024 were used (Table 1 & Figure 5) and if they get plotted to semi-logarithmic graph paper, the curve of Figure 5 is represented as a straight line (Figure 6).

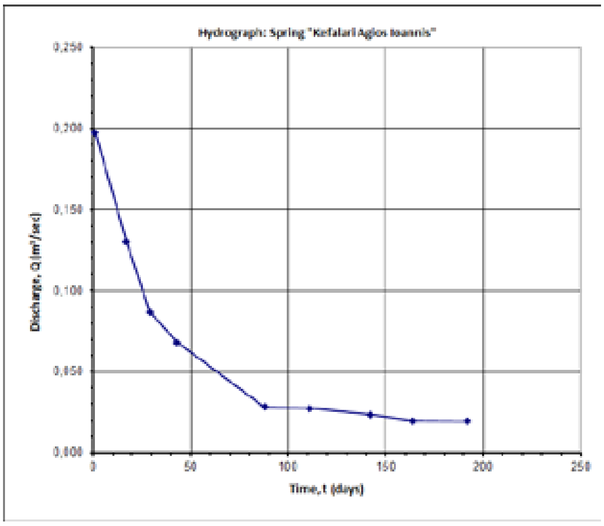

Figure 5. Hydrograph of the “Kefalari Agios Ioannis” spring based on the flow measurements, which were conducted from 18-04-2024 to 27-10-2024.

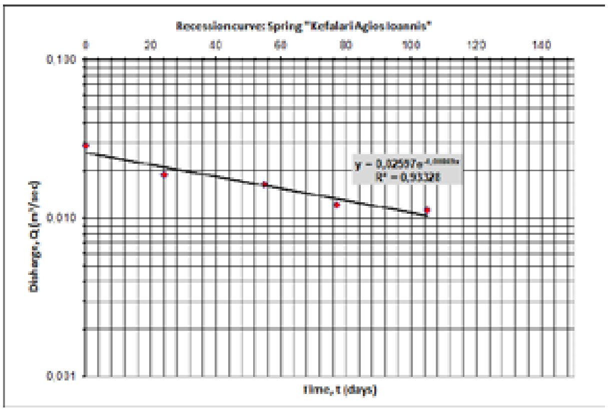

Figure 6. Semi-logarithmic graph paper of the “Kefalari Agios Ioannis” spring flow measurements, which were conducted from 14-07-2024 to 27-10-2024, used for the calculation of its recession coefficient.

The value of the recession coefficient derives from the hydrogeological characteristics of the aquifer, especially effective porosity and transmissivity (T). The recession coefficient of the “Kefalari Agios Ioannis” spring calculated from the flow measurements, which were conducted from 14-07-2024 to 27-10-2024 is 8.69×10^{-3} days^{-1} (Figure 6), which means that the water flows through the fractures and the intra-stratigraphic voids of the platy limestones (Ks-Pc.k) of the Pindos Unit (Soulios, 1985).

Discussion - Conclusions

The contact spring “Kefalari Agios Ioannis” discharges the karst aquifer that develops in the platy limestones (Ks-Pc.k) of the Pindos Unit at their contact with the underlying and impermeable red cherts, siltstones and “First Flysch” (Js-Ki.

fl) of the Pindos Unit.

The clarification of the hydraulic characteristics of the karst aquifer, through the “Kefalari Agios Ioannis” spring, is of immense importance for the sustainable management of water resources in the broader area of Dimitsana, which is continuously developing in terms of tourism. Additionally, the operation of the Open-Air Water Power Museum of the Piraeus Cultural Foundation, which is located immediately downstream of the spring, is inextricably linked to the functioning of the “Kefalari Agios Ioannis” spring.

The recession coefficient of the “Kefalari Agios Ioannis” spring calculated from the flow measurements which were conducted from 14-07-2024 to 27-10-2024 is 8.69×10^{-3} days^{-1}, which means that the water flows through the fractures and the intra-stratigraphic voids of the platy limestones (Ks-Pc.k) of the Pindos Unit. The aforementioned calculated value is consistent with the literature data for the recession coefficient of karst aquifers developed in the Pindos Unit and in equivalent units, which is on the order of 10^{-3} days^{-1} (Soulios, 1985; Giannatos, 1999; Karalemas, 2010).

It is noted that the hydrological year 2023-2024 was particularly dry, and the calculation of the «Kefalari Agios Ioannis” spring’s recession coefficient should be considered with special caution, as it has been derived from flow measurements, which are the result of prolonged drought and water scarcity. This might has caused different conditions of groundwater circulation, which are not uniform across the entire hydrogeological basin and becomes apparent under extreme hydrological conditions, either surplus (wet hydrological years) or deficiency (dry hydrological years), during which different sections and levels of the recharge area are activated or operate differently. It is noteworthy that the recession period lasted at least 105 days, from 14-07-2024 to 27-10-2024.

Therefore, the recalculation of the spring’s recession coefficient is considered necessary for the hydrological year 2024-2025 as well, which so far appears to be more representative compared to the previous one.

Acknowledgements

The research team extends its most heartfelt gratitude to the director and the staff of the Open-Air Water Power Museum of the Piraeus Cultural Foundation, for the time they dedicated and their invaluable assistance during the fieldwork. Additionally, we express our appreciation to Mayor of Gortynia Mr. Efstathios Koulis for his collaboration.

References

Aubouin, J., 1959. Contribution a l’ etude geologique de la Grece septentionale, les confins de l’ Epire et de la Thessalie. Ann. Geol. Pays Hell. 10, 526.

Blumenthal, M., 1933. Zur Kennthnis des Querprofils des zentralen und nordlichen Peloponnes. N. Jb. f. Miner. 70, 449-514.

De WeveR, P., 1975. Etude geologique de series apparaisant en fenetre sous l’allocthone pindique (serie de Tripolitza, serie epimetamorphique de Zarouchla), Peloponnese septentrional, Grece. These 3eme cycle.

Dercourt, J., 1964. Contribution a l’etude geologique d’un secteur du Peloponnese septentrional. Ann. Geol. Pays Hell. 15, 418.

Exindavelonis, P., 1988. Geological Map of Greece in scale 1:50,000, sheet “DIMITSANA” published by IGME, Athens.

Fleury, J., 1980. Les zones de Gavrovo-Tripolitza et du Pinde-Olonos (Grece continentale et Peloponnese du Nord). Evolution d’une plateforme et d’un bassin dans leur cadre alpin. In: Memoire de la Soc. Geol. Nord, 651.

Ford, D., Williams, P., 2007. Karst Hydrogeology and Geomorphology. Wiley-Blackwell.

Giannatos, G., 1999. Spring’s hydrodynamic analysis from rocks in which the fissure type permeability prevails. The wider area of the Ano Bouraikos catchment in the Pindos geotectonic rock unit. PhD, National and Kapodistrian University.

Karalemas, N., 2010. Qualitative and quantitative status of the water bodies of eastern Taygetos and of Mani and prospects for sustainable development. PhD, National and Kapodistrian University.

Lekkas, S., 1978. Contribution to the geological structure of the area southeast of Tripoli (Central Peloponnese). PhD, National and Kapodistrian University.

Lundberg, L., Worsfold, P., 1993. Hydrological characteristics of karst aquifers. Geological Society of America.

Ma, Y., Zhang, L., 2016. Hydrograph Recession Analysis of Karst Springs. Journal of Hydrology, 543, 107-115.

Maillet, E. 1905. Essais d’ hydraulique souterraine et. fluviale. Herman, 218, Paris.

Nikas, K, Antonakos, A, Kallergis, G, Kounis, G., 2010. International Hydrogeological Map of Europe: Sheet D6 “Athina”. Proceedings of the 12th International Congress, Patras, 2010 Bulletin of the Geological Society of Greece, Volume XLIII No 4, pages 1821-1830.

Soulios, G., 1985. Contribution to the hydrogeological study of karst aquifer systems in Greece. Aristotle University of Thessaloniki.

Struckmeier, W.F., Margat, J., 1995. Hydrogeological maps: a guide and a standard legend (Vol. 17). Hannover: Heise.

Thiebault, F., 1982. Evolution geodynamique des Hellenides externes en Peloponnese meridional (Grece) 6. Societe Geologique du Nord, 393.

Tsaila-Monopolis, S., 1977. Micropaleontological study and stratigraphic structure of the formations of the geotectonic Tripolis (Gavrovo) zone in the Peloponnese. Geological and Geophysical Studies 20(1), 1-136.

Zhou, Y., Li, W., 2010. Study on hydrograph recession of karst springs using the baseflow separation method. Hydrological Processes, 24(12), 1642-1651.

BULLETIN OF THE GEOLOGICAL SOCIETY OF GREECE, SP. PUBL.

EXTENDED ABSTRACT 077

Role of Earth Observation in Monitoring Santorini–Anydros Volcano-Tectonic Crisis

Foumelis M.[1], Papageorgiou E.[1], Trasatti E.[2], Tapete D.[3], Bitharis S.[1], Pikridas C.[1], Papazachos C.[1]
(1) Aristotle University of Thessaloniki (AUTh), Thessaloniki, Greece, mfoumelis@geo.auth.gr (2) Istituto Nazionale di Geofisica e Vulcanologia (INGV), Rome, Italy (3) Agenzia Spaziale Italiana (ASI), Rome, Italy

Background

The Santorini volcano is associated with one of the most destructive volcanic eruptions in human history, yet it remains insufficiently monitored. This is partly due to its behavioral pattern, characterized by long periods of rest interrupted by short and rapid episodes of unrest (Hooper, 2012). Indeed, the last well-documented unrest episode in 2011–2012 (Newman *et al.*, 2012; Parks *et al.*, 2012; Papageorgiou *et al.*, 2012), characterized by comprehensive instrumentation and quantitative measurements, occurred after approximately 60 years of quiescence since the 1950 volcano activity.

Despite the significance of the 2011–2012 unrest, post-crisis monitoring efforts were limited, sustained mainly by the Institute for the Study and Monitoring of Santorini Volcano (ISMOSAV; www.ismosav.gr), and without any coordinated activity at a national level. ISMOSAV is a non-profit organization established in the summer of 1995, with the primary objective of operating volcano monitoring networks and providing informed assessments regarding the state of the volcano. The monitoring efforts over the past 12 years were substantial enough to enable early detection and timely notification to relevant authorities, contributing to the governmental response when a new unrest phase began in mid-summer 2024.

The role of Earth Observation (EO) and geodetic imaging, specifically Interferometric Synthetic Aperture Radar (InSAR), is crucial for the systematic long-term monitoring of Santorini. Several studies utilized archive SAR missions from the European Space Agency (ESA), namely ERS and ENVISAT satellites, to characterize displacement fields from 1992 to 2010 (Papageorgiou *et al.*, 2012; Parks *et al.*, 2015), as well as during the 2011–2012 unrest phase (Foumelis *et al.*, 2013). Since October 2014, Copernicus Sentinel-1 mission has enabled actual continuous monitoring. While the ERS and ENVISAT era allowed accurate annual displacement measurements, the limited temporal sampling (i.e., long satellite repeat-cycles) prevented the detection of short-term behavioral changes of the volcano. On the contrary, systematic acquisitions from Sentinel-1 have proven adequate for capturing early indicators of deviations from background behavior.

EO-based Monitoring

This EO-based monitoring capability was made possible through the deployment of an operational solution using the SNAPPING service of the Geohazards Exploitation Platform (GEP) (Foumelis *et al.*, 2022). SNAPPING is a Persistent Scatterer Interferometry (PSI) chain integrated by AUTh on the GEP platform, facilitating access to Sentinel-1 surface motion measurements for users and EO practitioners. The SNAPPING service generates average Line-of-Sight (LoS) motion rate maps and displacement time series at both reduced spatial (at approx. 100 m) and full sensor resolutions (SNAPPING, 2022). A well-defined set of processing parameters optimized to the specific environment are defined and a dedicated application on GEP is designed to execute SNAPPING in a monitoring framework based on user defined temporal step.

During unrest events, near-real time PSI solutions were generated whenever a new Sentinel-1 acquisition was available, based on both online hosted SNAPPING service, as well as in-house GAMMA Multi-Temporal InSAR (MT-InSAR) processing. This dual-processing methodology serves as a verification mechanism for the detected displacement signals.

Surface Motion Measurements

In the period following the 2011–2012 unrest, the Santorini volcano experienced deflation centered on Nea

Kameni (Figure 1), extending as far as Thera Island, including Cape Skaros and the northern caldera walls. The observed motion rates of approximately -7.8 mm/yr remained elevated compared to pre-unrest levels of around -5 mm/yr, though slightly lower than the -9 mm/yr reported seven years after the 2011 event (Papageorgiou *et al.*, 2019). These observations suggest that the volcano was undergoing a prolonged deflation phase, gradually returning to its pre-unrest state before the onset of a new unrest in July 2024. Although the initial 2024 inflation signals were detected by InSAR and the local GNSS network of ISMOSAV, the confirmation of a new unrest phase was underlined by the onset of seismicity a few months later (AUTh Seismological Station, 2024). Since summer 2024, inflation of Santorini, the second episode of significant magnitude within the last 15 years, has continued through the end of the year. This local inflation was consistent in both displacement pattern and magma source location with the 2011–2012 unrest. However, it was also soon superimposed by a more significant event that occurred in the early part of February 2025 and originated from the broader Kolumbo–Anydros area. The Anydros event was shorter in duration but associated with deformation nearly two orders of magnitude greater than the prior Santorini caldera inflation. While the inner caldera magma source was deforming the volcanic complex at a rate of 10–12 cm per year over a six-month period, the Kolumbo–Anydros activity exhibited meter-level displacement rates within just two weeks, highlighting their distinct dynamics and potential implications. These differences are further reflected in the number and magnitude of the accompanying seismic events.

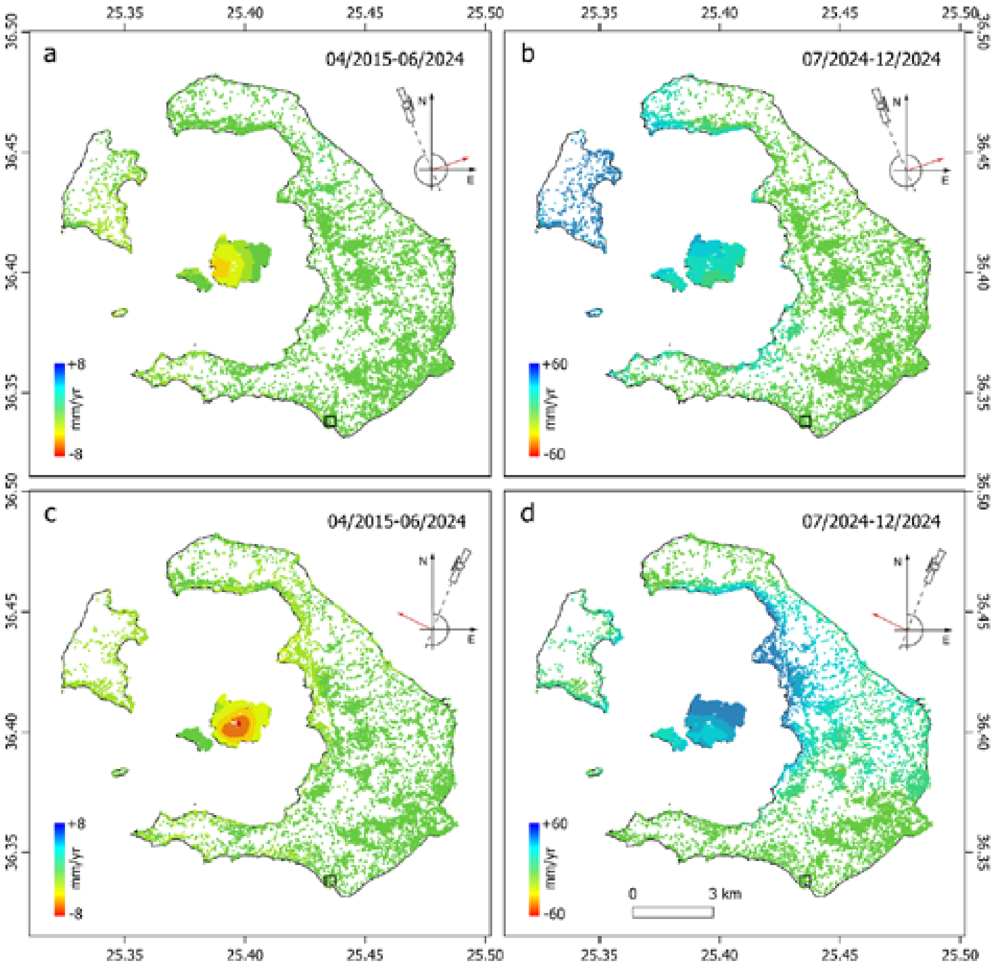

Figure 1. Sentinel-1 MT-InSAR LoS motion rates prior (a,c) and during (b,d) the 2024 unrest for the ascending 029 (a,b) and descending 109 (c,d) satellite tracks. Local reference point for InSAR processing is located in the southern part of the island (black square).

Discussion and Conclusions

The Earth Observation and Geospatial Applications Laboratory (EO.Lab) of AUTh has systematically monitored Santorini through InSAR, as part of the operational framework of ISMOSAV, using automatic solutions such as GEP SNAPPING, internal processing chains based on Copernicus SAR data, and collaborations with space agencies for complementary SAR monitoring. In this work, we present the evolution of surface displacements as measured by satellite InSAR techniques for the broader Santorini–Anydros region. We discuss the role of geodetic imaging techniques in volcano monitoring, their advantages, and complementarities with other geodetic and in-situ networks and finally, we emphasize the need to establish a local volcano observatory, involving scientists across multiple domains, integrating diverse techniques and equipment for real-time monitoring of this volcanic region and its surrounding areas.

Acknowledgements

The authors would like to thank the GEP platform providers for allocating resources to support the execution of services related to the monitoring of the Santorini volcano.

References

AUTh Seismological Station, 2024. Permanent Regional Seismological Network operated by the Aristotle University of Thessaloniki. Available online: http://geophysics.geo.auth.gr/ss/station_index_en.html.

Foumelis, M.; Trasatti, E.; Papageorgiou, E.; Stramondo, S.; Parcharidis, I., 2013. Monitoring Santorini volcano (Greece) breathing from space. Geophys. J. Int., 193, 161–170.

Foumelis, M.; J.M. Delgado Blasco, J.M.;F. Brito, F.; F. Pacini, F.; E. Papageorgiou, E.; P. Pishehvar, P., &and P. Bally, P., 2022. SNAPPING Services on the Geohazards Exploitation Platform for Copernicus Sentinel-1 Surface Motion Mapping, Remote Sensing, 14(23), 6075, https://doi.org/10.3390/rs14236075.

Hooper, A., 2012. A volcano's sharp intake of breath. Nat. Geosci., 5, 686–687.

Newman, A.V., Stiros, S., Feng, L., Psimoulis, P., Moschas, F., Saltogianni, V., Jiang, Y., Papazachos, C., Panagiotopoulos, D., Karagianni, E., & Vamvakaris, D., 2012. Recent geodetic unrest at Santorini Caldera, Greece. Geophys. Res. Lett., 39, L06309.

Papageorgiou, E.; Foumelis, M.; Parcharidis, I., 2012. Long- and Short-Term Deformation Monitoring of Santorini Volcano: Unrest Evidence by DInSAR Analysis. IEEE JSTARS, 5, 1531–1537.

Papageorgiou, E.; Foumelis, M.; Trasatti, E.; Ventura, G.; Raucoules, D.; Mouratidis, A., 2019. Multi-Sensor SAR Geodetic Imaging and Modelling of Santorini Volcano Post-Unrest Response. Remote Sens., 11, 259, https://doi.org/10.3390/rs11030259.

Parks, M., Biggs, J., England, P. et al., 2012. Evolution of Santorini Volcano dominated by episodic and rapid fluxes of melt from depth. Nature Geosci 5, 749–754, https://doi.org/10.1038/ngeo1562.

Parks, M.M., et al., 2015. From quiescence to unrest: 20 years of satellite geodetic measurements at Santorini volcano, Greece, J. Geophys. Res. Solid Earth, 120(2), 1309–1328, doi:10.1002/2014JB011540.

Surface motioN mAPPING (SNAPPING) Service on Geohazards Exploitation Platform. 2022. GEP SNAPPING Tutorial. Available online: https://docs.terradue.com/geohazards-tep/tutorials/Snapping.html.

17th INTERNATIONAL CONGRESS of the Geological Society of Greece

BULLETIN OF THE GEOLOGICAL SOCIETY OF GREECE, SP. PUBL.

EXTENDED ABSTRACT 078

Seismotectonic Features of the 2023 Strong Earthquake Sequence in Southeast Türkiye.

K.E. Fragkouli[1,2], G. Drakatos[2], S. Pavlides[3], S. Sboras[2].
(1) University of the Aegean, Mytilene, Greece, keafrag@gmail.com
(2) Geodynamics Institute, National Observatory of Athens, Athens, Greece
(3) Aristotle University of Thessaloniki, Thessaloniki, Greece.

Introduction / Background

Türkiye is one of the most seismically active countries in the world, and the East Anatolian fault is one of the largest and most active faults in the Eastern Mediterranean, as proven by the recent, destruvtive earthquake sequence in 2023. On February 6th, 2023, three earthquakes with magnitudes Mw > 6.5 struck within 11 hours, followed by another earthquake of Mw > 6 two weeks later. The aftermath of these events were thousands of casualties and an unprecedented infrastructure damage in Türkiye and Syria. Landslide phenomena and widespread liquefactions were a direct consequence of the earthquakes, further worsening the already immense destruction (Chadha, 2023). This study aims to better understand the sequence's behavior through an analysis of Coulomb static stress changes. More specifically, the four strongest earthquakes in the February 2023 sequence were attributed to four respective faults which have been modelled in order to be imported to the Coulomb 3.3 software (Toda et al., 2011). The Coulomb 3.3 software calculates the loading or unloading of stress on the modelled faults and in the surrounding area.

The Coulomb Failure Criterion determines the critical value of maximum shear stress without specifying the point where a rupture starts or how it will evolve. It is expressed by the relation $\Delta\sigma f = \Delta\tau_s + \mu' \Delta\sigma_n$, where $\Delta\sigma f$ is the difference in Coulomb stress failure. When $\Delta\sigma f > 0$, there is stress loading in the surrounding area, suggesting a higher likelihood of fault reactivation (triggering effect). On the contrary, when $\Delta\sigma f < 0$, there is stress release and a reactivation is potentially delayed. The fault or faults that are being triggered are referred to as source-faults, while the fault that receives the transferred stresses is referred as the receiver-fault. The stress change is strongly dependent by the receiver fault's geometric and kinematic attributes (Harris, 1998; Steacy et al., 2005; Toda et al., 2011).

Seismotectonics in East Türkiye

In East Türkiye the major tectonic structures are Caucasus Fault Zone which is a right-lateral strike-slip faults in the NW, Dead Sea Fault Zone (DSFZ) which is a 1000 km zone of left-lateral horizontal slip, Cyprus Arc which is a convergence boundary of the African and Anatolian plates, causing high seismicity begins from Cyprus to the Kahramanmaraş Triple Point, East of Karlıova Triple Junction where there is a compressional tectonic area of N-S and strike-slip faults (right-lateral & left-lateral) and the interconnected strike-slip zones of North Anatolian Fault Zone (NAFZ right-lateral) & East Anatolian Fault Zone (EAFZ left-lateral) (Taymaz et al., 2021; KOKUM & OZCELIK, 2020).

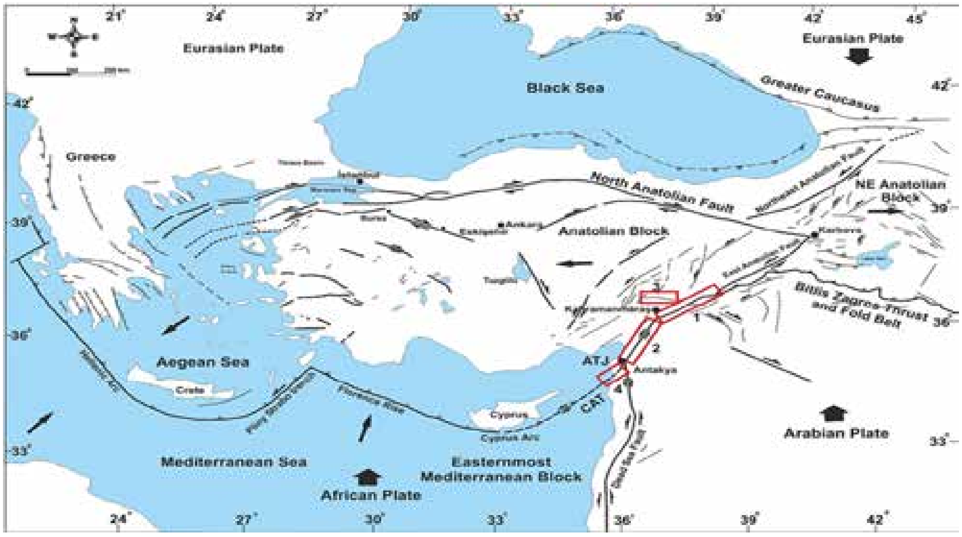

Figure 1: Tectonic map of East Mediterranean region (modified from Barka, 1992; Över et al., 2010).

More specifically, EAFZ facilitates the westward extrusion of the Anatolian plate, has a total length of 700 km. It consists of two branches: i) the Southern one, from Karlıova to Antakya, towards the DSFZ and the Cyprus Arc, and ii) the Northern one, from Celikhan to the Iskenderun Gulf, with a length of ~ 350 km. EAFZ constists of strike-slip faults with a normal component (h < 20 km) and is a zone of high seismic activity with magnitudes M > 6 during the past 300 years (Taymaz et al., 2021; KOKUM & OZCELIK, 2020).

The 2023 earthquake sequence

The study focuses on the four strongest earthquakes of the sequence, with M_w >6, all of which had shallow hypocentral depths. Their focal mechanisms indicate left-lateral strike-slip motion, a characteristic feature of the East Anatolian Fault Zone. The four strongest earthquakes appeal to a really rare phenomenon of multiplet earthquakes where magnitudes differ no more than $\pm 0.4 M_w$ and all shocks are considered to be mainshocks (Goldberg et al., 2023).

- February 6, 2023 (M_w 7.7): known as the earthquake of Nurdağı - Pazarcık - Kahramanmaras Earthquake, at 01:17 (local time) and a total duration of 80 seconds. The ground acceleration reached 1.5 g, with a rupture velocity of 3.2 km/s. It is a shallow earthquake of 8.6 km hypocentral depth with NE-SW stress orientation. Its epicentre is located at the Türkiye-Syria border, in the Kahramanmaraş (KMTJ) – Gaziantep region (32 km NNW). The rupture is considered to be dual, as it initiated on the Narli fault (20 km from the EAF), lasting for 20 seconds and then extended 50 km NE-SW (Karabulut et al., 2023; Wang et al., 2023; Melgar et al., 2023).
- February 6, 2023 (M_w 6.8): this earthquake is reffered as Nurdağı Earthquake and it struck just 11 minutes after the first shock (01:28 UTC), with epicentral depth 6.2 km. Its epicentre is located at the southern end of the EAFZ and its stresses oriented in a NE-SW direction (Karabulut et al., 2023; Wan et al., 2024).
- February 6, 2023 (M_w 7.5): this earthquake is known as Elbistan – Ekinözü Earthquake, it occurred just 9 hours after the first one, at 10:24 (UTC) with a total duration of 50sec. Its epicentral depth is 8.6 km, the maximum slip reached 7m and the length of the rupture was approximately 160 km (SOFTA et al., 2024; Chen et al., 2023; Over et al., 2023).
- February 20, 2023 (M_w 6.3): the earthquake of Uzunba – Antakya took place two weeks after the initial event. M_w 6.3, its epicentre was in the area where the EAF and Cyprus Arc meet, its hypocentral depth was deeper than the first three earthquakes, estimated approximately at 22 km. Despite its smaller magnitude, it caused significant damage, particularly in areas affected by the previous earthquakes. The fault responsible was blind and unmapped, its focal mechanism was a left-lateral strike-slip with a small horizontal component and the length of its rupture is estimated at 25 km (Barbot et al., 2023; Over et al., 2023; Karabulut et al., 2023; Gürboğa et al., 2023).

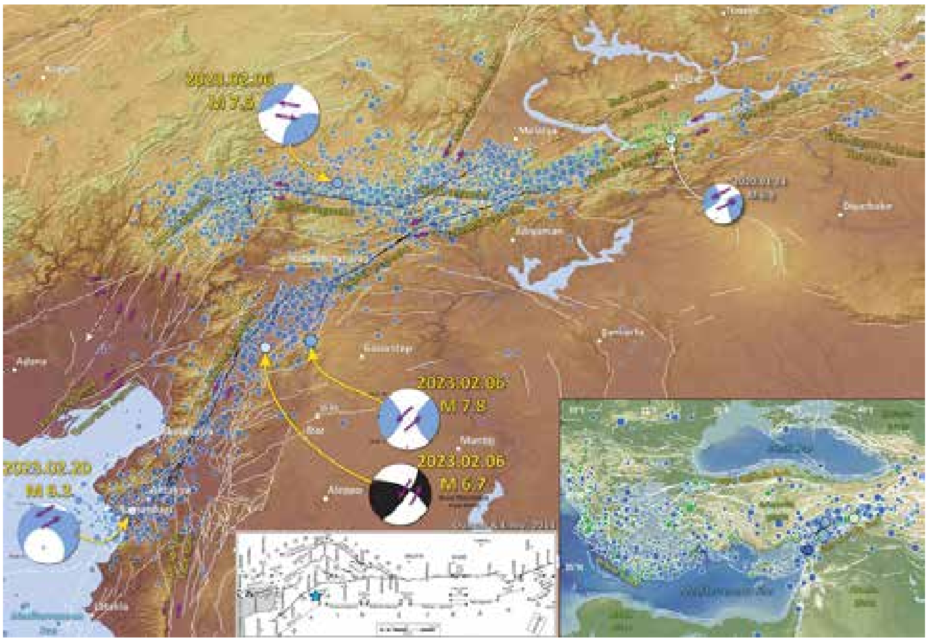

Figure 2: Epicentral map of the 2023 sequence (blue dots) with the four strongest earthquakes highlighted (USGS, 2023) (Duman & Emre, 2013).

Seismic Fault Modelling and static stress changes calculation

Firstly, we selected the nodal plane of the focal mechanisms that best fits: i) the fault direction and ii) the aftershock spatial distributions. The modelling was performed in the Coulomb 3.3 application in which we set the geometric and kinematic parameters (length and width are automatically calculated by the integrated scalar relationships of Wells & Coppersmith, 1994). After modelling the seismic sources, we applied the Coulomb Failure Criterion within the same application under the following scenario: we set in each fault rupture the ruptured fault(s) as the seismic source(s) and the faults that didn't yet rupture as receiver faults. Coulomb 3.3 software is based on the Coulomb Failure Criterion. Thus, we examined all the intermediate change of stress between the successive major ruptures of the earthquake sequence ('in-sequence' investigation).

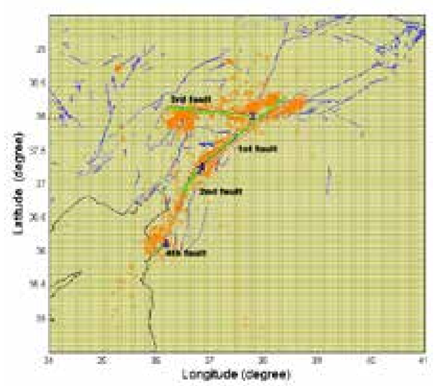

Figure 3: This figure shows the four modelled faults (1, 2, 3, 4) in Coulomb 3.3, along with the overlays of coastline (in black), regional faults (in blue) and seismic sequence of 2023 (in orange circles).

Results and conclusions

During the seismic sequence of the four strongest earthquakes of February 2023 in SE Türkiye, we investigated the Coulomb static stress changes which were caused after the fault rupture of the four strongest events. The results are shown in Figure 4 at depths close to hypocentral depth of the next earthquake. In more detail:

- The investigation of the first earthquake (06.02.2023, 01:17 UTC, 7.7 Mw) and its effect on the second event (06.02.2023, 01:28 UTC, 6.8 Mw) was conducted at the depth of 6.2km, which is close to the hypocentral depth of the latter. The results in Figure 4a indicate that the first earthquake triggered the second one, as the first fault loaded stress on the second fault.
- The investigation of both first and second earthquake suggests that they played a major role in accelerating the occurrence of the third event (06.02.2023, 10:24 UTC, 7.5 Mw). The results in Figure 4b, calculated at depth of 8.6 km which is the hypocentral depth of the third fault, indicate that the third fault was loaded with stress after the first two shocks.
- On the contrary, in the last case, we investigated the total stress change from the three earthquakes and its impact on the fourth event, two weeks later (20.02.2023. 17:04 UTC, 6.3 Mw), at the depth of 22 km, which is close to the hypocentral depth of the fourth fault. The results depicted on Figure 4c indicate that the fourth fault was not affected (white area) from the stress change produced by the first three earthquakes.

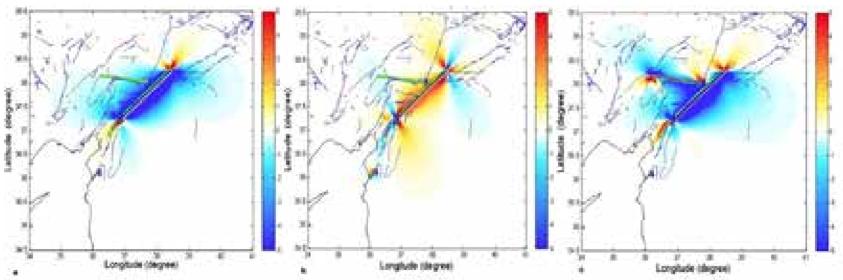

Figure 4: This figure shows the four modelled faults (1, 2, 3, 4) in Coulomb 3.3, along with the overlays of coastline (in black), regional faults (in blue) and the stress bar. The stress bar is coloured: in red tones for $\Delta\sigma f > 0$ (loaded stress), in white for $\Delta\sigma f=0$ (no stress change) and in blue tones for $\Delta\sigma f < 0$ (unloaded stress). Specifically: a. depicts the 1st fault as source-fault (with slip) and the 2nd as receiver fault, being loaded with stess, b. depicts 1st & 2nd faults as source faults and the 3rd fault as the receiver fault, being loaded with stress, c. depicts the cumulative effect of the first three faults as source faults and the 4th fault as receiver fault, which stands in an uncharged area.

Summarizing, the correlation between static stress changes and the local structural pattern played a critical role in determining the stress transfer within the faults. The stress patterns in the region were redistributed after each of the four shocks, with particularly interesting results. At least three of the four strongest earthquakes were related, each one charging stresses for the appearance of the next one. The fourth fault did not receive significant stress increase from the prior events, likely due to its deeper hypocenter and less optimal orientation within the broader stress field. The regional faults that had generated earthquakes in the recent past (Elazig 2020 & Palu 2010) appear to be recharged with stresses, confirmed by the 6 M_w earthquake in Akusagi-Kale, Elazığ, Türkiye, on 16 October 2024. This highlights the importance of integrating structural data when interpreting stress transfer and seismic hazard in complex fault systems.

Acknowledgements

I would like to express my sincere gratitude to all colleagues at NOA and especially Dr. O.J.Ktenidou and A.Papageorgiou for their support and guidance.

References

Barka, A.A., 1992. The North Anatolian Fault zone, Annales Tectonicae 6, 164 -195.

Barbot, S., Luo, H., Wang, T., Hamiel, Y., Piatibratova, O., Javed, M., Braitenberg, C. Gurbuz, G., 2023. Slip distribution of the February 6, 2023 Mw 7.8 and Mw 7.6, Kahramanmaraş, Turkey earthquake sequence in the East Anatolian Fault Zone, Seismica, 2, 1-17.

Chadha, R. K., 2023. An Mw 7.8 Earthquake on 6 February 2023 on the East Anatolian Fault, Turkey, Journal of the Geological Society of India, 99, 449–453.

Chen, W., Rao, G., Kang, D., Wan, Z., & Wang, D., 2023. Early Report of the Source Characteristics, Ground Motions, and Casualty Estimates of the 2023 Mw 7.8 and 7.5 Turkey Earthquakes. Journal of Earth Science, 20, 1-7.

Duman, T., & Emre, Ö., 2013. The East Anatolian Fault: geometry, segmentation and jog characteristics. Geological Society, 372, 495-529.

Goldberg, D., Taymaz, T., Reitman, N., Hatem, A., Yolsal-Çevikbilen, S., Barnhart, W., Serkan Irmak, T., Hatem, D., Ocalan, T., Yeck, W., Ozkan, B. Thompson Jobe, J.A., Shelly, D., Thompson, E., Duross, C., Earle, P., Briggs, R., Benz, H., Erman, C., Dogan, A.H., Altunas, C., 2023. Rapid Characterization of the February 2023 Kahramanmaraş, Türkiye, Earthquake Sequence. The Seismic Record, 3, 156–167.

Gürboğa, S., Kayadibia, O., Akıllıa, H., Arıkana, S., Tana, S., 2023. Preliminary Results of the Great Kahramanmaraş 06 February 2023 Earthquakes (Mw7.7 and 7.6) and 20 Feburary 2023 Antakya Earthquake (Mw 6.4), Eastern Türkiye. Turkish journal of Earth Science, 33, 22-32.

Harris, R., 1998. Introduction to special section: Stress triggers, stress shadows, and implications for seismic hazard. Journal of Geophysical Research B: Solid Earth, 103, 24347-24358.

Karabulut, H., Güvercin, S.E., Hollingsworth, J., Konca, A.O, 2023. Long silence on the East Anatolian Fault Zone (Southern Turkey) ends with devastating double earthquakes (6 February 2023) over a seismic gap: implications for the seismic potential in the Eastern Mediterranean region. Journal of the Geological Society, 180.

Kokum, M., Özcelik, F., 2020. An example study on re-evaluation of historical earthquakes: 1789 Palu (Elazığ) earthquake, Eastern Anatolia, Turkey. Bulletin of the Mineral, 161, 157-170.

Melgar, D., Taymaz, T., A. Ganas, A., Crowell, B., Öcalan, T., Kahraman, M., Tsironi, V., Yoslal-Cevikvil, S., Valkaniotis, S., Irmak, T.S., Eken, T., Erman, C., Ozkan, B., Dogan, A.H., Altuntaş, C., 2023. Sub- and super-shear ruptures during the 2023 Mw 7.8 and Mw 7.6 earthquake doublet in SE Türkiye. SEISMICA, 2.

Över, S., Özden, S., Pınar, A., Yılmaz, H., Ünlügenç, U. C., Kamacı, Z., 2010. Late Cenozoic Stress Field in the Çameli Basin, SW Turkey. Tectonophysics, 492, 60-72.

Över, S., Demirci,A., Ozden, S., 2023. Tectonic implications of the February 2023 Earthquakes (Mw7.7, 7.6 and 6.3) in south-eastern Türkiye, Tectonophysics, 866.

Softa, M., Kocbulut, F., Akgun, E., Aksoy, E., Sozbilir, H., Tatar, O., Karabacak, V., Ozkaymak, C., Utku, M., Ozdag, O.C., Cakir, R., Demir, A., Arslan, G., 2024. Surface rupture during the 6th of February 2023 Mw 7.6 Elbistan-Ekinözü (Kahramanmaraş) earthquake: implications for fault Fault Zone, Turkish Journal of Earth Science, 33, 1-21.

Steacy, S., Gomberg, J., Cocco, M., 2005. Introduction to special section: Stress transfer, earthquake triggering, and time-dependent seismic hazard, Journal of Geophysican Research, 110, 1-12.

Taymaz, T., Ganas, A., Yolsal-Çevikbilen, S., Vera, F., Eken, T., 2021. Source Mechanism and Rupture Process of the 24 January 2020 Mw 6.7 Do˘ganyol–Sivrice Earthquake obtained from Seismological Waveform Analysis and Space Geodetic Observations on the East Anatolian Fault Zone (Turkey), Tectonophysics, 804.

Toda, S., Stein, R., Sevilgen, V., Lin, J., 2011. Coulomb 3.3 Graphic-Rich Deformation and Stress-Change Software for Earthquake, Tectonic, and Volcano Research and Teaching-User Guide, Virginia, USA: U.S. Geological Survey Open-File Report 2011-1060.

Wan, Z., Dong, R., Wang, D., Xu, S., Wang, Z., Wang, Q., 2024. Along-Strike Variation of Rupture Characteristics and Aftershock Patterns of the 2023 Mw 7.8 Türkiye Earthquake Controlled by Fault Structure, Seismological Research Letters, 95, 2071-2080.

Wang, Z., Zhang, W., Taymaz, T., He, Z., Xu, T., Zhang, Z., 2023. Dynamic Rupture Process of the 2023 Mw 7.8 Kahramanmaraş Earthquake (SE Türkiye): Variable Rupture Speed and Implications for Seismic Hazard, Geophysical Research, 50, 1-11.

Wells, D., Coppersmith, J., 1994. New Empirical Relationships among Magnitude, Rupture Length, Rupture Width, Rupture Area, and Surface Displacement, Bulletin of the Seismological Society of America, 84, 974-1002.

17th INTERNATIONAL CONGRESS
of the Geological Society of Greece

BULLETIN OF THE GEOLOGICAL SOCIETY OF GREECE, SP. PUBL.

EXTENDED ABSTRACT 079

The Hellenic DataBase of Active Faults (HeDBAF): a new national geodatabase

Dimitrios Galanakis[1], Dimitris Sakellariou[2], Sotiris Sboras[3], Spyros Pavlides[4], Kyriaki Iordanidou[1], Charalambos Georgiou[1], Athanasios Ganas[2], Yiannis Koukouvelas[5], Charalampos Kranis[6], Spiros Lalexos[7] Theodora Rondoyanni[8], Efthymios Lekkas[9] and the EPPO Seismotectonics Committee.

(1) Hellenic Survey of Geology & Mineral Exploration, dgalanakis@eagme.gr (2) Hellenic Centre for Marine Research, (3) Geodynamics Institute National Observatory of Athens, (4) Geology Department, Aristotle University, Thessaloniki, (5) Geology Department, University of Patras, (6) Department Geology and Geoenvironment, National Kapodistrian University of Athens, (7) Earthquake Planning & Protection Organization (EPPO) (8) Head of Seismotectonics Committee of the Earthquake Planning & Protection Organization (EPPO), (9) President of the Earthquake Planning & Protection Organization (EPPO)

Abstract

The Hellenic DataBase of Active Faults (HeDBAF) is a national product of collaboration between scientists of all related to this subject academic and research institutes of Greece under the the auspices of the Earthquake Planning and Protection Organization (EPPO) and the supervision of its Seismotectonics Committee (Fig. 1). The main purpose of the geodatabase is to provide essential information to the scientific community and to whoever wants to have a synoptic or in detail information about the active faults of Greece, as well as to serve as a platform for geologists, engineers and the central and local administration, to in-depth studies. The HeDBAF geospatial database started to realize since 2021, including parametric and descriptive information about the active faults in the broader Hellenic region. The responsibility of implementation, management and hosting is held by the Hellenic Survey of Geology and Mineral Exploration (HSGME).

The HeDBAF adopts conceptual approaches and characteristics from other time-proven national databases of the world (e.g. INGV's DISS, IGME's QAFI, etc.). It is a multi-layered tool that hosts all available literature data (e.g. scientific articles, technical/project reports, thematic maps, etc.), targeting various groups of end-users: the primary target group is the scientific community which often needs medium- to small-scale information for geodynamic interpretations, large-scale data for local seismotectonic analyses, and appropriate parametric information for numerical modelling. The next target group is the engineers who need large-scale detailed surveying of the fault traces and ground ruptures, and fault models for the prediction of ground motion in the context of Seismic Hazard Assessment. Administration, government, security bodies and local authorities can benefit from this geodatabase as a decision-making tool for safety and rescue planning. Last, but not least, a broad range of citizens will be able to access principal theoretical and parametric information about active faults in areas they are interested in.

More important dataset includes faults with geomorphic marks, such as free faces, coseismic ruptures, fault scarps, triangular facets (flat-irons), or sometimes inferred faults based on geomorphological evidence, such as river deflections, linear mountain-fronts, *etc.* It should be mentioned that the geomorphological evidence is a complementary element for the more accurate geographical positioning of the fault trace and not for the existence of the fault. In the case of earthquake-related faults (seismic faults), the traces can correspond to primary ground ruptures. Among the purposes of this dataset is to provide also information necessary for *Surface Faulting Hazard* (SHA). This type of hazard assessment is crucial for building and infrastructure design, considering that a possible fault displacement could damage the foundations of any technical construction. Moreover, the detailed mapping of fault traces can contribute to fault linkage/segmentation scenarios. Such scenarios are also important, since they can inform us whether a possible rupture can be constrained or pass through neighbouring faults, increasing, thus, the magnitude potential.

The core of the geodatabase, i.e. the tectonic information, will be separated into two distinct, but interrelated, datasets: i) the Fault Traces (FT), and ii) the Fault Zones (FZ). The purpose of each dataset is to provide a different level of information covering different needs (Fig. 2). The former focuses on the mapping accuracy of faults, targeting on large- to medium-scale data (> 1:50,000). Faults originating from smaller scale maps are reassessed (if possible) using hi-resolution topographic data. Primary co-seismic ground ruptures are distinguished from geologically detected fault traces to better understand the surficial rupturing process for fault rupture hazard purposes. The Fault Zones dataset involves fault segmentation and earthquake rupture scenarios which are crucial for Seismic Hazard Assessment (SHA).

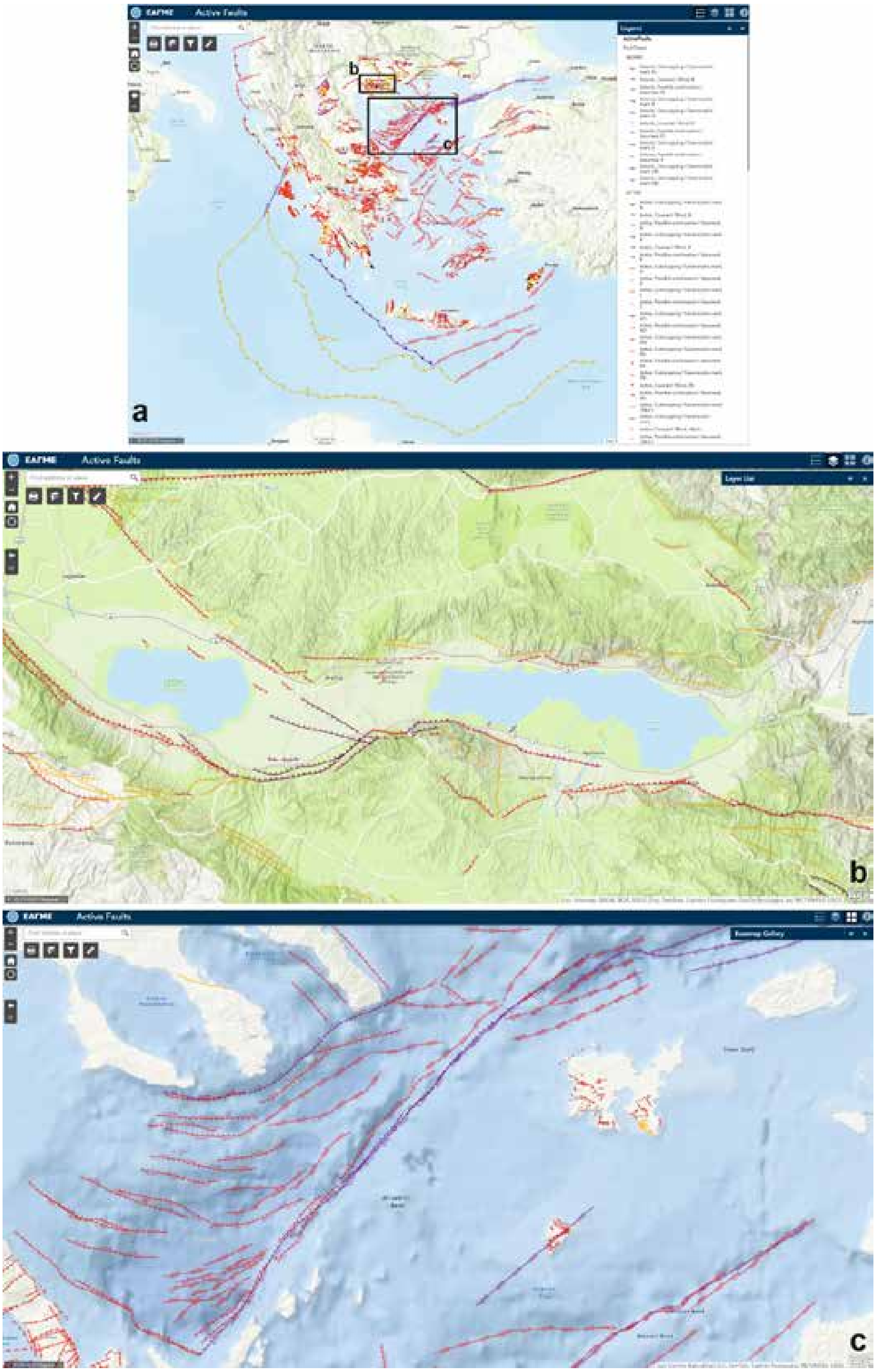

Figure 1. Snapshots of the Hellenic DataBase of Active Faults (HeDBAF) in its current status as seen in the dedicated website (https://activefaults.eagme.gr/en/) for various topographic backgrounds: (a) The broader area of Greece showing the locations of inset maps (b) and (c). (b) Focus on the Mygdonia Basin. (c) Focus on the North Aegean Basin, Lemnos and Aghios Efstratios islands.

Thus, the fault zones are represented by medium- to small-scale lineaments which also facilitate the visualization of large tectonic structures in small-scale maps. The HeDBAF, geodatabase is continuously updateable and upgradeable showing frequent improvements and enrichments.
Following the steps of the Database of DISS (DISS Working Group, 2021) and the Quaternary active faults database of Iberia QAFI (García-Mayordomo et al., 2012), the HeDBAF not only is the source of information, for most of the parametric information, clearly given (whether it is literature data, original data, empirical relationship, or expert judgement, all abbreviated as source-keys), but the methodology followed to extract this information is stated. This means that the end-user has at his/her disposal the origin of the parametric information and the distinction between real data or any other kind of estimation. In this way, the scientific and highly specialized working group of the geodatabase ensures that most of the parametric information will be filled in, leaving as few blank fields as possible.

The classification of the faults used in the Database is based on the definitions decided by the Seismotectonics Committee, as follows:

Seismic fault is defined as an active fault if its activation has been confirmed by a strong earthquake during the instrumental or historical period, by an observed surface seismic rupture or by a palaeoseismological investigation. It should be mentioned that the above definition does not exclude the existence of seismic faults identified by seismological, geophysical, geodetic or other instrumental observations.

A fault is characterized as Active when it documents displacement at least once during the Upper Pleistocene (in the last 126,000 years or so) and can therefore be the source of a future earthquake.
A fault is characterized as active when:

- it has produced a surface rupture associated with a historical or modern earthquake
- it has yielded soil ruptures dated during the Upper Pleistocene-Holocene period, as has been determined by excavating palaeoseismological trenches perpendicular to its trace
- it displaces or affects (e.g. folds) Upper Pleistocene-Holocene geological formations
- free faces with sclickenlines observed along the fault's length have not been eroded at places
- characteristic escarpments and tectonic scarps can be recognized along its length
- debris or talus cones develop at the base of the fault scarp
- morphotectonic structures (e.g. triangular facets, etc.) are shown along its length
- it cuts or displaces river or stream beds in a systematic way
- it demonstrates aseismic slip (proven by geodetic measurements or other indications)
- it is associated with seismic epicentres of the instrumental period or with the alignment of microearthquakes
- it has a structural relationship with another known active fault (it is subparallel, it branches, it has en echelon geometry, etc.)
- it is associated with active volcanism or hot springs
- the stress field of its last activation is roughly the same as the one given by the focal mechanisms in the same area.

A fault is characterized as Potentially Active when it documents displacement at least once during the Quaternary (in the last 2.600.000 years).
The Potentially Active faults:

- displace or affect (e.g. folds) quaternary geological formations but they have not been reactivated during the last 126.000 years
- there is no available geological data indicating their direct relation to strong earthquakes
- they show a small degree of correlation with the distribution of major earthquake epicenters of the instrumental period.
- geomorphological features (eg fault surfaces) along the fault traces are significantly eroded
- they have been identified on the basis of geophysical surveys in areas covered by recent deposits
- their direction is compatible with the active tectonic stresses prevailing in the area.

Non active faults (Inactive or Faults of Undetermined activity) are those for which there are no geological or other (seismological, historical, paleoseismological, geophysical) indications for their activation at least during the Quaternary period (last 2.600.000 years).

References

DISS Working Group (2021). Database of Individual Seismogenic Sources (DISS), Version 3.3.0: A compilation of potential sources for earthquakes larger than M 5.5 in Italy and surrounding areas. Istituto Nazionale di Geofisica e Vulcanologia (INGV). https://doi.org/10.13127/diss3.3.0

García-Mayordomo, J., Insua-Arévalo, J. M., Martínez-Díaz, J. J., Jiménez-Díaz, A., Martín-Banda, R., Martín-Alfageme, S., Álvarez-Gómez, J.A., Rodríguez-Peces, M., Pérez-López, R., Rodríguez-Pascua, M.A., Masana, E.& the QAFI Compilers Working Group (2012). The Quaternary active faults database of Iberia (QAFI v. 2.0). Journal of Iberian Geology, 38(1), 285-302.

EPPO Seismotectonics Committee: Vassiliki Avramea, Constantinos Athanassas, Nikolaos Zouros, Nikolaos Theodoulidis, George Kaviris, Ioannis Kalogeras, Vassiliki Kouskouna, Anastasia Kiratzi, Stylianos Lozios, Constantinos Makropoulos, Maria Manoussaki, Vasileios Margaris, Spyridon Mauroulis, Vassiliki Mouslopoulou, Panayiotis Papadimitriou, Gerasimos Papadopoulos, Constantinos Papazachos, Christos Papaioannou, Efthymios Sokos, Charalambos Fasoulas.

17th INTERNATIONAL CONGRESS
of the Geological Society of Greece

BULLETIN OF THE GEOLOGICAL
SOCIETY OF GREECE, SP. PUBL.

EXTENDED ABSTRACT 080

An investigation of the use of deep-neural-network-based seismic arrival time picking methods for the automatization of earthquake sequence monitoring: The case of the November 3, 2024 MW 5.3 Kassandra earthquake

Galanis O. [1], Panou A. [1]
(1) Aristotle University of Thessaloniki, Thessaloniki, Greece, ogalanis@geo.auth.gr

We use a pretrained deep neural network to pick seismic arrivals on continuous seismic records. With these picks we locate the events of an earthquake sequence.

Introduction

During the last decade, a number of machine learning techniques have been developed for seismology, and equally importantly, became available as open software. This, combined with the wide availability of open seismological data and open tools for their manipulation, sets the stage for significant improvements in both routine earthquake monitoring and seismological research. In the present work we investigate the use of deep-neural-network-based seismic arrival time picking methods for the automatization of earthquake sequence monitoring and we use the sequence of the November 3, 2024 M_W 5.3 Kassandra earthquake as a case study.

Data

On November 3, 2024, an earthquake of magnitude 5.3 (M_W) occurred off the coast of the Kassandra peninsula of Chalkidiki, Northern Greece, in an area of moderate seismicity. The subsequent aftershock sequence consisted of hundreds of events (indicatively, 430 earthquakes of magnitude 1.5M_L or larger were detected by the automatic location system of the Seismological Station of the Aristotle University of Thessaloniki, within the two months following the mainshock). A selected subset of these events was manually located and included in the bulletin of the Seismological Station of the A.U.Th. These events are shown in Figure 1.

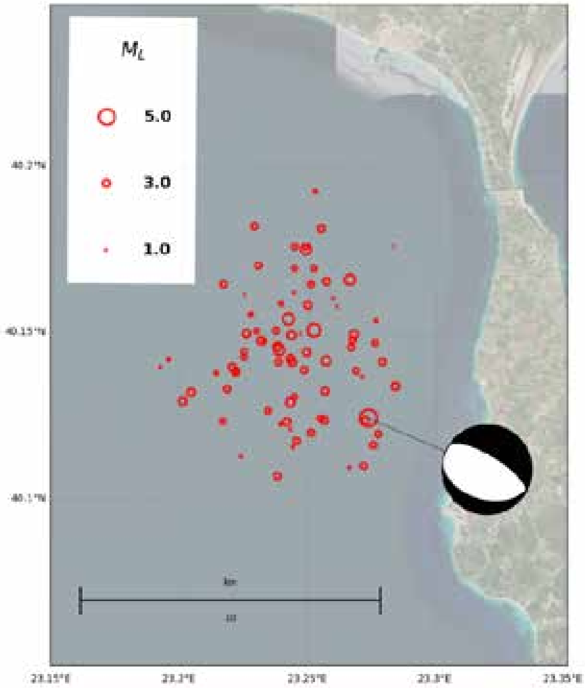

Figure 1. The epicenters of events with a manual solution included in the bulletin of the Seismological Station of the A.U.Th. The beachball plot corresponds to the focal mechanism of the mainshock (Mw=5.3, A.U.Th.).

The input data used in the present study, is the continuous recordings of broadband and strong motion stations in operation in the area around the sequence. These stations are selected from the around 350 stations available to the Seismological Station of A.U.Th., of which 50 are maintained by the A.U.Th. itself while the rest are provided by the other members of the Hellenic Unified

Seismological Network and other partners. The routine procedure is to first automatically calculate hypocenters and magnitudes in real time with the SeisComP seismological software package, which are then refined by designated human analysts. Analysts are instructed to at a minimum perform a manual analysis of every event for which the automatic magnitude (M_L) is 2.5 or greater. This results in two datasets, one of relatively higher quality but limited in size by the available humanpower of the Seismological Station and one of relatively lower quality but more extensive.

In the present study, we use deep-neural-network-based seismic arrival picks to locate the sequence, in order to obtain a dataset of sufficient quality and sufficient size to describe the spatial and temporal distribution of the events.

Implementation

We used the SeisBench toolbox (Woolam et al. 2022) which provides, among other tools, deep neural network models trained with a range of training datasets. Comparing models and training sets is out of the scope of the present work, so we used the EQTransformer model (Mousavi et al., 2020), trained with the Instance dataset which is a good starting point for most cases (Münchmeyer et al., 2022). A sample of the results is shown in figure 2. For associating the picks produced by EQTransformer, we used the GaMMA associator (Zhu et al. 2022). After association, each pick is associated with a specific event. In the final step the events are located using the NonLinLoc software (Lomax et al. 2014), which is also the software used for the routine manual location of earthquakes. For the routine manual location, we use a 1-D velocity model, and we did not change this for the present work. The end product of the process is a catalog of the events of the earthquake sequence. It also has to be mentioned that in addition to all the above software, we had to develop tools for thest downloading of the data, as well as manipulation, bookkeeping and reformatting. This also included tools to rapidly visually inspect phase picks and phase associations.

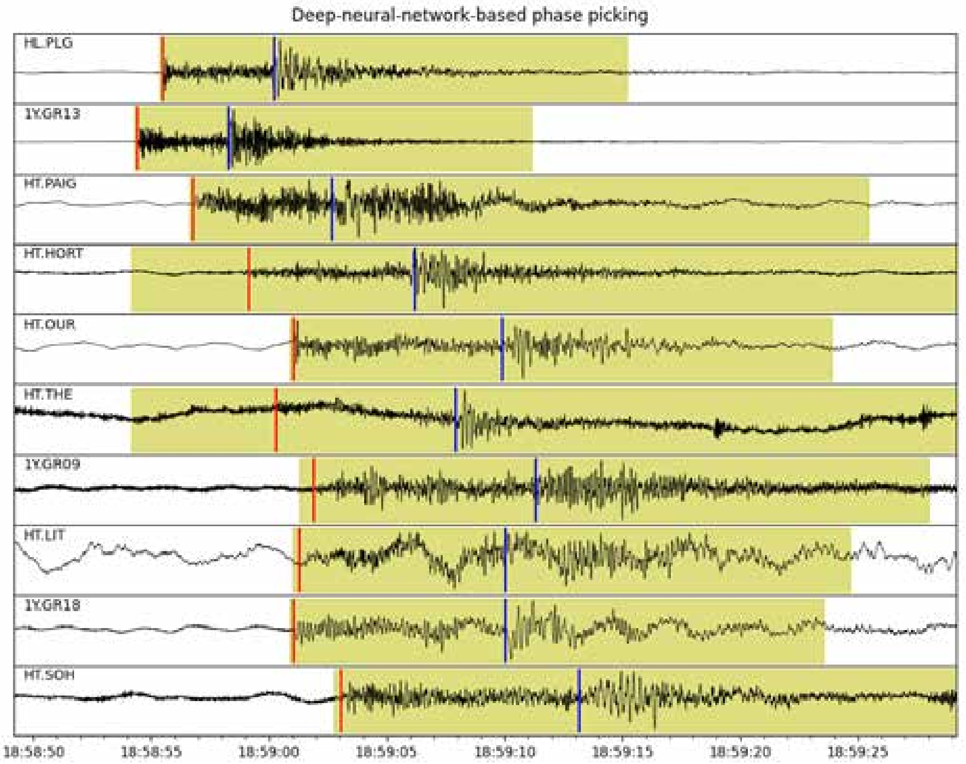

Figure 2. Example of the results of deep-neural-network-based picking. The yellow shadowed area corresponds to the time window characterized as the detection of an earthquake by the model. The red lines correspond to the P arrivals (technically the times where the probability of a P arrival is maximized) and the blue lines correspond to the S arrivals. The event shown has a magnitude of 1.7 (M_L) as determined by the automatic earthquake location system.

Results

The picking – association – location procedure resulted in the events shown in Figure 3. 1085 events were located in total. 11 foreshocks were detected, the first one occurring in October 31st. Although we scanned for P and S wave arrivals for the period starting in October 1st, not a single event was detected in the area of interest until the last hour of the month. This gives an indication of the system's resilience to false detections. The aftershocks persisted for the months following the mainshock with an average of more than one event per day during February 2025.

The focal depths of these events are < 20 km but they are not well constrained. This does not seem to be a problem of the location procedure as it was also observed in the far more rigorous manual locations. The error in the epicenter appears to be at least as small as that of the manual epicenter judging by their spatial distribution, especially taking into account that the deep-neural-network-based sample of earthquakes is about an order of magnitude larger than the manual sample. To confirm this, we also performed a double-difference relocation (hypoDD, Waldhauser and Ellsworth, 2000, Waldhauser, 2001) of all the events. The results of this relocation are shown in Figure 4.

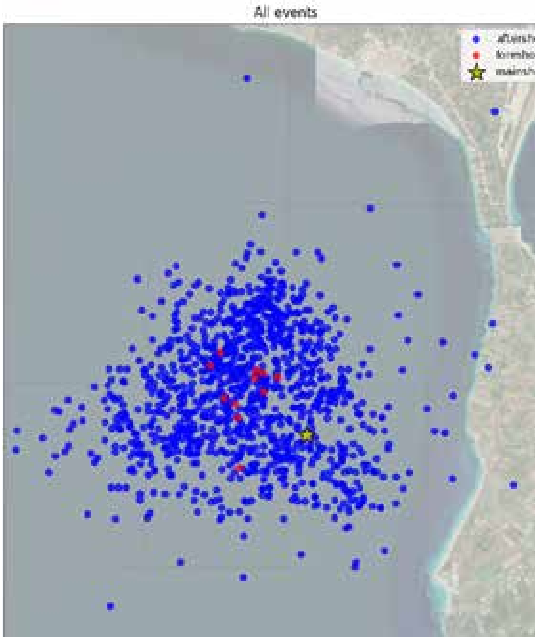

Figure 3. All the events located. The mainshock is marked with a star, while foreshocks and aftershocks are marked by red and blue points respectively.

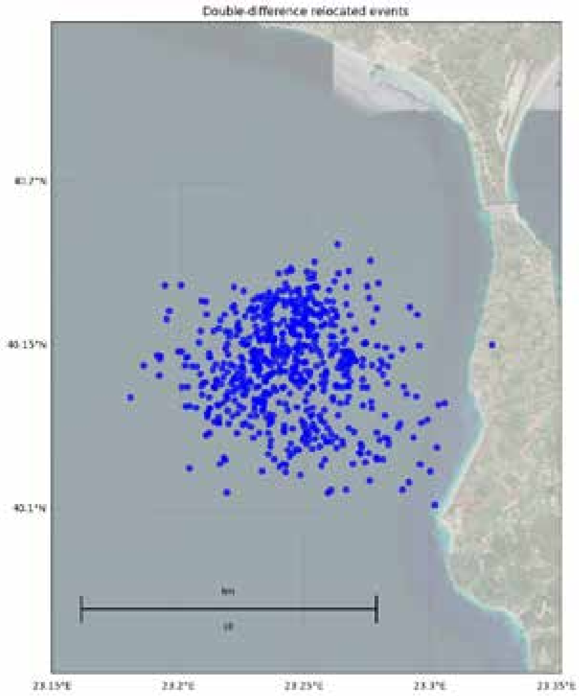

Figure 4. All the events relocated by the double-difference algorithm

The geometry of the fault is not apparent by the epicenter distribution, but taking into account the published focal mechanism it appears that the fault length is at most 10km which is compatible with an event of this magnitude or a slightly larger one. In a real-world application this sort of information would be helpful in the evaluation of the earthquake sequence the hours following the mainshock. For this reason, we mapped the events that occurred in the 12h following the mainshock. The results are shown in figure 5. We conclude that during this particular earthquake sequence there was no significant temporal change in the spatial distribution of the epicenters.

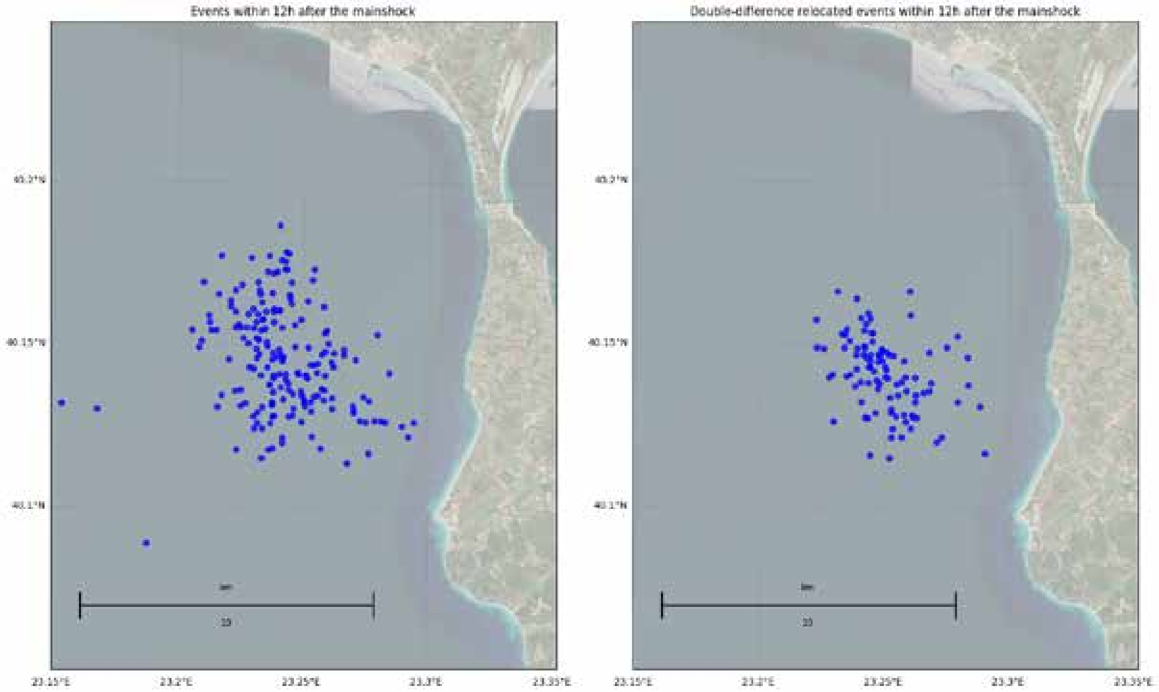

Figure 5. The events that occurred the 12 hours following the mainshock as located by NonLinLoc (left) and the subset that was successfully relocated by hypoDD

Finally, we calculated the rate of occurrence of the aftershocks, as the number of detected events within a 24h moving window. The results are shown in Figures 6, 7 and 8. We conclude that the aftershock sequence is very typical in this respect, as the rate of occurrence of aftershocks follows Omori's law in the short term (days) as well as in the long term (months).

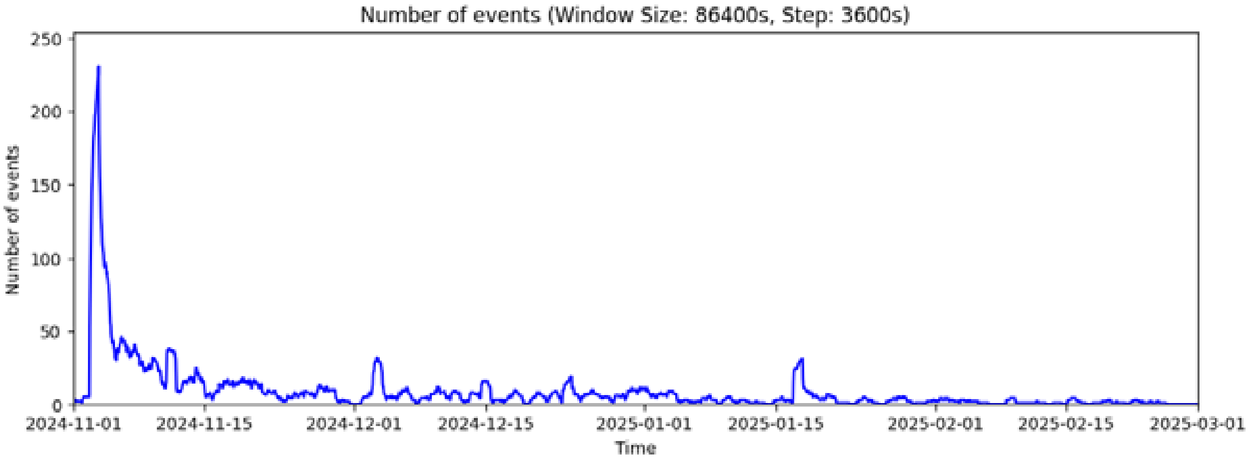

Figure 6. The rate of occurrence of earthquakes given as the number of detected events within a 24h moving window for the period covered by the present study.

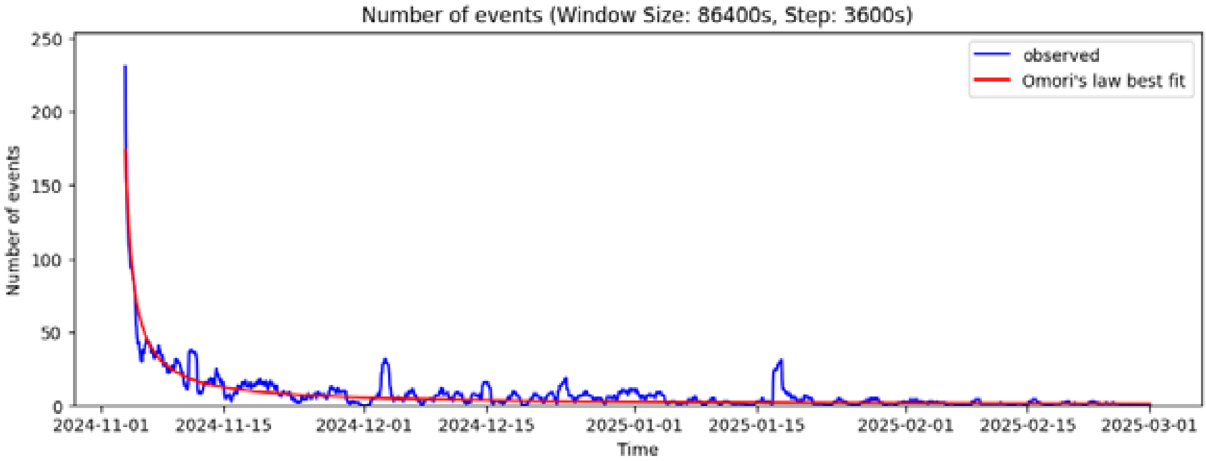

Figure 7. The rate of occurrence of aftershocks given as the number of detected events within a 24h moving window starting at the origin time of the mainshock. The rate of occurrence is shown with a blue line, and the least squares best fit for Omori's law is shown with a red line.

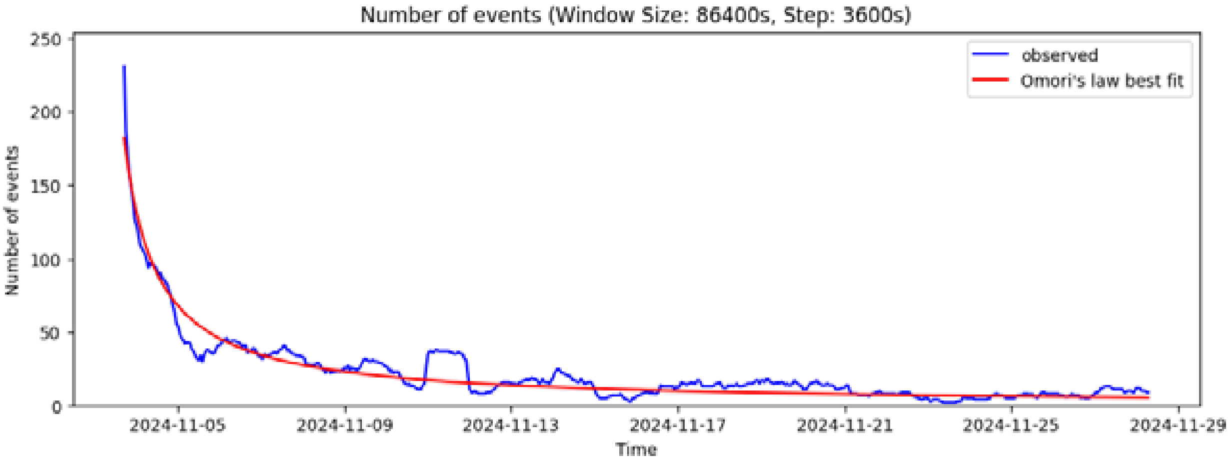

Figure 8. The rate of occurrence of aftershocks given as the number of detected events within a 24h moving window for a few weeks following the mainshock. The rate of occurrence is shown with a blue line, and the least squares best fit for Omori's law is shown with a red line.

Conclusions

Deep-neural-network-based seismic arrival time picking methods, can be used in combination with other tools and methods and using relatively modest computational resources, for the monitoring of earthquake sequences. This sort of automatization is a satisfactory compromise between the higher quality manual locations and larger quantity of "traditional" automatic pickers. We applied them retrospectively to a moderate size earthquake sequence, and we plan to use them in real time in the future.

Data sources

All graphs and maps were created with the Matplotlib library (https://matplotlib.org/). When not stated otherwise, managing and processing seismological data was performed with ObsPy (https://www.obspy.org/). The backgrounds of the maps were developed by ESRI (https://www.esri.com/). We used data from the FDSN networks: 1Y, BS, EG, HA, HI, HL, HP, HT, KO and MK (https://www.fdsn.org/networks/)

References

Beyreuther, M., Barsch, R., Krischer, L., Megies, T., Behr, Y., and Wassermann, J., 2010. ObsPy: A Python Toolbox for Seismology, Seismological Research Letters, 81 (3), 530-533.

Helmholtz-Centre Potsdam - GFZ German Research Centre for Geosciences and gempa GmbH, 2008. The SeisComP seismological software package. GFZ Data Services. doi: 10.5880/GFZ.2.4.2020.003.

Lomax A., Michelini A., Curtis A., 2014. Earthquake Location, Direct, Global-Search Methods, in: Meyers R. (Eds), Encyclopedia of Complexity and Systems Science. Springer, New York, NY.

Mousavi, S.M., Ellsworth, W.L., Zhu, W., Chuang, L.Y., Beroza, G.C., 2020. Earthquake Transformer: An Attentive Deep-learning Model for Simultaneous Earthquake Detection and Phase Picking. Nature Communications.

Münchmeyer, J., Woollam, J., Rietbrock, A., Tilmann, F., Lange, D., Bornstein, T., et al., 2022. Which picker fits my data? A quantitative evaluation of deep learning based seismic pickers. Journal of Geophysical Research: Solid Earth, 127, e2021JB023499.

Waldhauser, F., Ellsworth W.L., 2000. A Double-Difference Earthquake Location Algorithm: Method and Application to the Northern Hayward Fault, California, Bull. Seism. Soc. Am. 90, 1353-1368.

Waldhauser, F., 2001. hypoDD - A Program to Compute Double Difference Hypocenter Locations, U.S. Geological Survey Open-File Report 01-113, 25p.

Woollam, J., Münchmeyer, J., Tilmann, F., Rietbrock, A., Lange, D., Bornstein, T., Diehl, T., Giunchi, C., Haslinger, F., Jozinović, D., Michelini, A., Saul, J., Soto, H., 2022. SeisBench—A Toolbox for Machine Learning in Seismology. Seismological Research Letters 93 (3): 1695–1709.

Zhu, W., McBrearty, I. W., Mousavi, S. M., Ellsworth, W. L., Beroza, G. C., 2022. Earthquake phase association using a Bayesian Gaussian Mixture Model. Journal of Geophysical Research: Solid Earth, 127, e2021JB023249

17th INTERNATIONAL CONGRESS of the Geological Society of Greece

BULLETIN OF THE GEOLOGICAL SOCIETY OF GREECE, SP. PUBL.

EXTENDED ABSTRACT 081

Evolution of map-making from prehistoric times to the Middle Ages

Galazoudi E.[1], Bathrellos G.D.[2], Skilodimou H.D.[2], Koukouvelas I.K.[2], Nikolakopoulos K.[2]
(1) National & Kapodistrian University of Athens, Athens, Greece, egalaz@uoa.gr, (2) University of Patras, Patras, Greece

Introduction

The history of cartography—the art and science of map-making—is rich and fascinating, spanning millennia of human history. The relationship between humans and the environment dates back to ancient times. Most ancient cultures considered nature sacred (Manolas, 2010).

This connection between man and the environment is reflected, for example, in literary works, art, and maps. Maps have always been among the most important tools for comprehending the world and humanity's place in it, dating back long before the invention of writing.

Prehistoric humans used maps to depict their environment and to transmit their knowledge to future generations (Livieratos, 2007). Ancient Greeks considered themselves part of the natural environment, a perspective that influenced their daily lives, philosophy and religion. In antiquity, maps were created to help people understand and navigate the world.

Objectives

This paper describes the evolution of cartography or map-making from Prehistory to the Middle Ages. It explores the purposes of map-making, highlights the first examples of maps, discusses the contributions of ancient civilizations to map-making, of technology to the evolution of maps, and the role of geopolitical conditions in the formation of maps.

It also describes the significance of maps in understanding our world and the evolution of related theories. It examines the findings and observations concerning their thematic content and materials used in map-making during this period. It also presents the evolution of theories regarding the shape of Earth, its position in the Universe, and maps orientation.

Methods

The methodology for this paper initially included the search and collection of relevant bibliographic references. This bibliography includes Greek and international references about:

- the objectives and purposes of map creation
- the earliest examples of maps
- the contribution of ancient civilizations to the development of map creation
- the influence of geopolitical conditions on the formation and evolution of maps

The bibliography was searched and collected through Greek libraries, bibliographic databases, repositories of Greek - foreign Academic Institutions and online resources.

Subsequently, all the data collected was classified and processed. The maps were analysed in detail based on:

- their thematic content,
- the material used in their construction,
- the evolution of the Earth's outline and shape,
- the evolution of orientation over time.

The findings and observations derived from the data analysis were synthesized to draw conclusions, which are described in the concluding section.

Results

The first maps date back to the Paleolithic era (40,000 to 10,000 BC) and were created before the development of writing. Their purpose was educational and contained simple representations of the environment of primitive man. The material for recording primitive maps is rocks, known as petroglyphs (Brotton, 2015).

Babylonians introduced the fundamental principles of cartography, namely orientation and scale. They created the first map in 2500 BC, using clay tablets - the material - to make maps. They represented properties, city plans, as well as the world. The Babylonian view of the Earth was flat, circular and surrounded by the ocean (Snow et al., 2018).

By the end of the pre-Christian era, the ancient Greeks had laid the foundations of scientific cartography through three significant advances. First, Alexander the Great's expedition extended the then-known world to the Indus River, expanding geographical knowledge and reinforcing the need for cartographic mapping (Hunt, 2000). Second, Eratosthenes proved the sphericity of the Earth and calculated its circumference with remarkable accuracy. Third, Hipparchus invented a system of meridians and parallels, highlighting the need to develop map projections (Hunt, 2000).

Generally, the ancient Greeks contributed decisively to the evolution of cartography, introducing scientific and mathematical principles that formed the basis for its later development. They recognized the spherical shape of the Earth, leading to a more accurate geographical depiction (Livieratos, 2007). They used geometric methods and developed instruments for measuring geographical quantities. They focused on scientific observation through measurements to understand the universe. They invented projections and, through them, the mathematical organization of the Earth's surface while connecting measurements with precise calculations, such as Eratosthenes' measurement of the Earth's diameter, a pioneering transition from empirical to scientific observation (Livieratos, 2007).

Cartography during the Middle Ages remained stagnant. Maps or mappae mundi showed significant differences from ancient and modern times (Harley & Woodward, 1987). Their purpose was educational as well as to represent the time's geographical, religious and mythological concepts. T and O-type maps were religious and represented the world with Jerusalem in the center and the East at the top of the map (Woodward, 1987). One type of map showed the world as a circle divided into seven geographical zones - the "climates" of Eratosthenes - or the five zones of the Roman writer Macrobius (Hunt, 2000). Portolans are maps that appeared in the 13th century and depicted the coasts, intending to help sailors in their travels (Tolias, 1999).

Table 1. Evolution of the beliefs about Earth's place in the Universe: From Antiquity to Renaissance

Period	Earth's place in the Universe	Important Philosophers/Scientists
Antiquity	Geocentric model	Aristotle (384-322 BC),
	Heliocentric model	Aristarchus of Samos (310 BC - 230 BC)
	Geocentric model	Claudius Ptolemy (85-165 AD)
Middle Ages 5th to 15th century AD	Geocentric model	Official position of the Roman Catholic Church
16th century	Heliocentric model	Nicolaus Copernicus

The place of the Earth in the Universe has been an issue that has concerned humans throughout time. Table 1 shows the evolution of the perception.

In Antiquity, the dominant belief was the geocentric system, in which the Earth was the center of the world. The Sun, the planets and the Stars revolve around the Earth (Livieratos, 2007). However, Aristarchus of Samos (310 BC - 230 BC) introduced the theory of a heliocentric system (Crowe, 1990), in which the Sun is the center of the Universe and the Earth orbits around it, which was not adopted.

The geocentric system was maintained in the Middle Ages, with the official position of the church being that the Earth is stationary and the planets revolve around it. Copernicus refuted this view in the 16th century.

Table 2. Evolution of the theories about Earth's shape. From Antiquity to Middle Ages.

Period	Map	Person	Earth's shape	Orientation
8th century BC	Shield of Achilles	Homer	Flat circular	
600 BC	Babylonian world map	Babylonians	Circular disk	N
550 BC	Anaximander map	Anaximander	Circular disk	
510 BC	Anaximander map	Hecataeus	Circular disk	
580-500 BC		Pythagoras	Spherical and rotation around an axis	
340 BC		Aristotle	Spherical	
250 BC		Eratosthenes *	Spherical	N
270-180 BC		Crates **	Spherical	
180-120 BC		Hipparchus***	Spherica	
85 BC		Poseidonius ****	Spherical	
1st century BC	Geographical	Strabo	Spherical	
2nd century AD	Geographia	Claudius Ptolemy	Spherical	N
536 AD		Cosmas	flat and elongated	S
Middle Ages 5th – 14th century AD		Mappae mundi	One - dimensional or flat, with circular or rectangular shapes that did not reflect the real geomorphology of the earth	E

*First measurement of the Earth, **Created the first Globe, *** Invented a system of meridians and parallels, ****Second measurement of the Earth

The beliefs about the shape of the Earth.

The shape of the Earth has been another topic that has preoccupied people since ancient times. Table 2 displays the transition from simple initial beliefs to more complex scientific theories about the shape of the Earth.

In antiquity, there were differing beliefs about the shape of the Earth:

1. Flat Circular Disk: This idea was held by the Babylonians, Homer, Anaximander, Hecataeus, and the Ionians, who believed the Earth was a flat disk.
2. Spherical Shape: In contrast, philosophers such as Pythagoras, Aristotle, Eratosthenes, Crates, Hipparchus, Posidonius, Strabo, and Ptolemy supported the theory that the Earth is spherical. They based their conclusions on observations of stars and various natural phenomena over time. Eratosthenes played a key role in confirming the Earth's spherical shape by calculating its circumference.

In the Middle Ages, maps depicted the world as one-dimensional or flat, with circular or rectangular shapes that did not reflect the Earth's actual geomorphology. These maps often illustrated the world as a flat disk surrounded by water.

The shape of the Earth played a crucial role in the significant geographical discoveries of the late Middle Ages. An example was the discovery of America in the late 15th century. It prompted the exploration of new sea routes and the establishment of trade relations, while scientific contributions from Arab geographers and European scholars improved the knowledge and confidence of seafarers. This new concept played a significant role in reviving geographical knowledge and initiating the era of great discoveries.

In addition, the above table also illustrates how map orientation has evolved over time.

In Babylonian maps, the orientation was initially towards the North. However, the earliest maps created by the ancient Greeks did not have a precise orientation. It was not until the introduction of geographical coordinates that they began to orient their maps towards the North, as seen in Ptolemy's map. This description resulted from the astronomical, geometric, and physical observations made by the ancient Greeks.

During the Middle Ages, most mappae mundi were oriented toward the East for religious reasons. An exception to the above is the map of Cosmas the Indicator, which was oriented towards the South. The Arab maps were oriented towards the South to align with Mecca. The evolution of map orientation underscores the profound cultural significance of mapmaking.

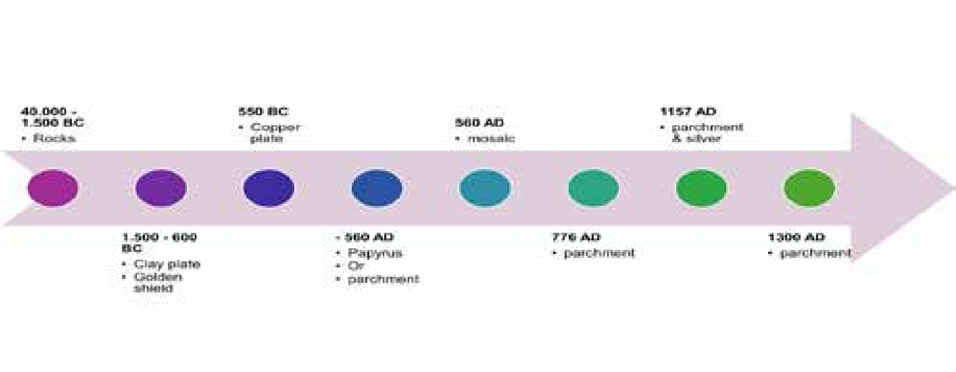

Figure 1. Evolution of the material used to make maps through time.

The above figure presents the evolution of the material used to make maps. Specifically, the depiction of maps began in the Paleolithic era, when prehistoric people drew their environment on rocks. Then, in Antiquity, it progressed from the clay tablets of Babylon to Homer and the golden shield of Achilles to the bronze tablet of Anaximander. During the Middle Ages, the most significant number of maps (or tablets) were either made of papyrus or parchment. Then, in Antiquity, from the clay tablets of Babylon to Homer and the golden shield of Achilles, we move on to the bronze tablet of Anaximander. In Antiquity, most maps (or tablets) were made of papyrus or parchment.

The transition from papyrus to parchment resulted from a combination of factors such as durability compared to papyrus, which was vulnerable to moisture and brittle. This durability allowed the preservation of texts for a more extended period, which was crucial to conserving religious texts and scriptures (di Curci, 2003). In addition, ease of use, availability, and the need for religious writing made parchment an essential material in the history of writing and cartography (di Curci, 2003). This transition began in the fourth, and by the end of the eighth century, most maps used parchment as constructed material.

In the Middle Ages, most maps were made of parchment. Exceptions are the Madaba mosaic map (560 AD) and the

Tabula Rogeriana map (1157 AD), which is made of parchment and silver. Towards the end of the Middle Ages, maps of animal skin (vellum), such as the Carte Pisane (1300 AD), were also made of parchment (Brotton, 2015).

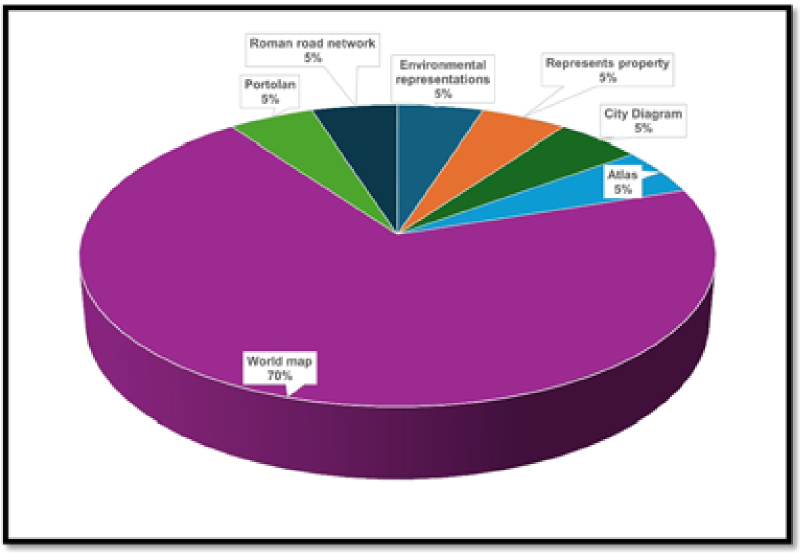

Figure 2. Distribution of types of maps, from Prehistory to the Middle Ages

Figure 2 presents the distribution of types of maps, from Prehistory to the Middle Ages, highlighting the diversity across numerous types.

World maps account for the most significant percentage of concerns, which indicates man’s interest in understanding the World on a global scale.

These maps were not only geographical but often incorporated both philosophical and religious concepts of the World.

The remaining types of maps are in the same percentages: Portolans, environmental representations, representations of property, city diagrams, geographical atlases, as well as maps of the Roman road network.

Conclusions

The high percentage of World maps demonstrates humanity’s inclination to understand the Earth, which was not only geographical but often incorporated both philosophical and religious concepts of the world.

The materials used for making maps have changed over time. In the past, people used rocks and clay tablets. Later, they made maps from metal, papyrus, and parchment. This progression illustrates technological advancements and emphasizes how these innovations have improved our comprehension of the world.

In Antiquity, the geocentric model of the Universe was dominant until Aristarchus of Samos proposed a heliocentric view, which was largely ignored. During the Middle Ages, the geocentric perspective continued to be upheld and supported by Church doctrine, demonstrating the enduring influence of ancient ideas.

Early thinkers like the Babylonians and Homer viewed the Earth as a flat disk. In contrast, philosophers such as Pythagoras and Aristotle later argued for a spherical Earth. During the Middle Ages, maps often depicted a flat world, ignoring true geomorphology.

Babylonian maps oriented northward, while early Greek maps lacked clear orientation. As the Greeks began to use geographical coordinates, they started orienting their maps to the north. In contrast, medieval mappae mundi were often oriented eastward for religious reasons, and Arab maps pointed south.

References

Brotton, J., 2015. Great maps. Dorling Kindersley Limited.

Crowe, M. J., 1990. Theories of the world from antiquity to the Copernican revolution. New York: Dover Publications.

di Curci, M. 2003. The History and Technology of Parchment Making. Lochac College of Scribes: Parchment Making

Harley, J. B., & Woodward, D. (Eds.)., 1987. The History of Cartography, Vol. 1: Cartography in Prehistoric, Ancient and Medieval Europe and the Mediterranean. (Vol. 1). THE UNIVERSITY OF CHICAGO PRESS.

Hunt, A., 2000. 2000 Years of Map Making. Geography, 85(1), 3–14.

Livieratos, E., 2007. 25 Centuries from Iones to Ptolemy and Rigas: A tour into Cartography and Maps. Ziti (in Greek)

Manolas, E. I. (Ed.). (2010). The Natural Environment in Ancient Greece. Department of Forestry and Environmental and Natural Resources Management, Democritus University of Thrace. (in Greek)

Snow, P., Houston, R., Mumford, S., Merritt, E., Darlison, M., & Stirling, H. (Eds.)., 2018. History of the world map by map. Dorling Kindersley Limited.

Tolias, G., 1999. The Greek nautical charts Portolans, 15th-17th centuries: A contribution to the Mediterranean cartography of recent times (1st ed.). Olkos (in Greek).

Woodward, D., 1987. Medieval Mappaemundi. In Cartography in Prehistoric, Ancient, and Medieval Europe and the Mediterranean Vol. 1, pp. 286–370.

17th INTERNATIONAL CONGRESS of the Geological Society of Greece

BULLETIN OF THE GEOLOGICAL SOCIETY OF GREECE, SP. PUBL.

EXTENDED ABSTRACT 082

Ground motion monitoring with low-cost multi-GNSS installations in Achaia, western Greece

Ganas A.[1], Anastasiou D.[2], Mavropoulos, G.[3], Karamitros, I.[1], Nikolakopoulos, K.[4], Tsironi, V.[1]
(1) National Observatory of Athens, Institute of Geodynamics, Athens, Greece aganas@noa.gr
(2) Dionysos Satellite Observatory, National Technical University of Athens, Heroon Politecniou 9, 157 80, Zografos
(3) ES Systems-Pressure & Flow Sensor Solutions, 62 Ioannou Metaxa Str, Koropi - Athens 19441, Greece
(4) University of Patras, Department of Geology, 26504 University Campus, Rio Patras, Greece

Abstract

In this contribution, we demonstrate the operational status of a new GNSS infrastructure in the western Gulf of Corinth (Greece) that is based on the collaboration of a multidisciplinary research team and on low-cost equipment. Our low-cost instrumentation includes a multi-GNSS dual-frequency chip (Ublox ZED F9P module) mounted on a Raspberry-Pi 4 compute module IO board together with an industry-standard MEMS accelerometer. It provides signal tracking for multi-GNSS systems (GPS, GLONASS, Galileo and BeiDou). The GNSS data are collected 24 hours 7 day 365 days per year, quality-checked and processed by use of the PRIDE-AR open-source software. The E, N, Up velocities for two sites (GEDP & KRHN) were estimated on the IGS20 reference frame. We tested our results against the velocities of neighbouring permanent GNSS stations with overall good agreement.

Introduction

There is a continuous need for integrating multi-parameter instrumental observations and measurements with Satellite Earth observation data towards continuous monitoring of the environment and infrastructures. This task attains more importance within the tectonic and seismically active area of the Greek "Supersite" (Fig. 1; Achaia, western Corinth Gulf). The significant level of geohazards in this region have made necessary the implementation of new technological approaches that could offer reliable augmentation to permanent networks (both geodetic and seismological; Nikolakopoulos et al. 2023). In this contribution, we demonstrate the design, construction and installation of a new GNSS infrastructure that is based on the collaboration of a multidisciplinary research team (funded by the PROION project) and on low-cost equipment.

The aim of the PROION project (https://proion-hellas.eu) was the development of a platform for the continuous monitoring of high importance infrastructures such as public buildings and dams. The methodology combines instrumental and remote sensing measurements along with fuzzy logic networks methods and machine learning algorithms (Nikolakopoulos et al. 2023). Specifically, measurements obtained by three-axis accelerometers, low cost GNSS receivers and Persistent Scatterer Interferometry (PS-InSAR) are fused and validated with high-precision 3D reference data derived from TLS surveys and UAV campaigns. The processing is based on soft computing algorithms while very accurate deformation maps are utilized for making decisions about the current and the future state of each infrastructure.

Our low-cost instrumentation includes a multi-GNSS dual-frequency chip (Ublox ZED F9P module) mounted on a Raspberry-Pi 4 compute module IO board together with an industry-standard MEMS accelerometer. It provides signal tracking for most global-coverage GNSS systems (GPS, GLONASS, Galileo and BeiDou). The GNSS data are collected 24/7/365, quality-checked and processed by use of open-source software. The combined-synergistic use of these new sensors is compatible with ground motion data provided by GNSS reference stations and accelerometers used by seismic agencies. Current work includes collection, reformatting, processing and archiving daily data from three test sites using 4G telemetry. The GNSS data support the on-going, pre-operational monitoring of three test sites (Fig. 1; Asteri dam, Department of Geology U. Patras, Krini landslide; Ganas et al. 2022) together with InSAR Copernicus data (Tsironi et al. 2022). For the first time, the displacement velocities of the NOA low-cost GNSS stations have been estimated to provide additional geodynamic information in an area with high rates of deformation. In this contribution we will present results for two sites GEDP (Patras; Fig. 1) and KRHN (Krini village; Fig. 1), respectively.

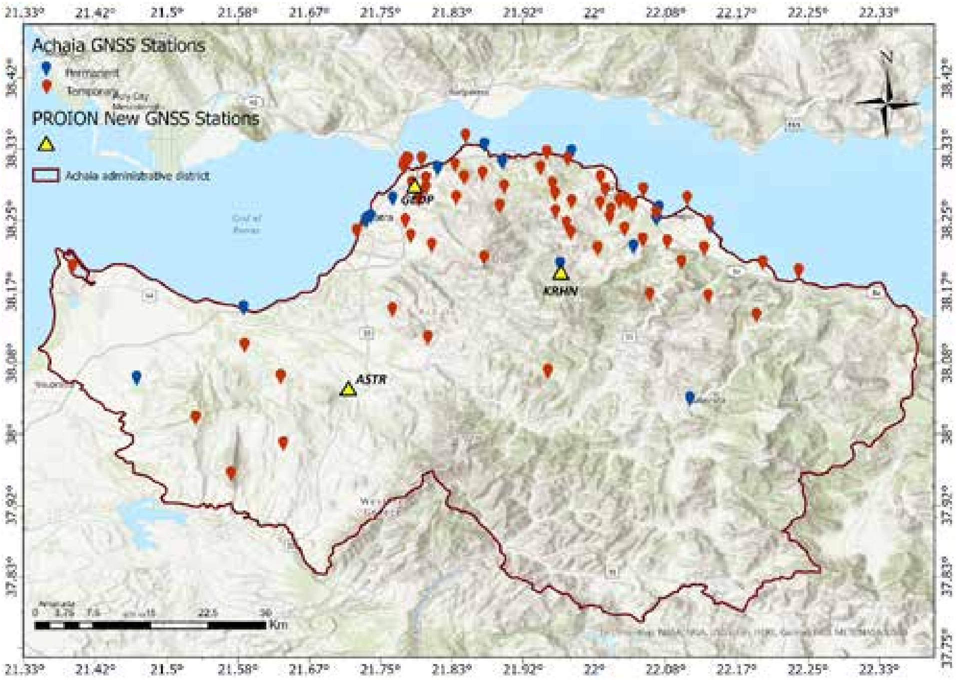

Figure 1. Relief map showing GNSS low-cost installations (yellow triangles; KRHN, GEDP, ASTR) in Achaia (part of the western Gulf of Corinth). Blue and red pins show other GNSS stations in the area.

Data and Methods

In actively deforming areas such as rift systems, it is essential to sample the deformation field thoroughly in both time and space to a) map the pattern of ground changes as well as the speed and direction of movement and b) constrain active fault source models. Surface displacements, tilts, and dilatation are easily measurable with modern geodetic techniques, such as the Global Navigation Satellite System (GNSS; Partheniou et al. 2019; Ganas et al. 2013, 2020; Briole et al. 2021).

In 2021 NOA established a local network of three (3) GNSS stations around the south coast of the Gulf of Corinth (Fig. 1; code names KRHN, GEDP and ASTR; Ganas et al. 2022). All stations were selected on horizon-free buildings, either on bedrock or on syn-rift sedimentary rocks, so that we make sure our data products record either tectonic or local motions. The benchmarks were drilled inside the roof tops and metallic bolts were placed (Fig. 2). GEDP and KRHN are new installations; KRHN occupied the same benchmark as the CRL station KRIN (https://nfo.crlab.eu/KRIN). Continuous measurements have been conducted on this network on a yearly basis since then by use of dual-frequency geodetic receivers (Ganas et al. 2024). With a combination of repeated GNSS measurements and continuous monitoring by 1-D InSAR (i.e., Tsironi et al. 2022), it is now possible to measure ground deformation over broad areas around the three GNSS sites and with satisfactory temporal and spatial resolution.

The data sampling interval was 1 s, and the data were collected on a 24 h basis. The RINEX files that were processed contain 8 observables of GPS satellites: C1C L1C D1C S1C C2W L2W D2W S2W. All station records were complete. Each station has been analyzed independently using the Precise Point Positioning (PPP) method which computes coordinates of each station separately. The low-cost data set was processed to obtain 24-h position solutions using the PRIDE-AR software (V3.0; Geng et al., 2019). Final products from the Wuhan IGS Analysis Center were employed for satellite orbits, clocks, attitude, and bias corrections. Daily files containing Earth Rotation Parameters (ERP) were also included in the processing. The latest ANTEX file published by IGS, including extensions for the station antenna, was also used. Zenith Total Delay (ZTD) was estimated using a stochastic walk model with a process noise of 0.0004 m/√s. The Vienna Mapping Function 3 (VMF3) was used as the troposphere delay model. Tidal corrections, including solid Earth tides, ocean tides, and pole tides, were applied with the FES2004 model as reference. Daily position files are converted into an annual series of positions, in which we obtain the displacements that have occurred since the beginning of our time series. The linear trend of the position time series was estimated using the Hector software (Bos et al. 2013). The N, E, Up position time series for station GEDP are shown in Fig. 3 (left panel) and for station KRHN in Fig. 3 (right panel), respectively.

Figure 2. Field photographs (2023) showing the GNSS low-cost installations a) top panel: at the Department of Geology University of Patras (code name GEDP). View to the west b) bottom panel: at the building in village Krini (code name KRHN). View to the east).

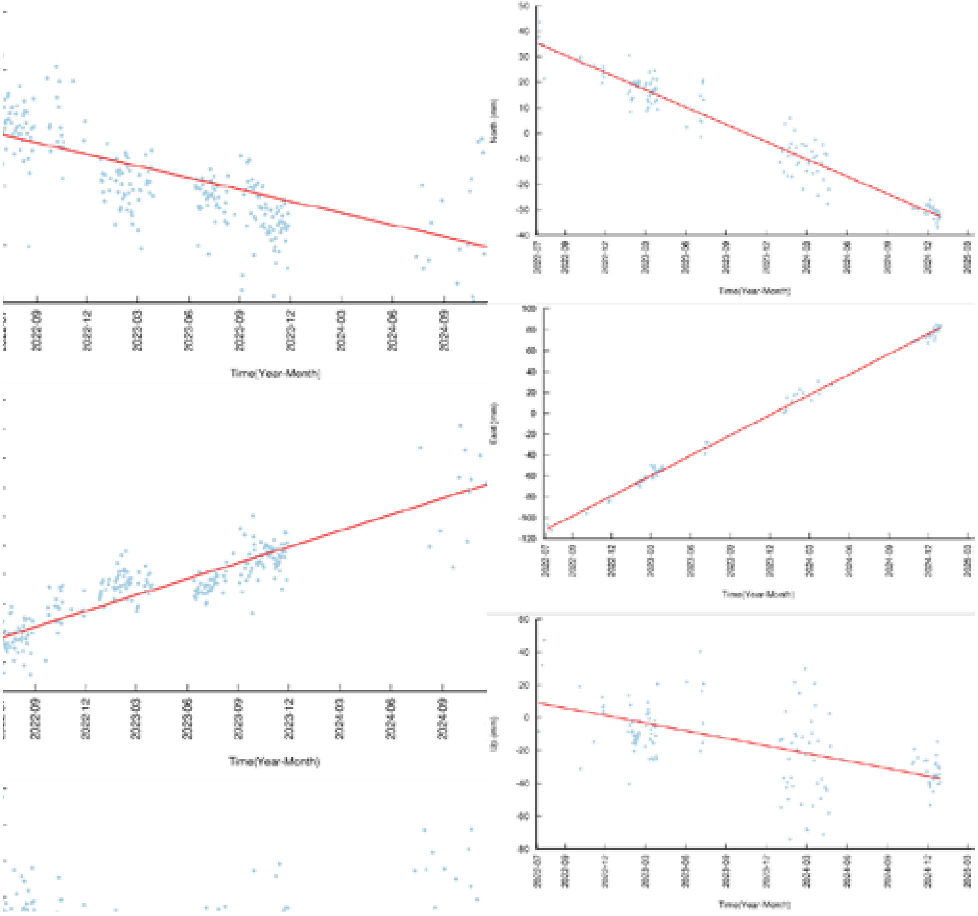

Figure 3. left) displacement vs time diagram of GNSS station GEDP (measurements 2022 – 2024), right) displacement vs time diagram of GNSS station KRHN (measurements 2022 – 2024). Three panels are shown from top to bottom (North, East, Up components). Missing data is due to telemetry gaps.

Results and Conclusions

The low-cost geodetic data were sampled at 1-s intervals, however, for data processing the RINEX files were resampled at 30-s. This is normal when daily coordinates are computed because the default PRIDE-AR configuration is to process 30-s RINEX files. The velocities for two sites (GEDP & KRHN; Fig. 3) were estimated on the IGS20 reference frame (Table 1). For comparison we provide the velocities of the permanent GNSS station PAT0 as reported by a) the Nevada geodetic laboratory (Blewitt et al. 2018; http://geodesy.unr.edu/NGLStationPages/stations/PAT0.sta) and b) by Briole et al (2021). PAT0 is located a few hundred metres to the SW of station GEDP, inside the U. Patras campus. The overall velocity trends between the two stations are in good agreement. We attribute the small differences in all three (3) velocity components to the short duration of the data for station GEDP (2 years) vs PAT0 (14 years) and to the different reference frames used (IGS20 for the low-cost data vs. ITRF14 for the permanent station data). The geology of the Patras University Campus (Palyvos et al. 2007) consists of Quaternary deposits, Plio-Pleistocene sedimentary rocks and unconsolidated soils. Characteristic lithologies include coastal sands, fluvial sands and gravels, Holocene deposits, weathering mantle of Plio-Pleistocene sediments, as well as alluvial and colluvial deposits.

A good agreement is also observed between the velocities of KRHN and KRIN (Table 1; see North and Up components). This station is located inside a slow-moving landslide on the eastern slope of mountain Panachaikon (Fig. 1), which is also monitored by InSAR (Tsironi et al. 2022). The Krini landslide is included in the landslide inventory of north Peloponnese (Koukis et al. 2009) and its formation/activation is attributed to a combination of lithology (Flysch), rainfall and proximity to the large active faults of the Gulf of Corinth. We note that station KRHN is co-located with a NOA meteorological station https://penteli.meteo.gr/stations/krini/ so that the GNSS displacement pattern may correlated with rainfall intensity and duration, especially during winter months. Such a correlation was already found for station KRIN (Tsironi et al. 2022).

Table 1. GNSS station velocities (East, North, Up) and their uncertainties. Values are in mm/yr. Station KRIN and PAT0[1] velocities are after Briole et al. (2021), PAT0 are after the Nevada Geodetic Laboratory (Blewitt et al. 2018).

Point	vEast	vE-unc	vNorth	vN-unc	vUp	vU-unc
KRHN	77.63	0.77	-27.17	0.58	-18.44	4.15
KRIN	111.60	1.30	-31.30	0.60	-19.70	1.30
GEDP	11.03	0.84	-4.03	0.74	-2.22	1.72
PAT0	8.14	0.21	-6.21	0.21	-0.46	0.72
PAT0[1]	8.10	0.30	-5.80	0.30	-0.30	0.60

Acknowledgements

This research has been co financed by the European Union and Greek national funds through the Operational Program Competitiveness, Entrepreneurship and Innovation, under the call RESEARCH – CREATE – INNOVATE (project code: T2EΔK-02396 *Multiparametric monitoring platform with micro-sensors of eNceladus hellenIc supersite*). We thank Vassiliki Charalampopoulou, Theodoros Athanassopoulos, Aggeliki Kyriou, Konstantinos Exarchos, George Bozionelos, Stratos Liadopoulos, Pierre Briole and Panagiotis Elias for their help with network setup and discussions. The low-cost GNSS rinex data are distributed open-access and are available at http://194.177.194.200/GPS/GEDP/ and http://194.177.194.200/GPS/KRHN/.

References

Blewitt, G., W.C. Hammond, C. Kreemer, 2018, Harnessing the GPS Data Explosion for Interdisciplinary Science, Eos, 99, https://doi.org/10.1029/2018EO104623

Bos, M.S., Fernandes, R.M.S., Williams, S.D.P., Bastos, L. 2013. Fast error analysis of continuous GNSS observations with missing data. J. Geodesy 2013, 87, 351–360.

Briole, P., A. Ganas, P. Elias, D. Dimitrov, 2021. The GPS velocity field of the Aegean. New observations, contribution of the earthquakes, crustal blocks model, Geophysical Journal International, Volume 226, Issue 1, Pages 468–492, https://doi.org/10.1093/gji/ggab089

Ganas, A., Marinou A, Anastasiou D., Paradissis D., Papazissi K., Tzavaras P., Drakatos G. 2013. GPS-derived estimates of crustal deformation in the central and north Ionian Sea, Greece: 3-yr results from NOANET continuous network data. Journal of Geodynamics, 67, 62– 71. http://dx.doi.org/10.1016/j.jog.2012.05.010

Ganas, A., Elias, P., Briole, P., Cannavo, F., Valkaniotis, S., Tsironi, V., Partheniou, E.I. 2020. Ground Deformation and Seismic Fault Model of the M6.4 Durres (Albania) Nov. 26, 2019 Earthquake, Based on GNSS/INSAR Observations. Geosciences, 10 (6), 210 https://doi.org/10.3390/geosciences10060210

Ganas, A., I. Karamitros, G. Mavropoulos, D. Anastasiou, T. Athanassopoulos, K. Nikolakopoulos, A. Kyriou, C. Kontopoulos, V. Charalampopoulou, V. Tsironi, 2022. A New Low-Cost GNSS and Strong Motion Instrument for Monitoring of Slopes and Critical Infrastructures Within the Greek “Supersite”. SafeThessaloniki 2022 – 9th International Conference on Civil Protection & New Technologies, 29 September-1 October, pp. 117-120, SafeThessaloniki 2022 Proceedings, ISSN 2654-1823

Ganas, A., Mavropoulos, G., Karamitros, I., Nikolakopoulos, K., Charalampopoulou, V., Anastasiou, D., Athanassopoulos, T., Kyriou, A., and Tsironi, V. 2024 A new low-cost GNSS instrument for monitoring of ground motions and critical infrastructures within the Greek “Supersite”, EGU General Assembly 2024, Vienna, Austria, 14–19 Apr 2024, EGU24-10188, https://doi.org/10.5194/egusphere-egu24-10188

Geng J, Chen X, Pan Y, Mao S, Li C, Zhou J, Zhang K, 2019. PRIDE PPP-AR: an open-source software for GPS PPP ambiguity resolution. GPS Solutions, 23(91):1-10. doi:10.1007/s10291-019-0888-1

Koukis, G., Sabatakakis, N., Ferentinou, M. et al. 2009. Landslide phenomena related to major fault tectonics: rift zone of Corinth Gulf, Greece. Bull Eng Geol Environ 68, 215–229. https://doi.org/10.1007/s10064-008-0184-8

Nikolakopoulos, K., V. Mpelogianni, P. Groumpos, A. Kyriou, A. Ganas, V. Charalampopoulou, and T. Athanasopoulos, 2023. Soft computing algorithms for infrastructure monitoring: preliminary results of PROION project. Proc. SPIE 12786, Ninth International Conference on Remote Sensing and Geoinformation of the Environment (RSCy2023), 127861S (21 September 2023); https://doi.org/10.1117/12.2680702

Palyvos, N., Pantosti, D., Stamatopoulos, L., & De Martini, P. M. 2007. Geomorphological reconnaissance of the Psathopyrgos and Rion-Patras Fault zones (Achaia, NW Peloponnesus). Bulletin of the Geological Society of Greece, 40(4), 1586–1598. https://doi.org/10.12681/bgsg.17063

Partheniou, E., A. Ganas and Sakkas V., 2019. Ground deformation from GNSS data following strong Ionian Sea earthquakes in 2014 and 2015: co-seismic offsets and station baseline changes. Bull. Geological Society of Greece, Special Publication 7, pp. 253-254.

Tsironi, V., Ganas, A., Karamitros, I., Efstathiou, E., Koukouvelas, I., Sokos, E. 2022. Kinematics of Active Landslides in Achaia (Peloponnese, Greece) through InSAR Time Series Analysis and Relation to Rainfall Patterns. Remote Sens., 14(4), 844. https://doi.org/10.3390/rs14040844

17th INTERNATIONAL CONGRESS of the Geological Society of Greece

BULLETIN OF THE GEOLOGICAL SOCIETY OF GREECE, SP. PUBL.

EXTENDED ABSTRACT 083

Geodetic monitoring of the 2024-2025 Santorini volcanic unrest using GNSS and InSAR data: preliminary results

Ganas A.[1], Briole P.[2], Tsironi, V.[1], Goutsos, G.[1], Madonis N.[1], Liadopoulos E.[1], Mintourakis, I.[1]
(1) National Observatory of Athens, Institute of Geodynamics, Athens, Greece aganas@noa.gr
(2) UMR 8538 CNRS - École Normale Supérieure - PSL, France

Abstract

Santorini is an active stratovolcano emplaced within a region of extensional faulting in South Cyclades, Greece. A two-month-long seismic crisis reaching Amorgos (NE of Santorini), together with GNSS measurements made before and during the crisis, provide insights into the relations between the volcano dynamics and its surroundings. The GNSS data show that Santorini inflated since the summer of 2024. We model this inflation with a magma source of ~ 8 × 10^6 m^3 located ~3.5 km under the north-central floor of the caldera, near the inflation centre of 2011-2012. The inflation phase ceased around 20 January 2025. Contemporaneously, the seismic activity, shifted to the north-east of Santorini near the islet Anydros. This phase lasted about ten days, before leading into a most intense phase that produced ground deformation measurable at large distances over the South Cyclades.

Introduction - Data and Methods

The Santorini volcanic Centre (Fig. 1; Thera, Thirasia, Kammeni etc.) is located within the Aegean micro-plate, which overrides the subducting Tethys lithosphere in a SSW direction. The subduction of Africa over the Cenozoic resulted in calc-alkaline volcanism which is presently distributed along the South Aegean Volcanic Arc, comprising volcanic islands of Quaternary age. The Santorini volcano has been activated during the historical era, producing important explosive eruptions (e.g., Parks et al. 2012). The seismicity of the broader area is related to the Quaternary NW-SE extensional regime, as well as to the volcanic processes (Bohnhoff et al., 2006; Dimitriadis et al., 2009; Briole et al. 2021). In 2011 - 2012, ground deformation was detected by use of GPS and Envisat satellite data confirmed that Santorini have risen as much as 14 cm between January 2011 and March 2012 (Papoutsis et al., 2013).

Since the summer of 2024 the Santorini volcanic Centre entered a new phase of unrest as GNSS data indicate the start of deformation onshore Thera, followed by an increase of the seismicity rates since January 2025. The seismic events were detected first inside the caldera, then spreading with intense activity towards the northeast until the islet Anydros, spanning an overall distance of 30 km, displaying a NE-SW orientation (Figure 1). The seismicity pattern indicates swarm characteristics with larger events not exceeding M_L = 5.3 according to the catalogue of the National Observatory of Athens (NOA, https://www.gein.noa.gr/services/cat.html). This intense phase generated significant activity in the Greek and international scientific community, which worked together to provide rapid scientific assessments of the phenomenon for the purposes of crisis management by the authorities. Figure 1 shows a map of the seismicity and the active faults (ticks on the downthrown block) from the NOAFAULTs database (Ganas, 2024).

In this extended abstract, we analyse the geodetic observations from eleven GNSS stations (Fig. 1): four located on Santorini, including two operating in 2011-2012 and used in previous works (e.g. Lagios et al., 2013), six located on the neighbouring islands, and one installed on 12 February on the islet of Anydros near the centre of the crisis. Figure 2 shows the time series of coordinates (East, North, Up) of GNSS station SANT calculated using the SCRS-PPP software. We also used InSAR time series analysis (ESA Copernicus satellite imagery) to monitor the ground deformation (Figure 3). A sequence of deformation phases appears in the time series of coordinates. There is initially a slow inflation starting during summer 2024, then a second phase that starts around January 20 and lasts until around February 3, followed by the most intense phase that ends on February 16. A fourth phase is underway at the time of writing this extended abstract. The second phase correlates in time with the seismicity shift to the north-east of Santorini. We model this inflation using the software WebObs (Beauducel et al. 2020; Briole et al. 2017) with a magma source of ~ 8 × 10^6 m^3 located ~3.5 km under the north-central floor of the caldera, near the inflation centre of 2011-2012. The inflation phase ceased around 20 January 2025.

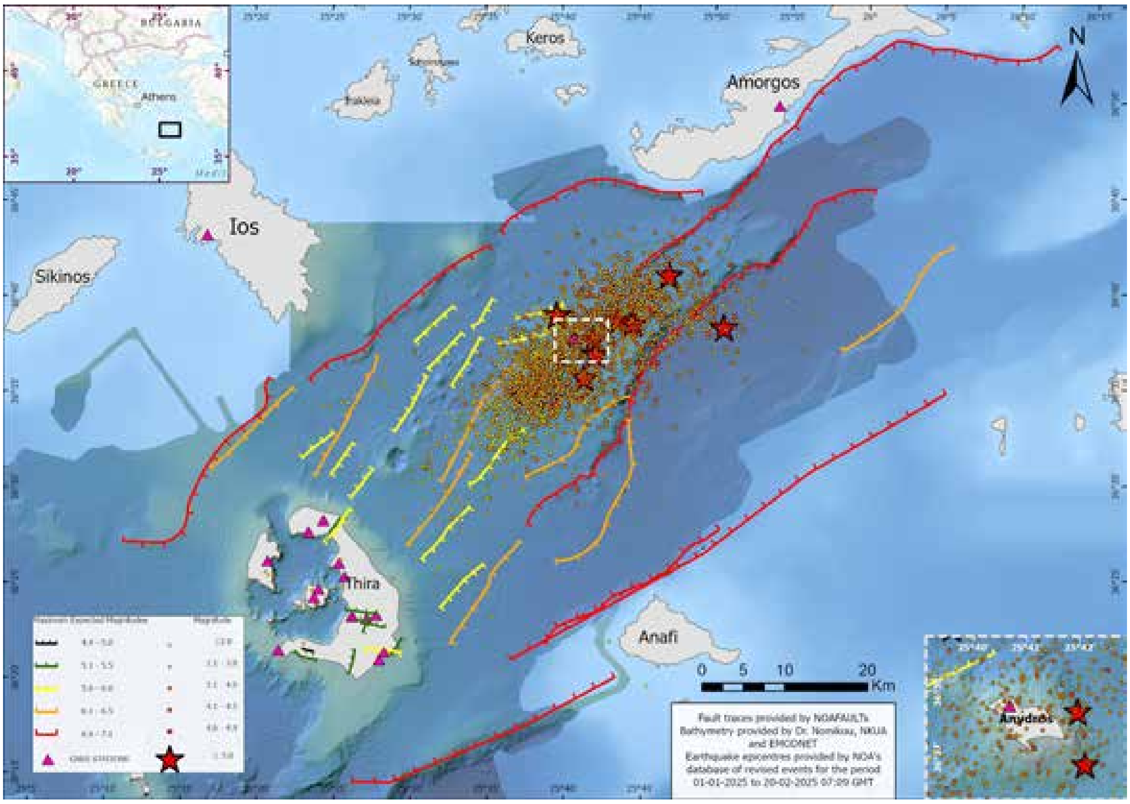

Figure 1. Location map showing GNSS stations (solid triangles) in South Cyclades and earthquake epicentres from the NOA seismicity catalog. Inset map shows location of study area within Greece.

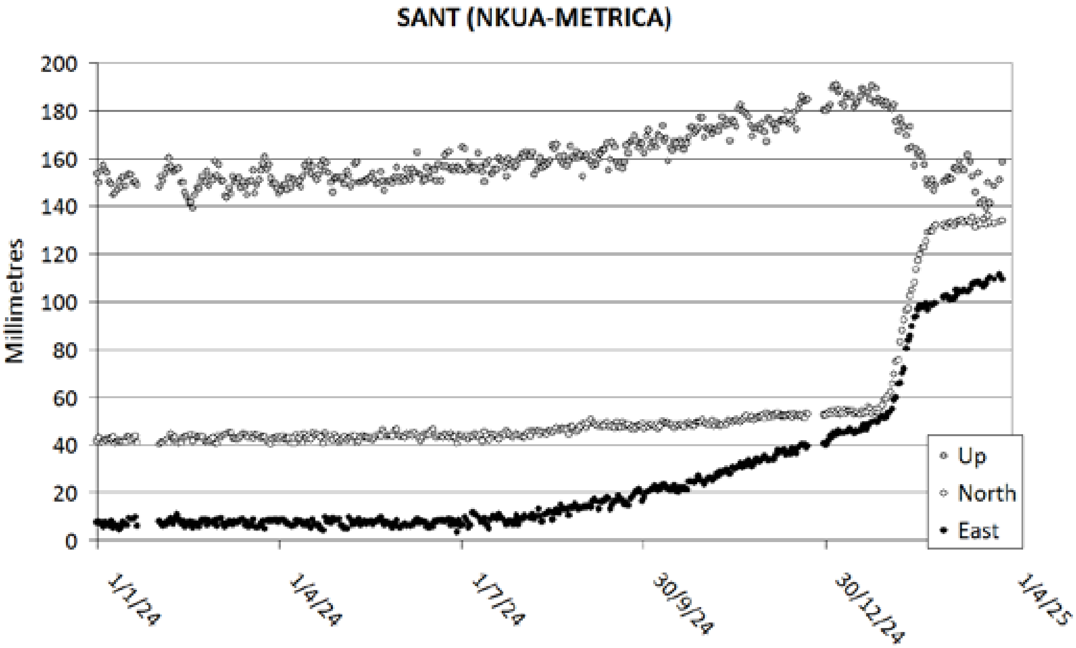

Figure 2. Graph showing time series of coordinates (East, North, Up) of GNSS station SANT (period 1/1/2024-25/3/2025).

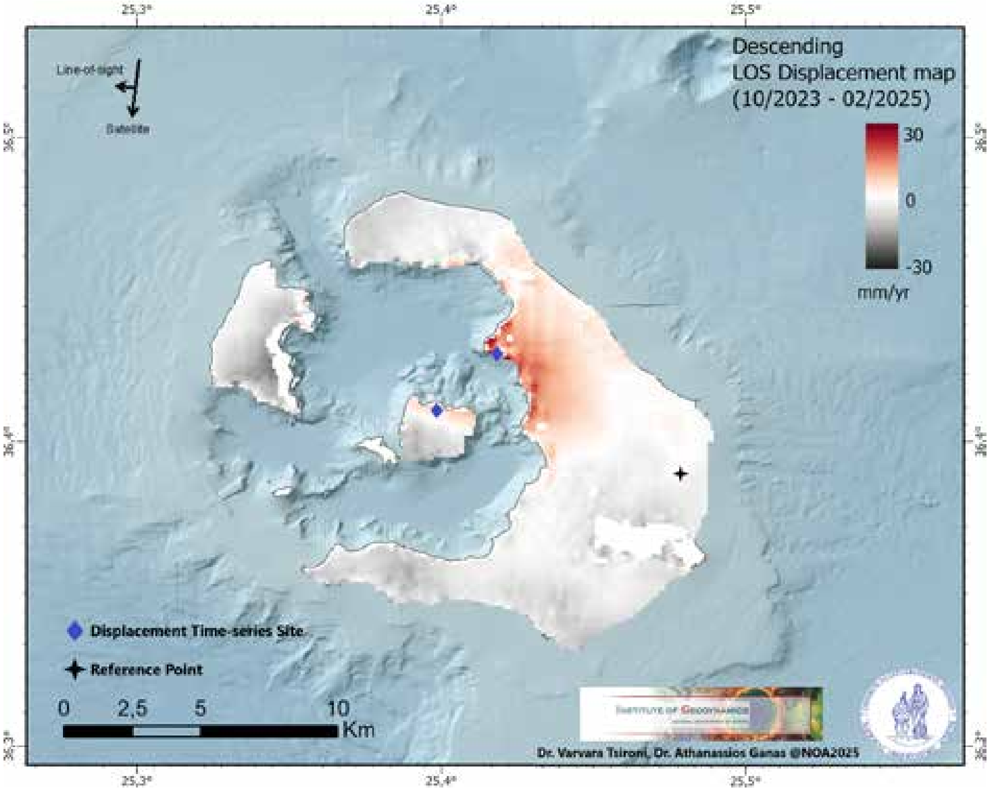

Figure 3. Map of Santorini showing InSAR displacement time series (descending orbit).

Acknowledgements

We acknowledge funding of this research by the project "*SAT4GAIA*". We thank Betty Charalampopoulou for administrative support. We are indebted to Francois Beauducel, Costas Synolakis, Paraskevi Nomikou, Dimitris Anastasiou and Vassilis Sakkas for discussions. The GNSS data used in this letter are made available by public and private GNSS networks of Greece under the coordination of the Greek Earthquake Planning & Protection Organisation (EPPO, https://oasp.gr/en). The following networks are gratefully acknowledged: HEPOS, NOANET, AUTH-ISMOSAV, NKUA, NTUA, HxGn-METRICA, URANUS & JGC. The geodetic equipment for the Anydros station was provided by the University of Patras (Panagiotis Elias). The GNSS campaigns and station installations were supported by the Hellenic Ministry of the Civil Protection, the Municipalities of Thera, Anafi, Amorgos, Iraklia and Sikinos. The faults mapped in Figure 1 are the "NOAfaults" available at http://doi.org/10.5281/zenodo.4304613

References

Briole, P., A. Ganas, P. Elias, D. Dimitrov, 2021. The GPS velocity field of the Aegean. New observations, contribution of the earthquakes, crustal blocks model, Geophysical Journal International, Volume 226, Issue 1, Pages 468–492, https://doi.org/10.1093/gji/ggab089

Beauducel, F., Lafon, D., Béguin, X., Saurel, J.M., Bosson, A., Mallarino, D., Boissier, P., Brunet, C., Lemarchand, A., Anténor-Habazac, C., Nercessian, A. & Fahmi, A.A., 2020. WebObs: The volcano observatories missing link between research and real-time monitoring, Frontiers in Earth Sciences, 8, https://doi.org/10.3389/feart.2020.00048

Bohnhoff, M., Rische, M., Meier, T., Becker, D., Stavrakakis, G. & Harjes, H.-P., 2006. Microseismic activity in the Hellenic Volcanic Arc, Greece, with emphasis on the seismotectonic setting of the Santorini–Amorgos zone, Tectonophysics, 423(1–4), 17–33, https://doi.org/10.1016/j.tecto.2006.03.024

Briole, P., 2017. Modelling of earthquake slip by inversion of GNSS and InSAR data assuming homogeneous elastic medium, Zenodo, http://doi.org/10.5281/zenodo.1098399

Briole, P., Ganas, A., Elias, P. & Dimitrov, D., 2021. The GPS velocity field of the Aegean. New observations, contribution of the earthquakes, crustal blocks model, Geophysical Journal International, 226(1), 468-492, https://doi.org/10.1093/gji/ggab089

Dimitriadis, I., Karagianni, E., Panagiotopoulos, D.G., Papazachos, C., Hatzidimitriou, P., Bohnhoff, M., Rische, M. & Meier, T., 2009. Seismicity and active tectonics at Coloumbo Reef (Aegean Sea, Greece): monitoring an active volcano at Santorini Volcanic Center using a temporary seismic network, Tectonophysics, 465, 136–149, https://doi.org/10.1016/j.tecto.2008.11.005

Ganas, A., 2024. NOAFAULTS KMZ layer Version 6.0 (version 6.0) [Data set]. Zenodo. https://doi.org/10.5281/zenodo.13168947

Lagios, E., Sakkas, V., Novali, F., Bellotti, F., Ferretti, A., Vlachou, K. & Dietrich, V., 2013. SqueeSAR™ and GPS ground deformation monitoring of Santorini Volcano (1992-2012): Tectonic implications, Tectonophysics, 594, 38-59, https://doi.org/10.1016/j.tecto.2013.03.012

Newman, A. V., S. Stiros, L. Feng, P. Psimoulis, F. Moschas, V. Saltogianni, Y. Jiang, C. Papazachos, D. Panagiotopoulos, E. Karagianni, and D. Vamvakaris (2012), Recent geodetic unrest at Santorini Caldera, Greece, Geophys. Res. Lett., 39, L06,309.

Papoutsis, I., Papanikolaou, M., Floyd, K., Ji, H., Kontoes, C., Paradissis, D. & Zacharis, V., 2013. Mapping inflation at Santorini volcano, Greece, using GPS and InSAR, Geophysical Research Letters, 40, 267-272, https://doi.org/10.1029/2012GL054137

Parks, M.M., Biggs, J., England, P., Mather, T.A., Nomikou, P., Palamartchouk, K., Papanikolaou, X., Paradissis, D., Parsons, B., Pyle, D.M., Raptakis, C. & Zacharis,V., 2012. Evolution of Santorini Volcano dominated by episodic and rapid fluxes of melt from depth, Nature Geosciences, 5, 749-754, https://doi.org/10.1038/ngeo1562

17th INTERNATIONAL CONGRESS
of the Geological Society of Greece

BULLETIN OF THE GEOLOGICAL SOCIETY OF GREECE, SP. PUBL.

EXTENDED ABSTRACT 084

Geodetic monitoring of the Methana volcano (central Greece) using campaign GNSS data: preliminary results

Ganas A.[1], Carnemolla F.[2], Karamitros, I.[1], Madonis N.[1], Georgakopoulos V.[1]
(1) National Observatory of Athens, Institute of Geodynamics, Athens, Greece aganas@noa.gr
(2) University of Catania, Department of Biological, Geological and Environmental Sciences, Catania, Italy

Abstract

This work presents the results from six (6) years of GNSS campaign observations on the Methana volcano, central Greece. The observations were collected by occupying five (5) benchmarks using dual frequency geodetic receivers during the period 2018 – 2024. The Methana data set was processed to obtain 24-h position solutions using the GIPSY-X software. For the first time, the displacement velocities of the NOA campaign GNSS stations have been estimated to provide additional geodynamic information in an active volcano area with two permanent stations.

Introduction

Methana peninsula is an active volcano, approximately 50 kilometres southwest of Athens (Central Greece, Fig. 1). The last onshore eruption took place in 230 BC in the Kameni Chora lava dome while the last offshore took place in 1700 AD north of Kameni Chora at a submarine volcano. Methana consists of mostly andesitic and dacitic rocks comprising lava flows and domes (Suesskoch et al. 1984). Volcanic domes are the most characteristic features of Methana, and are primarily andesitic to dacitic composition, are widely distributed across Methana and concentrated in the northern and central areas. They are marked by steep topographies and rugged terrains. Their widespread distribution points to multiple centers of volcanic activity over an extended geologic timeframe. A major increase in volcanic products has been determined at about 0.29–0.34 Ma (Pe-Piper and Piper, 2013), mostly on E–W faults, that was followed by minor andesite flows in the NW of the peninsula. In addition, the available magnetotelluric data (Tzanis et al. 2020) detected what appears to be a geothermal reservoir located underneath the central domes at a depth of approximately 1 km below sea level.

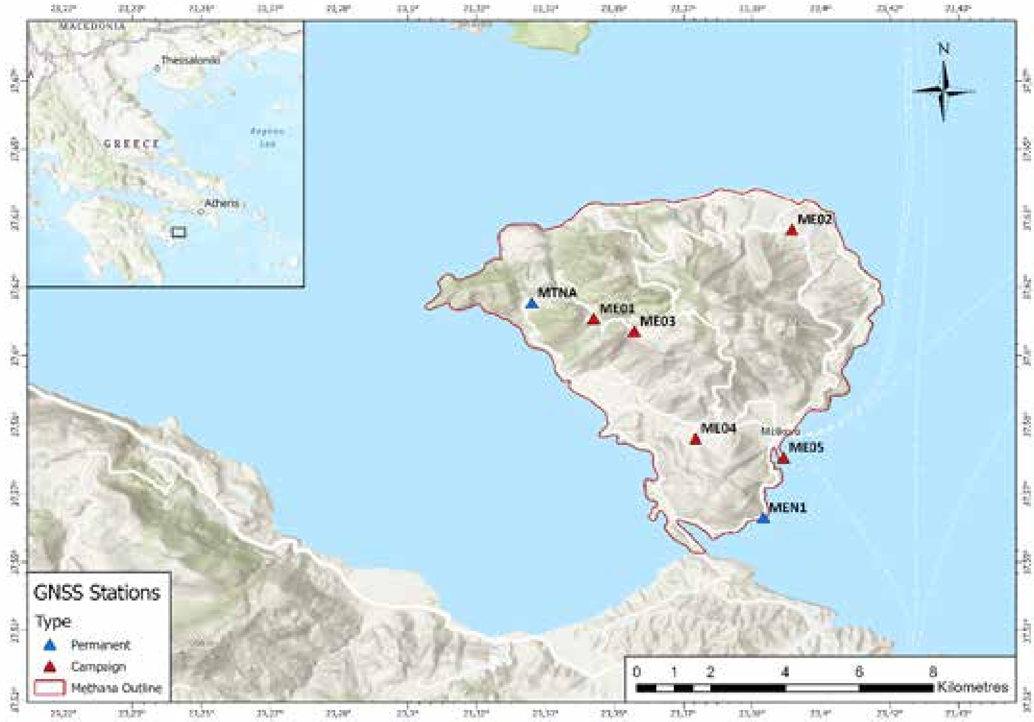

Figure 1. Relief map showing GNSS stations (solid triangles) in Methana peninsula. Inset map shows Methana location.

Data and Methods

In active volcanoes it is essential to sample the deformation field thoroughly in both time and space to adequately a) map the pattern of ground changes as well as the speed and direction of movement and b) constrain volcanic source models. Surface displacements, tilts, and dilatation are easily measurable with modern geodetic techniques, such as the Global Navigation Satellite System (GNSS; Ganas et al. 2016; Briole et al. 2021).

In 2018 NOA established a local network of five (5) geodetic benchmarks around Methana volcano (Table 1, Fig. 1). The local network was established on 20 and 21st October 2018 by Dr Athanassios Ganas and Mr. Ioannis Karamitros, MSc geologist. All points were selected on bedrock areas, either volcanic or limestone, so that we make sure our data products record either tectonic or volcanic motions. The benchmarks were drilled inside the bedrock and metallic bolts were placed (Fig. 2). Episodic measurements have been conducted on this network on a yearly basis since then by use of dual-frequency geodetic receivers. With a combination of repeated GNSS 3-D surveys and continuous monitoring by 1-D InSAR (i.e., Gatsios et al. 2020), it is now possible to measure ground deformation over broad areas in all sides of the volcano and with satisfactory temporal and spatial resolution.

Measurements have been conducted on the local network in 2018, 2019, 2020, 2023 and 2024 with dual-frequency GNSS receivers (LEICA GS08+). The data sampling interval was 10-s & 15 s, and the data were collected on an 8 h basis (2018 and 2019) and on 24-48 hrs (2020 onwards). The RINEX files contain 8 observables of GPS satellites: C1C L1C D1C S1C C2W L2W D2W S2W. All station records were complete. Each station has been analyzed independently using the Precise Point Positioning (PPP) method which computes coordinates of each station separately. The Methana data set was processed to obtain 24-h position solutions using the GIPSY-X software (version 2.2; Bertiger et al., 2020). The processing was performed using the final fiducial-free GPS orbits computed by the Jet Propulsion Laboratory. Ocean tidal loading was modeled using the FES2004 ocean tidal model (Lyard et al., 2006) and the wet zenith troposphere was modeled by the Global mapping Function (Boehm et al., 2006). Moreover, we used the antenna calibration file provided by the IGS and the second order ionospheric correction.

Table 1. List of the NOA local GNSS network locations around the Methana Volcano.

Point	Location	LONG	LAT	Occupation
ME01	Agia Sotira	23.345	37.609	2018, 2019, 2020, 2023, 2024a, 2024b
ME02	Agios Georgios	23.392	37.630	2018, 2019, 2020, 2023, 2024a
ME03	Lava dome Melissa	23.354	37.606	2018, 2019, 2020, 2023, 2024a
ME04	Dritsaiika	23.369	37.580	2018, 2019, 2020, 2023, 2024a, 2024b
ME05	Light House	23.390	37.575	2018, 2019, 2020, 2023, 2024b

Figure 2. Field photographs of GNSS measurements in Methana (2018 – 2019 campaigns).

Results and Conclusions

The Methana volcano geodetic data were sampled at 10-s & 15-s intervals, however, for data processing the RINEX files were resampled at 30-s. This is normal when daily coordinates are computed because the default GIPSY-X configuration is to process 30-s RINEX files. In addition, the station velocities were computed directly by GIPSY-X. The software has a set of scripts (*NetSplit.py*, *staFit.py, staSeries.py* etc.) able to compute time series, to detect outliers and to fit seasonal terms and finally to calculate the East, North & Vertical (Up) velocities based on the position time series. The velocities were estimated on the IGS20 reference frame (Table 2).

Geodetic monitoring using campaign observations could present significant drawbacks compared to continuous GNSS stations, mainly in the lack of data continuity, lower precision, and inability to monitor short-term phenomena (transients) or provide real-time data. Nevertheless, the recorded data quality of the Methana campaigns is high (Fig. 3; results from the Anubis software, open-source version). The GNSS velocity vectors of all volcano stations with available data are plotted in Fig. 4 (red are campaign, blue are permanent). There is notable agreement in the North component of the velocity between the neighbouring stations ME05 – MEN1 and MTNA – ME01 but there is a deviation on the East component which is under investigation.

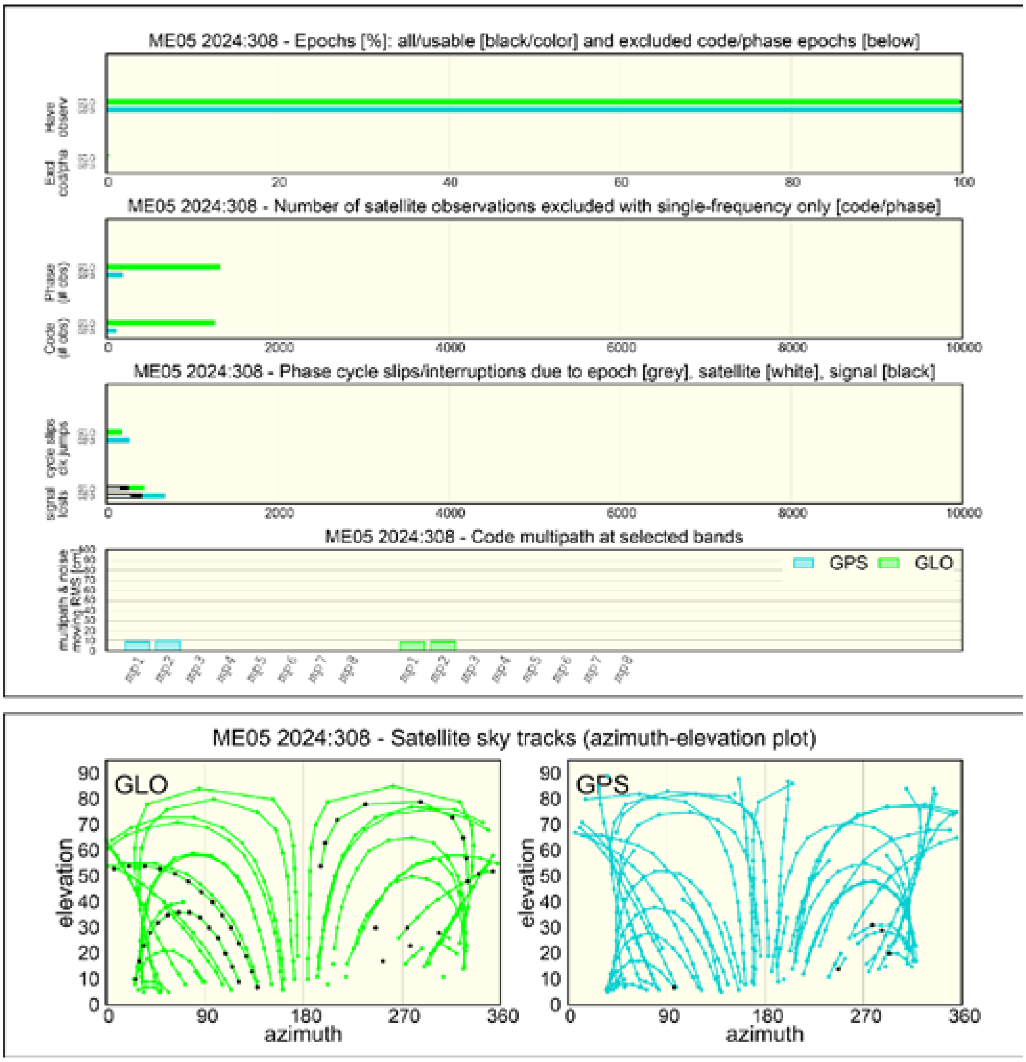

Figure 3. Data quality plot (GPS and GLONASS satellites) for station MEO5 (year 2024 DOY 308): upper panel) quality metrics for satellite observations, bottom panel) sky satellite tracks plot.

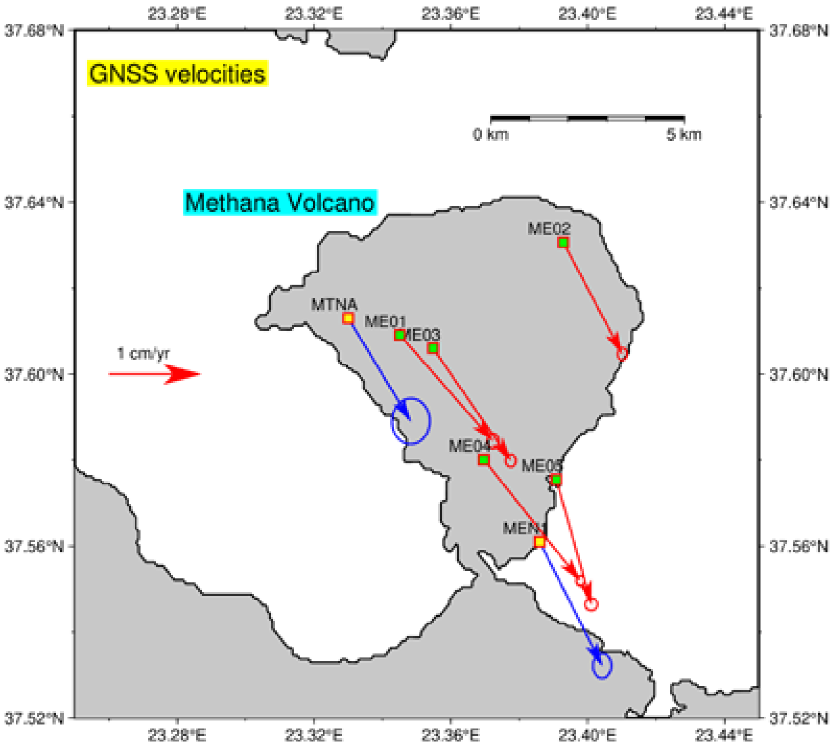

Figure 4. Map showing GNSS velocity vectors on the Methana volcano (campaign period 2018-2024). Blue vectors show permanent stations processed by NGL.

Table 2. GNSS station velocities (East, North, Up) and their uncertainties. The reference frame is IGS20 for the campaign stations and ITRF2014 for the permanent ones, respectively. Station MTHA velocities are provided by the EPOS Analysis Centre SGO-EPND and NTUA (Anastasiou and Papanikolaou pers. Commun.). NGL is the Nevada Geodetic Laboratory solution (Blewitt et al. 2018). Values are in mm/yr. Station MTHA, MENA and MEN1 are the same site with different code names. MTNA is an EPOS GNSS stations (EPOS, 2025).

Point	vEast	vE-unc	vNorth	vN-unc	vUp	vU-unc	Solution
ME01	10.11	0.26	-11.51	0.33	2.17	1.82	This study
ME02	6.41	0.21	-12.12	0.27	-1.23	1.02	This study
ME03	8.44	0.23	-12.20	0.28	0.73	1.05	This study
ME04	10.47	0.18	-13.13	0.23	-4.80	0.81	This study
ME05	3.79	0.28	-13.54	0.27	-2.39	1.43	This study
MTHA	7.12	0.14	-12.68	0.17	-0.55	0.18	SGO-EPND
MTHA	6.79	0.08	-13.08	0.26	-0.84	0.71	NTUA
MENA	7.20	0.30	-13.10	0.40	0.20	1.20	Briole et al. 2021
MEN1	6.78	0.41	-13.45	0.55	0.29	1.63	NGL
MTNA	6.79	0.84	-11.18	1.01	-1.66	3.57	NGL

Acknowledgements

We acknowledge support of this research by the project "*GEORISK – Developing Infrastructure and Provision of Services through Actions of Excellence to Reduce the Impact of Geodynamic Hazards*"

(MIS 5002541) which is implemented under the “Action for the Strategic Development of Research and Technology Organizations”, funded by the Operational Programme “Competitiveness, Entrepreneurship and Innovation” (NSRF 2014-2020) and co-financed by Greece and the European Union (European Regional Development Fund). We thank the four reviewers for constructive comments and our NOA colleagues Dr. G. Drakatos and Dr. Ch. Evangelidis for their administrative support. We are indebted to Ass. Prof. Dimitris Anastasiou and Dr V. Tsironi for discussions.

References

Bertiger, W., Bar-Sever, Dorsey, Y. A., Haines, B., Harvey, N., Hemberger, D., et al. 2020. GipsyX/RTGx, a new tool set for space geodetic operations and research. Advances in Space Research, 66(3), 469–489. https://doi.org/10.1016/j.asr.2020.04.015

Boehm, J., A. Niell, P. Tregoning, and H. Schuh, 2006. Global Mapping Function (GMF): A new empirical mapping function based on numerical weather model data, Geophys. Res. Lett., 33, L07304. https://doi.org/10.1029/2005GL025546.

Blewitt, G., Hammond, W. C., and Kreemer, C. 2018. Harnessing the GPS data explosion for interdisciplinary science, Eos, 99, https://doi.org/10.1029/2018EO104623.

Briole, P., A. Ganas, P. Elias, D. Dimitrov, 2021. The GPS velocity field of the Aegean. New observations, contribution of the earthquakes, crustal blocks model, Geophysical Journal International, 226, 1, 468–492, https://doi.org/10.1093/gji/ggab089

EPOS, 2025 (web site accessed 15 January 2025): https://gnss-metadata.eu/MOID/station.5e67e28bc074fb07db56feb2

Ganas, A., Chousianitis, K., Argyrakis, P., Tsimi, C., Papanikolaou, M., Papathanassiou, G., & Exarchos, K. 2016. Monitoring of surface displacements in the Kalochori area (Thessaloniki, Greece) using a local GNSS network. Bulletin of the Geological Society of Greece, 50(3), 1553-1562. http://dx.doi.org/10.12681/bgsg.11869

Gatsios, T., Cigna, F., Tapete, D., Sakkas, V., Pavlou, K., & Parcharidis, I. 2020. Copernicus Sentinel-1 MT-InSAR, GNSS and Seismic Monitoring of Deformation Patterns and Trends at the Methana Volcano, Greece. Applied Sciences, 10(18), 6445. https://doi.org/10.3390/app10186445

Lyard, F., Lefevre, F., Letellier, T. et al. 2006. Modelling the global ocean tides: modern insights from FES2004. Ocean Dynamics 56, 394–415. https://doi.org/10.1007/s10236-006-0086-x

Pe-Piper, G., Piper, D.J.W., 2013. The effect of changing regional tectonics on an arc volcano: Methana, Greece. J Volc. Geotherm. Research, 260, 146–163. https://doi.org/10.1016/j.jvolgeores.2013.05.011 .

Suesskoch, H., Bannert, D., Kalkreuth, W., Walliner, P., Strauss, M., Fytikas, M., Mazzuoli, R., 1984. Methana sheet, 1:50000 Geological Map of Greece. IGME, Athens.

Tzanis, A., A. Efstathiou, S. Chailas, E. Lagios, M. Stamatakis, 2020. The Methana Volcano – Geothermal Resource, Greece, and its relationship to regional tectonics. J Volc. Geotherm. Research, 404, 107035, https://doi.org/10.1016/j.jvolgeores.2020.107035

Integrated monitoring of the Milos geothermal site (Cyclades, Greece) using InSAR, GNSS and local seismic network data

Ganas A.[1], Kapetanidis, V.[2], Tsironi, V.[1], Karakonstantis, A.[2], Karamitros, I.[1]
(1) National Observatory of Athens, Institute of Geodynamics, Athens, Greece aganas@noa.gr
(2) National and Kapodistrian University of Athens, Department of Geology and Geoenvironment, Athens, Greece

Abstract

In this short paper, we update on the findings of a joint geodetic and seismological investigation of Milos (western Cyclades islands, Greece) since 2022 when we published out first short report in BGSG. The integrated monitoring includes the use of geodetic data (InSAR and GNSS) and the continuous recordings of a 24/7/365 local seismic network established by NOA in 2021 and upgraded in 2023. Our objective was to investigate the ground deformation and seismicity patterns and detect activity along fault zones of the island. We present evidence for on-going activity at 5-9 km depths along a NW-SE fault crossing Milos.

Introduction

The South Aegean Volcanic Arc (Kassaras et al. 2020), and in particular the Milos Island in western Cyclades offers a high potential for deep geothermal energy due to the well-known geothermal anomaly (Fytikas, 1977). Milos is a dormant stratovolcano with the most recent volcanic activity recorded about 380 ka-90 ka ago (Fytikas et al., 1986). The oldest K-Ar date on the lowest volcanic outcrops in the SW coast of Milos, gave an age of 3.5 Ma. Basement rocks occur in the SW, S and SE parts of the island. The seismicity around Milos is both shallow (4-15 km; Ganas et al. 2022) and intermediate depth (70-90 km), however, until 2021no clear patterns had emerged due to the lack of sufficient seismic stations. Several swarms have been reported in the literature, linking seismicity and ascent of magmatic fluids but without strong evidence (Sachpazi and Hirn, 1991; Baltatzis et al., 2001).

Figure 1. Relief map showing seismic stations (blue marks) and GNSS stations (red marks) in Milos Island. Inset map shows location of Milos in the south Aegean Sea.

Based on detailed chemical and isotopic analyses Wu et al. (2011) identified three types of hydrothermal vent fluids at Milos: cave vents, submarine brine vents and seawater-like vents. Using this distinction of measured samples, they are suggesting a conceptual geological model that consists of a shallow reservoir (<248°C) which is separated from a deep reservoir (>313°C) where subcritical phase separation happens. This work presents the monitoring strategy and the preliminary results. We installed a network of campaign & continuous GNSS (see Fig. 1) and INSAR Copernicus data are available in continuous processing (yearly rounds). Our aim is to monitor local surface displacements before and finally during the production states of the geothermal plants. GNSS and INSAR are two spatial geodetic methods with millimeter accuracy. GNSS provides information about the absolute 3D displacement at some point location while InSAR gives high spatial information (100-m pixel size) of relative displacement.

Data and Methods

During May 2021 and May 2023 NOA installed a local seismic network of seven (7) stations in the SE and East Milos (Fig. 1; blue dots). The sensors are GEOBIT C100 and were placed inside shallow (2-m) boreholes. Data telemetry is real-time (at 100 sps) using a commercial GSM network. The seismic network of Milos had a fair response to the main demands such as the increase in detectability of the local microearthquakes, as well as the characterization of seismic properties of the area such as the origin of the recorded noise (natural, anthropogenic). The earthquake magnitudes range from 0.4 to 3.4 on the local magnitude (M_L) scale. The recorded activity is mainly concentrated inside the Gulf of Adamas and in Southern Milos, along the NW-SE striking fault (Ganas et al. 2022), which might be associated with the March 1992 earthquake sequence (Delibasis and Drakopoulos, 1993; Papanikolaou et al. 1993).
In 2021 NOA established a local network of three (3) geodetic benchmarks at SE Milos (Fig. 1). The local network was established on 25th September 2021 by Dr Athanassios Ganas and Mr. Ioannis Karamitros, MSc geologist. All sites were selected in bedrock areas, to ensure that our receivers record either tectonic or volcanic motions. The benchmarks were drilled inside the bedrock and metallic bolts were placed. Episodic measurements have been conducted on this network on a yearly basis since then by use of dual-frequency geodetic receivers. In May 2023 NOA installed a low-cost GNSS station in western Milos (Fig. 1; code MILN) following the procedures established by the project PROION (Ganas et al. 2024). This station started recording 1-s GNSS observations on 12 November 2024. With a combination of repeated GNSS 3-D surveys and continuous monitoring by 1-D InSAR (i.e., Tsironi et al. 2024), it will be possible to measure ground deformation over broad areas in all sides of the geothermal site of Milos, and with satisfactory temporal and spatial resolution.
In terms of SAR geodetic data (1-D displacement time series) we used archived SAR Copernicus imagery (C-band) (Fig. 2). For the InSAR time series analysis we applied the SBAS algorithm that is part of LiCSBAS, an open-source package (Morishita et al., 2020). The available interferograms from the LiCSAR platform include 828 (ascending orbit) and 771 (descending orbit, respectively. During the phase unwrapping, decorrelated areas in the interferograms are masked where the phase noise coherence is < 0.2. Wrapped and unwrapped interferograms were geocoded with a pixel spacing of 0.001 degree (~100 m) and converted to the GeoTIFF format. The accuracy of this technique is about 2-3 mm/yr (Morishita et al. 2020; Tsironi et al. 2024).

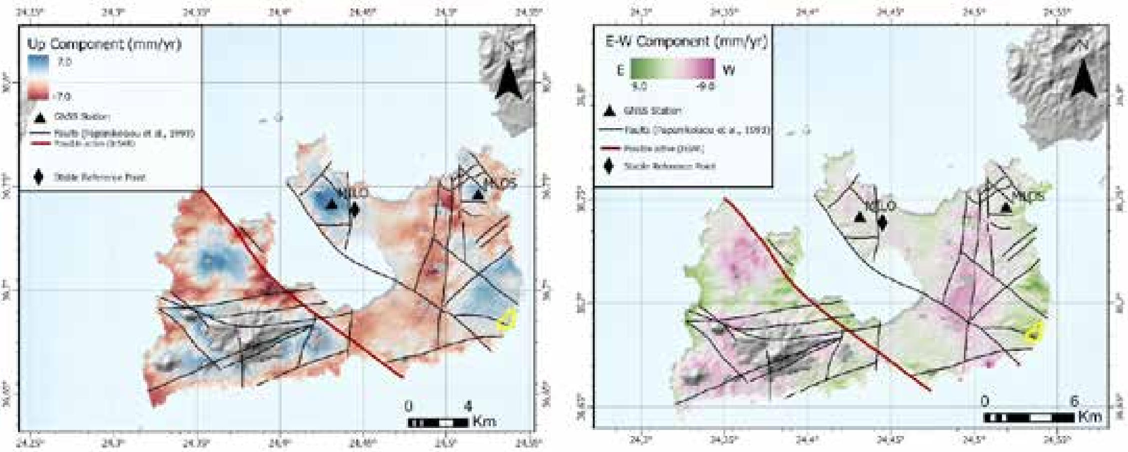

Figure 2. left panel) Up-Down ground motion map in units mm/yr, right panel) East-West velocity map based on InSAR data. Black lines indicate faults after Papanikolaou et al. (1993). The red line is an active fault based on InSAR. Diamond symbol indicates the reference point used in InSAR processing. MILO & MLOS are GNSS stations on the island. Grey areas indicate no data.

The InSAR data processing (period 2016-2024) resulted in the production of Up-Down and E-W velocity maps (Fig. 2; left is vertical and right is E-W motion) which indicates that there is divergent ground motion (opening) across the NW-SE fault onshore Milos (see red line in Fig. 2). The velocity difference across the fault reaches 1 cm/yr, that is well above the error. Moreover, the InSAR data provide evidence that this fault is active, and its surface trace can match an east-dipping fault plane where microseismicity is present (Fig. 3). A second area of interest is the mapped subsidence along the Zafeiria depression in east Milos (reaching 7 mm/yr.; Fig. 2 left) which abuts a N-S normal fault (west-dipping; Papanikolaou et al. 1993). The newly-installed GNSS station MILN will provide additional constraints to the InSAR results when its secular velocity is estimated with confidence (Fig. 3; after a period of 3-4 years; Briole et al. 2021). In western Milos there is no other geodetic point of reference while due to the rugged relief the atmospheric contribution to the InSAR signal may be considerable.

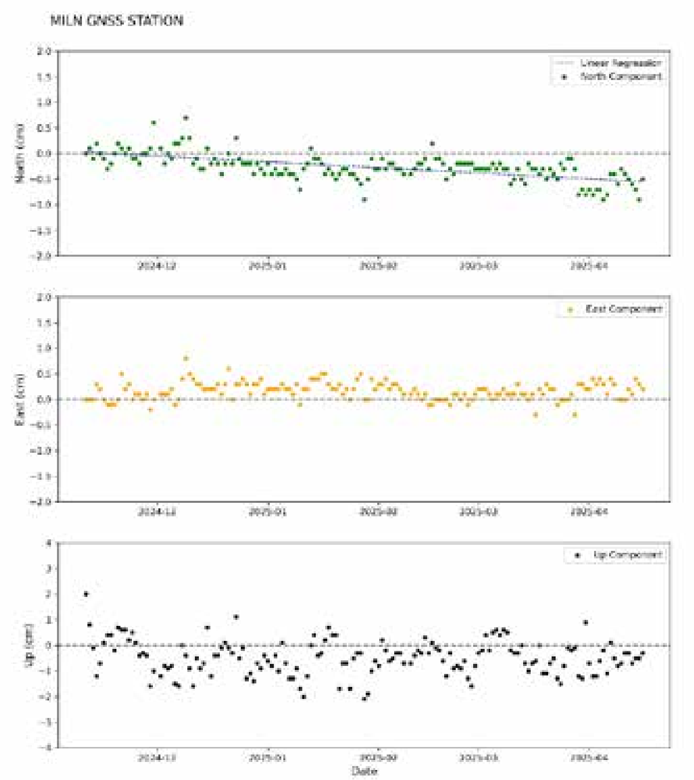

Figure 3. Graphs showing position time series of the low-cost GNSS station MILN (Agia Marina, western Milos). The daily positions were estimated with the on-line CSRS-PPP processing tool from the 30-s observations (code and phase) collected by the u-blox dual-frequency receiver and geodetic antenna. The panels show time series in North, East, Up components, respectively. Units in cm.

Results and Conclusions

During 2021-2024 the local seismic network recorded hundreds of microearthquakes in the broader Milos area, the majority of which occurred at shallow depths (< 10 km; Fig. 4). In order to improve the locations of hypocenters of the initial catalogue, which consists of 109 manually analyzed events and 589 additional detections made with the template matching technique (Chamberlain et al., 2018), we applied double-difference relocation with the HypoDD code (Waldhauser, 2001). Many small earthquakes are concentrated in the middle of the island (Gulf of Adamas) in tight spatial clusters, due to their strong waveform correlation. The clusters are aligned in a NW-SE orientation, following the strike of the main fault line that crosses Milos Island to the west of the epicenters (Papanikolaou et al. 1993). The overall length of the seismicity belt is 8 km and it is located on the eastern side of the Gulf of Adamas and in the airport area. Fig. 4 shows a seismicity map, where different colours / sizes represent different depths / magnitudes. The map indicates that the clustered seismicity beneath the Gulf of Adamas is located at focal depths of 6±1 km. Assuming a dip of 60° towards NE for the main fault that bounds the western shores of the Gulf (Fig. 2), its plane would roughly cross the hypocenters. It should be noted, however, that for a more precise determination of the absolute hypocentral depths, a local velocity model is required. This could become possible with the accumulation of more data from the local network in the future.

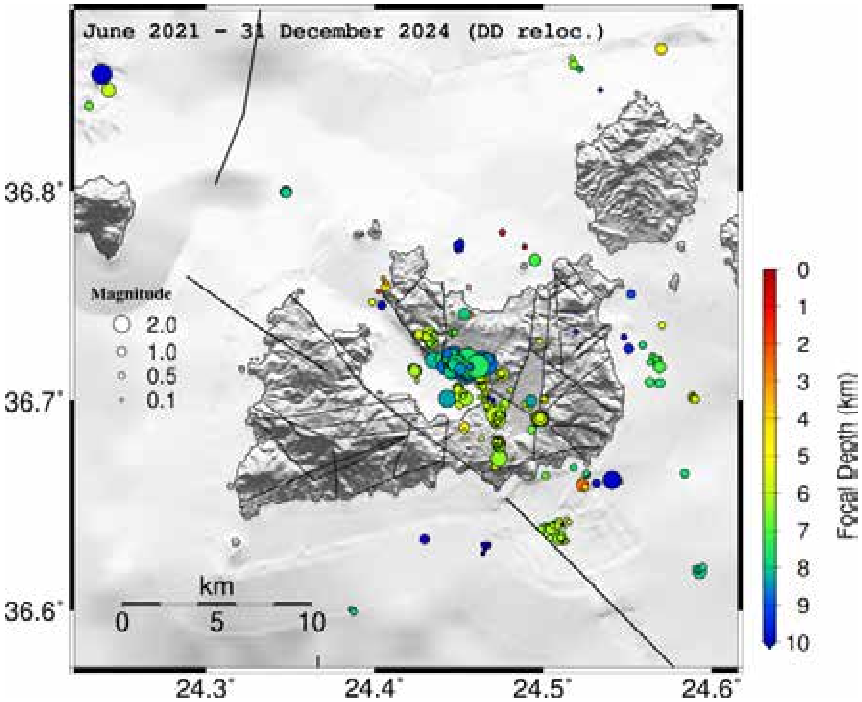

Figure 4. Seismicity map of Milos Island (period June 2021-2024) after relocation using the double-difference method (HypoDD).

Acknowledgements

We acknowledge support of this research by the project "*Seismological Monitoring of Milos Island"* funded by the Public Power Corporation Renewables SA (PPCR). The GNSS data from station MILN are freely available at http://194.177.194.200/GPS/MILN/ We thank Evangelos Spyridonos, Nikos Germenis, Konstantinos Exarchos, Nikolaos Madonis, Giorgos Goutsos and Stratos Liadopoulos for their help with network installations and data collection. We are indebted to our late colleague Ioannis Kassaras for discussions. We thank three reviewers for constructive comments. The views and opinions expressed in this paper are those of the contributors and do not necessarily reflect the views or positions of PPCR.

References

Briole, P., A. Ganas, P. Elias, D. Dimitrov, 2021. The GPS velocity field of the Aegean. New observations, contribution of the earthquakes, crustal blocks model, Geophysical Journal International, 226, 1, 468–492, https://doi.org/10.1093/gji/ggab089

Chamberlain, C.J., Hopp, C.J., Boese, C.M., Warren-Smith, E., Chambers, D., Chu, S.X., Michailos, K., Townend, J., 2018. EQcorrscan: Repeating and Near-Repeating Earthquake Detection and Analysis in Python. Seismol. Res. Lett. 89, 173–181. https://doi.org/10.1785/022017015

Delibasis, N., Drakopoulos, J., 1993: The Milos island earthquake of March 20, 1992 and its tectonic significance. Pageoph, Vol. 141, No 1, p. 43-58.

Fytikas, M. 1977. Geological and geothermal study of Milos island. Geol. & Geoph. Research, (1).

Fytikas, M., Innocenti, F., Kolios, N., Manetti, P., Mazzuoli, R., Poli, G., Rita, F., Villari, L., 1986. Volcanology and petrology of volcanic products from the island of Milos and neighbouring islets. J. Volcanol. Geotherm. Res., 28: 297-317.

Ganas A., A. Karakonstantis, V. Kapetanidis, V. Tsironi, I. Karamitros, E. Efstathiou, I. Karasante, and I. Kassaras, 2022. Ground deformation and microseismicity patterns onshore Milos, Cyclades, Greece. 16th International Congress of the Geological Society of Greece, 17-19 October 2022, Patras, Greece. Bulletin of the Geological Society of Greece, Sp. Publ. 10, pp. 663-664, ISBN: 978-960-98709-8-6.

Ganas, A., Mavropoulos, G., Karamitros, I., Nikolakopoulos, K., Charalampopoulou, V., Anastasiou, D., Athanassopoulos, T., Kyriou, A., and Tsironi, V. 2024. A new low-cost GNSS instrument for monitoring of ground motions and critical infrastructures within the Greek "Supersite", EGU General Assembly 2024, Vienna, Austria, 14–19 Apr 2024, EGU24-10188, https://doi.org/10.5194/egusphere-egu24-10188

Kassaras, I., Kapetanidis, V., Ganas, A., Tzanis, A., Kosma, C., Karakonstantis, A., Valkaniotis, S., Chailas, S., Kouskouna, V., Papadimitriou, P. 2020. The New Seismotectonic Atlas of Greece (v1.0) and Its Implementation. Geosciences, 10, 447 https://www.mdpi.com/2076-3263/10/11/447

Morishita, Y., Lazecky, M., Wright, T. J., Weiss, J. R., Elliott, J. R., & Hooper, A. 2020. LiCSBAS: An open-source InSAR time series analysis package integrated with the LiCSAR automated Sentinel-1 InSAR processor. Remote Sensing, 12(3), 424

Papanikolaou, D., Lekkas, E., Syskakis, D., Adamopoulou, E., 1993. Correlation of neotectonic structures with the geodynamic activity in Milos during the earthquakes of March 1992. Bull. Geol. Soc. Greece, Vol. XXVIII/3, p. 413-428.

Sachpazi, M., Hirn, A., 1991. Shear-wave anisotropy across the geothermal field of Milos, Aegean Volcanic arc. Geophys. J. Int., Vol. 107, p. 763-785.

Tsironi, V., Ganas, A., Valkaniotis, S., Kouskouna, V., Sokos, E., Koukouvelas, I., 2024. Active shortening and aseismic slip along the Cephalonia Plate Boundary (Paliki Peninsula, Greece): Evidence from InSAR and GNSS data. Tectonophysics, v. 884, 230400, https://doi.org/10.1016/j.tecto.2024.230400

Waldhauser, F., 2001. hypoDD-A Program to Compute Double-Difference Hypocenter Locations, U.S. Geol. Surv. Open File Rep. 01-113, 25 p.

Wu, S.F., You, C.F., Wang, B.S., Valsami-Jones, E., Baltatzis, E., 2011. Two-cells phase separation in shallow submarine hydrothermal system at Milos Island, Greece: Boron isotopic evidence. Geophys. Res. Lett. 38, p. 3–7.

Μπαλτατζής Ε., Δελήμπασης Ν., Valsami-Jones, E., Πυρλή Μ., & Baier, B. 2001. Relationship between hydrothermal fluids and microseismic activity on the south-east coast of Milos Island. Bulletin of the Geological Society of Greece, 34(4), 1441–1447. https://doi.org/10.12681/bgsg.17239 (In Greek, with English abstract).

17th INTERNATIONAL CONGRESS of the Geological Society of Greece

BULLETIN OF THE GEOLOGICAL SOCIETY OF GREECE, SP. PUBL.

EXTENDED ABSTRACT 086

NOAFAULTs: 12-yrs of studies and investigations towards building a geospatial database for active faults in Greece and surrounding areas

Ganas A.[1], Tsironi, V.[1], Goutsos, G.[1,2], Efstathiou E.[1], Tsimi, Chr.[1], Madonis, N.[1], and Georgakopoulos, V.[1],

(1) National Observatory of Athens, Institute of Geodynamics, Athens, Greece aganas@noa.gr
(2) National and Kapodistrian University of Athens, Department of Geology

Abstract

In this short paper, we update on the development of the NOAFAULTs geodatabase since 2013. Our objective was to create a nation-scale database of active faults in Greece and its adjacent regions, supporting the seismicity monitoring at the National Observatory of Athens (NOA) in tandem with an associated web-based query system. In the latest version V6.0 we added new data and fault traces, corrected for missing data, reviewed overlapping fault traces, added new thematic layers, and studied the kinematic and geometrical relations from the parametric data. NOAFAULTs can be used to investigate the ground deformation and seismicity patterns in Greece and surrounding areas and to detect new activity along fault zones. The Greek government, research institutions, and companies have widely used the active faults data from the previous versions of the database.

Introduction – Data and Methods

The NOAFAULTs geospatial database of active faults of Greece was first published in 2013 at BGSG (versions 1.0 & 1.1; Ganas et al. 2013; http://dx.doi.org/10.12681/bgsg.11079). Version 2.1 was published in 2018; Ganas et al. 2018); Version 3.0 was published in 2020 http://doi.org/10.5281/zenodo.4304613; Version 4.0 was published in 2022 https://zenodo.org/record/6326260; Version 5.0 in 2023 (Ganas et al. 2023; https://doi.org/10.5281/zenodo.8075517) followed by Version 6.0 in 2024 (https://doi.org/10.5281/zenodo.13168947).

The NOAFAULTs dataset was created towards compiling a digital database of fault traces, geometry and additional attributes (kinematics, slip rate, associated earthquakes etc.) following the Adria faults community effort in 2007 (Piccardi et al 2007). It has been constructed from published fault maps (that are contained in individual scientific papers) in peer-reviewed journals since 1972. The number of papers that have contributed with fault data in version 6.0 is 145. The authors have modified the fault trace in cases where the original map scale was too coarse, and the topography data (DEM) indicated a large distance between the digitized fault and the trace of the mountain front (in case of normal faults). No unpublished data are included in the database apart from the PhD theses of Caputo (1990), Ganas (1997), Valkaniotis (2009), Zervopoulou (2010) and the Kineta normal fault (fault code GR 3261) that was recently mapped by AG and it is part of a larger study under preparation. Selected fault data were also digitized from the neotectonic fault map series of Greece (Lekkas, 1995, 1996; Mountrakis et al. 1996). Data from neighbouring countries (Albania, North Macedonia, Turkey; e.g., Emre et al. 2018) were also incorporated as active fault systems in the Aegean crosscut national boundaries. The standard commercial software ARCGIS has been used to design and populate the database. The fault layer was produced at NOA by on-screen digitization of fault traces at the original map-scale (as drawn by the reference paper it was taken from) and is available through our web portal application https://arcg.is/04Haer supported by ESRI. The web-content of the database incorporates 27 thematic layers such historical seismicity, seismic and geodetic networks, isodepths of the subducted African slab, geodetic velocities (Briole et al. 2021) and many others. The capability to overlay geospatial data with near real-time earthquake epicentres, achieves an optimal monitoring of areas of high interest.

In version 6.0 (see Fig. 1), the number of 3088 active faults are included. 92% of the active faults are normal faults, 4% are strike-slip faults and only 3% represent the reverse faults. Also, reliable data on slip rates is available for 160 faults. Limited data on instrumental and historical seismicity are linked to 175 and 130 active faults, respectively. Data on fault lengths, slip per event etc. when available may be used to extract kinematic relations such as those pioneered by Wells and Coppersmith (1994).

In addition, a) surface-rupturing geological data and b) data on the proximity of epicentres of strong seismic events to the traces of active faults allows the identification of 173 rupturing faults (seismic faults; both exposed and blind) that are included in version 6.0. The NOAFAULTs database shows that nearly 52% of its active faults imply high seismic risk level in the broader area of Greece. These active faults can generate surface faulting or strong ground motions that can cause serious damage to buildings and infrastructures and therefore represent a significant hazard, particularly in the densely populated and industrialized areas of Greece. Since 2022 NOAFAULTs has contributed to the EFSM20 database (https://www.seismofaults.eu/efsm20; Basili et al. 2022).

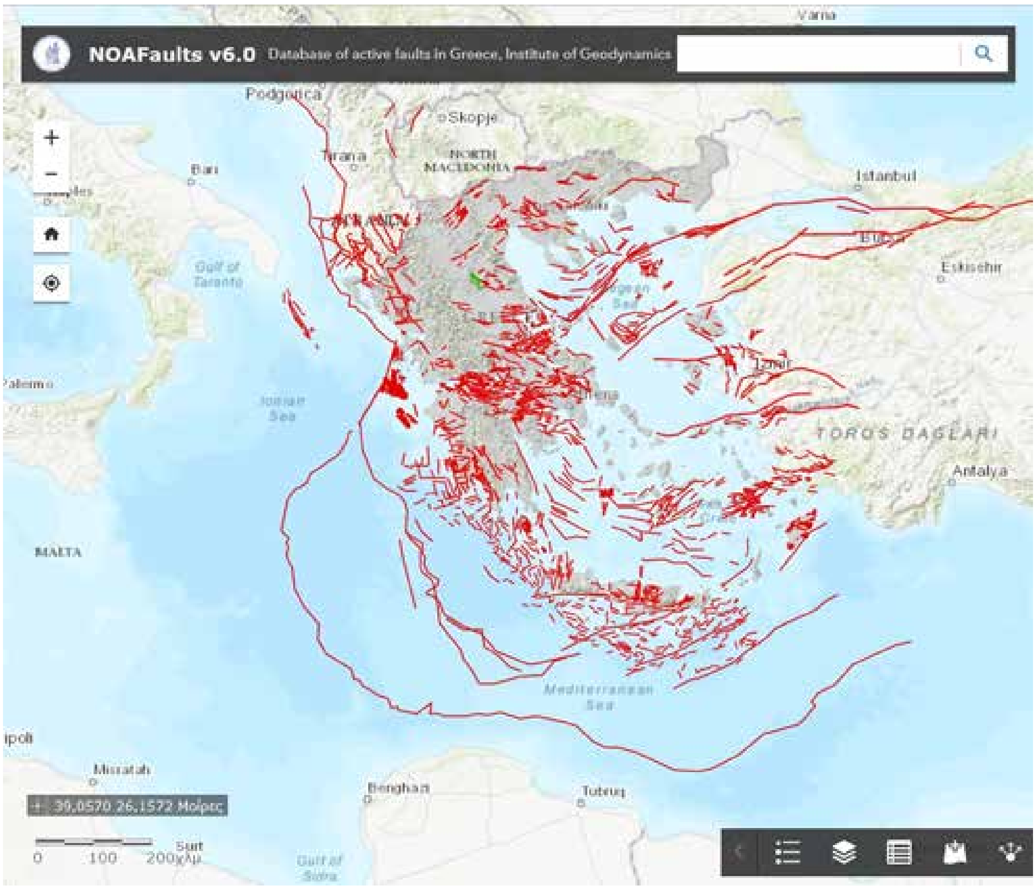

Figure 1. Relef map showing the NOAFAULTs V6.0 fault traces (red lines) in the broader Aegean area.

Results and Conclusions

Active faults serve as sources of strong and destructive earthquakes. Studies and investigations of active faults are necessary for anti-seismic protection and planning and for disaster prevention (Piccardi et al 2007; Emre et al. 2018; Maldonaldo et al. 2021). This study presents the updated nation-scale database of active faults in Greece and its adjacent regions, in tandem with an associated web-based query system. This database includes the active faults data included in 145 peer-reviewed scientific publications during the period 1972-2024. The data integration originates from regional-scale studies and surveys conducted at reference scales from 1:5.000 to 1:500.000. The information collected from these studies and surveys encompasses field mapping, geophysical profiles, measurements of offset horizons and landforms, C^{14} and cosmogenic isotope dating, as well as geometric and kinematic parameters of both exposed and blind faults, earthquake sequences and their characteristics. These data have been acquired and analyzed utilizing a uniform technical standard framework and reviewed by NOA experts. Our system hosts this database accessible through a Web Geographic Information System (GIS) application, enabling browsing, querying, and downloading functionalities via a web browser. Users can incorporate map layers and obtain fault data in OGC-compliant GIS software for further analysis through these services. The Greek government, research institutions, and companies have widely used the active faults data from the previous versions of the database.

Future Objectives

Our aim for the next version of the database (V7.0) is to review the existing data so that the fault traces are digitized in such a way that every user can correctly represent the kinematics of the faults, as well as to correct existing ambiguities. Another important step into the development of the NOAFAULTs is the application of a semi-automatic procedure towards filling out the attribute fields for each new digitized fault trace that will be considered for inclusion into the database.

Acknowledgements

We acknowledge support of this research by the project "*HELPOS - Hellenic Plate Observing System - MIS 5002697)* the GSRT-funded project KRIPIS-ASPIDA "*Infrastructure Upgrade for Seismic Protection of the Country and Strengthen Service Excellence through Action*", the National industry-academia project '*Platform of multidimensional monitoring with micro sensors of Enceladus of Hellenic Supersite-PROION*' with grant number: MIS-5070928 and the HORIZON Geo-Inquire project (EU- project number 101058518). We are indebted to Emmanouela Konstantakopoulou, Nikoletta Andritsou, George Evangelou, Elisavet Kollia, Michael Delagas, Athanassia Oikonomou, Fotini Kounavi, Panagiotis Savvaidis, Anna Fokaefs, and Vasiliki Kanavou for their contribution with earlier versions of the database. We thank many Greek and foreign colleagues from the active tectonics community for their feedback and continuous support.

References

Basili R., Danciu L., Beauval C., Sesetyan K., Vilanova S., Adamia S., Arroucau P., Atanackov J., Baize S., Canora C., Caputo R., Carafa M., Cushing M., Custódio S., Demircioglu Tumsa M., Duarte J., Ganas A., García-Mayordomo J., Gómez de la Peña L., Gràcia E., Jamšek Rupnik P., Jomard H., Kastelic V., Maesano F., Martín-Banda R., Martínez-Loriente S., Neres M., Perea H., Sket-Motnikar B., Tiberti M., Tsereteli N., Tsironi V., Vallone R., Vanneste K., Zupančič P. 2022. European Fault-Source Model 2020 (EFSM20): online data on fault geometry and activity parameters. Istituto Nazionale di Geofisica e Vulcanologia (INGV). https://doi.org/10.13127/efsm20

Briole, P., A. Ganas, P. Elias, D. Dimitrov, 2021. The GPS velocity field of the Aegean. New observations, contribution of the earthquakes, crustal blocks model, Geophysical Journal International, Volume 226, Issue 1, Pages 468–492, https://doi.org/10.1093/gji/ggab089

Caputo, R. (1990). Geological and structural study of the recent and active brittle deformation of the Neogene-Quaternary basins of Thessaly (Central Greece). Ph.D Thesis, Aristotle University of Thessaloniki

Emre, Ö., Duman, T. Y., Özalp, S., Şaroğlu, F., Olgun, Ş., Elmacı, H., and Çan, T. 2018. Active fault database of Turkey, B. Earthq. Eng., 16, 3229–3275, https://doi.org/10.1007/s10518-016-0041-2

Ganas, A., 1997. Fault Segmentation and Seismic Hazard Assessment in the Gulf of Evia Rift, central Greece. Unpublished PhD thesis, University of Reading, November 1997.

Ganas A., Oikonomou I.A. and Tsimi Ch., 2013. NOAfaults: a digital database for active faults in Greece. Bulletin of the Geological Society of Greece, vol. 47 (2), 518-530, http://dx.doi.org/10.12681/bgsg.11079

Ganas, A., Tsironi, V., Kollia, E., Delagas, M., Tsimi, Ch., Oikonomou, Ath. 2018. Recent upgrades of the NOA database of active faults in Greece (NOAFAULTs). 19th General Assembly of WEGENER, September 2018, Grenoble, sciencesconf.org:wegener2018:219400

Ganas, A., V. Tsironi, E. Efstathiou, E. Konstantakopoulou, N. Andritsou, V. Georgakopoulos, Ch. Tsimi, A. Fokaefs and N. Madonis, 2023. The National Observatory of Athens active faults of Greece database (NOAFAULTs) version 2023. In: Book of Abstracts of the 8th International Colloquium on Historical Earthquakes, Palaeo- Macroseismology and Seismotectonics, Bulletin of the Geological Society Special Publication No. 11, pp. 36-38, ISBN: 978-618-86841-1-9.

Ganas, A., 2024. NOAFAULTS KMZ layer Version 6.0 (version 6.0) [Data set]. Zenodo. https://doi.org/10.5281/zenodo.13168947

Lekkas et al., 1995. Neotectonic Map of Zakynthos.

Lekkas et al., 1996. Neotectonic map of Cephalonia.

Maldonado, V., Contreras, M., and Melnick, D. 2021. A comprehensive database of active and potentially-active continental faults in Chile at 1:25 000 scale, Figshare [data set], https://doi.org/10.6084/m9.figshare.13268993

Mountrakis, D., Kilias, A., Pavlides, S., Sotiriadis, L., Psilovikos, A., Astaras Th, V. E., ... & Skordilis, M. 1996. Neotectonic map of Greece, Langadhas sheet. Earthquake planning and protection organisation and European centre on prevention and forecasting of earthquakes. scale, 1:100,000).

Piccardi, L., L, Toth, E. Vittori, S. Aliaj, G. Cello, WD. Cunningham, G. Drakatos, A. Gosar, D. Herak, M. Herak, S. Sebela, E. Sulstarova, G. Windhoffer, B. Glavatovic, A. Kiratzi, A. Ganas, M. Omerbashich, S. Pavlides, L. Petro, G. Sijaric, B. Tomljenovic, & E. Tondi, 2007. A first attempt at compiling a map of active faults of the Adria region. Geophysical Research Abstracts, Vol. 9, 09228, Sref-ID: 1607-7962/gra/EGU2007-A-09228. © European Geosciences Union 2007.

Valkaniotis, S. 2009. Correlation between Neotectonic structures and Seismicity in the broader area of Gulf of Corinth (Central Greece). Unpublished PhD Thesis, Aristotle University

Wells, D.L. and Coppersmith, K. 1994. New empirical relationships among magnitude, rupture length, rupture width, rupture area, and surface displacement. Bull. Seismol. Soc. Am., 84, pp. 974-1002.

Zervopoulou, A. 2010. Neotectonic Faults of the Wide Area of Thessaloniki in association with foundation Soils (Doctoral dissertation, Ph. D. Thesis, University of Thessaloniki.

17th INTERNATIONAL CONGRESS
of the Geological Society of Greece

BULLETIN OF THE GEOLOGICAL SOCIETY OF GREECE, SP. PUBL.

EXTENDED ABSTRACT 087

Climatological analysis and Trend Assessment of Climate Indices in two forest areas of Greece experienced extreme fire events in 2023.

Gasteratou Amalia[1], Kostopoulou E.[1]
(1) University of the Aegean / Department of Geography, Mytilene, Greece, geoha22003@aegean.gr

Introduction / Background

Forests cover 39% of the EU's land area. In recent years, large forest fires have repeatedly affected Europe, in particular the Mediterranean countries (EEA, 2024). Particularly, the year 2023 has recorded the highest temperatures in the history of humanity. The year 2023 was a tipping point for the wildfires in Greece (first in EU countries with 42% of the total burnt area), which suffered the largest wildfire ever recorded in Europe. Following the destructive wildfires on the island of Rhodes in July, dozens of new wildfire ignitions in August across the country have been recorded. The most severe one was located in its northeast region, including the Dadia-Lefkimi-Soufli Forest National Park. European Forest Fire Information System (EFFIS) estimates that over 94,000 hectares of natural land were burnt in this single wildfire. Over 45,000 hectares of forests went into flames in Greece, and 65% of areas burnt were within the country's biodiversity reservoir of Natura 2000 (ESOTC, 2023). Fire danger is influenced by weather in the short term, and by climate when considering longer time intervals. In this work, the emphasis is on observed changes of weather and climate patterns on regional scale, as well as trend assessment in climate indices. The extremes considered include temperature extremes and precipitation, as well as compound events. Climate strongly influences fire activity, and the sequence of multiple weather and climate extremes, such as co-occurrence of hot and dry events, leads to more severe fires. Positive temperature, negative humidity and zonal wind anomalies correlate with large fires (Smith et al., 2020). According to the recent report of the United Nations Economic Commission for Europe's International Cooperative Program on Assessment and Monitoring of the Effects of Atmospheric Pollution on Forests (ICP Forests, 2023), it was identified that the outbreaks of forest mortality and their occurrence is partly explained by the simultaneous occurrence of extreme heat and drought events. Weather and climate play an important role in fire occurrence. Therefore, this study aims to provide local-scale understandings of the climatological characteristics of temperature and total precipitation in two Protected Areas in Greece, the National Park of Dadia ("Dadia") and the nature reserve Vounokalathos in Southern Rhodes ("Rhodes"). Therefore, the object of this study is the detailed climatological analysis of these two forest areas in Greece that are among the Protected Areas, which were most affected by the major fires of 2023. The analysis in this study is divided into three parts. The first is the climatological analysis based on key meteorological indicators of Climate Change. Using observed data in the regions of interest from 1981 to 2023, this study characterizes changes observed over the last 43 years for two key climatic parameters (e.g. mean, maximum and minimum air temperature at 2m and precipitation), at the annual and seasonal scales. Second, the analysis of meteorological observations in each site of interest was carried out through calculations of the deviations (commonly called anomalies) of average min/max/mean temperature and total precipitation from the average/total represented by the 30-year normals (1991-2020) according to the standards and requirements of the World Meteorological Organization (WMO). Third, assessment of the co-existence of positive temperature anomalies and negative precipitation anomalies (warm/dry) during the same fire season for the observed period (1981-2023) at each site were conducted. The detection of Dry-Warm each year's fire season is based on the pre-calculated temperature/precipitation anomalies from the 1991-2020 average. We showed that, in "Dadia" the fire season of 2023, with the greatest ecological disaster ever recorded in the region, is described as Dry-Warm, while for "Rhodes" Dry-Warm detected in 2020 and 2021 fire seasons. The results suggest a general trend towards higher temperatures. The statistically significant climatic indices that, according to scientific literature have been linked to both the risk of severe forest fires, stress and tree mortality in forest ecosystems (Carnicer et al. 2022; Guion, et al. 2022; Jones et al. 2022), are defined and examined in this study. Trends in extreme temperature indices were statistically more significant than trends in extreme precipitation indices in both sites of interest.

Objectives

The primary objective of this study is to analyze the trends and variability of extreme weather indices in the Dadia-Lefkimi-Soufli Forest National Park ("Dadia") and the nature reserve Vounokalathos in Southern Rhodes ("Rhodes") study sites of Greece. A secondary objective is to determine whether climate change has caused temporal changes in meteorological elements in the regions of interest. Detecting changes in the temporal patterns of temperature and precipitation is a prerequisite for developing effective adaptation options and strategies for the future. By examining patterns and changes in the local climate system, the study provides new insights into the climate-induced impacts on wildfire activity, as they put into perspective the underlying combinations of weather and climate conditions that are conducive to wildfires based on daily climate data for the period 1981–2023.

Methods

To understand and evaluate the meteorological dynamics, precipitation patterns, and other fundamental climatic elements shaping the environmental landscapes of the study sites, this study employs trend and statistical analysis methods. The methodology consists of three main parts: the selection of the geographical sites in which the indices would be assessed; the collection of daily meteorological data to calculate averages for each parameter at monthly, seasonal and annual timescales, as well as long term averages for the climatological reference period of 1991-2020 (climatological analysis). Additionally, 27 climate indices are calculated on an annual timescale for the observed period (1981-2023) at each site, and finally the performance (existence, magnitude, and statistical significance at 95% level of confidence of potential trends) of the indices is analyzed using Kendall's Tau correlation coefficient and Theil-Sen slope estimator methods (trend analysis). Figure 1 presents a time series graph that shows the annual values of all 27 indices for the observation period and linear regression tests of climate indices. Linear decadal trends are represented by solid red lines, while dashed lines (blue color) represent 10-year smoothed moving average. The study sites are located in two forest areas in Greece that were among the Protected Areas, which were most affected by the major fires of 2023, namely the National Park of Dadia ("Dadia") and the nature reserve Vounokalathos in Southern Rhodes ("Rhodes"). These two sites were selected due to their significant biodiversity that is threatened by the negative impacts associated with the increased, uncontrolled large-scale forest fires over the past decade (Spanos et al., 2021). The climatological analysis is based on long-term observational datasets of meteorological parameters, including temperature, precipitation, wind speed, wind direction and relative air humidity. Meteorological data used in this analysis were obtained from the National Aeronautics and Space Administration Prediction of Worldwide Energy Resources (NASA POWER) satellite-based weather system as a single-point dataset. The analysis also used fire point records from EFFIS. The extreme indices were calculated by using the 'ClimInd' package (Reig-Gracia et al., 2019). Climate indices integrate changes in the frequency, intensity and duration of key extreme climate indicators, as defined by the Expert Team on Climate Change Detection and Indices (ETCCDI). For the calculation of indices, daily values of mean temperature (TM), maximum temperature (TX), minimum temperature (TN), and daily precipitation (RR) are required. Specifically, a total of 27 climate extreme indices were estimated for each location, 15 temperature and 8 precipitation indices. Table 1 provides a description of climate indices. In the second part of the detailed climate analysis, we consider seasonal statistics to analyze "hot and dry" compound extremes focus on precipitation deficits and high temperatures over a common period, in this case fire seasons per year for the observed period (1981-2023) at each site. The condition for characterizing a fire season of a given year as "Dry-Warm" is when the deviation of total precipitation is <10% and the deviation of maximum temperature >0.5 °C. We calculated the anomalies of precipitation and maximum temperature in order to produce the Figure 2 with "Dry-Warm" anomalies located in quadrant I (top-right) and those with wet-cold in quadrant III (bottom-left). It should be noted that for easier interpretation, in the case of the fire season's total precipitation parameter the deviations are expressed as a percentage, with the mean set at 0% instead of 100% (Royé, 2020).

Table 1. Definitions and units of climate air temperature and precipitation indices used in this study.

Indices	Definitions	Units
TXx / TNx	Annual maximum value of daily TX / TN (the hottest days / warmest night of the year)	°C
TX10p / TN10p	Percentage of days when TX < 10th / TN < 10th percentile (cold days / nights) of the year	% days
TN90p	Percentage of days when TN > 90th percentile (warm nights) of the year	% days
XTG / BIO10	Annual max of TM / Mean Temperature of Warmest Quarter of the year	°C
DD17	Difference days above/below Tx17 (days TX > 17 °C)-(days TX < 17 °C)	days
TR	Annual count of Tropical Nights of the year (days TN > 20 °C)	days
WSDI	Annual count of days with at least 6 consecutive days when TX > 90th percentile	days
GD4	Growing degree days. Sum of degree days of TG over 4 °C	degree days
HD17	Heating degree days. Accumulated degree when TG is below 17 °C	degree days
HI	Heat Index. Combines TM and relative humidity to determine equivalent temperature	degree days
STX32	Sums TX32. Sum of degree days when TX ≥ 32 °C on the interval June-August.	degree days
TA_O / TM_S	Growing season (April to October / May to September) mean TM of the hear	degree days
WKI	Winkler index Sum of degree days > 10 °C of TG (April 1 - October 31)	degree days
BIO18	Precipitation of Warmest Quarter of the year	mm
GSR	Growing season (April to October) total precipitation	mm
RTI / PRCPTOT	Annual total precipitation / Annual total precipitation on wet days (rainfall ≥ 1 mm)	mm
R95tot	Annual rainfall that exceeded the 95th percentile in the period from 1981 to 2023	mm
D95p	Very wet days of the year. Days with precipitation > 95th percentile.	days
DR1mm / DR3mm	Wet days 1 / 3mm. Total number of wet days ≥ 1 / ≥ 3mm of the year	days
R10mm	Annual count of days with rainfall ≥ 10 mm	days
SDII	Simple Daily Intensity Index. Mean precipitation on wet days, with rainfall ≥ 1 mm for one year	mm/day

Results

The results of the climatological analysis indicated that 2023 is ranked as the warmest for both sites of interest, according to historical mean temperature data for the period 1981-2023. On the other hand, annual precipitation shows a mixed signal. According to the analysis of the precipitation anomalies (deviations from the long-term mean 1991-2020), it shows that 2008 marked the driest year for "Dadia" and 1990 for "Rhodes" in more than 40 years. Specifically, the calculated annual precipitation deviations for both sites for the period of 1981-2023 showed -44.9% of the mean annual precipitation (569.6 mm) for "Dadia" and -47.8% of the mean annual precipitation (626.2 mm) for "Rhodes" according to the 1991–2020 climatology. The deviations of 2023 average annual mean temperature from the 1991-2020 mean, were 1.9ºC for "Dadia" and 1.0ºC for "Rhodes" above reference mean. Analysis of the climate indices revealed a general warming trend in both sites, which is consistent with global warming (Carnicer et al., 2022). Table 2 presents the decadal trends for the two Greek sites during the period 1981–2023, with bold numbers indicating statistically significant slopes, $p < 0.05$). Increases in the TNx index (see Table 2 and associated plots) indicate a rising potential for Tropical Nights, consistent with global trends for this index (Dunn et al., 2020). Table 2 indicates that computed index related to Tropical Nights (TN > 20 °C) has positive decadal trends for both sites. Decadal increasing trend in Tropical Nights (TR) is more prominent in "Dadia", statistically significant decadal trend amounting to 10.3 days per decade respectively; TR has a statistically significant positive trend at "Rhodes", amounting to 5.6 days per decade (Table 2). The increasing intensity of Tropical Nights is clearly evident in "Dadia", where the value of tropical nights recorded in 1993 increased almost six times, from 10 in 1993 to 56 in 2023, the highest value observed during the 1981–2023 period (Figure 1). In contrast, "Rhodes" increased at a rate of about half of (5.6 tropical nights per decade) the northern "Dadia" (Figure 1). The TXX index observed at "Dadia" has been around 40°C for 12 out of the 43 years (1981-2023), reaching 43.3°C in 2007 (maximum) and 41.4°C in 2023. In "Rhodes", the maximum and minimum value of TXX is 36.6°C (2021) and 36.4°C (1989) respectively. The northern site (latitude > 40 ◦N) have statistically significant linear increasing decadal trends than the site in the southern Greece (latitude < 40 ◦N) in the annual maximum values of TX (TXx), as displayed in Figure 1. The TXx has statistically significant positive trend of 0.6◦C at "Dadia", when there was no statistically significant trend at "Rhodes" (Table 2). Dry conditions are also observed by precipitation indicators, where in 2023 the duration of precipitation during the germination period of the plant (GSR) decreased by 17% compared to 2022, while extreme precipitation indicators increased, for example the DR95tot, which increased by 26% in one year, and the D95p, which increased by 5 days in total since 2022. Trends in GSR of statistically significant increasing values are indicative, with a value of +24.2 per decade at "Dadia" (Table 2). For the warm season duration index (WSDI), both sites showed significantly increasing trends. Strong decreasing trends in cold days (TX10p) and cold nights (TN10p) indices were found at both sites. In general, a weak trend towards drier conditions is observed in "Rhodes", which is in good agreement with previous studies on climate trends in the Mediterranean region and Greece over the recent decades (Kostopoulou et al., 2005; Giannakopoulos et al.,2011; Kostopoulou et al., 2012; Lelieveld et al., 2014; Kostopoulou et al., 2023). A statistically significant upward trend was identified for the extreme climate index STX32 throughout the study period only at "Dadia". Additionally, the annual mean temperature index for the April-October growing season (TA_O) showed a positive trend of 0.3°C/decade in "Rhodes" and 0.4°C/decade in "Dadia". Likewise, the annual mean temperature index for the May-September season (TM_S) showed a significant positive trend of 0.5°C/decade in "Dadia", followed by "Rhodes" with a trend of 0.3°C/decade (Table 2). Figure 1 reveals that the magnitude of heat extremes increased significantly, while cold extremes decreased at a faster rate. Precipitation changes varied between the sites (Figure 1). Results showed a significant increase in temperature and a decrease in precipitation only in "Rhodes" site, indicating a warming and drying trend due to climate change. High rate of change in both regions was observed in the DD17, with a statistically significant positive trend of 12 (20.4) days per decade at "Dadia" ("Rhodes"), as displayed in Table 2.

Table 2. Decadal trends in annual climate indices for 2 Greek sites during the period 1981–2023 (numbers in bold indicate statistically significant slopes, $p < 0.05$).

Indices	«Dadia»	«Rhodes»	Indices	«Dadia»	«Rhodes»
TXx	**+0.6**	+0.3	STX32	**+33.5**	+0.5
TNx	**+0.5**	**+0.3**	TA_O	**+0.4**	**+0.3**
TX10p	**-1.5**	**-1.8**	TM_S	**+0.5**	**+0.3**
TN10p	**-1.6**	**-1.7**	WKI	**+92.1**	**+72.4**
TN90p	**+3.2**	**+3.8**	BIO18	+2.9	-13.7
XTG	**+ 0.5**	**+0.3**	GSR	**+24.2**	+7
BIO10	**+0.7**	**+0.5**	PRCPTOT	**+ 35.8**	-33
DD17	**+12**	**+20.4**	R95tot	+ 1.9	-2.9
TR	**+10.3**	**+5.6**	RTI	**+ 34.7**	-31.5
WSDI	**+8.7**	**+6.5**	D95p	**+ 1.4**	-1.4
GD4	**+175.5**	**+125.3**	DR1mm	**+ 3.6**	0
HD17	**-127.8**	**-44.4**	DR3mm	+2.4	-1.3
HI	**+0.6**	**+0.4**	R10mm	+ 1.2	**-1.8**

A temperature of 18ºC is generally used as the baseline for calculating the scores, as reported in the study by Karagiannidis et al. (2024). Therefore, the findings highlighting a warming trend of the regions under study are particularly concerning. Evergreen oaks can recover better after dry periods than deciduous oaks, as they continue their growth after the summer drought. Low soil water availability in spring is more detrimental to deciduous oak growth (Valeriano et al., 2021). According to the results, a decreasing trend in the HD17 index was found in both study areas. In “Dadia” forest, degree days <17°C are decreasing at a rate of about 128 per decade, while in the “Rhodes” forest, the decrease is quite slower, at about 44 degree days per decade (Table 2). In parallel, the same findings of decreasing trend, were found by Doshi et al. (2023), for the European continent. Conversely, all other degree day indices showed an opposite trend, with the largest increase in the rate of change found in growing degree days (GD4) index (sum of degree days of TM over 4 °C), which increased by 175.5 (125.3) degree days per decade at “Dadia” (“Rhodes”), as shown in Table 2. These findings again agree with those of Doshi et al. (2023), where the GD4 index showed the highest upward trend across all months in Europe. The trend patterns of some extreme precipitation climate indices show geographic variation, large and expected variability, in contrast to the remarkable consistency of extreme temperature climate indices across both study locations. All precipitation indices exhibited increasing trends in the “Dadia” region in the northern parts of the country, while some decreasing trends were observed at “Rhodes” in the southernmost part of the country (Figure 1). Moreover, at the southernmost site of “Rhodes”, the rate of decrease in the total annual precipitation (RTI) reaches 31.5mm/decade (Figures 1). These results for the locations of interest are in general agreement with global findings (IPCC, 2007, 2023; Boegelsack et al., 2018).

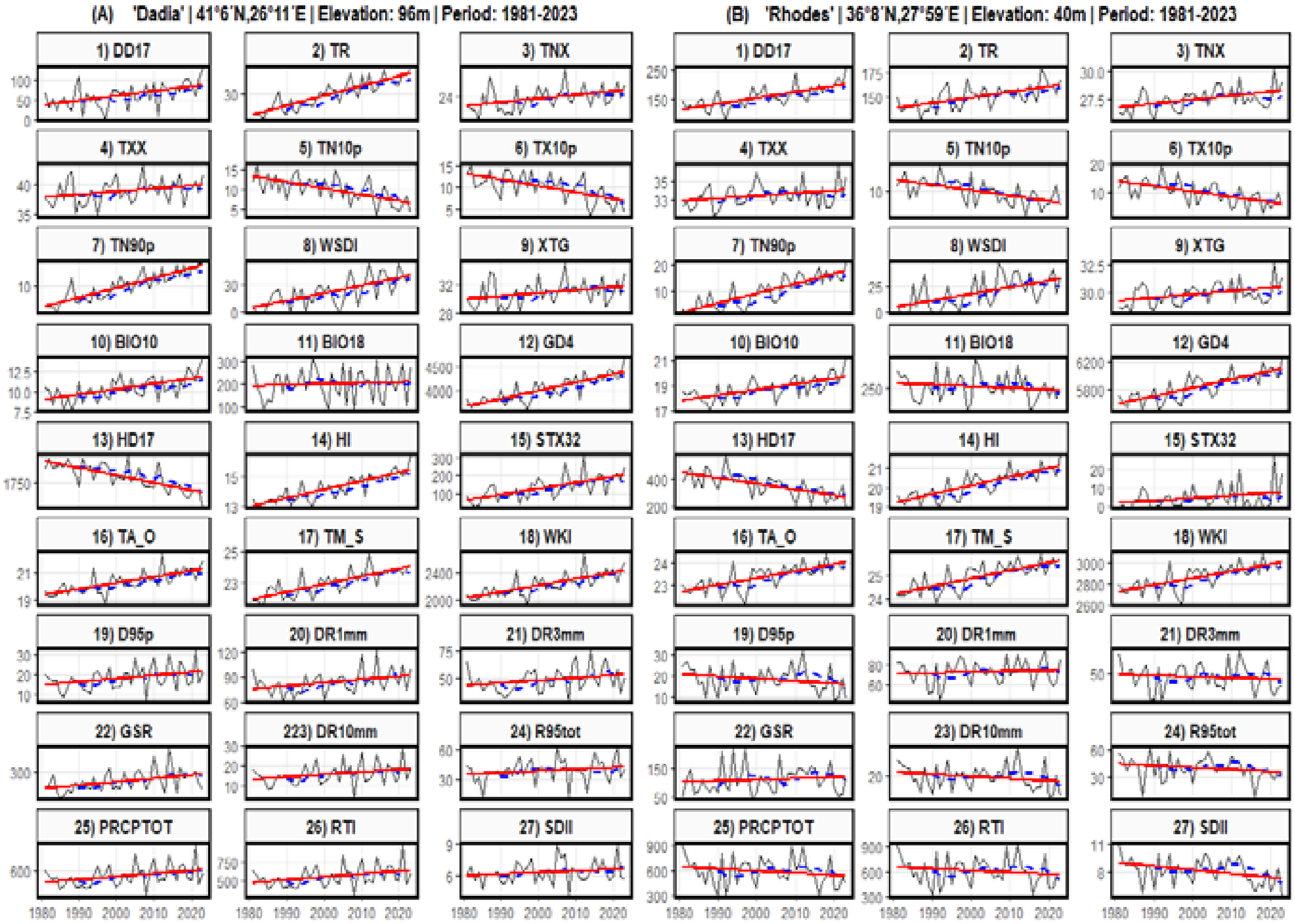

Figure 1: The annual trend magnitudes of all climate indices in (A) “Dadia” and (B) in “Rhodes” (1981-2023).

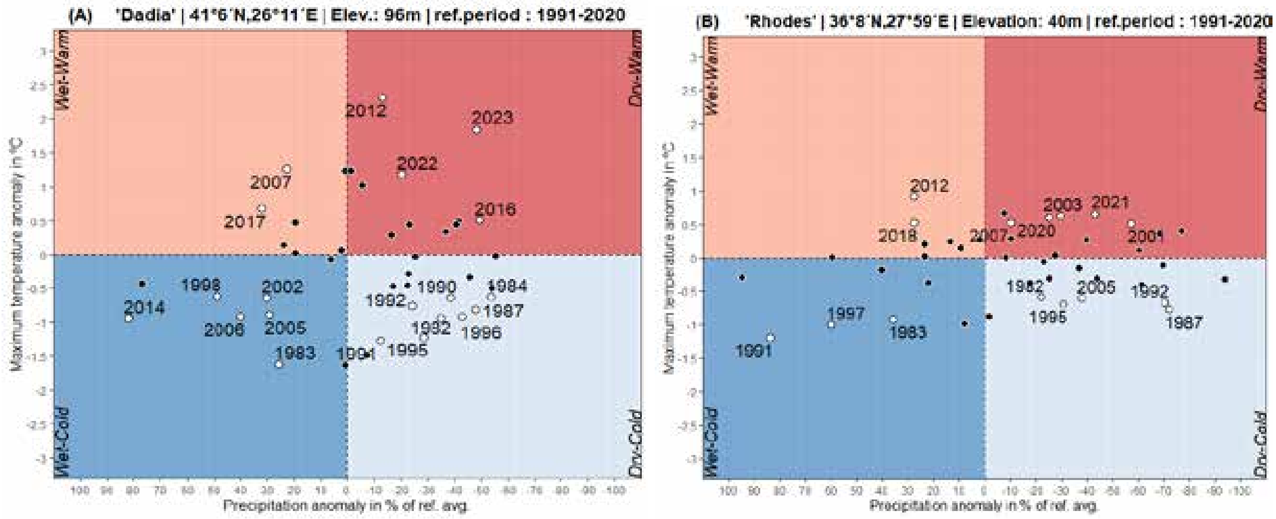

Figure 2: Temperature (maximum) and Precipitation Anomalies in Fire Season (May to October) from 1981 to 2023 (A) in "Dadia" and (B) in "Rhodes" site. Each chart shows each year's characterization as Wet-Warm (top left), Wet-Cold (bottom left), Dry-Warm (top right) and Dry-Cold (bottom right) in quadrants.

The most catastrophic fire season of all, 2023 in "Dadia", is classified as Dry and Warm (Figure 2). Maximum temperature anomalies were 1.8°C above the 1991–2020 average (28.2°C), and a decrease in precipitation amount of 48.4% (mean 214.1 mm). The maximum temperature increased by 0.7 °C compared to 2022. The 2013 fire season's maximum temperature deviation increased from 0.5°C above the 1991–2020 average to 1.8°C over 10 years (2013-2023) and precipitation anomaly values recorded from -40.8% deviation into -48.4% of reference period in the same decade. Respectively in "Rhodes", in 2023 fire season the estimated maximum temperature anomalies were 0.6°C above the 1991–2020 average (26.7°C), and a decrease in precipitation amount of 7.4% (mean 89.8 mm) (not shown in Figure 2). In the same decade from 2013 to 2023 fire season's estimated anomalies of temperatures increased from 0.03°C in 2013 to 0.6°C in 2023 and precipitation anomalies of 2013 increased from -27.6% to -7.5%. Although the 2023 fire season wasn't characterized as Dry and Warm (thus it is not shown in Figure 2), 2022 had remarkable deviations. Maximum temperature anomalies in fire season estimated 0.3°C above the 1991–2020 average, slightly smaller deviation than 2023. Precipitation anomalies in the 2022 fire season estimated negative at 39.6%, a huge difference from 2023 with the enormous damages in the natural reserve of Vounokalathos. According to the literature, the assessment of extreme drought events at both annual and three seasonal scales, i.e., previous winter (December-February), current spring (March-May) and current summer (June-August) best captures absolute water availability (Adams et al. 2017, Senf et al. 2020, Bose et al. 2024). So, these estimations from the year before the disastrous 2023 may be explained the fire severity. Also, 2020 and 2021 fire seasons were estimated as Dry and Warm in "Rhodes" (Figure 2). Thus, three consecutive fire seasons were characterized by favorable fire-weather conditions. Overall, the magnitude of the "Rhodes" 2023 fire season's Dry and Warm event was smaller (in terms of amplitude) compared to the "Dadia" event.

Conclusions

We analyzed the observed climate-driven changes in summer wildfires in two typical Mediterranean forest regions in Greece. The analysis indicates that the northernmost site is most impacted by hot extremes and compound hot-dry extremes, with changes being sensitive to temperature index used, while the southernmost site is most impacted by dry extremes and compound hot-dry extremes, with changes not being sensitive to the precipitation index used. In addition, we propose that climate change affects temperature and precipitation patterns, creating drier and extremely warm conditions that are more likely to lead to forest fires. This strengthens the evidence that climate change increases the frequency and/or severity of fire weather, with a high fire risk due to a combination of high temperatures, low humidity, low rainfall, and often high winds at the sites of interest. However, establishing a direct causal link between a single case and climate change remains challenging as some events would still occur even without climate change. It is therefore important to understand the changes in frequency and intensity at which these events occur. Moreover, it is concluded that to be effective, the management of forest ecosystems and forest fires must be accompanied by long-term knowledge of all the parameters associated with forest fires (climate, vegetation, soil, topography, etc.), which vary locally. More research is, of course, necessary to fully understand the effects of heat stress, which should be supported by real-time data collection and analysis in the field.

References

Adams, H.D.; Zeppel, M.J.B.; Anderegg, W.R.L.; Hartmann, H.; Landhäusser, S.M.; Tissue, D.T.; Huxman, T.E.; Hudson, P.J.; Franz, T.E.; Allen, C.D.; et al. 2017. A Multi-Species Synthesis of Physiological Mechanisms in Drought-Induced Tree Mortality. Nat. Ecol. Evol., 1, 1285–1291

Boegelsack, N., Withey, J., O'Sullivan, G. and McMartin, D. 2018. A Critical Examination of the Relationship between Wildfires and Climate Change with Consideration of the Human Impact. Journal of Environmental Protection, 9, 461-467. DOI 10.4236/jep.2018.95028.

Bose AK, Doležal J, Scherrer D, Altman J, Ziche D, Martínez-Sancho E, Bigler C, Bolte A, Colangelo M, Dorado-Liñán I, et al. 2024. Revealing legacy effects of extreme droughts on tree growth of oaks across the Northern Hemisphere. Sci Total Environ.926:172049. DOI: 10.1016/j.scitotenv.2024.172049. Epub 2024 Mar 27. PMID: 38552974.

Carnicer, J., Alegria, A., Giannakopoulos, C. et al. 2022. Global warming is shifting the relationships between fire weather and realized fire-induced CO2 emissions in Europe. Sci Rep 12, 10365. DOI: https://doi.org/10.1038/s41598-022-14480-8

Copernicus Climate Change Service 2024. European State of the Climate (ESOTC) report of 2023. Press releases Copernicus Climate Change Service (C3S). DOI 10.24381/bs9v-8c66

Doshi S. C., Lohmann G., Rimbu N., Ionita M.(2023. Spatiotemporal trend analysis of climate indices for the European continent. Journal of Water and Climate Change, 14 (9): 3112–3130. DOI 10.2166/wcc.2023.183

Dunn, C. J., O'Connor C. D., Abrams J., Thompson M. P., Calkin D. E., Johnston J. D., Stratton R., and Gilbertson-Day J. 2020. Wildfire risk science facilitates adaptation of fire-prone social-ecological systems to the new fire reality. Environmental Research Letters 15(2):025001. DOI 10.1088/1748-9326/ab6498

European Environment Agency - EEA (2024). Forests and forestry. EU-European Union. Modified 04 Dec 2024. Available from: https://www.eea.europa.eu/en/topics/in-depth/forests-and-forestry [Accessed: on 16 January 2025]

European Forest Fire Information System - EFFIS (2023). Data and services (europa.eu). Data and services. European Centre for Medium-Range Weather Forecasts (ECMWF). EC - European Commission. Available from: https://effis.jrc.ec.europa.eu/applications/data-and-services [Accessed: on 10 June 2024]

Expert Team on Climate Change Detection and Indices, ETCCDI: i) Karl et al., 1999; ii) Peterson, 2005; iii) Klein Tank et al., 2009).

Giannakopoulos C., Kostopoulou E., Varotsos K.V., Tziotziou K., Plitharas A. 2011. An integrated assessment of climate change impacts for Greece in the near future. Reg. Environ. Chang., 11, 829–843.

Intergovernmental Panel on Climate Change-IPCC 2007. Climate Change 2007. The Physical Science Basis Contribution of Working Group I to the Fourth Assessment Report of the IPCC (ISBN 978 0521 88009-1 Hardback; 978 0521 70596-7 Paperback)

Intergovernmental Panel on Climate Change-IPCC 2023. Summary for Policymakers. In: Climate Change 2023: Synthesis Report. Contribution of Working Groups I, II and III to the Sixth Assessment Report of the Intergovernmental Panel on Climate Change [Core Writing Team, Lee H., and Romero J. (eds.)]. IPCC, Geneva, Switzerland, pp. 1-34, DOI 10.59327/IPCC/AR6-9789291691647.001

Karagiannidis, A.; Lagouvardos, K.; Kotroni, V.; Galanaki, E. 2024. Expected Changes in Heating and Cooling Degree Days over Greece in the near Future Based on Climate Scenarios Projections. Atmosphere, 15, 393. https:// doi.org/10.3390/atmos15040393

Kostopoulou, E., Jones, P. 2005. Assessment of climate extremes in the Eastern Mediterranean. Meteorol. Atmos. Phys. 89, 69–85 DOI 10.1007/s00703-005-0122-2

Kostopoulou, E., Giannakopoulos C., Hatzaki M., and Tziotziou K. 2012. Climate extremes in the NE Mediterranean: Assessing the E-OBS dataset and regional climate simulations. Climate Research 54, no. 3: 249 - 270.

Kostopoulou, E.; Giannakopoulos, C. 2023. Projected Changes in Extreme Wet and Dry Conditions in Greece. Climate, 11, 49. DOI 10.3390/cli11030049

Matzarakis, A., Nastos, P. 2024. Greece 2023: Crazy Summer or New Normal—Lessons Not Learned. Atmosphere 15, no. 10: 1241. DOI 10.3390/atmos15101241

Michel A, Kirchner T, Prescher A-K, Schwärzel K, editors (2023) Forest Condition in Europe: The 2023 Assessment. ICP Forests Technical Report under the UNECE Convention on Long-range Transboundary Air Pollution (Air Convention). Online supplementary material, 48 p. Eberswalde: Thünen Institute. Available at http://icp-forests.net/page/icp-forests-technical-report

Paparrizos, S., Matzarakis, A., 2016. Present and future assessment of Growing Degree Days over selected Greek areas with different climate conditions. Meteorology and Atmospheric Physics, DOI 10.1007/s00703-016-0475-8

Reig-Gracia Fergus 2019. ClimInd: Climate Indices. R package version 0.1-3, https://cran.r-project.org/web/packages/ClimInd. Accessed 11 Jan. 2023. DOI 10.32614/CRAN.package.ClimInd.

Roγé Dominic. 2020. «Visualize climate anomalies». R-bloggers. www.r-bloggers.com. Accessed 11 Jan. 2023.

Smith, A.J.P., Jones, M.W., Abatzoglou, J.T., Canadell, J.G. & Betts, R.A. 2020. ScienceBrief Review: Climate change increases the risk of wildfires Critical Issues in Climate Change Science, edited by: C. Le Quéré, P. Liss, P. Forster. DOI 10.5281/zenodo.4570195. This ScienceBrief Review was supported by the European Commission via projects CRESCENDO, 4C, and VERIFY (grants no. 641816, 821003, 776810).

Senf, C., Buras, A., Zang, C. S., Rammig, A., & Seidl, R. 2020. Excess forest mortality is consistently linked to drought across Europe. Nature Communications, 11(1), Article 6200. DOI:10.1038/s41467-020-19924-1

Spanos, K.; Skouteri, A.; Gaitanis, D.; Petrakis, P.; Meliadis, I.; Michopoulos, P.; Solomou, A.; Koulelis, P.; Avramidou, E. 2021. Forests of Greece, their multiple functions and uses, sustainable management and biodiversity conservation in the face of climate change. Open J. Ecol., 11, 374–406.

Valeriano, C., Gazol, A., Colangelo, M., Gonzalez de Andres, E., Camarero, J.J., 2021. Modeling climate impacts on tree growth to assess tree vulnerability to drought during forest dieback. Front. Plant Sci. 12, 672855

17th INTERNATIONAL CONGRESS of the Geological Society of Greece

BULLETIN OF THE GEOLOGICAL SOCIETY OF GREECE, SP. PUBL.

EXTENDED ABSTRACT 088

A flood hazard assessment tool using satellite based high resolution land cover dataset within Google Earth Engine

Gemitzi A.[1], Kopsidas O.[1], Stefani F.[2], Polymeros A.[3], Bellos V.[1], Falalakis G.[4]

(1) Department of Environmental Engineering, Democritus University of Thrace, Xanthi, Greece, agkemitz@env.duth.gr (2) National School of Public Administration and Local Government, Athens, Greece (3) Ministry of Rural Development and Food, Athens, Greece (4) Ministry of Education and Religion, Directorate of Secondary Education Rhodope, Greece

Introduction / Background

Floods are one of the natural disasters that pose a real threat for communities all over the world, especially in areas of low altitude with mild slopes and in coastal zones, impacting thus significantly human life. Floods may result in loss of human life, property damage, infrastructure damage and subsequent economic losses (Guha-Sapir *et al.,* 2014; Pabi *et al.,* 2021; Venkataramanan *et al.,* 2019). Another serious flood implication is the displacement of people, which can be temporary or long-term, depending on the severity of the flood and the availability of resources to support those who have been displaced (International Federation of Red Cross and Red Crescent Societies, 2021).

Thus, there is need for proactive flood disaster risk management (Pabi *et al.,* 2021), for any flood type like flash floods, river floods and flooding in urban areas, which can be greatly facilitated nowadays by remotely sensed information (Ajmar *et al.,* 2017)]. The EU Directive 2007/60 requires EU member states to take a number of measures to reduce the negative impacts of floods on human health, the environment, and economic activities, including the identification of areas at risk of flooding, the development of flood risk maps and management plans, and the implementation of flood risk reduction measures. As climate change is expected to bring more frequent extreme precipitation events, floods are expected to pose a serious threat for human society and environment and within this context flood hazard mapping is of major importance for urban and spatial planning and land use management (Hosseini *et al.,* 2020; Ran *et al.,* 2019).

There are several methods to identify flood prone areas, but the main tool is numerical modeling. The conventional way is to identify the catchment which runoffs to the vulnerable area and implement a hydrological rainfall-runoff model which derives a flood hydrograph at the catchment outlet. Except for the previous framework, there are several approaches such as multi-criteria decision-making tools, statistical methods, and Machine Learning techniques [Hosseini *et al.,* 2020; Rafiei-Sardooi *et al.,* 2021), which can be incorporated in the general methodology.

As previously mentioned, the EU Directive 2007/60 is the main tool for the European Union to define the strategy and to derive the policies for flood management. However, this framework has some drawbacks: a) the inundated areas are produced using numerical modeling, which in general suffer from uncertainties. Moreover, the low quality or even the lack of historical data from flood events makes the calibration of the required parameters no feasible and hence uncertainty is increased; b) Flood Hazard Maps are one snapshot in a specific time moment and they cannot incorporate all the changes which affect the flooded area, such as the land use modifications, the urbanization, the construction of several manmade structures, the rainfall variability over time, etc.

Therefore, there is a gap between this static tool of EU Flood Hazard Maps and the real world which changes every day. During the last years, Remote Sensing (RS) techniques to identify the inundated areas after a flood event are rising and indicate a potential. For example, researchers used Sentinel-1 images in order to assess the performance of hydraulic modeling in a historical flood event (Zotou *et al.,* 2020)] Other researchers developed the FLOMPY toolbox to identify flooded areas in the past using Sentinel-1 images (Karamvasis *et al.,* 2021) and they used Synthetic Aperture Radar approaches to support flood modeling (Zotou *et al.,* 2022). There are also works utilized the Google Earth Engine (GEE) based on Sentinel-1 images, in which they identified the flood susceptibility of an area, namely which areas are more vulnerable to be flooded based on historical and topographic data (Mehravar *et al.,* 2023) or they focused on the built-up area effect on flooding.

To the best of our knowledge, flood hazard mapping is based on hydrological modeling while there is no approach that uses remote-sensed and constantly updated images of flood data which can be used to assess the output of the EU Flood Hazard Maps. Besides, this is the first time a constantly updated flood hazard assessment tool is available for use by every interested stakeholder. In this work, a methodology for the assessment of flood hazard and the associated socioeconomic implications is presented based on the land cover dataset produced by Artificial Intelligence (AI) namely Dynamic World (Brown *et al.,* 2022), which is updated constantly following the revisit time of Sentinel 2, i.e., two to five days, and provides information on flooded areas at a 10 m spatial resolution. The assessment is built within GEE platform, and evaluates the flooding probability at the pixel level, computing the number of times each pixel is categorized as flooded in the Dynamic World dataset for a given time period.

The methodology is applied in the River Basin District (RBD) of Thrace in NE Greece and it was compared against the latest Flood Hazard Maps developed for the study area according to the requirements of the EU Directive 2007/60 (EU Parliament, 2007). Our work highlights the advantages of using near-real time updated information on floods, complementary to the EU Flood Hazard Maps which are derived for a specific time moment. Its simplicity makes it an ideal instrument to overcome barriers encountered between scientific advances and policy adjustments, since it is implemented within a simple GEE code, and hence it is also readily available for use in other areas around the world. Apart from that, we also applied the tool in the region of Thessaly, Greece, in order to identify the flood impact after the recent catastrophe due to the Storm Daniel which hit the Mediterranean basin in early September of 2023.

Methods / Results

The flood hazard assessment approach presented herein builds on the global near-real time land use/land cover (LULC) product Dynamic World (Brown *et al.,* 2022), which is the result of the joint effort of Google and the World Resources Institute. It is available through the GEE platform and can be viewed in the GEE public data catalog. Aim of this initiative was to release a global LULC dataset, updated in near-real time that could capture the dynamic nature of Earth's surface. A detailed description of the methodology and training material can be found in the Dynamic World web page (Google and World Resources Institute Dynamic World App., 2024). Dynamic World is produced applying Artificial Intelligence (AI) principles using GEE and AI Platform. It is based on the European Space Agency's Sentinel-2 Top of Atmosphere (TOA) images, which are classified into 9 land use / land cover classes, using deep learning techniques. It has the spatial resolution of the original Sentinel-2 TOA product, i.e., 10 m, and it is updated globally every 2-5 days depending on the location, following the revisit time of Sentinel-2. The classification technique assigns per-pixel probabilities across nine land cover classes: Water, Trees, Grass, Crops, Shrub and Scrub, Flooded Vegetation, Built-up Area, Bare Ground, Snow and Ice. The Dynamic World classification has been applied to all historic Sentinel-2 TOA images, i.e., from June 2015 and it is constantly updated as soon as new images become available.

Concerning the flood hazard assessment presented in this work, the class of Flooded Vegetation is of particular interest, as it describes vegetated conditions related to flood. In the Dynamic World, each land cover class is represented by a different band. In this work, each pixel in every Dynamic World image of the study area, demonstrating the highest probability in the Flooded Vegetation class, is considered to be flooded area and it is assigned a value of 1, whereas in all other cases the pixel is assigned a zero value. Summing the values of each pixel across the whole time series, i.e., from June 2015 until today, corresponds to the number of times the specific pixel is viewed in flood conditions. All computations were performed within the GEE Platform with a Java Script code freely available using the link provided in the data availability section. The whole process is schematically depicted in Figure 1.

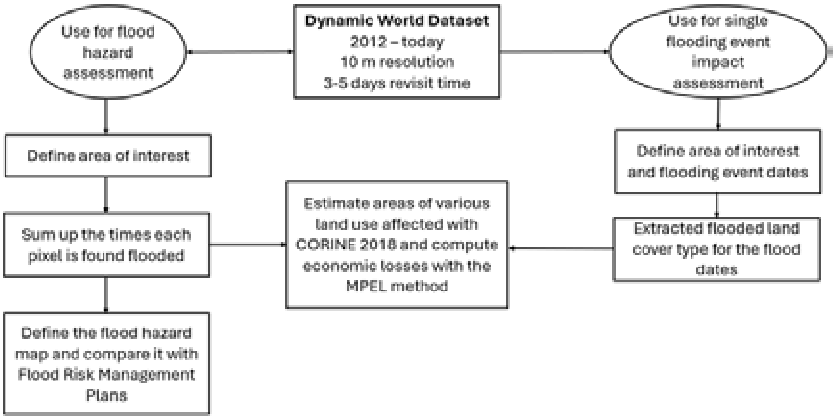

Figure 1. Flow chart of the flood hazard mapping approach

The results obtained with DW dataset in the Thrace RBD are shown in Figure 2a, whereas Figure 2b shows the frequency of flooding of various flooding areas. Comparison of the two independent datasets in Thrace Water District, which occupies an area of 11,250 km^2, revealed certain areas where Dynamic World did not detect flood conditions whereas the Flood Hazard Map indicates them as inundated area which corresponds to the rainfall with return period of 100 years. This is expected since the two datasets correspond to different repeat periods and does not mean that DW underestimates or the Flood Hazard Map overestimates flood hazard conditions. Those areas correspond to 444,3 km^2 (Figure 3). The areas that both datasets assign as flood cover 122.7 km^2. However, the most interesting outcome is that there is an area of 194.6 km^2 which has been observed as a flooded area at least once since 2015 in DW. This is a certain miss of the 100-year return flood data set. Those areas are observed along the eastern and northeastern areas of Thrace WD, within the basin of River Evros.

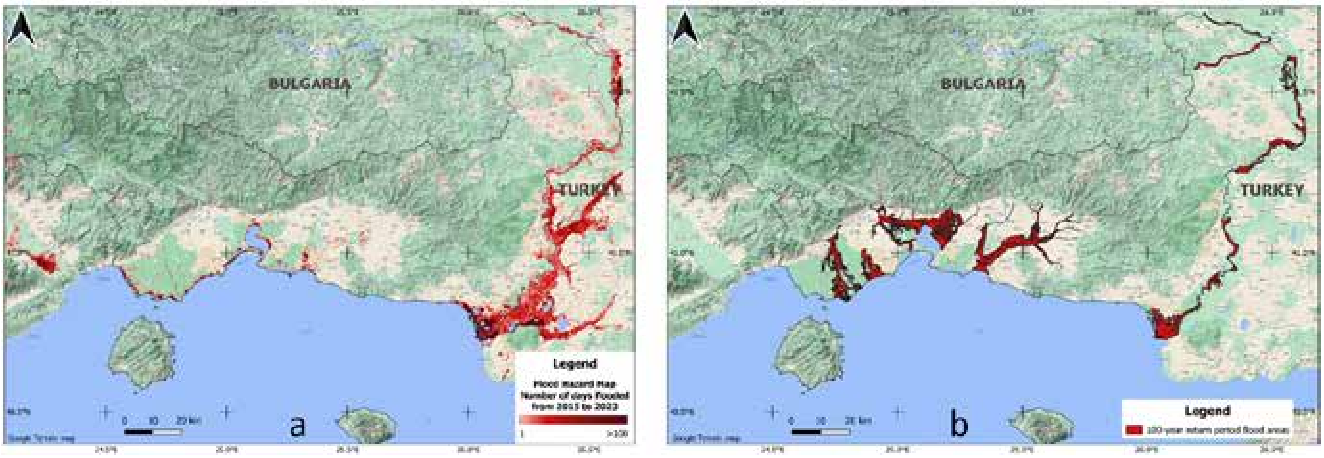

Figure 2. a) Flood Hazard Map of the broader Thrace RBD based on the methodology presented herein, covering the 2015 – 2023 period**, b)** 100-year return period Flood Hazard Map as defined for Thrace RBD, Greece

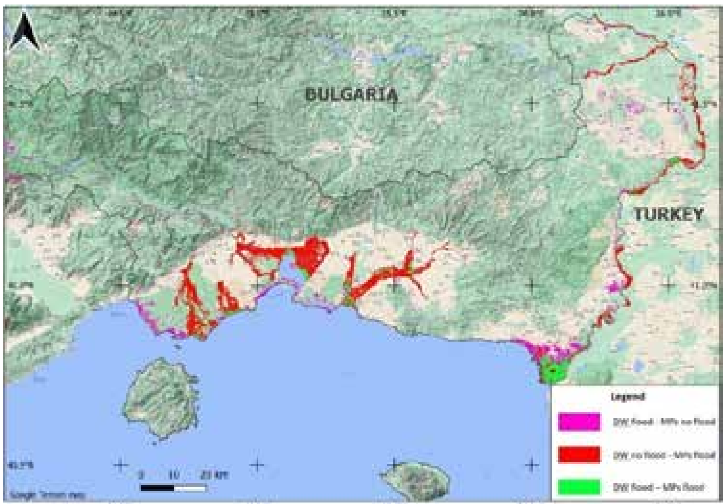

Figure 3. Comparison of the Flood Hazard Map of the Thrace RBD based on the methodology presented herein against the 100-year Flood Hazard Map based on the Flood Management Plan

Except for the application of DW in Thrace, we defined the flooding area prior and after the recent Medicane Daniel. Specifically, a tremendous flood event occurred in early September 2024 as a result of Storm Daniel, which caused dramatic impacts mainly on the region of Thessaly, in Central Greece (Figure 4). More than 750 mm of rainfall were recorded at the meteorological station of Zagora village near Mount Pelion, which approximates twice the annual rain of Athens (Nasa Earth Observatory, A Deluge in Greece). In Figure 5 the flooded area is plotted against how many times it is flooded, demonstrating that the flood impact of Daniel changed dramatically the distribution of flooded areas, with more than 50 km^2 observed as flooded for the first time.

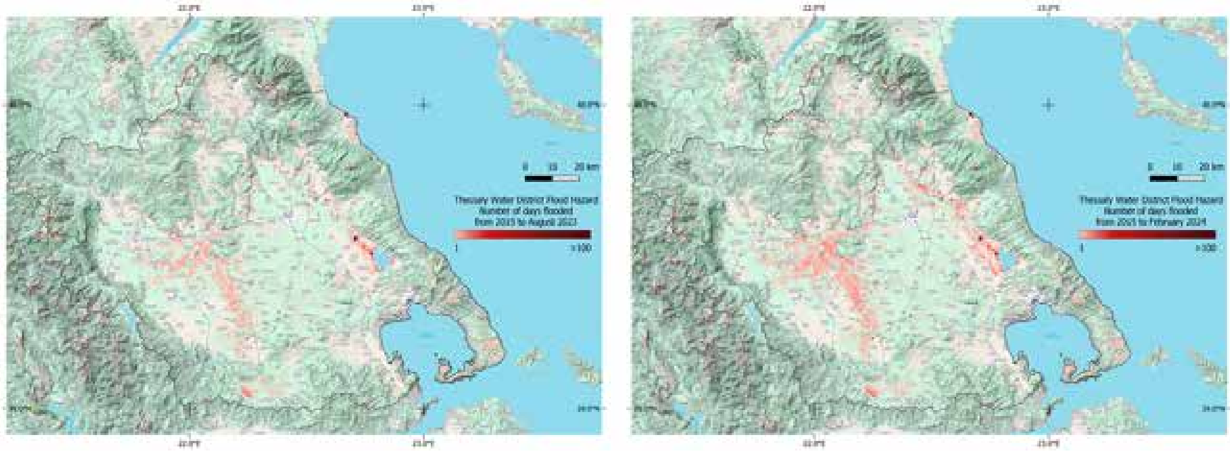

Figure 4. Flooded area prior to storm Daniel (left) and after storm Daniel (right)

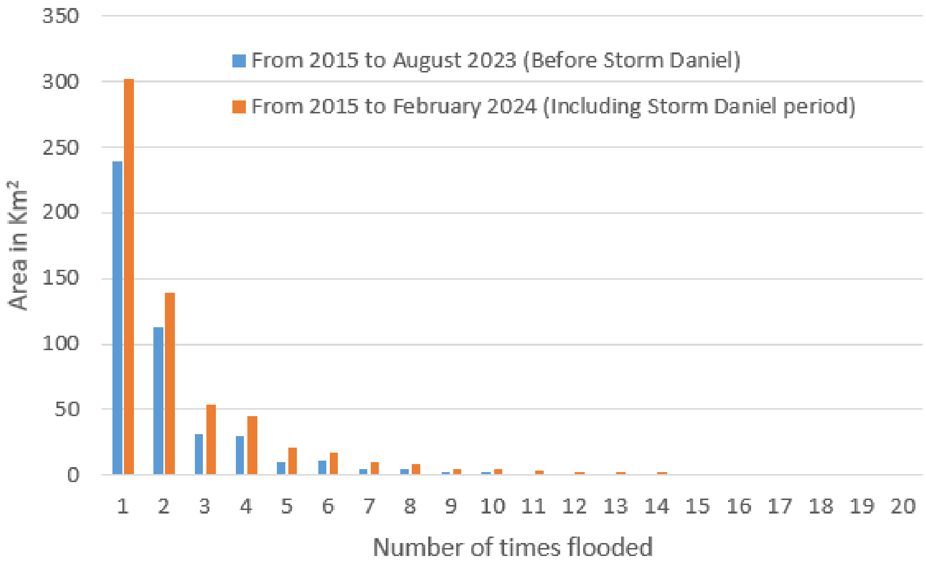

Figure 5. Flooded area against how many times is flooded before and after storm Daniel

Conclusions

In this work, we developed an open tool based on remote sensed images obtained by the Google Earth Engine, and specifically on Sentinel 2 images, for identifying the time series of flooded areas with a continuous update. This tool is implemented in the Thrace water district (Greece) and the outcome of the proposed tool is compared with the corresponding Flood Hazard Maps of the EU Directive 2007/60. It is found that there are discrepancies between the model product (i.e. the Flood Hazard Maps) and the real-world picture. We applied DW tool for identifying the flooded area after the recent Storm Daniel, which hit Greece in September of 2023 and specifically the region of Thessaly. Our major findings are presented in the following paragraphs.

First, we shall keep in mind that the conventional Flood Hazard Maps within the Flood Management Plans, are created on a probability basis using modeling tools and should be regarded as future potential flooding areas. Besides, these maps are derived assuming that there are no changes at the configuration of the vulnerable area. Our results indicated that there is space for improvement in those Flood Hazard Maps combining information from satellite-based observations. The DW dataset approach, presented in this work, offers a means of verification of the modeling results, especially by enhancing them in flooded areas which are not depicted in the Flood Hazard Maps. Regarding the reliability of this dataset, it should be noted that it has been rigorously examined and tested with a large Expert Consensus dataset and the results indicated top qualitative performance in each comparison category among the examined land cover datasets. Hence, the presented methodology, taking advantage of emerging techniques and datasets, helps policy makers acquire better and timely information on flood hazard, so as to improve the planning of protective measures.

Second, Sentinel 2 mission has a global coverage and covers all Earth's continents, large islands, along with inland and coastal water bodies, with a revisit frequency of 5 days. However, cloud cover may restrict acquisition of useful images, resulting in lower data availability in flooded areas with increased cloud cover and therefore the results obtained with DW dataset should be regarded as the minimum number of days the specific area is observed as flooded. It is very likely that some flood events are not detected by satellite observations due to cloud cover and are not included in the DW dataset. As the methodology is based on AI classification, there is always a slight possibility of misclassification, i.e., a dry pixel may appear falsely flooded and vice versa. Nevertheless, DW is an extensively evaluated dataset of high accuracy. Since it is a constantly updated dataset, its quality is expected to improve in the future versions. The probability for a specific area to have no RS history data is very low and thus the methodology works at the global scale. Moreover, since the Sentinel 2 mission operates from 2015, the data history covers a relatively short time period, which however can be extended back to early '80s combining data from Landsat missions. This can be a very challenging future extension of the present work.

Finally, the growing production of freely available datasets related to environmental monitoring based on remote sensing and AI technologies can be used to tackle the tremendous impacts on natural and human ecosystems due to flooding. The innovation of our approach consists of:

- The development of an algorithm using the Google Earth Engine platform in order to utilize the high-spatial resolution of the Dynamic World data.
- The deployment of a user-friendly tool which can be used for the effective communication of scientific findings to government and policy makers but also to all community actors and will encourage social acceptability of improved flood anticipation policies.
- The evidence of the usefulness of the tool, demonstrating the inadequacy of the River Flood Management Plans against the outcome of the tool in the Thrace Water District.

References

Ajmar, A., Boccardo, P., Broglia, M., Kucera, J., Giulio-Tonolo, F., Wania, A., 2017. Response to Flood Events. In Flood Damage Survey and Assessment, Geophysical Monograph Series, pp. 211–228 ISBN 9781119217930.

Brown, C.F., Brumby, S.P., Guzder-Williams, B., Birch, T., Hyde, S.B., Mazzariello, J., Czerwinski, W., Pasquarella, V.J., Haertel, R., Ilyushchenko, S., 2022. Dynamic World, Near Real-Time Global 10 m Land Use Land Cover Mapping. Sci Data, 9, 251, doi:10.1038/s41597-022-01307-4.

EU Parliament,2007. Floods Directive, Directive 2007/60/EC.

Google and World Resources Institute Dynamic World App, 2024. Available online: https://dynamicworld.app/ (accessed on 25 March 2024).

Guha-Sapir, D., Hoyois, P., Below, R., 2014. Annual Disaster Statistical Review 2014 The Numbers and Trends Centre for Research on the Epidemiology of Disasters (CRED).

Hosseini, F.S., Choubin, B., Mosavi, A., Nabipour, N., Shamshirband, S., Darabi, H., Haghighi, A.T., 2020. Flash-Flood Hazard Assessment Using Ensembles and Bayesian-Based Machine Learning Models: Application of the Simulated Annealing Feature Selection Method. Science of the Total Environment 711, 135161, doi:10.1016/j.scitotenv.2019.135161.

International Federation of Red Cross and Red Crescent Societies, 2021. DISPLACEMENT IN A CHANGING CLIMATE Localized Humanitarian Action at the Forefront of the Climate Crisis, Geneva.

Karamvasis, K., Karathanassi, V., 2021. FLOMPY: An Open-Source Toolbox for Floodwater Mapping Using Sentinel-1 Intensity Time Series. Water (Basel), 13, 2943, doi:10.3390/w13212943.

Mehravar, S., Razavi-Termeh, S.V., Moghimi, A., Ranjgar, B., Foroughnia, F., Amani, M., 2023. Flood Susceptibility Mapping Using Multi-Temporal SAR Imagery and Novel Integration of Nature-Inspired Algorithms into Support Vector Regression. J Hydrol (Amst), 617, 129100, doi:10.1016/j.jhydrol.2023.129100.

Nasa Earth Observatory A Deluge in Greece.

Pabi, O., Egyir, S., Attua, E.M., 2021. Flood Hazard Response to Scenarios of Rainfall Dynamics and Land Use and Land Cover Change in an Urbanized River Basin in Accra, Ghana. City and Environment Interactions 12, doi:10.1016/j.cacint.2021.100075.

Rafiei-Sardooi, E., Azareh, A., Choubin, B., Mosavi, A.H., Clague, J.J., 2021. Evaluating Urban Flood Risk Using Hybrid Method of TOPSIS and Machine Learning. International Journal of Disaster Risk Reduction, 66, doi:10.1016/j.ijdrr.2021.102614.

Ran, J., Nedovic-Budic, Z., 2019. Designing an Information Infrastructure for Policy Integration of Spatial Planning and Flood Risk Management. In Environmental Information Systems, IGI Global, pp. 520–554.

Venkataramanan, V., Packman, A.I., Peters, D.R., Lopez, D., McCuskey, D.J., McDonald, R.I., Miller, W.M., Young, S.L. A , 2019. Systematic Review of the Human Health and Social Well-Being Outcomes of Green Infrastructure for Stormwater and Flood Management. J Environ Manage 246, 868–880, doi:10.1016/j.jenvman.2019.05.028.

Zotou, I., Bellos, V., Gkouma, A., Karathanassi, V., Tsihrintzis, V.A., 2020. Using Sentinel-1 Imagery to Assess Predictive Performance of a Hydraulic Model. Water Resources Management, 34, 4415–4430, doi:10.1007/s11269-020-02592-7.

Zotou, I., Karamvasis, K., Karathanassi, V., Tsihrintzis, V.A., 2022. Potential of Two SAR-Based Flood Mapping Approaches in Supporting an Integrated 1D/2D HEC-RAS Model. Water (Basel), 14, 4020, doi:10.3390/w14244020.

17th
INTERNATIONAL CONGRESS
of the Geological Society of Greece

BULLETIN OF THE GEOLOGICAL
SOCIETY OF GREECE, SP. PUBL.

EXTENDED ABSTRACT 089

How medial tephra records contribute to proximal tephrochronology: Case study of Nisyros Volcano

G. Gençalioğlu Kuşcu [1], G. Uslular [2]
(1) Department of Geological Engineering, Muğla Sıtkı Koçman University, Muğla, Türkiye, gkuscu@mu.edu.tr
(2) Polar Research Institute, TÜBİTAK Marmara Research Center, Kocaeli, Türkiye

Introduction

Santorini and Nisyros are considered the most important caldera-type volcanoes in terms of volcanic risk in the South Aegean Active Volcanic Arc, Figure 1A). The recent earthquake swarms in the Christiana-Santorini-Kolumbo volcanic system between Santorini and Amorgos Islands have been causing concern not only in Santorini and neighboring islands, but also in Türkiye since the end of January 2025. The possibility of a volcanic eruption in this volcanic field reminded us of widespread tephra units in the geological past such as the Santorini Minoan tephra, spread to western Anatolia. Therefore, the other active volcanic field of the SAAVA, Kos-Nisyros-Yali, closer to Turkish mainland becomes more important. Terrestrial medial/distal tephra sequences are especially valuable in the case of island arc volcanoes where most of the tephra deposited within the sea and not readily accessible. The purpose of this study is to document the medial Nisyros tephra on Datça peninsula (Muğla, SW Türkiye) and discuss how they contribute to the understanding of tephrochronological issues in the proximal region.

Kos-Nisyros-Yali Volcanic Field and Nisyros Medial Tephra

Kos-Nisyros-Yali, is the site for one of the most powerful eruptions in the Quaternary (i.e. Kos Plateau Tuff, Keller et al., 1990) (Figure 1B). Despite the well constrained geology, distribution and chronology of tephra units of Santorini, there are some uncertainties in tephra distribution and eruption frequency for Nisyros volcano. The ^{40}Ar/^{39}Ar age of Kos Plateau Tuff (KPT) eruption is 161.3 ± 1.1 ka (Smith et al., 1996), and Nisyros-Yali are considered post-KPT volcanic centers. The geochronology of the Nisyros tephra units has been constrained just recently. The K-Ar method was the most widely used for the pre-caldera Nisyros tephra units, but did not provide accurate ages (e.g. Keller et al., 1990). Absence or rarity of K-bearing phases or excess Ar in some crystals were problems related to K/Ar dating, resulting in older ages. Other methods (^{14}C, O isotopes, fission track) were employed for the caldera-forming tephra, and use of distal marine tephra for stratigraphy and correlation also produced conflicting and wide range of ages.
Regarding the Nisyros tephra dispersal, only caldera forming rhyodacitic/rhyolitic Lower and Upper Pumice units (63.1 ± 4.7 ka and 58.4 ± 2.7 ka, respectively; Popa et al., 2020) were considered significant in the literature. Even if deposited on neighboring islands or Turkish coast, pre-caldera tephra was thought to be eroded later on (Longchamp et al., 2011). However, pre-caldera Kyra unit (previously estimated as 24-38 ka) was reported in one locality on Datça (0.9 m) and Tilos (1.2 m) (Keller et al., 1990; Sterba et al., 2011).

Results

In order to contribute to the tephrochronology of Nisyros volcano, we conducted field studies and tephra hunting on Datça peninsula, that revealed 6 new outcrops and confirmed the occurrence of Nisyros Kyra reported earlier (Gençalioğlu-Kuşcu and Uslular, 2018). We collected andesitic and dacitic pumice lapilli deposited on KPT with an unconformity in between (Figure 2). Zircon, monazite, and apatite crystals were separated from Datça pumice fall tephra for U-Th/He geochronology, and abundant apatite crystals proved to be useful. Plagioclase and hornblende crystals were also separated for ^{40}Ar/^{39}Ar geochronology from another Kyra tephra location. The weighted mean of combined ^{40}Ar/^{39}Ar and (U–Th)/He ages was calculated as 133.5 ± 3.4 ka (Gençalioğlu Kuşcu et al., 2020).

Conclusions

Identification of new medial Nisyros tephra on Datça Peninsula, together with their detailed characterization contributes to the proximal tephrochronology of Nisyros volcano. The weighted mean age of 133.5 ± 3.4 ka for Kyra tephra conforms with the recent ages of younger explosive and effusive units, revealing a more precise tephrostratigraphy. As a caldera volcano accumulating silicic magma, Nisyros possesses volcanic risk to surrounding islands and Turkish mainland. Therefore, medial tephra distribution and identification, correlation and geochronology of these tephra units are vital to get the full picture of this relatively less known, but potentially dangerous volcanic system. Further volcanological and geochronological work is needed to determine the distribution of medial tephra and determine the eruption frequency for the Nisyros volcano.

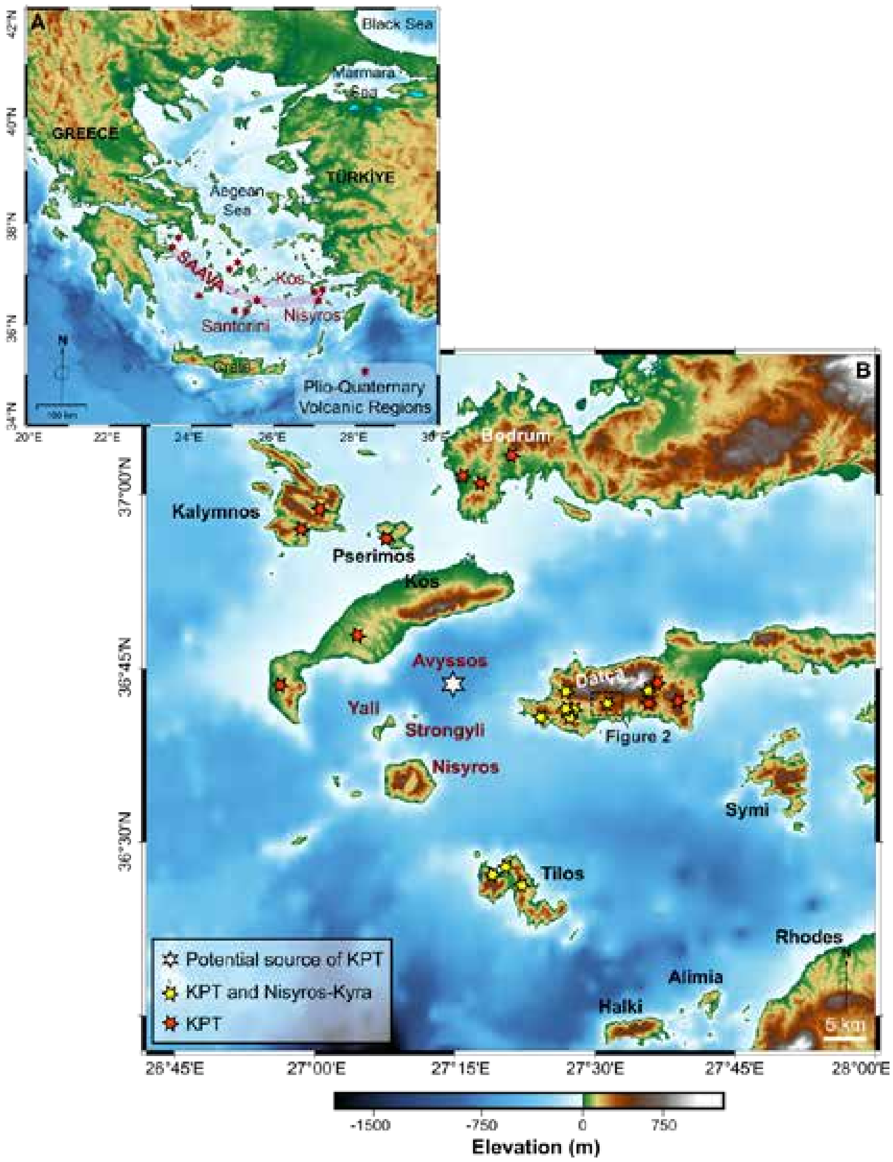

Figure 1A. Map showing the volcanic centers of the South Aegean Active Volcanic Arc (SAAVA); B. DEM image (30-m resolution SRTM) showing the Kos-Nisyros-Yali volcanic system. Occurrences of KPT on Datça-Bodrum Peninsulas and neighboring islands are modified from Ercan et al. (1984), Allen et al. (1999), Pe-Piper et al. (2005), and Gençalioğlu Kuşcu (2012). Nisyros Kyra tephra on Datça peninsula and Tilos island are from Gençalioğlu Kuşcu and Uslular (2018) and Sterba et al. (2011), respectively. The rectangle on the Datça peninsula shows the Sındı location of Figure 2, where Nisyros Kyra overlies the KPT and fluvial deposits.

Figure 2. General view of the andesitic Kyra fallout overlying the KPT and fluvial deposits on Datça peninsula.

Acknowledgements

The research was funded by Scientific Research Project Office of Muğla Sıtkı Koçman University, Türkiye (through BAP Projects 10/47; 15/070 and 15/077), and TÜBİTAK Scientific and Technical Research Council of Türkiye (grant number 113Y328).

References

Allen, S.R., Stadlbauer, E., Keller, J., 1999. Stratigraphy of the Kos Plateau Tuff: product of a major Quaternary explosive rhyolitic eruption in the eastern Aegean, Greece. Int.J. Earth Sci. 88, 132–156.

Ercan, T., Günay, E., Baş, H., Can, B., 1984. Datça Yarımadasındaki Kuvaterner yaşlı volkanik kayaçların petrolojisi ve kökensel yorumu (Petrology and genetical interpretation of the Quaternary volcanic rocks on Datça Peninsula) MTA Dergisi, 97/98. pp. 45–56 (in Turkish).

Gençalioğlu-Kuşcu, G. 2012. Bodrum ve Datça Yarımadası Piroklastik İstiflerinin Jeolojik ve Petrografik İncelenmesi, 10/47 no'lu Muğla Üniversitesi BAP Proje Raporu, (in Turkish).

Gençalioğlu-Kuşcu, G. and Uslular, G., 2018. Geochemical characterization of mid-distal Nisyros tephra on Datça peninsula (southwestern Anatolia). Journal of Volcanology and Geothermal Research, 354, 13-28.

Gençalioğlu-Kuşcu, G., Uslular, G., Danišík, M., Koppers, A., Miggins, D.P., Friedrichs, B. and Schmitt, A.K., 2020. U–Th disequilibrium, (U–Th)/He and 40Ar/39Ar geochronology of distal Nisyros Kyra tephra deposits on Datça peninsula (SW Anatolia). Quaternary Geochronology, 55, 101033.

Keller, J., Rehren, T.H., Stadlbauer, E., 1990. Explosive volcanism in the Hellenic arc. In: Hardy, D.A., Keller, J., Galanopoulos, V.P., Fleming, N.C., Druitt, T.H. (Eds.), Thera and the Aegean World, III, Proceedings of the Third International Congress, Santorini, Greece, 3–9 September 1989. vol. 487. The Thera Foundation, p. 13–26.

Longchamp, C., Bonadonna, C., Bachmann, O., Skopelitis, A., 2011. Characterization of tephra deposits with limited exposure: the example of the two largest explosive eruptions at Nisyros volcano (Greece). Bull. Volcanol. 73, 1337–1352.

Pe-Piper, G., Piper, D.J.W., Perissoratis, C., 2005. Neotectonics and the Kos Plateau Tuff eruption of 161 ka, South Aegean arc. J. Volcanol. Geotherm. Res. 139, 315–338.

Popa, R. G., Guillong, M., Bachmann, O., Szymanowski, D., & Ellis, B. (2020). U-Th zircon dating reveals a correlation between eruptive styles and repose periods at the Nisyros-Yali volcanic area, Greece. Chemical Geology, 555, 119830.

Smith, P.E., York, D., Chen, Y., Evansen, N.M., 1996. Single crystal 40Ar–39Ar dating of Late Quaternary paroxysm on Kos, Greece: concordance of terrestrial and marine ages. Geophys. Res. Lett. 23, 3047–3050.

Sterba, J.H., Steinhauser, G., Bichler, M., 2011. On the geochemistry of the Kyra eruption sequence of Nisyros volcano on Nisyros and Tilos, Greece. Appl. Radiat. Isot. 69, 1605–1612.

Evaluation of PAHs sorption behavior in coals and cokes

Georgaki M. [1], Karapanagioti H.K.[2], Wojtaszek-Kalaitzidi M.[3], Kalaitzidis S.[1*]
(1) Department of Geology, University of Patras, Rio-Patras, GR 265 04, Greece, skalait@upatras.gr (2) Department of Chemistry, University of Patras, Rio-Patras, GR 265 04, Greece (3) Institute of Energy and Fuel Processing Technology, 1 Zamkowa Street, Zabrze, Poland

Research Highlights

This study investigates the sorption behavior of phenanthrene in coals and cokes, highlighting the influence of coal rank and maceral composition on phenanthrene sorption capacity.

Introduction / Background

Organic petrography has become an important tool in environmental research, particularly in studying the sorption capacities of polycyclic aromatic hydrocarbons (PAHs) in various types of coal (e.g., Ligouis *et al*., 2005; Kalaitzidis *et al*., 2006; Yan *et al*., 2011). This is important as it provides insights into the interactions between PAHs and organic matter, which are critical for predicting the behavior and environmental fate of these pollutants in natural systems. PAHs refer to a broader category of harmful and toxic organic pollutants widely distributed in nature (Van der Oost *et al*., 2003; White *et al*., 2016; Patel *et al*., 2020). Some of these compounds can be mutagenic or carcinogenic in living organisms, leading to their classification as priority pollutants (ATSDR, 1995).

Phenanthrene ($C_{14}H_{10}$) belongs to PAHs and is a hydrophobic organic pollutant, due to its potential toxicity to humans and other living organisms, as well as its prevalence and persistence in the environment (Hussar *et al*., 2012). It is commonly used in sorption studies as a model organic chemical and is also used in this study. Previous studies showed that the sorption of phenanthrene in low-rank coals is controlled, among others, through the inertinite content (e.g. Kalaitzidis *et al*., 2006).

Objectives

In the current study, the sorption behavior of phenanthrene in a series of various rank coals such as lignite, bituminous coals, semi-anthracite and anthracite, as well as naturally coked coals and industrial cokes, is examined (Figure 1). The rank series represents a wide range of coal basins and coal-forming periods, ranging from Gondwana coals from Australia and South Africa, Laurasian coals from China and Poland, and Neogene lignite from the Czech Republic, thus demonstrating variable physical and chemical characteristics and most importantly, maceral contents (Table 1). The main purpose of this study is to evaluate the impact of coal rank upon sorption attributes, but also to test the hypothesis that sorption will increase proportionally to carbonized material (e.g. inertinite content) in higher-rank coals, as it was observed for low-rank coals (Kalaitzidis *et al*., 2006).

Methods

In total twenty-two samples were analyzed, comprising lignite (ERT_3,_4), bituminous coal (ERT_5,_6,_7,_10,_11, _12,_13,_14,_15,_16), anthracite (ERT_1,_2,_8,_9), naturally coked coals (ERT_18,_19) and industrial cokes (ERT_17,_20,_21,_22). On the representative samples proximate, ultimate and petrographical analyses were conducted. Proximate analysis was performed according to ASTM (D3174; D3175; D3302, 2004). Ultimate analysis was carried out using a Carlo Erba EAGER 200 Automatic Analyzer according to ASTM D5373, 2004. Maceral analysis was performed according to ISO 7404-3 (2009) using a Leica DMRX coal-petrography microscope (ICCP, 1998, 2001; Sýkorová *et al*., 2005; ASTM D5061, 2007; Pickel *et al*., 2017). Vitrinite reflectance (Ro%) and bireflectance (Rbi%) were measured according to ISO 7404-5 (2009) using Leica MPV/SP spectral photometer and AxioImager M1m/Zeiss+MSP 400 Spectrophotometer.

Additionally, all samples were tested for their sorption capacity in batch triplicate reactors at the same initial phenanthrene concentration (Co) of 250 μg/L. Based on the sorption and petrographical analysis results, nine samples were selected for further sorption experiments of phenanthrene at concentrations (Co), ranging from 20 to 200 μg/L (Kleineidam *et al*., 1999; Karapanagioti and Sabatini, 2000; Karapanagioti *et al*., 2001), as well as for BET analysis.

The surface area, pore volume and pore size distribution of selected samples were determined by nitrogen gas (N_2) adsorption-desorption with the Tristar 3000 Analyzer (Micrometrics® GA, USA) using the Brunauer, Emmett, and Teller (BET) equation, at the Laboratory of Heterogeneous Catalysis, Department of Chemistry of the University of Patras.

Results and Discussion

Proximate analysis determines that the moisture varies from 0.7 to 10.0 wt% (on an as-received basis). The ash yield shows a high variability with values ranging from 2.5 to 64.8 wt% (db). The volatile matter yields vary from 2.9 to 58.8

wt% (daf). The carbon content of the samples ranges from 59 to 95 wt% (daf). Hydrogen and nitrogen fluctuate from 0.3 to 6.2 wt% and 1.1 to 2.3 wt% (daf), respectively. Sulfur content varies from 0.1 to 3.9 wt% (daf).

Table 1. Samples characteristic, rank, results of proximate and ultimate analyses, vitrinite reflectance and bireflectance.

Sample	**Location**	**Ash** (wt.%, db)	**VM** (wt.%, daf)	**Ro%**	**Rank**
ERT_1	South Africa	14.2	11.3	2.31	Anthracite C
ERT_2	China	12.8	10.6	3.37	Anthracite B
ERT_3	Germany	2.5	58.8	0.32	Lignite B
ERT_4	Czech	2.6	54.4	0.30	Lignite B
ERT_5	Australia	22.2	31.5	0.73	Bituminous C
ERT_6	Australia	11.6	21.7	1.28	Bituminous B
ERT_7	Australia	16.6	20.5	1.52	Bituminous A
ERT_8	Australia	10.1	8.6	4.38	Anthracite A
ERT_9	Australia	12.1	10.9	4.63	Anthracite A
ERT_10	Australia	5.3	24.0	1.20	Bituminous B
ERT_11	Australia	7.0	18.2	1.61	Bituminous A
ERT_12	Australia	47.4	17.4	1.90	Bituminous A
ERT_13	Australia	5.4	19.8	1.20	Bituminous B
ERT_14	Poland	9.6	29.4	1.11	Bituminous B
ERT_15	Poland	6.0	36.8	0.87	Bituminous C
ERT_16	Poland	7.8	25.5	1.25	Bituminous B
				Rbi%	
ERT_17	Australia	12.0	6.3	5.52	Coke
ERT_18	Australia	64.8	18.6	4.75	Coked coal
ERT_19	Australia	64.6	15.8	3.70	Coked coal
ERT_20	Poland	11.0	2.9	4.72	Coke
ERT_21	Poland	13.0	4.1	1.43	Coke
ERT_22	Poland	12.1	3.0	4.89	Coke

VM: volatile matter; Ro%: vitrinite reflectance; Rbi%: bireflectance; ar: as-received basis; db: dry basis; daf: dry, ash-free basis.

The petrographical analysis indicates that huminite is the dominant maceral group in the lignite samples ranging from 85.6 to 92.6 vol%, on an organic matter basis. Vitrinite is the dominant maceral in the bituminous coal and anthracite samples, ranging from 56.9 to 100 vol%, where two of them (ERT_8,9) were anthracite A with 100 vol% vitrinite. Inertinite content in lignite samples is generally low (<9 vol%), while in bituminous coal and anthracite, it ranges from 3.3 to 40.7 vol%. Liptinite content is up to 10.6 in lignite and bituminous coal samples. Naturally coked and coke samples were dominated by binder phase (69.6-95.0 vol%) and less filler phase (5.0-30.0 vol%).

The phenanthrene sorption distribution coefficient (Kd, $Kd = qe \times Ce^{-1}$) at the same initial phenanthrene concentration (Co) of 250 μg/L ranges from 1,024 to 37,329 L/Kg, with samples ERT_14 and ERT_1 displaying the lowest and the highest values, respectively. Of the 9 samples selected for further sorption experiments, samples ERT_3, ERT_18, and ERT_19 show the highest sorption capacity at both high (Co=180 μg/L) and low concentrations (Co=15 μg/L). Anthracite (ERT_1) exhibited nonlinear sorption behavior (Freundlich exponent $N > 1$), while bituminous coals (ERT_6, _11, _14 _15, _16), showed a correlation between inertinite content and sorption nonlinearity ($N < 1$). Coke samples (ERT_18, _19) displayed the highest organic carbon-normalized sorption capacity (Koc, $Koc = Kd \times foc^{-1}$) at low phenanthrene concentrations.

The BET analysis reveals that the surface areas vary from 1.0 to 41.2 m^2/g. Pore volume ranges from 0.0056 to 0.062 cm^3/g. Samples ERT_18 and ERT_19 with high surface area also exhibit high pore volume. The pore size ranges from 62 to 303 Å.

Considering the above, the sorption behavior seems to be affected by the coal rank, except for the lignite (ERT_3) sample. However, if the organic carbon content is considered, it follows the same pattern observed in a previous study (Kalaitzidis *et al*., 2006), which found a positive correlation between inertinite content and Koc, indicating that as inertinite content increases, sorption capacity also increases.

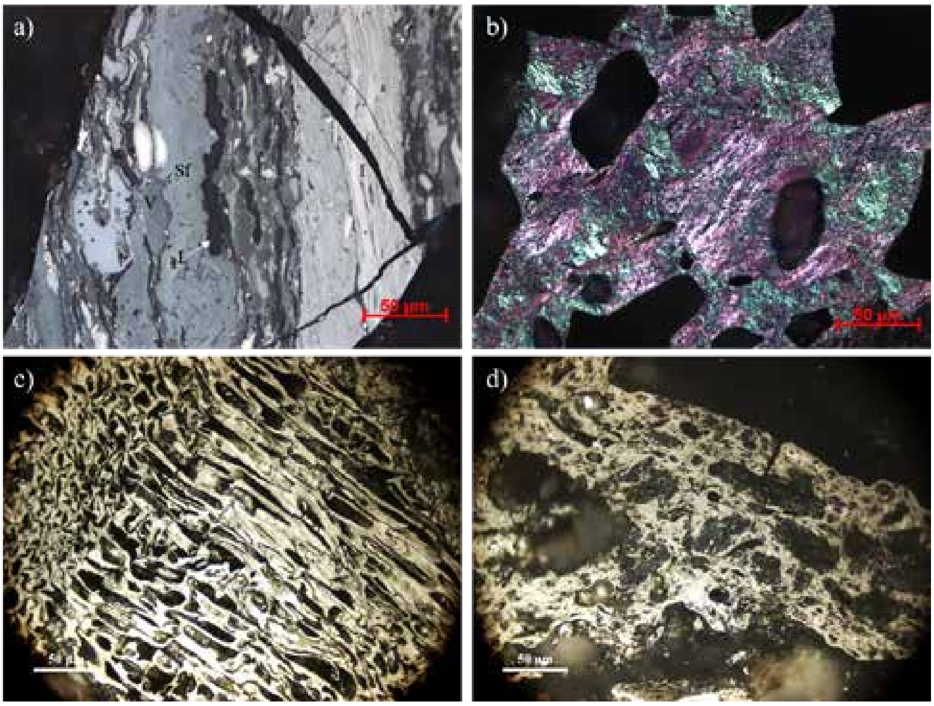

Figure 1. Photomicrographs of selected samples; a) ERT_14 bituminous B coal, V: vitrinite, Sf: semifusinite, L: liptinite, I: inertinite; b) optical texture of coke sample ERT_20; c) view of inertinite in naturally coked coal ERT_19; d) view of naturally coked coal sample ERT_18.

Conclusions

The anthracite (ERT_1) exhibited the highest sorption capacity (Kd) from all samples, but also its behavior was totally different from the rest samples. Anthracite had a nonlinear Freundlich exponent (N) higher than 1, which suggests that the more the sorbed phenanthrene the higher the affinity of the sorbent for phenanthrene. Bituminous coals (ERT_6, _11, _14 _15, _16) sorption behavior seemed to be affected by the inertinite content in terms of their nonlinearity (N<1); nonlinearity increases (N decreases) with increasing inertinite amount. The two coke samples (ERT_18, _19) demonstrated the highest sorption affinity (Koc); which is the sorption capacity normalized for the fraction of organic carbon content for phenanthrene at low concentrations.

Acknowledgments

The authors would like to thank Ms. Vasiliki Kostopoulou and Mr. Dimitrios Bampagenes for conducting laboratory experiments. Dr. Dimitrios Vachliotis, Laboratory of Instrumental Analysis, Faculty of Sciences, University of Patras, is also acknowledged for performing the Carlo Erba analysis.

References

Agency for Toxic Substances and Disease Registry (ATSDR), 1995. Toxicological profile for Polycyclic Aromatic Hydrocarbons (PAHs). Atlanta, GA: U.S. Department of Health and Human Services, Public Health Service.

American Society for Testing and Materials (ASTM) D3174, 2004. Standard Method for Ash in the Analysis Sample of Coal and Coke from Coal. 2004 Annual Book of ASTM Standards, Gaseous Fuels; Coal and Coke, vol. 05. ASTM, Philadelphia, PA, pp. 322–326 06.

American Society for Testing and Materials (ASTM) D3175, 2004. Standard Method for Volatile Matter in the Analysis Sample of Coal and Coke. 2004 Annual Book of ASTM Standards, Gaseous Fuels; Coal and Coke, vol. 05. ASTM, Philadelphia, PA, pp. 327–330 06.

American Society for Testing and Materials (ASTM) D3302, 2004. Standard Method for Total Moisture in Coal. 2004 Annual

Book of ASTM Standards, Gaseous Fuels; Coal and Coke, vol. 05. ASTM, Philadelphia, PA, pp. 352–358 06.

American Society for Testing and Materials (ASTM) D5061, 2019. Standard Test Method for Microscopical Determination of the Textural Components of Metallurgical Coke. 2019 Annual Book of ASTM Standards, Gaseous Fuels; Coal and Coke, vol. 05. ASTM, West Conshohocken, PA, pp. 278–283.Kalaitzidis, S., Karapanagioti, H., Christanis, K., Bouzinos, A. and Iliopoulou, E., 2006. Evaluation of peat and lignite phenanthrene sorption properties in relation to coal petrography: the impact of inertinite. Int. J. Coal Geol., 68: 30-38.

American Society for Testing and Materials (ASTM) D5373, 2004. Standard Test Methods for Instrumental Determination of Carbon, Hydrogen and Nitrogen in Laboratory Samples of Coal and Coke. 2004 Annual Book of ASTM Standards, Gaseous Fuels; Coal and Coke, vol. 05. ASTM, Philadelphia, PA, pp. 504–507 06.

Hussar, E., Richards, S., Lin, Z. Q., Dixon, R. P., & Johnson, K. A., 2012. Human health risk assessment of 16 priority polycyclic aromatic hydrocarbons in soils of Chattanooga, Tennessee, USA. Water, Air, & Soil Pollution, 223, 5535-5548.

International Committee for Coal Petrology (ICCP), 1998. The new vitrinite classification (ICCP System 1994). Fuel 77 (5), 349–358.

International Committee for Coal Petrology (ICCP), 2001. The new inertinite classification (ICCP System 1994). Fuel 80, 459–471.

International Standard Organisation (ISO) 7404-2, 2009: Methods for the Petrographic Analysis of Coals—Part 2: Method of Determining Microscopically the Reflectance of Vitrinite. International Organization for Standardization, Geneva, Switzerland, 7 p.

International Standard Organisation (ISO) 7404-3., 2009. Methods for the Petrographic Analysis of Coals—Part 3: Method of Determining Maceral Group Composition., International Organization for Standardization, Geneva, Switzerland, 7 p.

International Standard Organisation (ISO) 7404-5, 2009. Methods for the Petrographic Analysis of Coals—Part 5: Method of Determining Microscopically the Reflectance of Vitrinite. International Organization for Standardization, Geneva, Switzerland, 12 p.

Kalaitzidis, S., Karapanagioti, H., Christanis, K., Bouzinos, A. and Iliopoulou, E., 2006. Evaluation of peat and lignite phenanthrene sorption properties in relation to coal petrography: the impact of inertinite. Int. J. Coal Geol., 68: 30-38.

Karapanagioti, H.K., Kleineidam, S., Sabatini, D.A., Grathwohl, P. and Ligouis, B., 2000. Impactsof Heterogeneous Organic Matter on Phenanthrene Sorption: Equilibrium and Kinetic Studieswith Aquifer Material, Environ. Sci. Technol., 34, 406-414.

Karapanagioti, H.K., Sabatini, D.A., 2000. Impacts of heterogeneous organic matter on phenanthrene sorption: different aquifer depths. Environ. Sci. Technol. 34, 2453–2460.

Kleineidam, S., Rügner, H., Ligouis, B., & Grathwohl, P., 1999. Organic matter facies and equilibrium sorption of phenanthrene. Environmental Science & Technology, 33(10), 1637-1644.

Ligouis, B., Kleineidam, S., Karapanagioti, H.K., Kiem, R., Grathwohl, P., and Niemz, C., 2005. Organic petrology: a new tool to study contaminants in soils and sediments. In: E. Lichtfouse, J. Schwarzbauer, D. Robert (Eds.), Environmental chemistry, Green Chemistry and Pollutants in Ecosystems. Springer-Verlag, Berlin, p. 89-98.

Patel, A. B., Shaikh, S., Jain, K. R., Desai, C., & Madamwar, D., 2020. Polycyclic aromatic hydrocarbons: sources, toxicity, and remediation approaches. Frontiers in Microbiology, 11, 562813.

Pickel, W., Kus, J., Flores, D., Kalaitzidis, S., Christanis, K., Cardott, B.J., Misz-Kennan, M., Rodrigues, S., Hentschel, A., Hamor-Vido, M., Crosdale, P., Wagner, N., ICCP, 2017. Classification of liptinite–ICCP System 1994. International Journal of Coal Geology, 169, 40-61.

Sýkorová, I., Havelcová, M., Trejtnarová, H., Matysová, P., Vašíček, M., Kříbek, B., Suchý, V., Kotlík, B., 2009. Characterization of organic matter in dusts and fluvial sediments from exposed areas of downtown Prague, Czech Republic. International Journal of Coal Geology, 80(2), 69-86.

Van der Oost, R., Beyer, J., & Vermeulen, N. P., 2003. Fish bioaccumulation and biomarkers in environmental risk assessment: a review. Environmental toxicology and pharmacology, 13(2), 57-149.

White, A.J., Bradshaw, P.T., Herring, A.H., Teitelbaum, S.L., Beyea, J., Stellman, S.D., Steck, S.E., Mordukhovich, I., Eng, S.M., Engel, L.S., Conway, K., Hatch, M., Neugut, A.I., Santella, R.M., Gammon, M.D., 2016. Exposure to multiple sources of polycyclic aromatic hydrocarbons and breast cancer incidence. Environ. Int. 89-90, 185–192.

Yan, C., Yang, Y., Liu, M., Nie, M., & Zhou, J. L., 2011. Phenanthrene sorption to Chinese coal: Importance of coal's geochemical properties. Journal of hazardous materials, 192(1), 86-92.